

**PARTICLE-BASED SMOOTHED PARTICLE HYDRODYNAMICS AND
DISCRETE-ELEMENT MODELING OF THERMAL BARRIER COATING
REMOVAL PROCESSES**

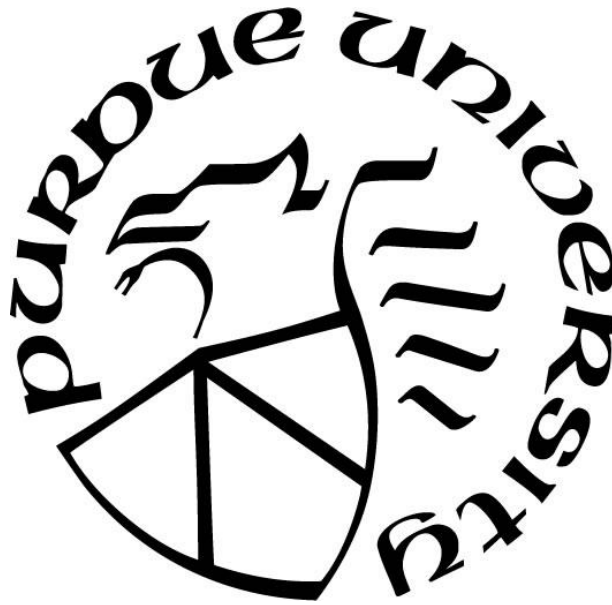
by
Jian Zhang

A Dissertation

Submitted to the Faculty of Purdue University

In Partial Fulfillment of the Requirements for the degree of

Doctor of Philosophy



School of Mechanical Engineering

West Lafayette, Indiana

December 2021

THE PURDUE UNIVERSITY GRADUATE SCHOOL
STATEMENT OF COMMITTEE APPROVAL

Dr. Jing Zhang, Co-Chair

Department of Mechanical and Energy Engineering

Dr. Carl Wassgren, Co-Chair

School of Mechanical Engineering & School of Industrial and Physical Pharmacy

Dr. Marcial Gonzalez

School of Mechanical Engineering

Dr. Dan Daehyun Koo

School of Engineering and Technology

Dr. Babak Anasori

Department of Mechanical and Energy Engineering

Approved by:

Dr. Nicole L. Key

For my wife Guanying Chen and my daughter Xinyi Zhang

ACKNOWLEDGMENTS

Most importantly, I would like to express my sincere gratitude to my academic advisors, Professor Jing Zhang and Professor Carl Wassgren, for their expert academic advice, invaluable guidance, and generous assistance during my studies and research at Purdue University. I would also like to acknowledge my committee members, Professor Marcial Gonzalez, Professor Dan Daehyun Koo, and Professor Babak Anasori, for serving as my committee members, and for their invaluable contribution during my studies.

The work is partially supported by the “Human Resources Program in Energy Technology (No. 20194030202450)” of the Korea Institute of Energy Technology Evaluation and Planning (KETEP), granted financial resources from the Ministry of Trade, Industry & Energy (MOTIE) Republic of Korea, and by the National Research Foundation of Korea (NRF) grant funded by the Korea government (MSIP) (2018R1A5A6075959). I would like to express my deep thanks to Professor Yeon-Gil Jung from Changwon National University, Dr. Jingxiao Xu from Livermore Software Technology Company, Dr. Bing Chen from Shanghai Jiaotong University, and Dr. Yanmei Zhang from the China University of Petroleum, who assisted me with my research.

I would like to thank my lab mates Dr. Lingbin Meng, Xuehui Yang, Sugrim Sagar, Tejsh Dube, and many others, who gave me help in many aspects.

I am forever grateful to my parents, Zhenmei Wang and Bingsheng Zhang, my sister Xunsun Zhang, my wife, Guanying Chen, and my daughter, Xinyi Zhang, for their love and support during my doctoral studies.

TABLE OF CONTENTS

ABSTRACT.....	16
1. INTRODUCTION	18
1.1 Background	18
1.2 TBC Removal Process - A Review	27
1.2.1 Grinding	28
1.2.2 Abrasive Water Jet.....	33
1.3 Particle-Based Modeling Methods.....	36
1.3.1 SPH method	36
1.3.1.1 Kernel Approximation of A Function	37
1.3.1.2 Particle Approximation.....	37
1.3.1.3 SPH Method Advantages and Limitations	39
1.3.2 DEM Model	40
1.3.2.1 Governing Equations in DEM	40
1.3.2.2 DEM Method Advantages and Limitations.....	41
1.4 Problem Statement	42
1.5 Objective and Research Tasks of the Thesis.....	43
1.6 Structure of the Thesis	43
2. REMOVAL AND REPAIR TECHNIQUES FOR THERMAL BARRIER COATINGS: A REVIEW	45
2.1 Introduction.....	45
2.2 Removal Methods for Thermal Barrier Coated Components	46
2.2.1 Blasting Methods	46
2.2.1.1 Grit Blasting with Abrasive Media.....	46
2.2.1.2 Grit Blasting with Solid CO ₂	47
2.2.1.3 Pencil Grit Blasting	47
2.2.2 Chemical Stripping	48
2.2.2.1 Autoclaving Process	48
2.2.2.2 Aqueous Stripping Solution Containing Acid Fluoride Salt	49
2.2.2.3 Acid Stripping.....	50
2.2.3 Water Jet	51

2.2.3.1	Non-abrasive Water Jet	51
2.2.3.2	Localized Water Jet	52
2.2.3.3	Computer Numerically Controlled Abrasive Waterjet	53
2.2.4	Laser Ablation	53
2.3	Repair Methods for Thermal Barrier Coated Components.....	55
2.3.1	Plasma Spraying	55
2.3.1.1	Suspension Plasma Spraying (SPS).....	55
2.3.1.2	Plasma Spray Technique	56
2.3.1.3	Laser-Induced Breakdown Spectroscopy (LIBS).....	57
2.3.2	Chemical Paste.....	57
2.3.2.1	Partially Stabilized Zirconia	57
2.3.2.2	Scandia Ytria Stabilized Zirconia (SYSZ) Ceramic Paste	58
2.3.2.3	Gel Repairing.....	59
2.3.2.4	Composite Preform.....	60
2.4	Assessment of Different Coating Removal and Repair Techniques.....	61
2.5	Summary and Remarks	65
3.	NUMERICAL SIMULATION OF IMPACT BEHAVIOR OF CERAMIC COATINGS USING SMOOTHED PARTICLE HYDRODYNAMICS METHOD	66
3.1	Introduction.....	66
3.2	Model Description	68
3.2.1	Smoothed Particle Hydrodynamics (SPH) Method.....	68
3.2.2	Numerical Model Details.....	70
3.3	Results and Discussion	73
3.3.1	Damage of the Ceramic Coating Layer	73
3.3.2	Deformation of Spherical Impacting Particle	86
3.4	Experimental Comparison	88
3.5	Summary and Future Work.....	89
4.	NUMERICAL SIMULATION OF REMOVING THERMAL BARRIER COATINGS USING ABRASIVE WATER JET WITH SMOOTHED PARTICLE HYDRODYNAMICS METHOD	91
4.1	Introduction.....	91
4.2	Model Description	93
4.2.1	The SPH Method	93

4.2.2	SPH Model Details	94
4.2.2.1	Geometry of The Model	94
4.2.2.2	Material Constitutive Model.....	95
4.2.2.3	Material Properties	96
4.2.2.4	Boundary Conditions and Model Design Matrix	98
4.2.2.5	Erosion Analytical Model.....	98
4.3	Results and Analysis	99
4.3.1	Effect of Incident Angle on The Morphology of The Impact Pit	99
4.3.2	Effect of Abrasive Concentration on Morphology of The Impact Pit	102
4.3.3	Effects of Impacting Time on Impact Pit Hole Morphology.....	103
4.3.4	Analytical Erosion Model.....	104
4.4	Summary	105
5.	MODELING OF MACHINING OF EB-PVD CERAMIC COATINGS USING SMOOTHED PARTICLE HYDRODYNAMICS METHOD.....	107
5.1	Introduction.....	107
5.2	Model Validation and Convergence Studies.....	110
5.2.1	Mechanical Validation.....	110
5.2.2	Thermal Validation	113
5.3	Modeling of Ceramics Cutting Process	115
5.3.1	Columnar Grain Ceramic Cutting Model	115
5.3.2	Cutting Tool Model	116
5.3.3	Materials and Damage Models	117
5.4	Results and Discussion	119
5.4.1	Effect of Cutting Depth on Cutting Force and Coating Temperature Increase	119
5.4.2	Effect of Cutting Speed on Cutting Force and Coating Temperature Increase	121
5.4.3	Effect of Cutting Tool's Edge Radius on Cutting Force	122
5.4.4	Effect of Cutting Tool's Rake Angle on Coating Temperature Increase	125
5.5	Summary and Future Work.....	128
6.	MODELING OF MACHINING PROCESS OF EB-PVD CERAMIC COATINGS USING DISCRETE ELEMENT METHOD.....	129
6.1	Introduction.....	129
6.2	DEM Model Description.....	131
6.2.1	Governing Equations in DEM	131

6.2.2	Model Parameter Calibration.....	132
6.2.3	Columnar Grain Microstructure Model and Boundary Conditions.....	133
6.3	Results and Discussion	134
6.3.1	Model Calibration Parameter Results.....	134
6.3.2	Effect of Cutting Speed on Cutting Force and Chip Morphology.....	134
6.3.3	Effect of Cutting Depth on Cutting Force and Chip Morphology.....	136
6.3.4	Cutting Force and Cutting Speed Correlation	144
6.4	Summary.....	145
7.	MODELING OF FAILURE MECHANISMS OF THERMAL BARRIER COATING WITH REALISTIC STRUCTURE USING DISCRETE ELEMENT METHOD.....	147
7.1	Introduction.....	147
7.2	DEM Model	149
7.2.1	Geometrical Model	149
7.2.2	Governing Equations in DEM	150
7.2.3	Model Calibration.....	151
7.2.4	Fracture Criterion.....	153
7.3	Results and Discussion	153
7.3.1	Indentation Test	153
7.3.2	Mode I - Erosion (Near Surface Cracking/Lateral Cracking)	154
7.3.3	Mode II - Compaction Damage	156
7.3.4	Mode III - Foreign Object Damage	158
7.4	Summary.....	160
8.	FRACTURE MECHANISM MAP FOR CERAMIC MACHINING	162
9.	CONCLUSIONS AND FUTURE WORK	164
9.1	Conclusions.....	164
9.2	Contributions of the Thesis Work.....	166
9.3	Future Work	167
	REFERENCES	168
	VITA.....	183
	LIST OF PUBLICATIONS	184

LIST OF TABLES

Table 2.1. Removal Methods for Thermal Barrier Coated Components.....	62
Table 2.2. Repair Methods for Thermal Barrier Coated Components.....	65
Table 3.1. Parameters used in the Mie–Grüneisen equation of state for the SPH ceramic layer. [82].	71
Table 3.2. JH-2 parameters of finite element ceramic layer [86].	72
Table 3.3. Design matrix of impact velocities V_x and V_z components (m/s) at three impact angles 0° , 30° , and 60°	73
Table 4.1. JH-2 model parameters for the TBC layer [106].	97
Table 4.2. The parameters in the Gruneisen equation for the water jet and abrasive particles [82 100].	97
Table 4.3. Design matrix of processing parameters used in the model.	98
Table 5.1. JH-2 parameters of ceramic coating [106].....	118
Table 6.1. Simulated mechanical properties of the EB-PVD ceramic coating using the calibrated DEM parameters compared against the experimental data in the literature [148-150]	134
Table 7.1. Calibrated mechanical properties of the EB-PVD ceramic coating from the experimental data in the literature [148-150] and the simulated DEM results from this study.....	152

LIST OF FIGURES

Figure 1.1. Trend and forecast for the global aircraft engine blade market [4].	19
Figure 1.2. Ceramic TBC market share, by product type, 2016 [7].	19
Figure 1.3. Thermal barrier coating structure and associated layers. The typical thickness of each layer is also given [8].	20
Figure 1.4 Schematic illustrating the types of damage in an engine environment [8].	21
Figure 1.5. TBCs loss: (a) spalled and delaminated [10]; (b) distress[11]; (c) erosion [12].	21
Figure 1.6. The temperature gradient in a TBC system across different layers [9].	23
Figure 1.7. Sintering shrinkage in the outer zone of TBC results in tension in the outermost columnar grains, which pull on TGO interfaces [15].	24
Figure 1.8. Growth of the TGO eventually results in damage to the TGO and its interfaces [15].	25
Figure 1.9. Micrographs illustrating the effect of FOD in an EB PVD TBC (0.5mm angular alumina particle at an estimated 100m/s) [16, 17].	26
Figure 1.10. Schematics of the cutting process in (a) a ductile failure mode, and(b) a brittle failure mode [25].	28
Figure 1.11. A typical grinding experimental system (a) and diamond grits over grinding wheel (b) [30, 31].	29
Figure 1.12. Machine unit diagram [29].	30
Figure 1.13. Localized deformation and fracture with different tip radius [29].	31
Figure 1.14. The SEM images at different cutting speeds: (a) 11 m/min; (b) 44 m/min; (c) 670 m/min [33].	32
Figure 1.15. A typical microstructure of an EB-PVD (right) and APS (left) TBC [35].	32
Figure 1.16. A schematic diagram of the failure modes for an APS and EB-PVD TBC [35].	33
Figure 1.17. Erosion damage to an APS [36] and EB-PVD [35] TBC.	33
Figure 1.18. TBC removal without damaging bond coat using AWJ process [37].	34
Figure 1.19. Waterjet stripping of TBC on a turbine blade [37].	34
Figure 1.20. Turbine component coating before and after removal AWJ process [39].	35
Figure 1.21. Investigation of the influence of the machining angle during the AWJ processes[37].	35
Figure 1.22 SPH particle approximations in a two-dimensional problem domain Ω with a surface S . W is the smoothing function that is used to approximate the field variables at particle i using	

averaged summations over particles j within the support domain with a cut-off distance of κh_i [40].	38
Figure 1.23. Discrete element: (a) 2D circular particle; (b) 3D spherical particle [43]	40
Figure 2.1. Schematic of coating removal using solid CO_2 [48].	47
Figure 2.2. Coating removal process [49].	48
Figure 2.3. Coating repair process [49].	48
Figure 2.4. Schematic of the removal of the ceramic layer with the presence of ceramic material in the cooling hole [50].	49
Figure 2.5. Schematic of ceramic layer removal by exposure to a caustic solution at an elevated temperature and pressure [50].	49
Figure 2.6. Schematic of a cross-sectional view of an airfoil portion of a gas turbine engine turbine component [51].	50
Figure 2.7. Schematic of a gas turbine engine nozzle section [55].	51
Figure 2.8. Schematic of a cross-sectional view through a substrate region [55].	52
Figure 2.9. Schematic of a localized spalled region of the ceramic layer [56].	52
Figure 2.10. Schematic of using water jet to remove the spalled region and form a tapered profile [56]	53
Figure 2.11. T working principle of a laser system [57].	54
Figure 2.12. Schematic cross-sectional view of an exemplary TBC to be processed [58].	54
Figure 2.13. The schematic of using SPS technique to repair the cracked TBC [59].	56
Figure 2.14. Generalized Schematic of LIBS [60].	57
Figure 2.15. Schematic of the damaged coating [63].	58
Figure 2.16. Cross-sectional side view of a typical TBC system [64].	59
Figure 2.17. The localized spallation in the TBC system having been repaired using the in-situ methods and the TBC patch composition of the present invention [64].	59
Figure 2.18. Schematic representation of a cross-section of a coated turbine component, wherein the coating includes a damaged portion [66].	60
Figure 2.19. A process flow chart for repairing a damaged portion of a coated metal component [66].	61
Figure 2.20. Schematic representation of a cross-section of a coated composite preform [66].	61
Figure 3.1. SPH model of a spherical alumina particle impacting on an alumina coating.	71

Figure 3.2. Side view of the impact with different velocities and impact angles (a) 100 m/s & 0°, (b) 100 m/s & 30°, (c) 100 m/s & 60°, (d) 200 m/s & 0°, (e) 200 m/s & 30°, (f) 200 m/s & 60°, (g) 300 m/s & 0°, (h) 300 m/s & 30°, and (i) 300 m/s & 60°.....	74
Figure 3.3. von Mises stress distributions in the coating layers at the end of impact: (a) 100 m/s & 0°, (b) 100 m/s & 30°, (c) 100 m/s & 60°, (d) 200 m/s & 0°, (e) 200 m/s & 30°, (f) 200 m/s & 60°, (g) 300 m/s & 0°, (h) 300 m/s & 30°, and (i) 300 m/s & 60°.....	75
Figure 3.4. Total energy evolutions of the coating layer at different impact angles and velocities. (a) 100 m/s & 0°, 30°, 60°; (b) 200 m/s & 0°, 30°, 60°; (c) 300 m/s & 0°, 30°, 60°.....	76
Figure 3.5. Internal energy evolution of the coating layer at different impact angles and velocities. (a) 100 m/s & 0°, 30°, 60°; (b) 200 m/s & 0°, 30°, 60°; (c) 300 m/s & 0°, 30°, 60°.....	78
Figure 3.6. The final total energy values of SPH coating layer at different impact angles and velocities at the end of impact at 100 ms.....	80
Figure 3.7. The final internal energy values of SPH coating layer at different impact angles and velocities at the end of impact at 100 ms.....	81
Figure 3.8. Internal energy of the coating as a function of the square of the vertical velocity component of the particle.....	82
Figure 3.9. von Mises stress and penetration behavior of the coating layers after the impact: V_x and V_z are (a) $V_x=0$ m/s & 259.8 m/s, (b) 150 m/s & 259.8 m/s, and (c) 259.8m/s & 259.8 m/s.....	83
Figure 3.10. Coating penetration depth as a function of particle's vertical velocity component.	83
Figure 3.11. von Mises stress distribution in the FEM layer of the combination 300 m/s & 0°..	84
Figure 3.12. von Mises stress distribution evolutions of SPH coating layer at the combination 100 m/s & 0° at different times. (a) 1 ms; (b) 4 ms; and (c) 50 ms.	85
Figure 3.13. The spherical particle deformation after the impact: (a) 300 m/s & 0°, (b) 200 m/s & 0°, (c) 100 m/s & 0°.....	86
Figure 3.14. The spherical particle deformation after the impact: (a) 300 m/s & 0°, (b) 300 m/s & 30°, (c) 300 m/s & 60°.....	86
Figure 3.15. Kinetic energy evolutions of the spherical particle at different impact velocities. ..	87
Figure 3.16. Kinetic energy evolution of the spherical particle at different impact angles.....	87
Figure 3.17. The spherical particle's maximum, minimum and range of kinetic energy values at different impact velocities: 300 m/s & 0°, 200 m/s & 0° and 100 m/s & 0°.	88
Figure 3.18: Cross sectional view of the experimental impact pit of YSZ ceramic coating [91].	89
Figure 4.1. A precision abrasive waterjet process removing thermal barrier coating from a turbine blade component [96].	92

Figure 4.2. The side view of the SPH model for the TBC layer removal using the AWJ process. The abrasive particles in the water jet are enlarged to show their existence. The inset shows the 3D view of the SPH model.	95
Figure 4.3. TBCs' typical features of the impact pit hole with incident angle 90°: (a) isometric view of simulation results, (b) top view of simulation results, (c) top view of experiment result [98].	100
Figure 4.4. The cross-sectional profiles of the impact pit holes with different incident angles: 30°, 45°, 60°, and 90°. (a) Simulated results from this study, (b) experiment result from Ref. [98]. (Water jet direction is towards the left).	101
Figure 4.5. Pit hole depth's dependent on the vertical velocity component (V_z). The fitted curve using the 2 nd order polynomial is also shown.	102
Figure 4.6. Cross-sectional views of impact pit hole profiles with abrasives (a) Simulated results (b) experiment results [98]. (Water jet direction is towards left).	103
Figure 4.7. Cross-sectional views of the pit holes at different impacting times: (a) simulation results; (b) experiment results [98]. The curved arrows show the deepest points gradually shift to the right as the AWJ process proceeds, due to 30° of incident angle.	104
Figure 4.8. Simulated erosion rates at different incident angles. The analytical model [109] is also included for comparison.	105
Figure 5.1. Cross-sectional view of an EB-PVD thermal barrier coating, which shows the columnar grains [113].	108
Figure 5.2. Side views of the impact bars of (a) undeformed SPH01, (b) undeformed SPH02, (c) undeformed SPH03, (d) undeformed FEM, (e) deformed SPH01, (f) deformed SPH02, (g) deformed SPH03, and (g) deformed FEM.	110
Figure 5.3. Reduction of the bar length vs. time for the SPH and FEM models.	111
Figure 5.4. Evolution of kinetic energy for the SPH and FEM models.	112
Figure 5.5. The kinetic energy of the SPH bars at different normalized particle densities.	113
Figure 5.6. Temperature distribution in the SPH model.	114
Figure 5.7. Temperature vs. length for the SPH model (solid lines) and the analytical solution (Eq. 2, dotted lines) at different moments.	114
Figure 5.8. Ceramic coating cutting model set-up. (a) The whole model shows the ceramic coating and cutter, (b) Top view of the ceramic coating, (c) the magnified local view of the ceramic coating to illustrate the columnar grains, (d) the side view of the columnar grains corresponding to (c). The gray regions in (c) and (d) are artificial for better visualization of the columnar grains.	115
Figure 5.9. Side view of cutting tools and their finite element mesh, with different radii of cutting edge angle R : (a) $R=10\text{ }\mu\text{m}$; (b) $R=0\text{ }\mu\text{m}$. The rake angle and clearance angle are also labeled.	116
Figure 5.10. Main cutting force F_x evolution at different cutting depths.	119

Figure 5.11. Main cutting force F_x at the stable stage at different cutting depths. SPH model vs. fracture mechanics analytical solution [133].	120
Figure 5.12. Maximum temperature evolution in the ceramic layer for different cutting depths	121
Figure 5.13. Main cutting force F_x evolution under different cutting speeds	121
Figure 5.14. Maximum temperature evolution in the ceramic layer at different tool cutting speeds	122
Figure 5.15. Stress distribution at different cutting tool edge radii: (a) $R=10\text{ }\mu\text{m}$; (b) $R=0\text{ }\mu\text{m}$. The tool rake angle is 26.6° .	123
Figure 5.16. Cutting force evolution at different cutting tool edge radii.	124
Figure 5.17. Maximum temperature evolution in the ceramic layer at different cutting tool edge radii.	125
Figure 5.18. Stress distribution with the tool rake angle of 11.6° . The cutting tool edge radius is $10\text{ }\mu\text{m}$.	126
Figure 5.19. Cutting force evolution F_x under different tool rake angles.	127
Figure 5.20. Maximum temperature evolution in the ceramic coating under different tool rake angles.	127
Figure 6.1. DEM model parameter calibration tests: (a) uniaxial compression test; (b) uniaxial tensile test, and (c) fracture toughness test.	132
Figure 6.2. Cross-sectional view of an EB-PVD thermal barrier coating, which shows the columnar grain structure [151].	133
Figure 6.3. DEM cutting model of the TBC layer. The cutting tool is also shown.	133
Figure 6.4. Chip formations at different speeds: (a) $v=2\text{ m/s}$; (b) $v=4\text{ m/s}$; (c) $v=8\text{ m/s}$.	135
Figure 6.5. Horizontal cutting force at different cutting speeds.	135
Figure 6.6. Evolutions of the number of broken bonds at different cutting speeds.	136
Figure 6.7. Chip formations at different cutting depths: (a) $d=5\text{ }\mu\text{m}$, (b) $d=25\text{ }\mu\text{m}$, and (c) $d=75\text{ }\mu\text{m}$. The red color represents the broken bonds.	137
Figure 6.8. Horizontal cutting force (F_x) at different cutting depths: (a) $d=5\text{ }\mu\text{m}$; (b) $d=25\text{ }\mu\text{m}$; (c) $d=75\text{ }\mu\text{m}$. $t_1 \sim t_5$ are the five key moments that will be discussed in Figure 9.	138
Figure 6.9. Cracks distribution and chips deformation at five key moments ((a) t_1 , (b) t_2 , (c) t_3 , (d) t_4 , and (e) t_5 .) for three cutting depths: (1) $d=5\text{ }\mu\text{m}$; (2) $d=25\text{ }\mu\text{m}$; and (3) $d=75\text{ }\mu\text{m}$.	140
Figure 6.10. Evolution of the number of broken bonds under different cutting depths.	142
Figure 6.11. Evolution of cutting energy under different cutting depths.	143
Figure 6.12. Side views of the cutting models where the contact forces between particles are shown.: (a) $d=5\text{ }\mu\text{m}$; (b) $d=25\text{ }\mu\text{m}$; (c) $d=75\text{ }\mu\text{m}$.	144

Figure 6.13. The DEM calculated cutting force at different cutting depths, compared with the analytical solution [26].	145
Figure 7.1. Cross-sectional microstructure of TBC system with columnar structure [166].	150
Figure 7.2. DEM model extracted from SEM image with realistic columnar grains and inter-columnar zone.	150
Figure 7.3. DEM model parameter calibration tests: (a) uniaxial compression test; (b) uniaxial tensile test, and (c) fracture toughness test.	152
Figure 7.4. Indentation test DEM model [163].	153
Figure 7.5. Indentation test results: (a) DEM model; (b) experiment result [163].	154
Figure 7.6. Cross-section of an eroded sample of TBCs showing mode I (near-surface cracking) mode [164].	155
Figure 7.7. Crack distribution and TBC deformations of DEM model corresponding to mode I.	155
Figure 7.8. 1 st principal stress distribution with mode I.	156
Figure 7.9. Cross-section of an eroded sample of TBCs showing mode II (compaction damage) mode [164].	157
Figure 7.10. Crack distribution and TBC deformations of DEM model corresponding to mode II.	157
Figure 7.11. 1 st principal stress distribution with mode II.	158
Figure 7.12. Cross-section of an eroded sample of TBCs showing mode III (foreign object damage) mode [164].	159
Figure 7.13. Crack distribution and TBC deformations of DEM model corresponding to mode III.	159
Figure 7.14. 1 st principal stress distribution with mode III.	159
Figure 7.15. Crack distribution and TBC deformations of DEM model corresponding to mode III.	160
Figure 7.16. 1 st principal stress distribution with mode III.	160
Figure 8.1 Fracture mechanism map for ceramic machining: processing parameters vs fracture mode.	163

ABSTRACT

Thermal barrier coatings (TBCs) made of low thermal conductivity ceramic topcoats have been extensively used in hot sections of gas turbine engines, in aircraft propulsion and power generation applications. TBC damage may occur during gas turbine operations, due to either time- and cycle-dependent degradation phenomena, external foreign object damage, and/or erosion. The damaged TBCs, therefore, need to be removed and repaired during engine maintenance cycles. Although several coating removal practices have been established which are based on the trial-and-error approach, a fundamental understanding of coating fracture mechanisms during the removal process is still limited, which hinders further development of the process.

The objective of the thesis is to develop a particle-based coating removal modeling framework, using both the smoothed particle hydrodynamics (SPH) and discrete element modeling (DEM) methods. The thesis systematically investigates the processing-property relationships in the TBC removal processes using a modeling approach, thus providing a scientific tool for process design and optimization.

To achieve the above-mentioned objective, the following research tasks are identified. First a comprehensive literature review of major coating removal techniques is presented in Chapter 2. Chapter 3 discusses an improved SPH model to simulate the high-velocity particle impact behaviors on TBCs. In Chapter 4, the abrasive water jet (AWJ) removal process is modeled using the SPH method. In Chapter 5, an SPH model of the cutting process with regular electron beam physical vapor deposition (EB-PVD) columnar grains is presented. In Chapter 6, a 3D DEM cutting model with regular EB-PVD column grains is discussed. In Chapter 7, a 2D DEM cutting model based on the realistic coating microstructure is developed. Finally, in Chapter 8, based on the particle-based coating removal modeling framework results and analytical solutions, a new fracture mechanism map is proposed, which correlates the processing parameters and coating fracture modes.

The particle-based modeling results show that: (1) for the SPH impact model, the impact hole penetration depth is mainly controlled by the vertical velocity component. (2) The SPH AWJ simulation results demonstrate that the ceramic removal rate increases with incident angle, which is consistent with the fracture mechanics-based analytic solution. (3) The SPH model with regular

EB-PVD columnar grains shows that it is capable to examine the stress evolutions in the coating with columnar grain structures, which is not available if a uniform bulk coating model was used. Additional analysis reveals that the fracture of the columnar grains during the cutting process is achieved through deflection and fracture of the grains, followed by pushing against neighboring grains. (4) The 3D DEM model with regular coating columnar grains shows that, during the coating removal process, a ductile-to-brittle transition is identified which depends on the cutting depth. The transition occurs at the critical cutting depth, which is based on the Griffith fracture criterion. At small cutting depths, the ductile failure mode dominates the cutting process, leading to fine cut particles. As the cutting depth exceeds the critical cutting depth, a brittle failure mode is observed with the formation of chunk-like chips. (5) The 2D DEM model with the realistic coating microstructure shows that there are densification and fracture during the foreign object compaction process, which qualitatively agrees with the experimental observations. (6) The newly proposed coating fracture mechanism map provides guidance to predict three fracture modes, i.e., ductile brittle, and mixed ductile-brittle, as a function of processing parameters, including the cutting depth and cutting speed. The map can be used to determine the processing conditions based on required TBC removal operations: rough cut (brittle mode), semi-finish (mixed ductile-brittle mode), and finish (ductile mode).

1. INTRODUCTION

1.1 Background

Functional coatings are one of the greatest important components for the equipment of power generation including the power generation units, gas turbine engines, and jet propulsion engines. As one of the functional coatings, Ceramic TBCs have attracted increased attention for their excellent performance in advanced applications especially for gas turbine engines [1]. They exist on the surface of the hot section in the turbine engines and can keep the metallic substrates away from hot gases and thus provide thermal protection of insulation. Due to their superb performance in elevating the turbine engine's operating temperatures and thus minimizing the cooling demand TBCs have the ability to increase the engine efficiency, diminish the emissions, and thus complete the high-performance goals [2]. As reported in the literature, about 190°C can be reduced while the TBCs are applied in the component of turbine blade engines. Such a significant reduction in temperature is crucial for the improvement of engine efficiency and ability to high-temperature performance. This reduction in temperature has led to an increase in high-temperature capability and increased engine efficiency. With the help of TBCs, the engine power can increase about 8% the fuel consumption can reduce about 15-20%, and the exhaust gas temperature can increase about 200 K. Using a specific example to illustrate, there are more than 10 million gallons of fuel saved while the energy reduced by using TBCs is applied to engine propulsion [3].

There will be a big input of resources to the global aircraft engine blade market especially for the countries such as India and China. It is expected that the global aircraft engine blade market will have explosive growth due to the development of commercial and military aircraft. As shown in Figure 1.1, the global aircraft engine blade market is expected to reach an estimated \$37.8 billion by 2025 with a compound annual growth rate (CAGR) of 3% to 5% from 2014 to 2025 [4]. The expected strong growth in the global blade market is from the increasing demand for cargo aircraft and the component replacement of engine blades. Due to the technology development in advanced material, it is possible to produce higher lightweight turbine blades. Thus, TBCs, which work as a crucial component in the blades, keep increasing. The global TBCs market is expected to grow from USD 15,577.92 Million in 2019 to USD 23,062.32 Million by the end of 2025 at a CAGR of 6.75% [5]. The aircraft gas turbine industry as a segment should increase to a total of USD 694.8

million by 2021[6] and is expected to expand at a CAGR of 6.7%, in terms of revenue, over the forecast period (2017-2025). As shown in Figure 1.2, the ceramic segment 33.5% accounts for the largest revenue share in the market, owing to the high thermal resistance characteristics of ceramic TBCs [7].

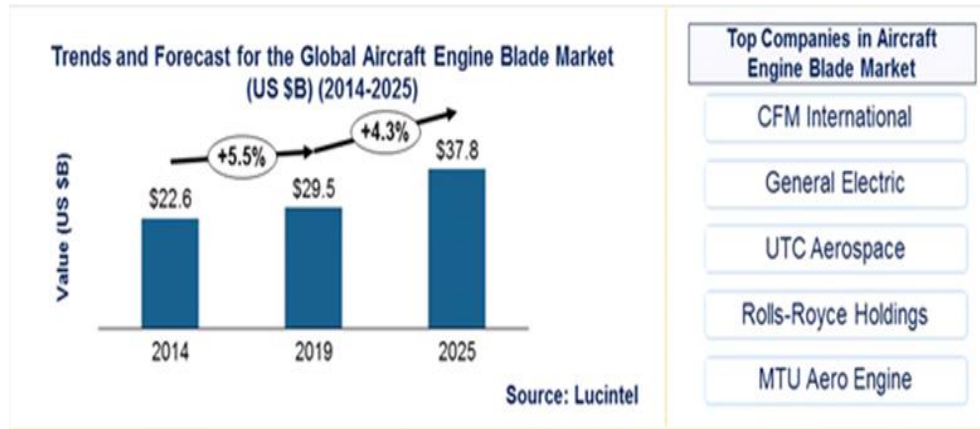


Figure 1.1. Trend and forecast for the global aircraft engine blade market [4].

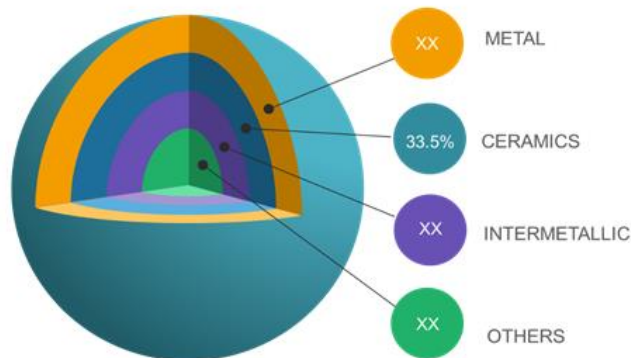


Figure 1.2. Ceramic TBC market share, by product type, 2016 [7].

The properties of TBC systems can be significantly affected by the coating layers' structure and phase composition. At the same time, the interface adhesion between the ceramic coating and metal also has significant effects. As shown in Figure 1.3, a typical TBC system usually contains four layers [8]:

1. A ceramic top coat, typically composed of yttria-stabilized zirconia (YSZ).
2. A thin thermally grown oxide (TGO) layer, which acts as a protecting layer to retard oxygen diffusion and oxidation of the superalloy substrate.
3. A metallic bond coat, typically composed of NiCoCrAlY.

4. A Ni-base superalloy substrate [8].

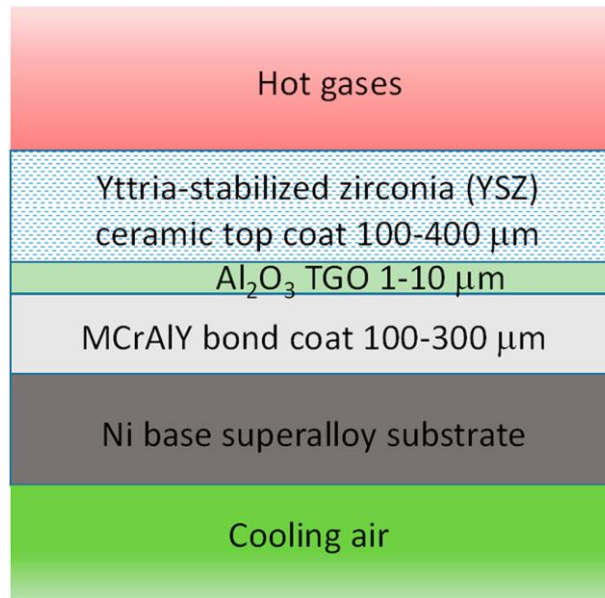


Figure 1.3. Thermal barrier coating structure and associated layers. The typical thickness of each layer is also given [8].

Due to the special requirements of turbine blade engines, TBCs must have the ability to resist environmental erosion and internal mechanical damage. As shown in Figure 1.4 and Figure 1.5 subjected to different kinds of degradation including surface erosion, foreign object damage (FOD) interface oxidation, throughout periodic turbine engine operations, TBC failure can happen in a multitude of ways. The word “failure” of TBCs is defined as that the coating layers eroded or damaged and can not satisfy the requirements as a functional coating. In general, the TBC can be considered to be failed when the top coat layer flakes off and lose the function of thermal insulation. Due to the failure of TBCs critical component damage is induced and thus can decrease the lifecycle of turbine components [9]. There are multiple mechanisms for the failure of the TBCs and this complexity makes the performance of the TBCs study difficult.

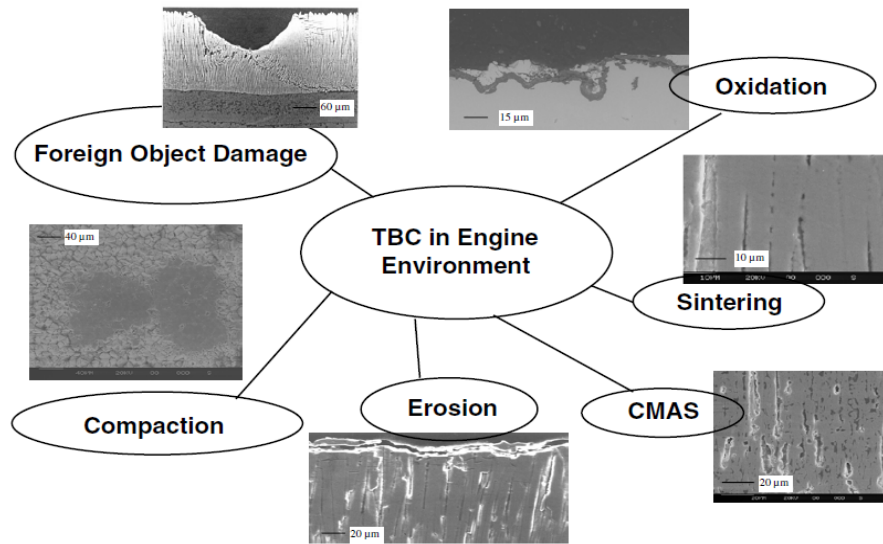


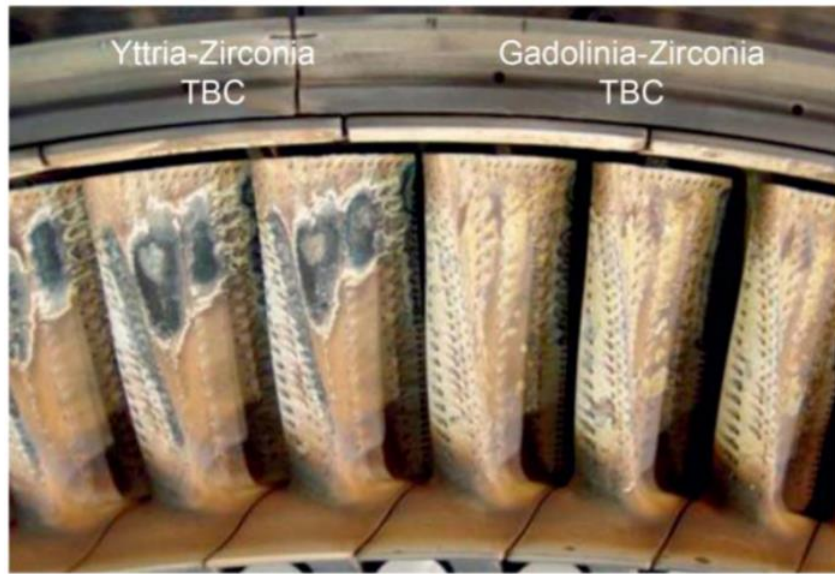
Figure 1.4 Schematic illustrating the types of damage in an engine environment [8].



(a)

Figure 1.5. TBCs loss: (a) spalled and delaminated [10]; (b) distress[11]; (c) erosion [12].

Figure 1.5 continued



(b)



(c)

Failure of the TBC system is usually caused by the following factors [13]:

1. Top coat degradation

- (i) Difference in the thermal expansion coefficient

The cracks occur in the ceramic top layer caused by the difference in the thermal expansion coefficient among different TBCs layers in the coating layer system while TBC serves as a component for thermal insulation in a gas turbine engine. As shown in Figure 1.6, a 100-300 °C temperature drop happens in the top coating layer for a small thickness of coating layer 0.1-0.5

mm [14]. When cracks came out in the top coating layer, the complete failure of the TBC system occurs while the oxygen diffuses to the bond coat.

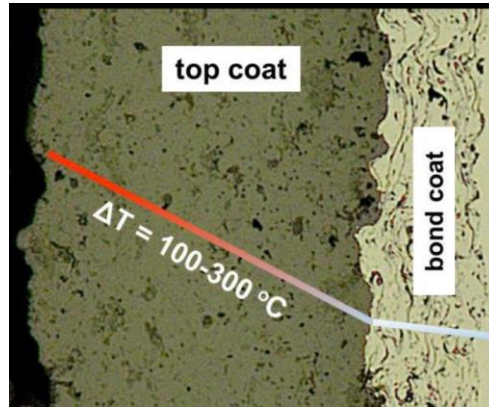


Figure 1.6. The temperature gradient in a TBC system across different layers [9].

(ii) Sintering in the top coating layer

Sintering comes out due to the densification of the TBC layer followed by diminishing porosity and micro-cracks inside the material. The Sintering shrinkage is usually observed under an up temperature of 1100°C in a TBC system [15]. Firstly, it comes out in the outer surface of the top layer, where the temperature is highest. In contrast, the shrinkage in the interface existing between the substrate alloy and the bond coat is much smaller. As shown in Figure 1.7, ‘mud flat’ cracks are formed due to the columnar grains’ contraction In EB-PVD coating [15].

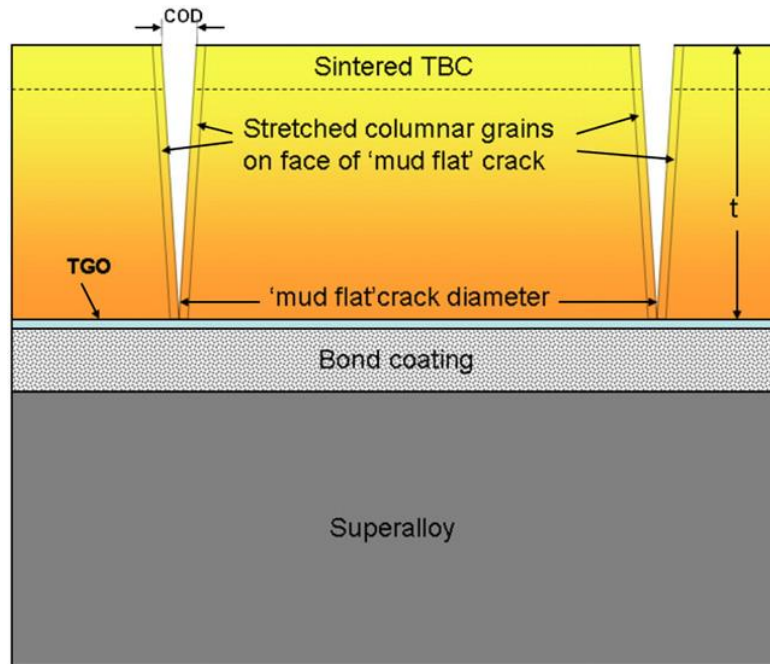


Figure 1.7. Sintering shrinkage in the outer zone of TBC results in tension in the outermost columnar grains, which pull on TGO interfaces [15].

2. Bond coat oxidation and inter-diffusion

(i) Bond coat oxidation

Compared with the top layer, the bond coat plays a more complex role and is poorly understood. In most practical cases, the bond coat oxidation is primarily responsible for the coating failure. While exposed to high temperatures, an oxide layer, usually defined as TGO, came out which is caused by the bond coat layer's oxidation. As shown in Figure 1.8, while the TGO grows to a crucial thickness, it can generate the spallation of the top layer and thus give rise to the failure of the TBC system.

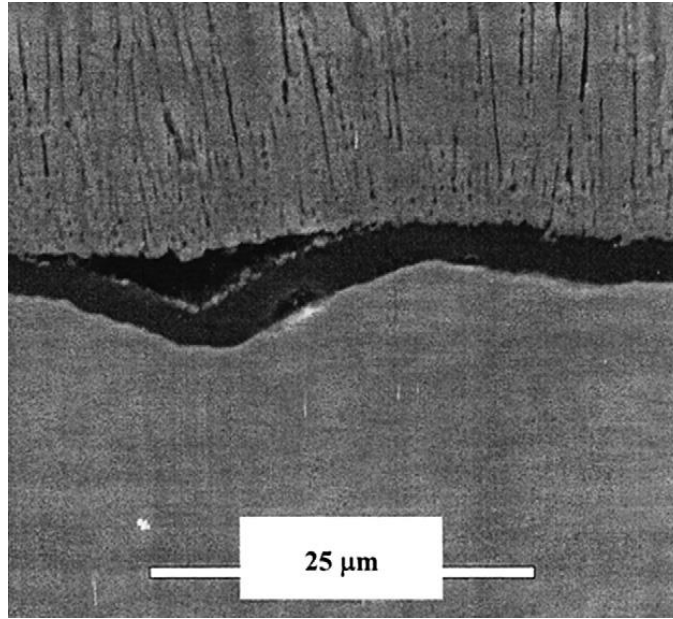


Figure 1.8. Growth of the TGO eventually results in damage to the TGO and its interfaces [15].

(ii) Bond coat inter-diffusion

In the high-temperature environment, the performances of Al in the bond coat layer and the substrate metal layer are different. As a result, Al can diffuse from the bond coat layer to the substrate metal layer [15]. This phenomenon is defined as bond coat inter-diffusion. At the same time, some refractory elements move outward from the substrate metal layer to the bond coating layer which can increase the TGO growth and thus cause the coating's oxidation resistance to decrease.

3. Particle impact and erosion damage

The particle impact spalling or erosion damage mode are shown in Figure 1.9. Even most of the larger particles have already been sieved, small particles can still go to the engine system and impact the TBC layer. The erosion and spalling phenomena can be observed while the high-speed particles impact the TBC layer and cause damages on the leading edge. Usually, it is difficult to pass by the impacting for particles with a diameter of more than 20μm. The previous study showed that particles with a diameter of more than 100μm with tip speeds ranging from 500 to 600m/s can generate enough kinetic energy for TBC erosion. The particles with a diameter of more than 500μm can generate enough energy to cause the spallation from the bond coating layer [15].

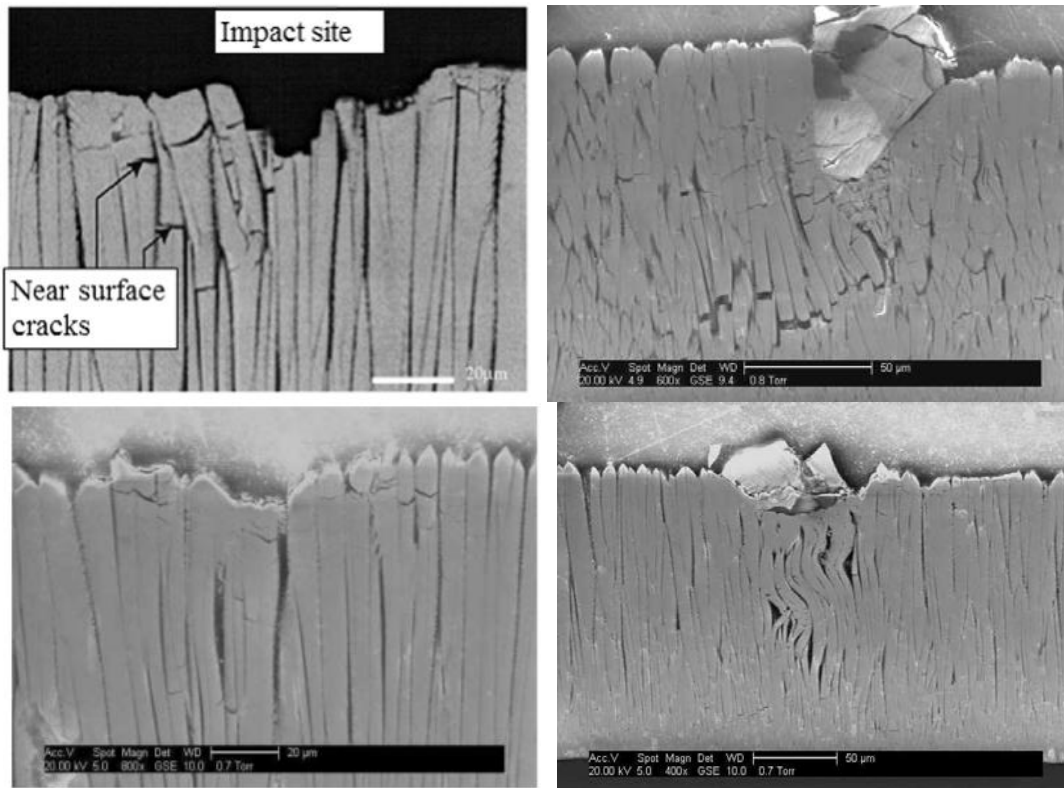


Figure 1.9. Micrographs illustrating the effect of FOD in an EB PVD TBC (0.5mm angular alumina particle at an estimated 100m/s) [16, 17].

As concluded above, spallation is a dominant mode of failure. Another is the particle impact erosion of the TBC [8]. while the TBCs are eroded or damaged, the substrate metal layer will be exposed directly to the high gas flow. This will incur the failure of the engine components and thus the parts of the system. More serious accidents may be caused finally. So, TBCs must be carefully repaired locally or globally or replaced once they are eroded or damaged. Maintenance, repair, and overhaul play an increasingly important role. Especially manufacturers of aircraft engines obtain about 30%-50% of their profit by maintenance, repair, and overhaul and they save up to 75% of new parts cost when maintenance, repair, and overhaul are carried out [18]. For instance, compared with the high price of each finished turbine blade usually over \$10,000, A guideline for the coating cost is for EB-PVD TBC only \$120 to \$200 per part. The refurbish price is low [19].

Considering the lower refurbishment price for these parts, TBC usually is repaired or replaced for some time during their lifetime. For an "overhaul" refurbishment, TBCs need to be removed completely before applying a new one. To support the industry's most advanced, heavy-duty gas turbine, GE is to invest up to \$60 million over the next decade in its existing Global

Repair Service Center to create a new HA Global Repair Engineering and Development Center [20].

The removal and repair techniques become crucial to refurbish TBC since TBC damage is normal due to the complicated environment for the TBC works. To improve the manufacturing process of the TBC refurbish, the damage process needed to be first deeply understood. Besides, to fully protect the bond coat and substrate undamaged during the TBC removal process, it is important to further investigate the TBC removal process. Furthermore, the coating service life depends not only on the service environment but also on its chemical composition, its structure and adhesive strength at the ceramic layer/bond coat interface [20]. Due to the high strain tolerance and long lifetime obtained from the special columnar grain microstructure, EB-PVD TBCs are considered to be the first choice for the turbine blade system [15]. So, understanding the failure mechanism of thermal barrier coating becomes very important, especially for the EB-PVD coating with the real column grain structure.

1.2 TBC Removal Process - A Review

As a brittle material, the major challenge for machining of TBCs is their high hardness, high brittleness, and low fracture toughness [21]. However, brittle materials still show some ductile properties no matter how brittle the materials are. The ductility of a material is defined as the material's ability to undergo permanent deformation through elongation or bending without fracturing [22]. As shown in Figure 1.10, brittle materials experience a transition from the ductile cutting mode to the brittle cutting mode when the machining depth is increased from small to large [23-25]. In Ref. [26], an alumina ceramic orthogonal cutting experiment was conducted. The chip deformations at different cutting depths from 0.2 mm to 1.2 mm were observed. During the cutting process, the powdery chips were generated while the cutting depth is small, and the chunk-like chips come out while a huge cutting depth is applied. The length of the cutting chips under different cutting depths was nearly proportional to the depth of cut except for the cutting depth below 0.4 mm. For a small cutting depth of 0.2 mm, powdery chips were produced, and chip shapes were unstable. It was concluded that the cutting force varied periodically. Each period of periodic fluctuations represented one chip formation. With the increase of the cutting depth, the periodicity became more evident [26]. There exist two kinds of periodic fluctuations: one is abrupt periodic fluctuation, the other is small fluctuation. For the cutting process, the abrupt periodic fluctuations

are corresponding to the chunk-like chips, which represents the brittle failure while the small periodic fluctuation are corresponding to the powdery chips, which means the ductile failure [26].

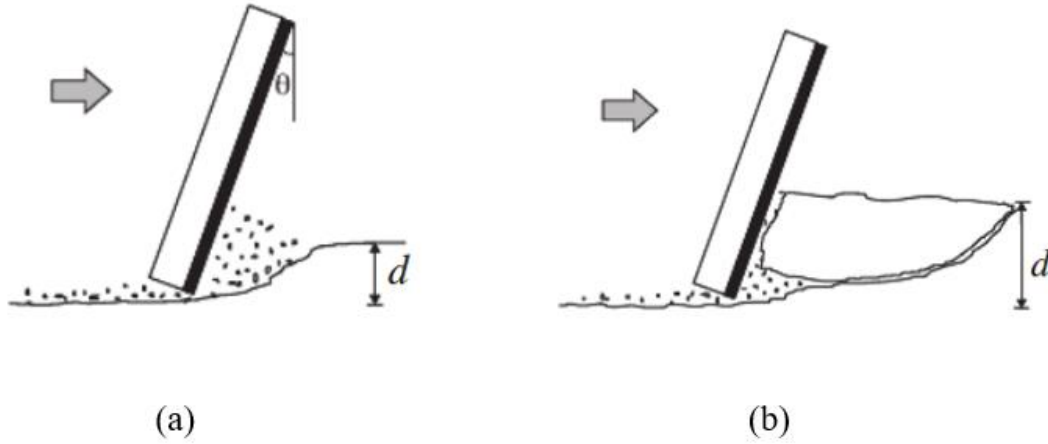


Figure 1.10. Schematics of the cutting process in (a) a ductile failure mode, and (b) a brittle failure mode [25].

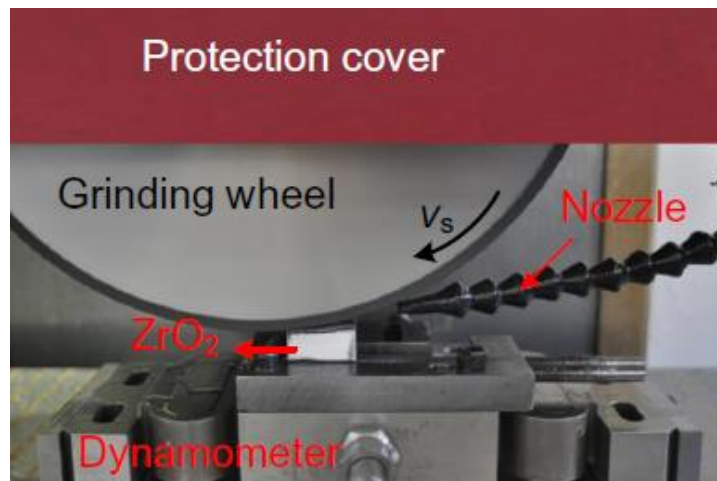
Due to the super hardness of TBCs, the cutting tool in the machining process is hard to penetrate the TBC layer. It is easy to observe the chips and cracks during the TBCs' manufacturing process. Micro-cracks are critical, which is caused by the considerable decreasing mechanical strength during the machining process. On the other hand, the cutting tool is easily damaged due to the high degree of hardness and fracture toughness. The low thermal conductivity is another reason because it can accelerate the cutting tool attrition [27]. To meet the increasing demand for the TBCs removal process, machining technologies with high efficiency are needed.

The TBCs removal and repair techniques are introduced in Chapter 2. As mentioned in Chapter 2, several methods have been used to remove the damaged TBCs such as grinding, chemical stripping, abrasive water jet, and laser ablation. In this thesis, the methods of grinding and abrasive water jet will be focused on.

1.2.1 Grinding

As shown in Figure 1.11, the diamond grinding wheel is an efficient way that could meet the requirements for the TBCs removal process. To obtain a high grinding efficiency during the high-performance ceramics coating manufacturing process, it is important for choosing proper grinding

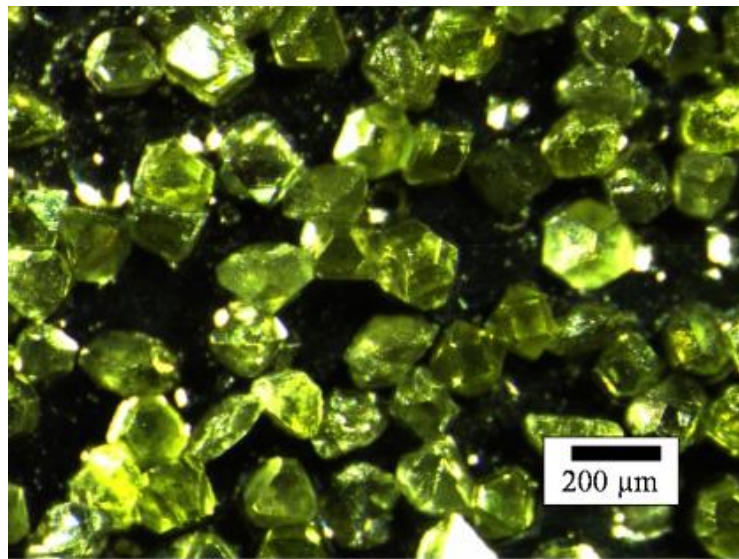
parameters to get the maximum removal rate. Properly choosing the operating parameters is critical for the highly efficient TBCs grinding process at maximum removal rate and also is important to obtain good surface integrity. The reduction of grinding costs through using higher removal rates is restricted due to the strength degradation caused by surface damage. To obtain the optimal grinding parameters in a reasonable methodological way, fully understanding the grinding mechanisms and surface damage evolution processes are critical [28]. The first of the fundamentals of the TBCs grinding process is the machining unit (Figure 1.12). It can determine the magnitude and the range of the critical stress for deformation or fracture of the material. The TBCs' removal is caused by the cumulation of deformation or fracture on a microscopic scale at the point where the abrasive diamond acts. For the grinding process, the size and density of defects play an important role. TBC removal process is in a plastic deformation mode while the stress field is less than the defects. On contrary, the removal of the TBC happens in a brittle fracture mode while the stress field is higher than the defects. [29].



(a)

Figure 1.11. A typical grinding experimental system (a) and diamond grits over grinding wheel (b) [30, 31].

Figure 1.11 continued



(b)

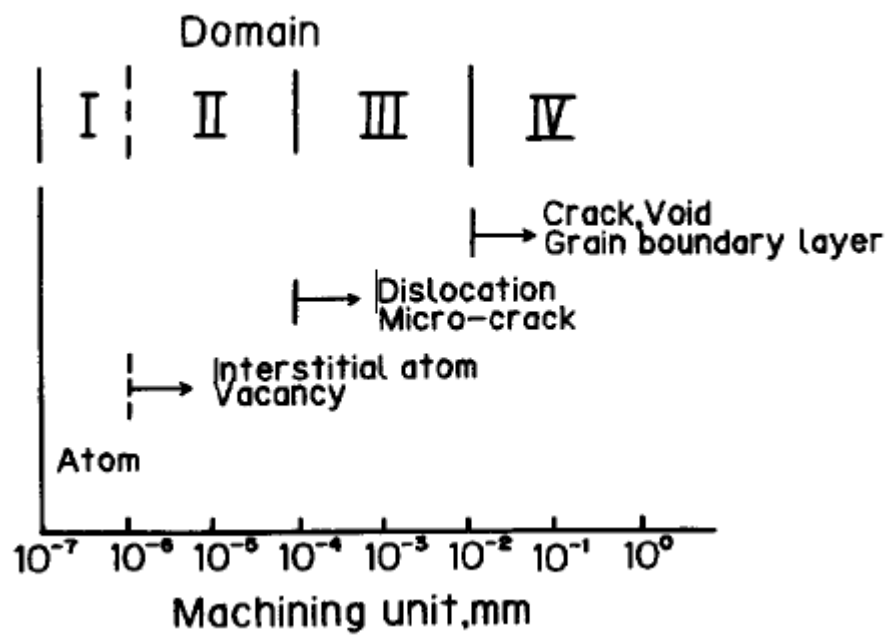


Figure 1.12. Machine unit diagram [29].

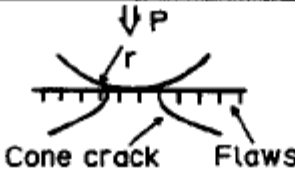
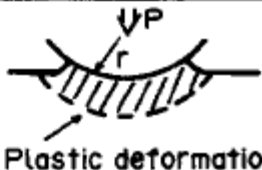
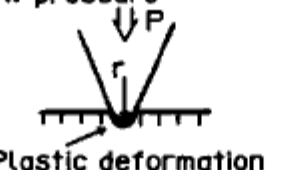
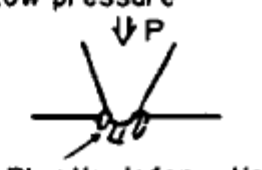
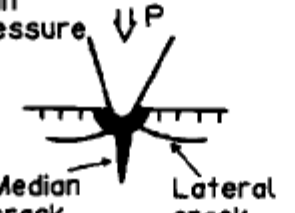
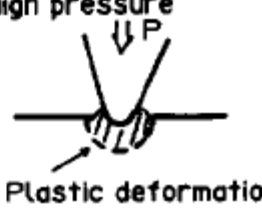
	Brittle materials	Ductile materials
Large radius of tip	 <p>Cone crack Flaws</p>	 <p>Plastic deformation</p>
Small radius of tip	<p>Low pressure</p>  <p>Plastic deformation</p>	<p>Low pressure</p>  <p>Plastic deformation</p>
	<p>High pressure</p>  <p>Median crack Lateral crack</p>	<p>High pressure</p>  <p>Plastic deformation</p>

Figure 1.13. Localized deformation and fracture with different tip radius [29].

The localized deformation and fracture of materials with different tip radius are shown in Figure 1.13. It can be seen that the indentation test using a small tip radius displays an amount of helpful information for optimizing the grinding process of TBC. The median and lateral cracks come out with a small tip radius and the cone crack generates with a large tip radius [29].

At the same time, as a grinding parameter, grinding speed also plays an important role during the grinding process especially for the high-speed grinding process. By selecting a high-speed grinding process, it is easy to decrease the maximum chip thickness and thus reduce the grinding force to a large degree. Increasing the wheel's grinding velocity can move the grinding mode towards the ductile mode and thus can improve the surface quality (Figure 1.14) [32].

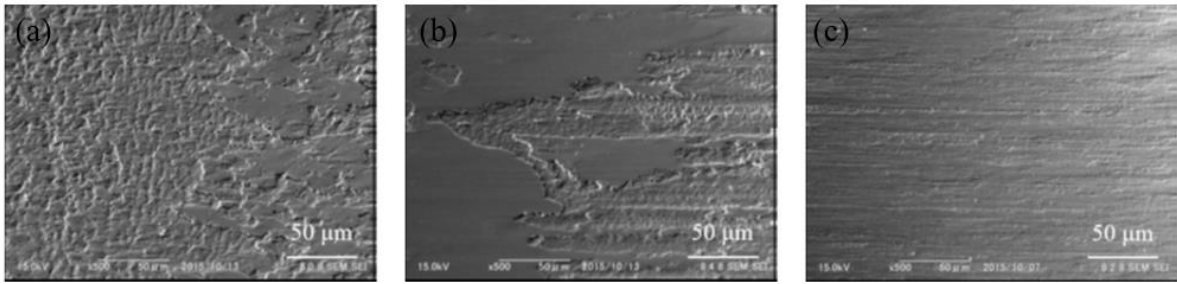


Figure 1.14. The SEM images at different cutting speeds: (a) 11 m/min; (b) 44 m/min; (c) 670 m/min [33].

On the other hand, during the grinding process, the responses of the ceramic coating are not only related to the grinding parameters but also are affected by the TBC microstructure that determines the coating's mechanical properties to a great extent, such as hardness and toughness. As two main kinds of TBC, APS and EB-PVD coating has totally different microstructures (Figure 1.15). As shown in Figure 1.16 and Figure 1.17, the failure mode of different kinds of TBC is obviously different. Due to the special columnar strain-tolerant microstructure, the grinding mechanisms of EB-PVD coating should also be particularly [34]. To understand this special process, a more detailed study needs to be conducted.

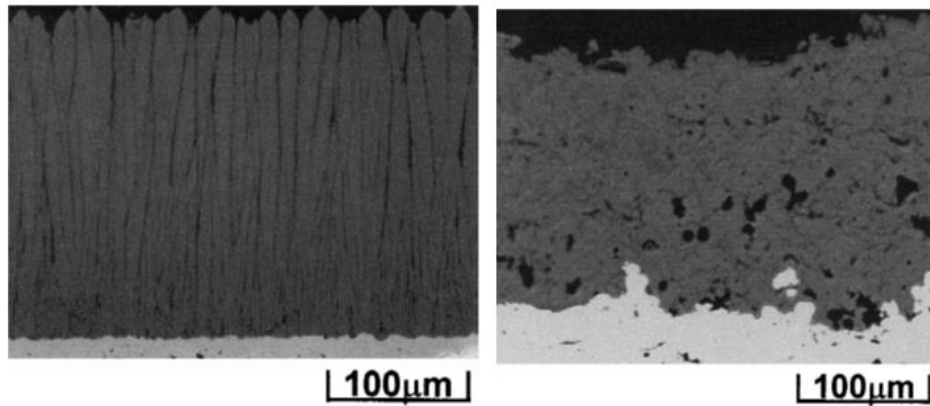


Figure 1.15. A typical microstructure of an EB-PVD (right) and APS (left) TBC [35].

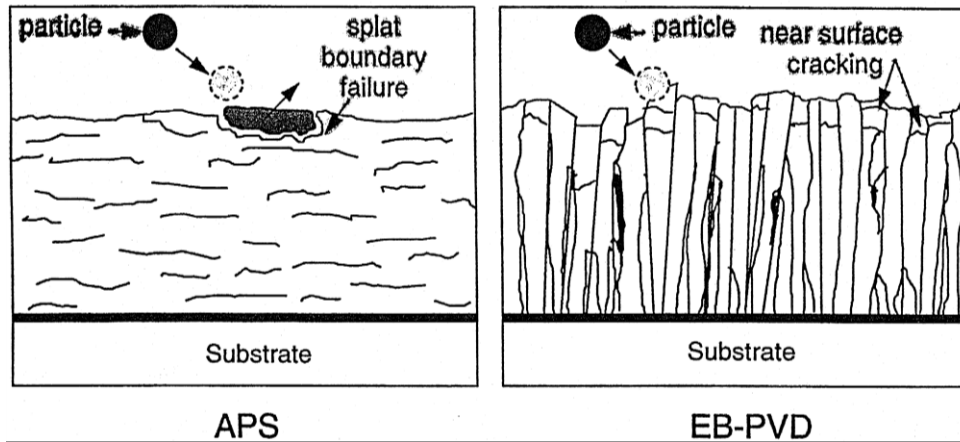


Figure 1.16. A schematic diagram of the failure modes for an APS and EB-PVD TBC [35].

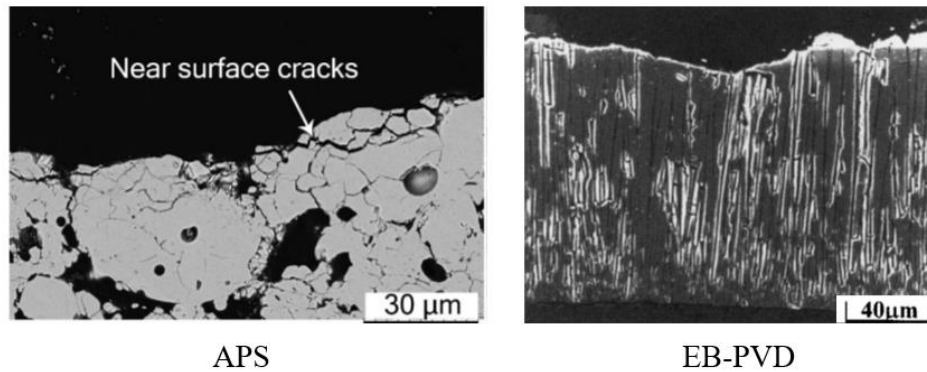


Figure 1.17. Erosion damage to an APS [36] and EB-PVD [35] TBC.

1.2.2 Abrasive Water Jet

For the conventional overhaul TBC removal process, the TBC (top layer) and the bond coat (metallic) layer are typically completely removed in several machining steps, which consist of both mechanical grid blasting and chemical striping. However, the removal mode without influencing of bond coat is preferable. As one of the most flexible non-conventional structuring techniques for TBC materials, water jet-controlled depth machining was proved to be a promising way for selective TBC removal without damaging or contaminating the bond coat layer (Figure 1.18, Figure 1.19 and Figure 1.20) [37]. Abrasive water jet coating processes are emerging as a greener alternative to acid baths and grit blasting and works especially well on tough coating, like MCrAlY ceramic TBCs. AWJ processes remove the coating iteratively using CNC programming. The controller governs The grinding speed, feed rate, and water jet pressure and the distance between

the water-jet nozzle and the surface can be governed by the controller. Abrasive size can vary depending on the application and is usually proprietary to that process [38].

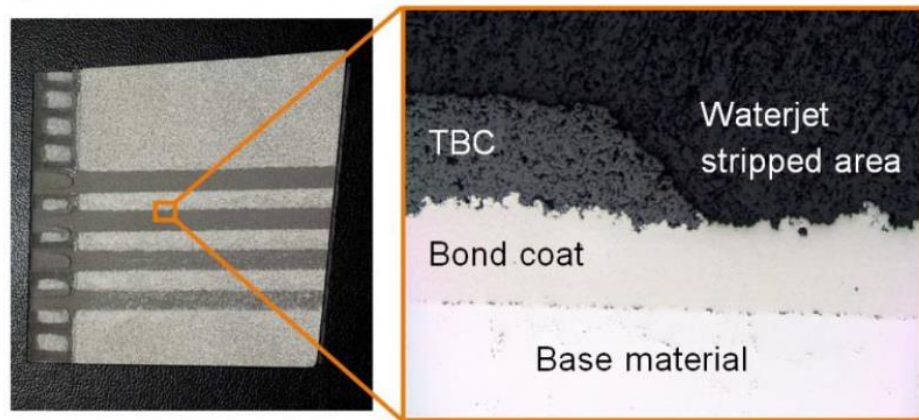


Figure 1.18. TBC removal without damaging bond coat using AWJ process [37].



Figure 1.19. Waterjet stripping of TBC on a turbine blade [37].

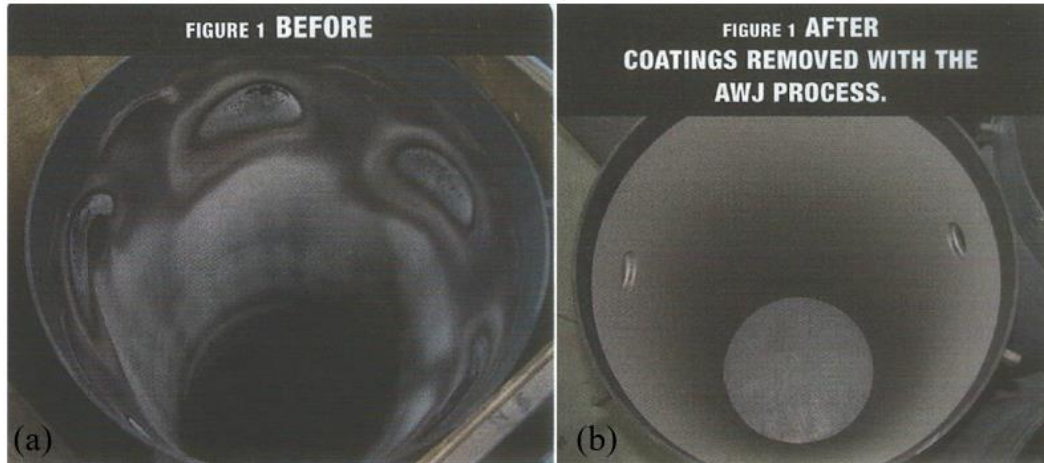


Figure 1.20. Turbine component coating before and after removal AWJ process [39].

During the AWJ processes, the machining angle plays an important role in the AWJ machining processes together with the water jet pressure, abrasive particle density, and size, and the distance of the water-jet nozzle [37].

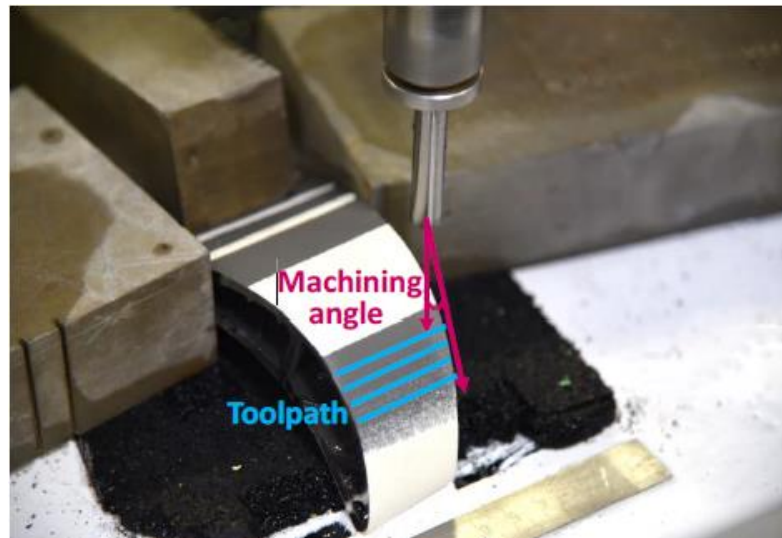


Figure 1.21. Investigation of the influence of the machining angle during the AWJ processes[37].

In summary, the type of method used for removing the damaged TBC depends on multiple factors. There is not a universal method applicable to all coating systems. The selection of the coating removal process must be specific to damaged coating systems, based on their composition, type of damages, and available resources [8].

Due to the complicated environment for the TBCs work, many processes are nearly impossible to complete in the lab. With the increase of computing power and the development of computing means, various simulation methods were performed to gain insight into the TBC removal process in addition to laboratory experiments.

1.3 Particle-Based Modeling Methods

For TBCs' removal processes' modeling, the previous simulation results are mainly based on the traditional grid-based numerical methods such as the finite element method (FEM). In comparison, as one of the particle-based methods, the SPH method has shown to be very useful to model the high-speed particles to accommodate their extremely large deformation, which is important for the brittle fracture of ceramic materials. As a mesh-free, Lagrangian particle method, the SPH method can be used to handle large distortions [40]. It is particularly suitable to study some fast-transient dynamics problems and the severe deformation of the particle. In the meanwhile, the modeling of TBC removal using the SPH method is less reported. Based on this fact, the SPH is selected to simulate the impact process of small sand particles, the water jet removal process. In this work, the SPH model will also be applied to simulate the surface grinding process with a TBC system [41]. The SPH simulation results will help deeply understand the impact, removal, and grinding process. Meanwhile, the discrete element method (DEM) has shown an apparent advantage to simulate granular materials such as rock, ceramic, and concrete. It can obtain the cracks' initiation and propagation process with no additional fracture criteria. DEM will also be selected to use simulate the grinding process and the erosion process. The cracks' initiation and propagation during the grinding and erosion processes will be observed and concluded and it can help to reveal the details of the TBCs' grinding and failure mechanisms [42, 43, 44, 45].

1.3.1 SPH method

As one of the earliest mesh-free methods, SPH method was initially applied to astrophysical problems since the particles in space move like liquid and gas flow. After that SPH method is extended to high-velocity impact and penetration problems for materials' dynamics response. While the SPH method was used for hydrodynamics problems initially, the governing equations were partial differential equations with strong formation [40]. These equations usually consist of

the variables of density, velocity, and energy. The solution of these partial differential equations contains two-step: kernel approximation and particle approximation. For kernel approximation, a smoothing function was selected to represent the partial differential equations and their derivatives [41]. For particle approximation, a series of particles are used to represent the computation domain. Then, each particle's variables can be calculated through the summation with their closest neighbor particles in the support domain [41].

1.3.1.1 Kernel Approximation of A Function

In kernel approximation, a smoothing function was selected to represent the partial differential equations and their derivatives. As a smoothing function, it should meet three basic rules: the normalization condition, the Delta function property, and the compact condition. The kernel approximation of a function $f(x)$ used in the SPH method starts from the following identity [40]:

$$f(x) = \int_{\Omega} f(x') \delta(x-x') dx' \quad (1)$$

where f is a function of the position vector x , and $\delta(x-x')$ is the Dirac delta function given by [40]:

$$\delta(x-x') = \begin{cases} 1, & x = x' \\ 0, & x \neq x' \end{cases} \quad (2)$$

In (1), Ω is the volume of the integral that contains x . While the Delta function $\delta(x-x')$ is substituted by a smoothing function $W(x-x', h)$, the kernel approximation of $f(x)$, $\langle f(x) \rangle$, can be obtained [40]:

$$\langle f(x) \rangle = \int_{\Omega} f(x') W(x-x', h) dx' \quad (3)$$

1.3.1.2 Particle Approximation

In particle approximation, a series of particles are used to represent the computation domain. As shown in Figure 1.22, the computation domain or the boundaries could be represented by the distributed particles. There are no specific mesh and formation relationships between the particles. The distributed particles are usually in an arbitrary form, which could be generated by some mesh generation tools or mathematic discretization method.

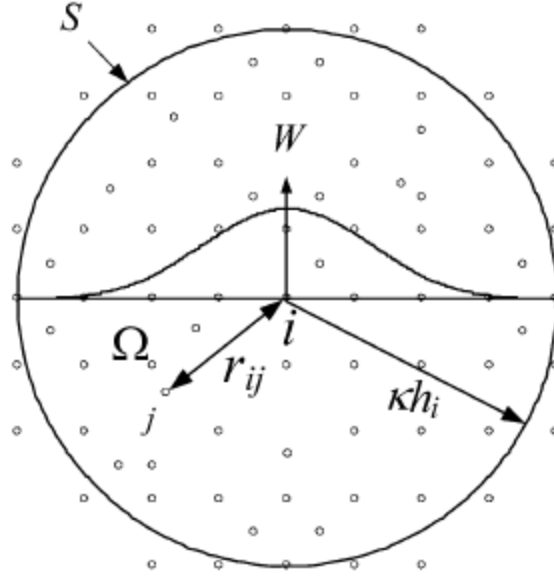


Figure 1.22 SPH particle approximations in a two-dimensional problem domain Ω with a surface S . W is the smoothing function that is used to approximate the field variables at particle i using averaged summations over particles j within the support domain with a cut-off distance of κh_i [40].

With the particle approximation, the kernel approximation expressed in (3) can be transferred to the discretized form as follows [40]:

$$f(r_i) = \sum_{j=1}^N \frac{m_j}{\rho_j} f(r_j) W(r_i - r_j, h) \quad (4)$$

$$W(r_i - r_j, h) = \frac{1}{h} \Theta \left[\frac{r_i - r_j}{h(r, y)} \right] \quad (5)$$

where m and ρ are the mass and density of a particle, respectively. W is a kernel function, h is a smoothing length of the kernel to control the size of the summation domain. $W(r_i - r_j, h) \rightarrow \delta$ when $h \rightarrow 0$, where δ is the Dirac function. In general, the compact support is defined by the smoothing length h and a scale factor κ that determines the spread of the specified smoothing function. So the compact support means [40] :

$$W(r_i - r_j, h) = 0 \quad \text{when } |r_i - r_j| > 0 \quad (6)$$

The cubic β -spline function is probably the most usually used smoothing function and it first proposed by Monaghan and Lattanzio [41]:

$$W(R, h) = \alpha_d \times \begin{cases} \frac{2}{3} - R^2 + \frac{1}{2}R^3, & 0 \leq R \leq 1, \\ \frac{1}{6}(2 - R)^3, & 1 \leq R \leq 2, \\ 0, & R \geq 2. \end{cases} \quad (7)$$

where α_d is $1/h$, $15/7\pi h^2$, $3/2\pi h^3$, respectively, in one-, two- and three-dimensional space [41].

1.3.1.3 SPH Method Advantages and Limitations

Compared with traditional grid-based methods, SPH method has lots of special advantages [40, 41].

1. In SPH method, the computation domain is represented by distributed particles that have no fixed connectivity. Based on this characteristic, it is much easier for SPH to deal with large deformation problems.
2. As a Lagrangian-based method, using SPH method is convenient to obtain the time history of movement and deformation and to track the moving features of the entire physical system. As a result, the free surface identification, the moving interface and deformable boundary conditions are easy to deal with SPH method.
3. In SPH method, the physical system on a continuum scale is represented by a set of particles. Thus, it is much easier to generate complex and multiple-scale geometries with fine particles.
4. SPH method also can be used for no continuum problems with different scales from nano-engineering at micro and nanoscale to space explosion problem at astronomic scale.
5. Compared to the grid-based method, it is easier for SPH method to simulate the three-dimensional problem.

As particle-based methods, SPH still has some limitations [40, 41]:

1. One of the most difficult points is to set the boundary conditions because the particles around the boundary vary with time.
2. The maximum number of particles and duration of a virtual simulation are limited by computational power, and both are not as efficient as grid-based methods.
3. The selection of proper kernel function is very important, which could limit the accuracy of the SPH method.

1.3.2 DEM Model

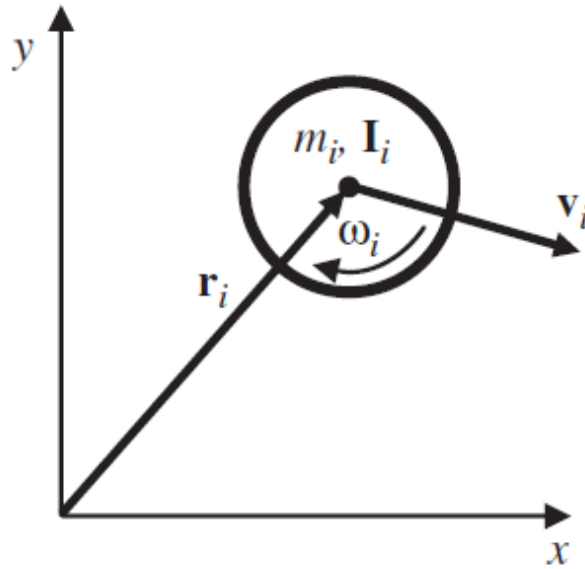
1.3.2.1 Governing Equations in DEM

DEM is a particle-scale numerical method for modeling the bulk behavior of granular materials proposed by Cundall and Strack [42]. In DEM, each particle is treated as a rigid 2D disc or 3D sphere (Figure 1.23). The particles are connected using contact bonds. Particle motions obey Newton's second law [43]:

$$m_i \frac{dv_i}{dt} = \sum_{j=1}^{k_i} (F_{c,ij} + F_{d,ij}) + m_i g \quad (8)$$

$$I_i \frac{d\omega_i}{dt} = \sum_{j=1}^{k_i} T_i \quad (9)$$

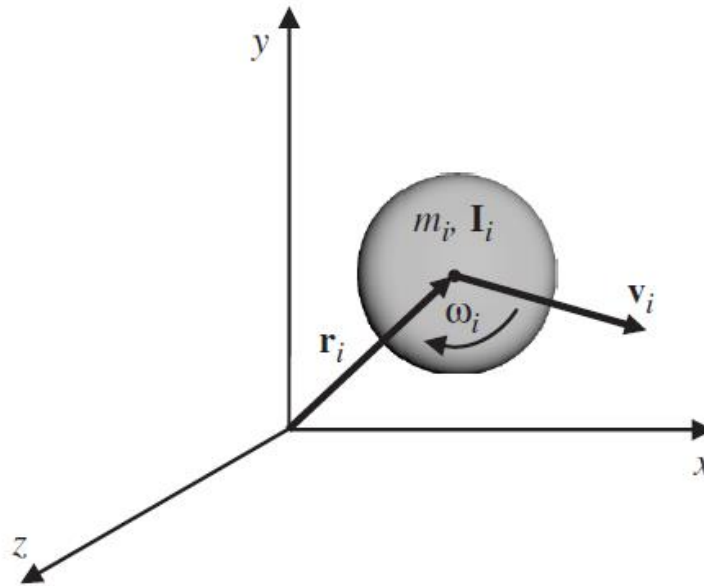
where v_i and ω_i are the vectors of the linear and angular velocities of an i th particle, respectively, m_i is the weight; I_i is inertia; $F_{c,ij}$ is the contact force of particle j to particle i , $F_{d,ij}$ is the damping force between particle j and i , and T_i is the resultant force moment [43].



(a)

Figure 1.23. Discrete element: (a) 2D circular particle; (b) 3D spherical particle [43] .

Figure 1.23 continued



(b)

1.3.2.2 DEM Method Advantages and Limitations

DEM has some special advantages over the traditional grid-based numerical methods [44].

1. The advantage of using DEM compared to continuum-based techniques is in cracking and fragmentation starting and spreading because the DEM system is naturally disconnected.
2. DEM is a widely used method for the simulation of granular flow and rock mechanics situations.
3. Compared with physical experiments, it is easy to catch the details of the micro-dynamics of powder flows.
4. DEM has shown advantages for predicting complex fracture patterns in ceramics without fracture criteria.

As particle-based methods, DEM still has some limitations [45]:

1. Due to the limitation of the computational power, DEM is not as efficient enough as the grid-based method such as FEM.
2. The contacts between particles are critical and it is very difficult to select ideally contacts.

3. The unit particles are disk and sphere shape and cannot be deformed and broken.

1.4 Problem Statement

As mentioned above, due to TBCs' exclusively properties such as high degree hardness and fracture toughness, low thermal conductivity, together with its special microstructures and the high requirement for aircraft components, the TBCs machining is a challenging task. The type of removing methods and the selection of machining parameters must be specific to damaged coating systems, which are based on their composition, type of damages, and available resources. Meanwhile, Due to the complicated environment for the TBCs' work, many processes are nearly impossible to complete in the lab. The simulations can be conducted in addition to laboratory experiments to deeply understand the TBC removal processes.

To date, the mechanisms of TBCs removal processes have been extensively studied from experiments and simulations, which provide the guidance for selecting the removal methods and machining processing parameters. However, due to the complicated environment for the TBCs' work and removal processes, many processes are impossible to complete in the lab and the details of the experiments are nearly impossible to observe. Meanwhile, the previous simulation results are mainly based on the traditional grid-based numerical methods such as the finite element method (FEM), and the special microstructures especially for columnar grain structure of EB-PVD coating are also seldom considered.

In this thesis, a particle-based modeling framework that spans the impact model, cutting model, water-jet model, and indentation model will be developed to investigate the TBC removal process. All the models are extracted from the real structure or directly built with the real TBC structure, especially the columnar grain structure from EB-PVD coating. The impact behavior simulating a spherical particle on TBC coating, which is impossible to complete in the lab, will be built using SPH method coupling with FEM method. An abrasive water-jet model will be developed based on previous experiments using SPH method. The simulation results will be validated through the experimental results and more details of the AWJ removal processes, especially which are not easily observed from experiments, will be discussed. Meanwhile, to study the TBC grinding processes, orthogonal cutting models will be developed using the SPH and DEM method individually. Both models are extracted from the columnar grain structure of EB-PVD coating. The effects of cutting parameters will be studied based on these two models. Furthermore,

to study the failure mode of EB-PVD coating, a DEM model based on the real structure from SEM image will be built. The indentation tests under the different sizes of indenter will be selected to study the failure mode. The effects of the TBC microstructure will be minimized with the models in the real structure.

1.5 Objective and Research Tasks of the Thesis

The objective of the thesis is to systematically illuminate the process-property relationships in the TBC removal processes using particle-based methods, the SPH and DEM methods, and thus providing a design and optimization tool for the coating removal processes.

To achieve the above-mentioned objective, the following research tasks are identified.

1. Provide a comprehensive literature review of the existing techniques to remove and repair the damaged thermal barrier coatings, with a focus on the top ceramic coat.
2. Develop an SPH model that is capable of understanding the high-velocity particle impact processes.
3. Build the SPH and DEM models that are capable of understanding of TBC surface grinding process.
4. Develop an SPH model for TBC removal using the AWJ method.
5. Construct a DEM model based on the realistic coating structure to understand the failure mechanism of the thermal barrier coating.
6. Proposes a new coating fracture mechanism map, which correlates the processing parameters and coating fracture modes and serves as a reference for ceramic grinding.

1.6 Structure of the Thesis

This thesis is organized as follows.

Chapter 1 states the background of the TBC failure mechanisms, the requirements for TBC removal and repair processes, the theory of the particle-based methods, and the objectives of this work.

Chapter 2 provides a comprehensive literature review of the existing techniques for removing and repairing the damaged thermal barrier coatings.

Chapter 3 focuses on the impact failure of TBC under a spherical particle using the SPH method. The effects of impact angle and velocity on the morphology changes of the impact pit and impacting particles, and their associated stress and energy will be investigated.

Chapter 4 studies the abrasive water jet impact behavior of ZrO_2 TBC using the SPH method. The effects of different abrasive concentrations, incident angles, and drilling time on the impact behavior of TBCs will be studied. The simulation results will be compared with the experiment results. In addition, an analytical erosion model will be introduced to calculate and verify the erosion rate.

Chapter 5 elaborates a model based on the columnar grain microstructure of EB-PVD coating to simulate the machining process of the thermal barrier coatings using SPH method. The cutting processing parameters, such as cutting depth, cutting speed, cutting tool's edge radius, and rake angle, on the cutting force and temperature change, will be studied. An analytical model based on the fracture mechanics will be introduced to calculate and verify the cutting force under different cutting depths. The thermal mechanics will be considered.

Chapter 6 presents a model based on the columnar grain microstructure of EB-PVD coating to simulate the machining process of the thermal barrier coatings using DEM method. The effect of cutting processing parameters, including cutting depth and cutting speed, on the cutting force and coating morphology will be studied. The transition depth or the critical cutting depth will be calculated using the Griffith fracture criterion. The maximum cutting force under different cutting depths will be calculated under an analytical model based on brittle fracture mechanics.

Chapter 7 discusses a DEM model based on the realistic structure of the coating image to understand the failure mechanism of the thermal barrier coating. An indentation test will be taken, and the results will be compared with the experiment results.

Chapter 8 proposes a new coating fracture mechanism map, which correlates the processing parameters and coating fracture modes.

Chapter 9 presents the conclusions and recommended future work.

2. REMOVAL AND REPAIR TECHNIQUES FOR THERMAL BARRIER COATINGS: A REVIEW

A version of this chapter has been published in the International Journal of Surface Engineering and Coatings (doi: 10.1080/00202967.2020.1750204).

Abstract: A comprehensive literature review of the existing techniques for removing and repairing of damaged thermal barrier coatings is presented, with the focus on top ceramic coats. The advantages and disadvantages of each technique are compared and assessed. The review shows that there is not a universal method applicable to all coating systems. The selection of the coating removal and repair process must be specific to damaged coating systems, based on their composition, type of damages, and available resources. This review will provide an inside look at various approaches in an effort to meet the different coating repair needs.

2.1 Introduction

Maintaining large-scale turbine, generator, and boiler components as those found in power generation plants and jet engines, represent a significant operational cost and time. The combination of intense stresses placed on the components and contaminants introduced into the components requires that such large-scale systems follow a strict maintenance and inspection schedule. Unfortunately, this results in these machines being taken "off-line" for a period of service. Every hour of downtime results in significant lost revenue, particularly in power generation plants.

Many gas turbine engine components are subject to high temperatures, which has exceeded the melting temperature of the substrate component, which may be constructed from a nickel superalloy, for example. Cooling features and TBCs are applied to protect the substrate from these extremely high temperatures. The application of the thermal barrier coating can help improve the components' lifetime and the hot section's Functional performance. Ceramic coating has great significance in improving substrate metal components and bond coat's thermal-physical-chemical-mechanical compatibility. In most situations, spallation is a dominant failure mode. The increasing interfacial activity caused by undesirable additives can reduce the life of thermal barrier coating. During engine operation, thermal barrier coatings may become spalled, delaminated, chipped, or eroded, for example, due to debris or environmental degradation. Any component with a damaged

thermal barrier coating must either be replaced or repaired during maintenance of the engine. The typical Thermal Coating (TBC) is either completely removed from the component and reapplied or it's removed locally and reapplied at that spot.

In summary, the type of method used for repairing the damaged TBC depends on various factors such as the extent of damage of the ceramic coating, the desired quality of repair, available equipment, and the substrate characteristics.

The objective of this work is to conduct a comprehensive literature review of the existing techniques to remove and repair the damaged thermal barrier coating, with a focus on the top ceramic coat. The work will lay out a foundation of the modeling work in the following year.

2.2 Removal Methods for Thermal Barrier Coated Components

2.2.1 Blasting Methods

2.2.1.1 Grit Blasting with Abrasive Media

Grit blasting is the operation of forcibly propelling a stream of abrasive material against a surface under high pressure to smooth a rough surface, roughen a smooth surface, shape a surface or remove surface contaminants [46]. During grit blasting, incident particles have a strong influence on the subsurface microstructure both of the matrix and precipitates. Precipitates depleted zone was formed during cycling both in the specimen and fatigue crack surface layer. Simultaneous formation of the aluminum-rich oxide film was observed at both surfaces. Measurements revealed a slight increase in hardness of the subsurface layer of grit-blasted specimens in comparison with untreated material [47].

Compared with traditional chemical learning methods, abrasive blasting is an environment friendly way for removing ceramic coating. The abrasive media is directly from the natural environment. At the same time, for the blasting process, there is no greenhouse gas generated. The surface roughness is strongly affected by the impact particle size and the distance from grit-blast gun to the surface [46].

However, the color of the ceramic coating and the substrate metal is similar to each other and it makes the distinction between the coating and the base metal difficult. From this aspect, it is easily to generate the uneven and increase the surface roughness.

2.2.1.2 Grit Blasting with Solid CO₂

The solid CO₂ [48] was used to grit blast the ceramic coating layer by the spray gun. The combination methods of IR lamps irradiation and preheating the coating and substrate were used to protect the substrate. During the process of grit blasting, the solid CO₂ sublimated into gas due to the kinetic energy from high speed and thermal energy from the heating and irradiation process. When the Solid CO₂ is sublimated to gas, the volume grows drastically, which could produce powerful shock waves. The shock wave removed the coating surface, the existed cracks, and the particles which have been blasted off or which have poor adhesion to the coating. The shock wave increases with the sublimation. Therefore, with the increase of the pressure of transport of solid CO₂, the rate of removal increases.

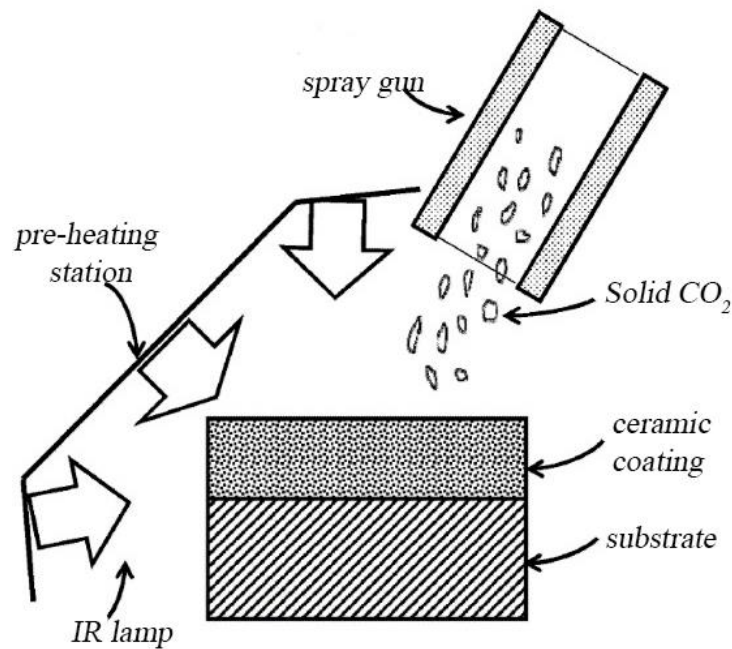


Figure 2.1. Schematic of coating removal using solid CO₂ [48].

2.2.1.3 Pencil Grit Blasting

The method pencil grit blast [49] was used to remove the oxides and fragments of localized ceramic coating later. The other ceramic coating layers were covered by the type of mask to be not affected by the grit blasting. The grit blasting media is Alumina. The surface roughness after grit blasting should be over 300 μm . Finally, the new layer of ceramic coating was deposited on the textured surface to repair the layer.

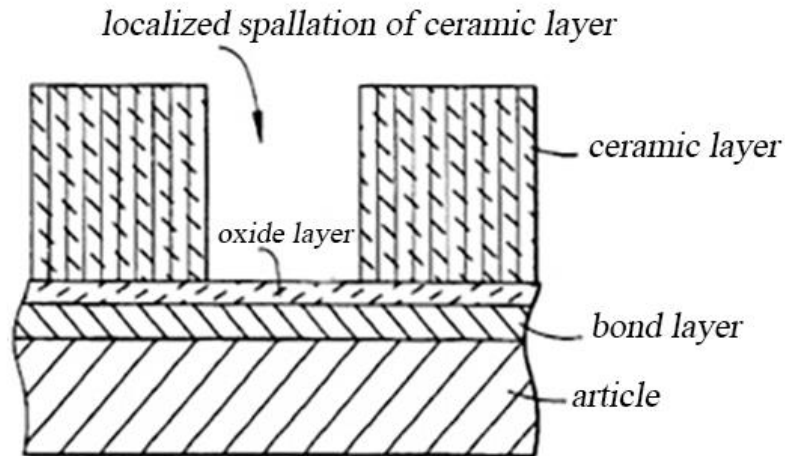


Figure 2.2. Coating removal process [49].

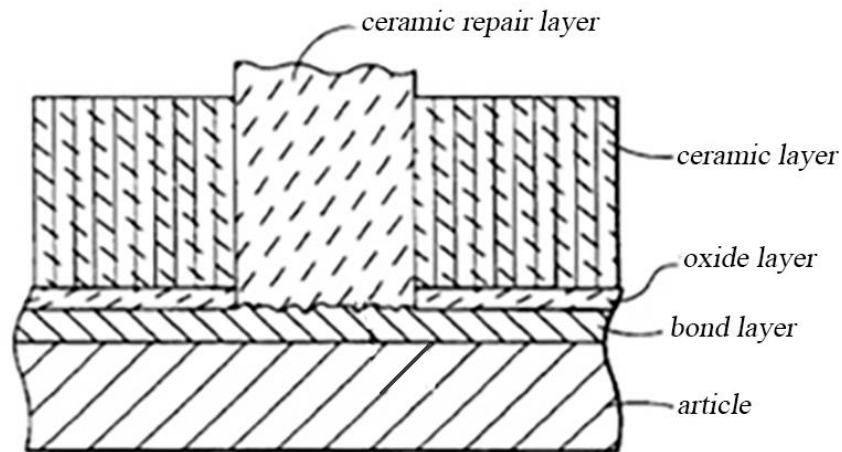


Figure 2.3. Coating repair process [49].

2.2.2 Chemical Stripping

2.2.2.1 Autoclaving Process

The aim of the autoclaving process [50] is to remove the ceramic layer without the damaging bonder layer and cooling holes and deposit the new ceramic layer on the surface of the blade. As the cooling holes exist, the ceramic material was deposited into cooling holes during the ceramic deposition process. By using autoclaving process, the ceramic surface is removed under the caustic solution at an elevated temperature and pressure in an autoclave. The temperature and pressure of autoclaving process are around 150 °C to around 300 °C and about 0.7 MPa to about 21 MPa.

Potassium hydroxide (KOH), sodium hydroxide (NaOH), ammonium hydroxide (NH₄OH) lithium hydroxide (LiOH), trimethylamine ((CH₃)₃N; TEA), tetramethylammonium hydroxide ((CH₄)₄NOH; TMAH) were mixed as the caustic to weaken the chemical bonding [50]. It usually took 2-8 hours, which depends on the properties of the ceramic layer. After the autoclaving process the cooling holes were subjected to the locally ultrasonic energy with the solution of water or glycerol, which the ceramics material was removed from the cooling holes. The autoclaving method can change or repair the ceramic layer without accumulating extra ceramics inside the cooling holes.

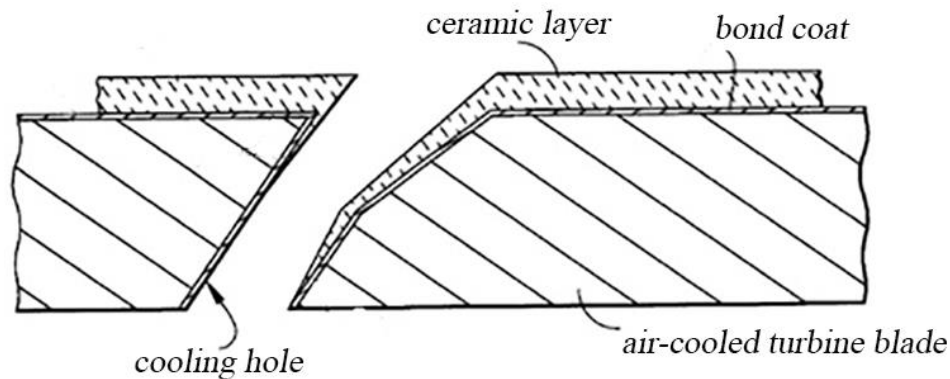


Figure 2.4. Schematic of the removal of the ceramic layer with the presence of ceramic material in the cooling hole [50].

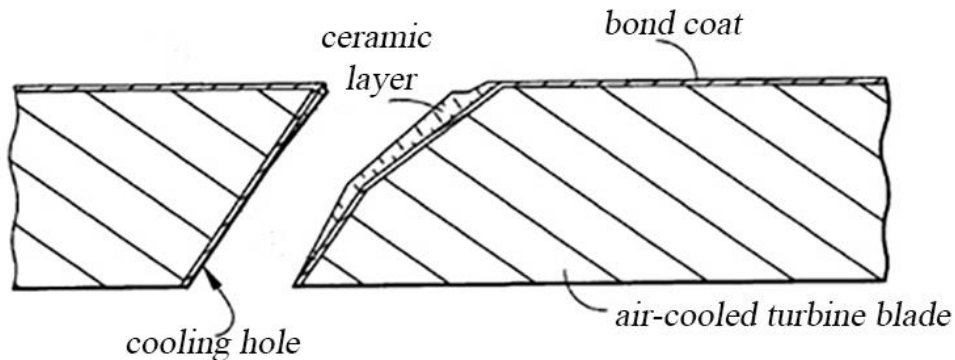


Figure 2.5. Schematic of ceramic layer removal by exposure to a caustic solution at an elevated temperature and pressure [50].

2.2.2.2 Aqueous Stripping Solution Containing Acid Fluoride Salt

Aqueous stripping with the acid fluoride salt method [51] is used to remove the ceramic layer from a substrate without damaging the bond coat. The ceramic layer is removed by exposure

to the aqueous stripping solution. The aqueous stripping solution includes acid fluoride salt and corrosion inhibitor. Acid fluoride salt that is usually ammonium bifluoride (NH_4HF_2) or sodium bifluoride (NaHF_2) was dissolved in the deionized water with the ratio of 20-100 %. The corrosion inhibitor contains about 10-30% of sulfuric acid, 10-30% of 1,3-diethylthiourea, and 30%-60% of alkyl pyridines. The total volume present of corrosion inhibitors is 0.5%. The acid fluoride could convert Zirconia to Zirconium and corrosion inhibitor could protect the metal substrate. The operating temperature is about 140°F. to about 170°F and the stripping, time is about 4-5 hours. This process could also be combined with ultrasonic treatment. The ultrasonic treatment can be continued until the TBC is completely removed or at least sufficiently loosened so that it can be removed by brushing or pressure spray rinsing which could shorten the processing time to 2-5 hours.

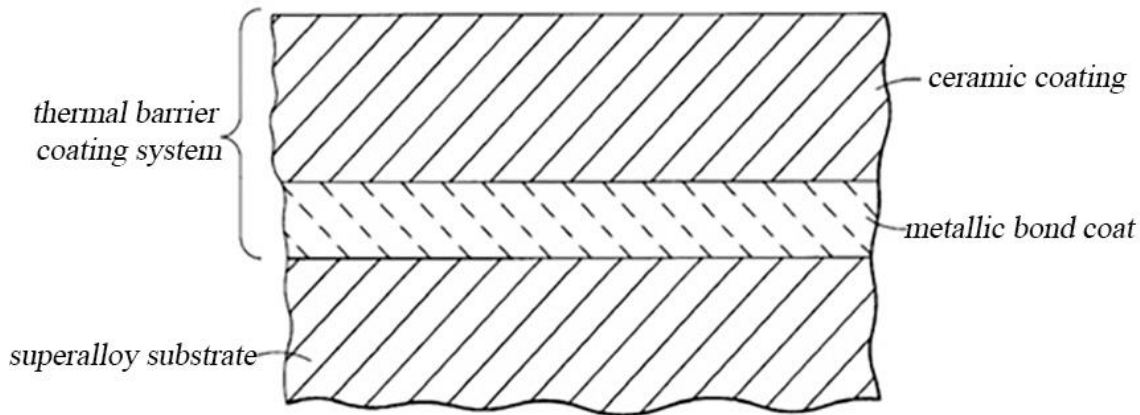


Figure 2.6. Schematic of a cross-sectional view of an airfoil portion of a gas turbine engine turbine component [51].

2.2.2.3 Acid Stripping

Acid Stripping is also known as “Acid Pickling” [52] when metals are treated using acid baths. Stronger acids are commonly used such as sulfuric acid, but the acid mixture depends on the application. The peeling process usually requires separate removal of top coatings (yttrium partially stabilized zirconia, YPSZ) and adhesive coatings (MCrAlY , where M retains Co, Ni, or both). The surface morphology[53, 54], metallurgical structure, and chemical composition are used to characterize the blade and blade surface after removing NiCrAlY coating. One of the problems of acid stripping is intergranular corrosion (IGA). Because of IGA, many original equipment manufacturers and users limit component maintenance to one cycle. The acid stripping will also

leave pollutants and pollute the interface. Acids need to be masked to avoid removing internal coatings and subsequent exposure. A poor mask can destroy internal components, which may have to be scrapped. Because pickling is a batch production process, sometimes due to acid changes the whole set of industrial gas turbine components will be damaged [52].

2.2.3 Water Jet

2.2.3.1 Non-abrasive Water Jet

The non-abrasive water [55] jet method uses the non-abrasive liquid jet to remove the ceramic layer from both the inner and outer surface. The liquid jet is normal to the surface of the TBC layer and the surface of the substrate. Therefore, the non-abrasive water jet could remove the ceramic coating layer without destroying the inner part even though the ceramic coating layer has the same chemical components as the substrate. Besides, the jet also influences the surface roughness, which could promote the adhesion of new ceramic coating layers. The non-abrasive jet is used with the water medium. The water pressure could be 40,000 psi (about 2800 bar) to 60,000 psi (about 4100 bar).

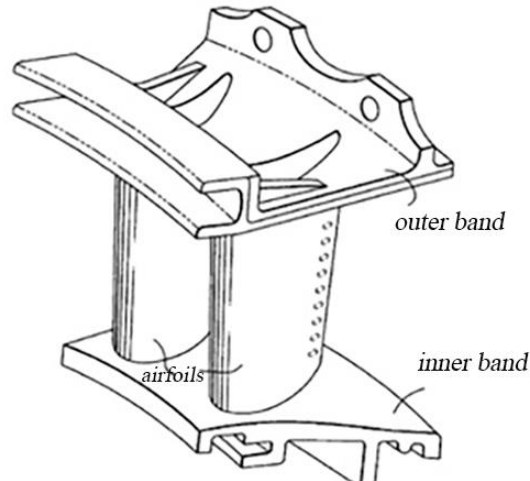


Figure 2.7. Schematic of a gas turbine engine nozzle section [55].

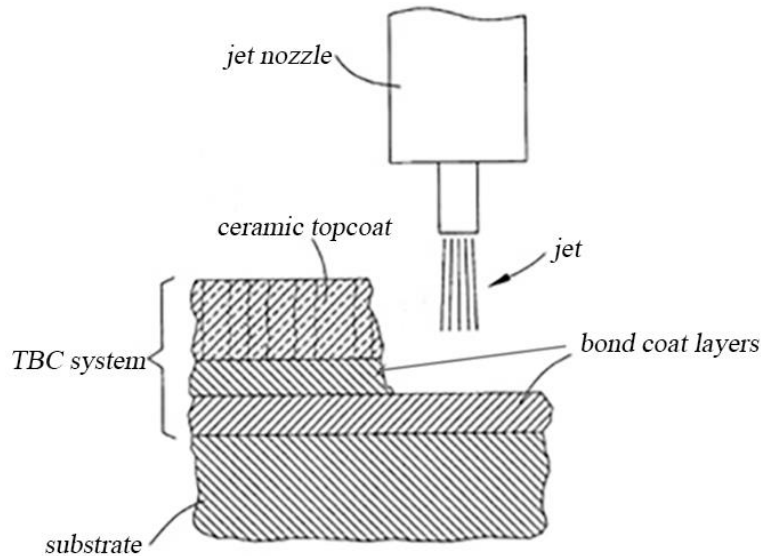


Figure 2.8. Schematic of a cross-sectional view through a substrate region [55].

2.2.3.2 Localized Water Jet

The turbine shown in Figure 2.9 was oxidized and corroded due to the hot combustion gasses. By using the localized water jet method [56], the component of the turbine was removed and cleaned to remove the loose oxides and contaminants such as grease, oils, and soot. Then the water jet was programmed to localize the accurate shape of the spalled region and remove the ceramic coating from the spalled region. The undamaged coating was not influenced due to the localized water jet. A new local TBC layer is recoated on the spalled region after cleaning.

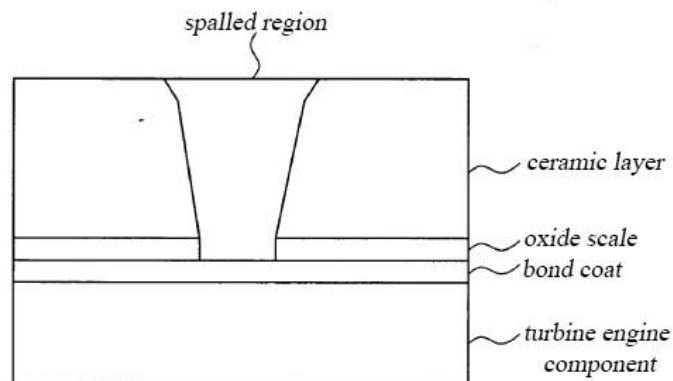


Figure 2.9. Schematic of a localized spalled region of the ceramic layer. (10. thermal barrier coating system 12. bond coat 14. the turbine engine component 16. Ceramic layer 18. oxide scale 20. spalled region) [56].

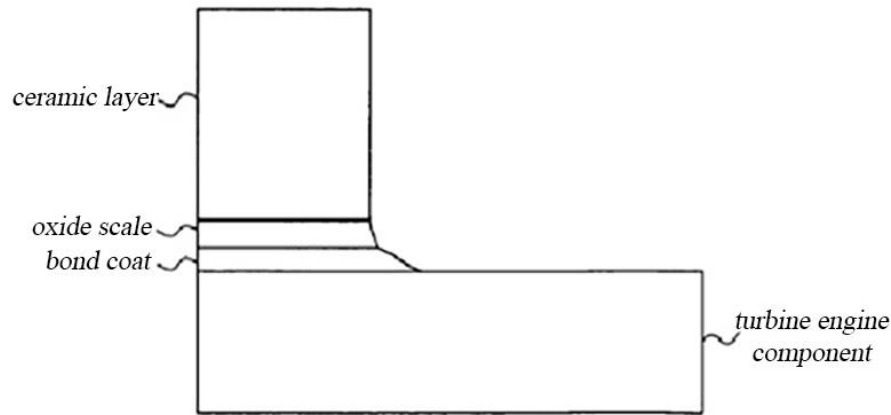


Figure 2.10. Schematic of using water jet to remove the spalled region and form a tapered profile [56] .

2.2.3.3 Computer Numerically Controlled Abrasive Waterjet

A five-axis computer numerically controlled (CNC) AWJ [53] removes the coating in iterative steps. During the removal process, the distance between the AWJ to the surface is controlled by the computer, which is determined by the feedback from computer sensors. By using computer sensors, the coating thickness and surface roughness contour can be reconstructed as the removal process. The immediately computed information is compared with the design and thus create the new information for the next step.

It is very effective while the surface requirement of removal coating is restricted. The CNC AWJ not only has the high efficiency but also is accuracy enough. It has widely been used in the coating removal process.

2.2.4 Laser Ablation

Figure 2.11 [57] shows the working principle of the laser system. Work head receives the laser signal, and the laser signal passes through the focusing lens to the samples. The scanner could control the location of the samples. After a section was ablated, the work head could be moved to another region and repeat the process. The pulse rate is around 10-15 kHz. The beam could be moved in any form of the motion to ablate the sample. The diameter of the YGA laser beam is 0.5 mm and 0.5 in for CO₂ laser beam typically. When a region has been ablated, the work head can be located in a new location and move along the blade to achieve an even ablation. The power output of the laser is 1-2 kw. As is shown in Figure 2.12, the TBC layer protects the substrate

material, and the oxide layer is between the TBC layer and the substrate layer. When the TBC layer is damaged during thermal damage, the laser ablation method could be used to remove the failure TBC layer. Compared with the methods of grit blasting and chemical stripping, laser ablation is more advanced. It makes the removal process more precision, reduces the chemical waste, and increases the work efficiency and safety. Because of these advantages, laser ablation can decrease the component failure and eliminate the requirements for destructive evaluation. Since the components and parts in aerospace are very expensive, this will directly leads to large cost savings during engine overhaul or repair [58].

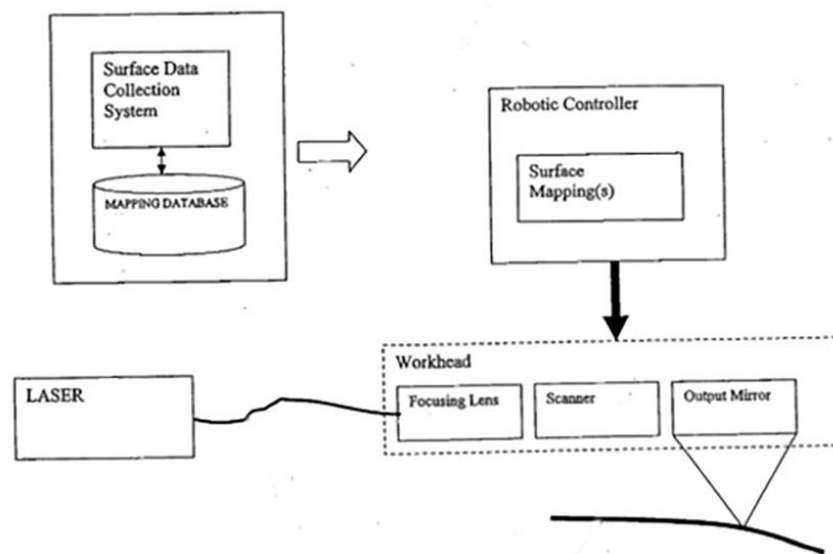


Figure 2.11. T working principle of a laser system [57].

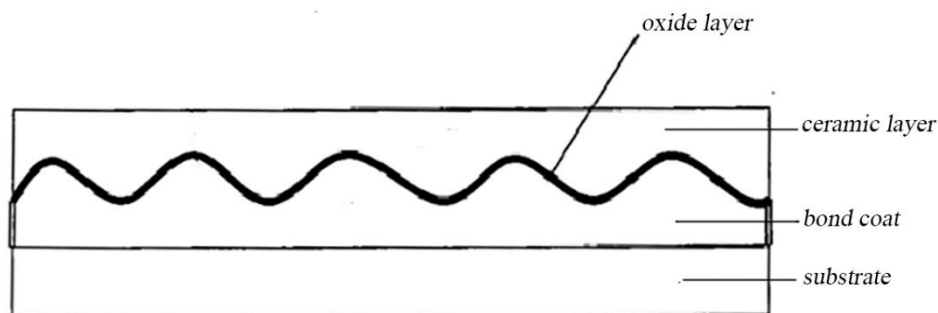


Figure 2.12. Schematic cross-sectional view of an exemplary TBC to be processed [58].

2.3 Repair Methods for Thermal Barrier Coated Components

2.3.1 Plasma Spraying

2.3.1.1 Suspension Plasma Spraying (SPS)

Suspension Plasma Spraying [59] is often used to repair the sections with vertical cracks or defined gaps. By comparing with traditional plasma spraying, the smaller particles could be used in the suspension plasma spraying to produce the fine columns to repair the vertical cracks or defined gaps. Therefore, it could provide strain tolerance to the coating layer during the thermal bearing process. Besides, the repair layer of SPS is polycrystalline and has no obvious lamellar features, which could be used to repair the gas turbine engines. Although the ceramic microstructure of the repairing layer is different from the original EB-PVD layer, the microstructure of the SPS repair layer can also provide a long lifetime. Finally, the repaired areas were flushed to obtain a finished surface.

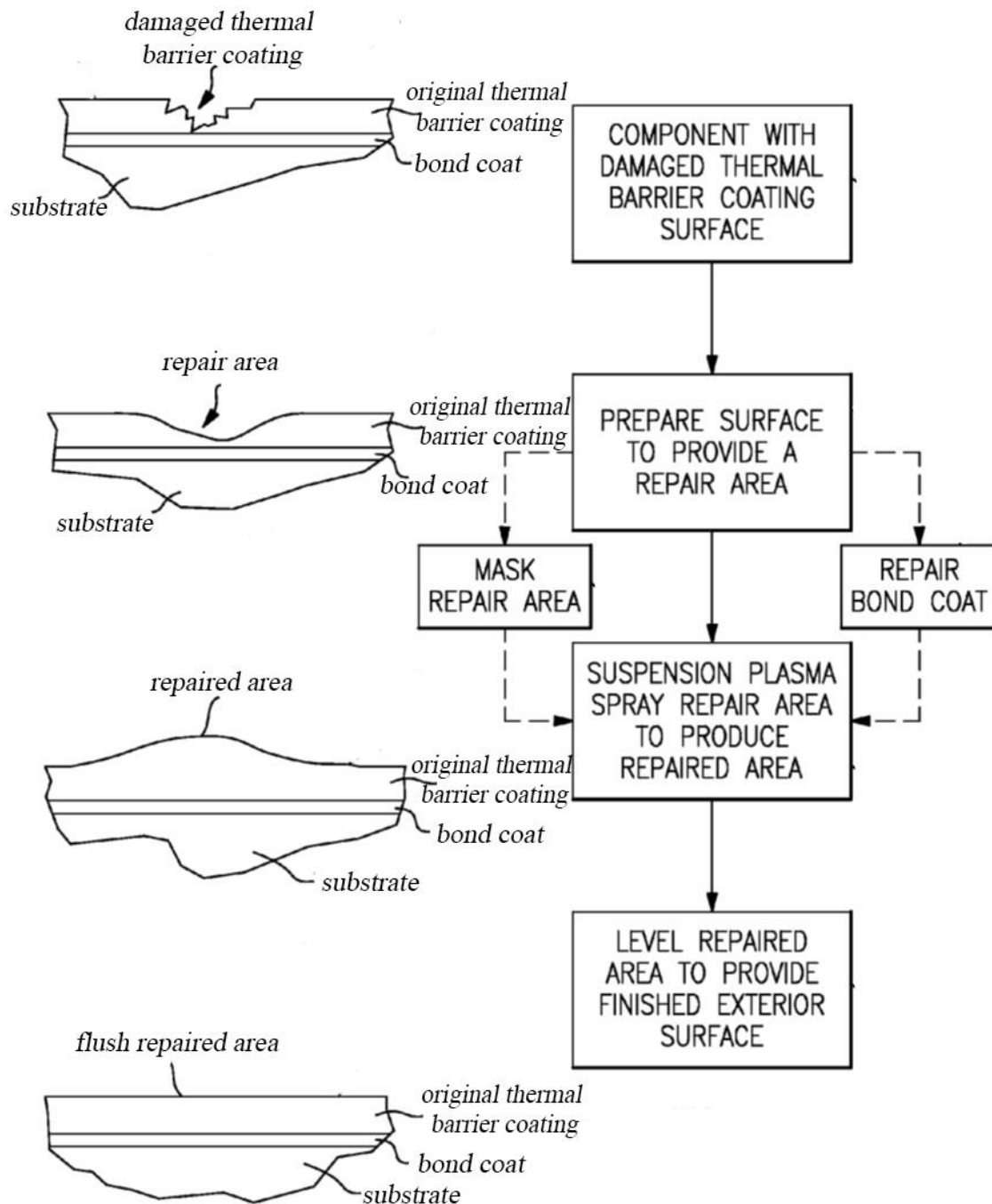


Figure 2.13. The schematic of using SPS technique to repair the cracked TBC [59].

2.3.1.2 Plasma Spray Technique

The plasma spray technique [49] is often used to repair the less complicated surface. If a cooling hole exists, fibers or flowing gas is used to prevent the closure. The repair layers have

good thermal cycle resistance. The grain structures of the ceramic repair layer are shown in Figure 2.13. The repair layer is usually higher than the substrate, and the repairing surface was polished until the level is substantial to the original ceramic layer. By using this method, the repairing TBC layer presents good thermal cycle resistance, especially for the thin platinum aluminide bond layer.

2.3.1.3 Laser-Induced Breakdown Spectroscopy (LIBS)

As an optical technique, LIBS is an effective way to obtain the sample's chemical information (Figure 2.14). The laser ablation is the most basic part of LIBS process. From the target surface, small amounts of material are vaporized and ejected [60]. Compared to other elemental analysis methods, LIBS has compelling advantages. It can be used to remove the surface contaminant precisely. In addition, if the very precise laser ablation is used, the contaminants can be selected to remove from a substrate metal surface [61, 62].

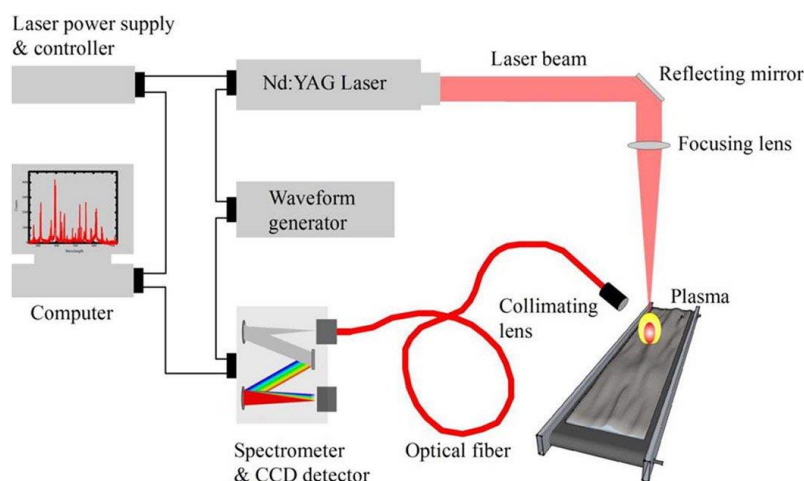


Figure 2.14. Generalized Schematic of LIBS [60].

2.3.2 Chemical Paste

2.3.2.1 Partially Stabilized Zirconia

Figure 2.15 shows the thickness of the damaged thermal coating layer is around 75 μ m to 300 μ m. In this method, the partially stabilized zirconia sol-gel [63] is used to repair the damaged TBC layer. Then, the solution is evaporated to leave the partially stabilized zirconia precursor. By repeating this process, it could achieve the suitable thickness of the precursor. The partially stabilized zirconia sol-gel was prepared by combining alkoxides of Zirconium and yttrium in

ethanol or isopropanol or by combining Zr-prop oxide in propanol and Y-methoxy ethoxide in ethoxyethanol, plus ethanol. It was used to repair the damaged area, and then the solvent was evaporated until the suitable thickness of the repair layer was produced. Finally, the partially stabilized zirconia was burned under 900°C to produce the thermal barrier layer.

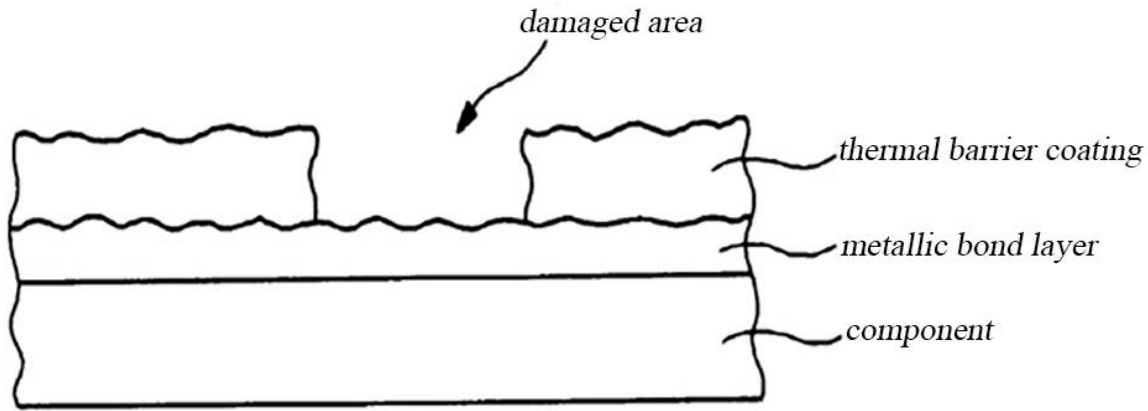


Figure 2.15. Schematic of the damaged coating [63].

2.3.2.2 Scandia Yttria Stabilized Zirconia (SYSZ) Ceramic Paste

Figure 2.16 and Figure 2.17 are cross-sectional side views of a typical damaged TBC coating system. The localized spallation is observed in the damaged TBC [64]. The ceramic paste contains scandia yttria-stabilized zirconia and an organic binder. The course of SYSZ particles is $30\mu\text{m}$ to $50\mu\text{m}$. The organic binder includes ethanol, UCON lubricant, and SR350 or SR355 silicone resin. The alternative organic binder includes propanol, methanol, methyl ethyl ketone, toluene, glycerine, cellulose, and polyvinyl alcohol. During the repairing process, the TBC patch was dried under 65°C to 70°C to prevent the phenomenon of violent volatilization and bubbling. Then the TBC patch was dried under 300°C - 700°C so that the silicone resin was transferred to silicone resin with high strength. When the TBC patch was used in the turbine, silica bonds were formed due to the high temperature of the operating turbine, and the TNC patch fully cures during the operating temperature of the turbine which is about 900°C to 1000°C .

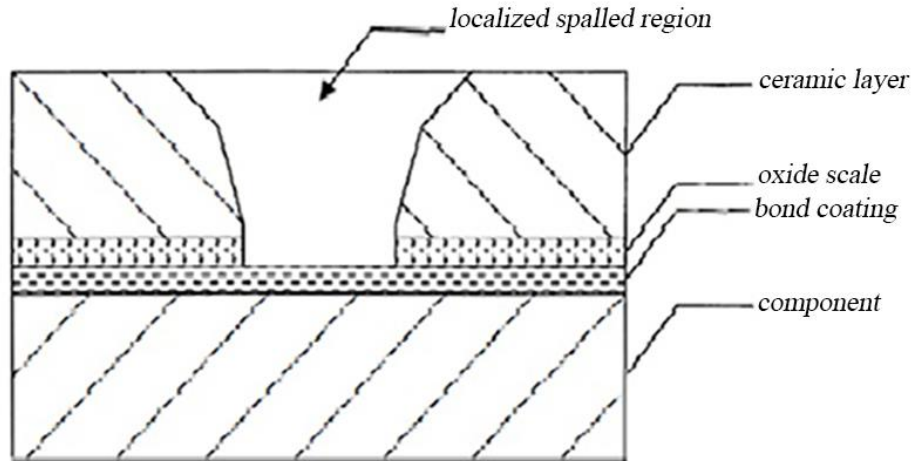


Figure 2.16. Cross-sectional side view of a typical TBC system [64].

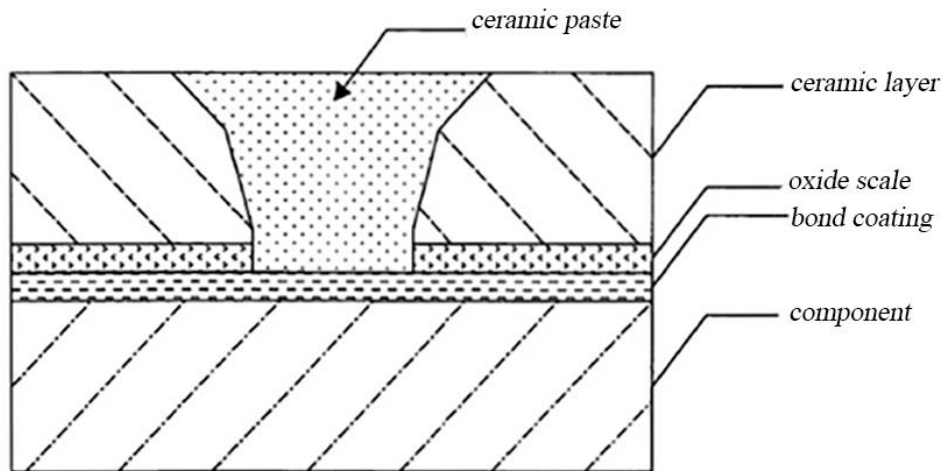


Figure 2.17. The localized spallation in the TBC system having been repaired using the in-situ methods and the TBC patch composition of the present invention [64].

2.3.2.3 Gel Repairing

The gel [65] is applied to the thermal barrier coating surface and then heated. The heating occurs in two stages. First is heating to remove impurities and volatile material from the gel. The second stage of heating involves curing the actual gel coating to the thermal barrier protective layer. The coating or slurry contains zirconia filler. The curing of the slurry component transforms precursors into oxide matrices. Depending on the intended application, the gel can also be applied in layers with different percentage compositions of zirconia filler.

2.3.2.4 Composite Preform

The composite preform method [66] is developed to repair a metal component especially for damaged coatings portions of the turbine. By sintering mixture particles of the coating layer and brazing alloy, the composite preform was produced and then deposited on the surface of the metal component that the damaged coating layer has been removed. The composite preform and metal surface were bonded by brazed joint by heating under appropriate temperature. As shown in Figure 2.18, once the composite prefab is prepared, additional coatings may be optionally placed on the surface of the composite prefab. For example, the TBC layer with the same composition as the TBC layer of the metal turbine component (Figure 2.19) can be deposited on the composite prefabricated piece. In addition, an oxide layer of the same composition as the oxide layer of the metal turbine components can be deposited on the composite prefabricated to facilitate bonding between the TBC layer and the composite prefabricated. The thickness of each additional coating is approximately the same as the corresponding layer on the metal turbine components.

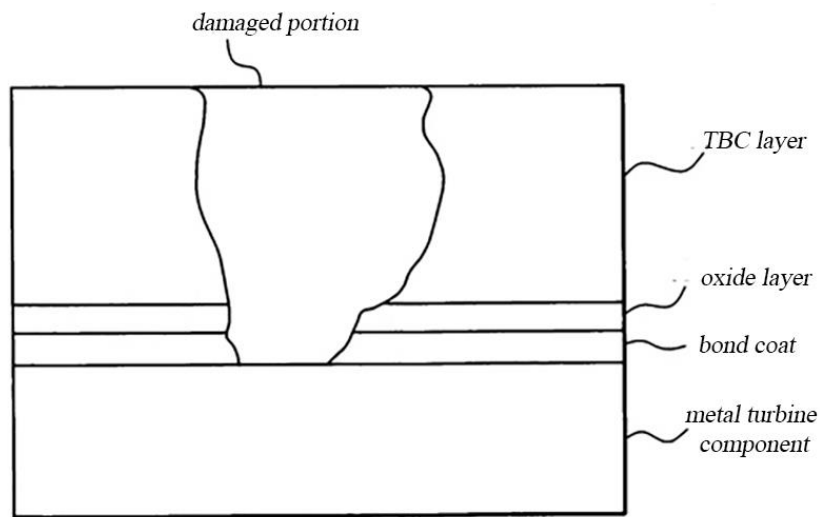


Figure 2.18. Schematic representation of a cross-section of a coated turbine component, wherein the coating includes a damaged portion [66].

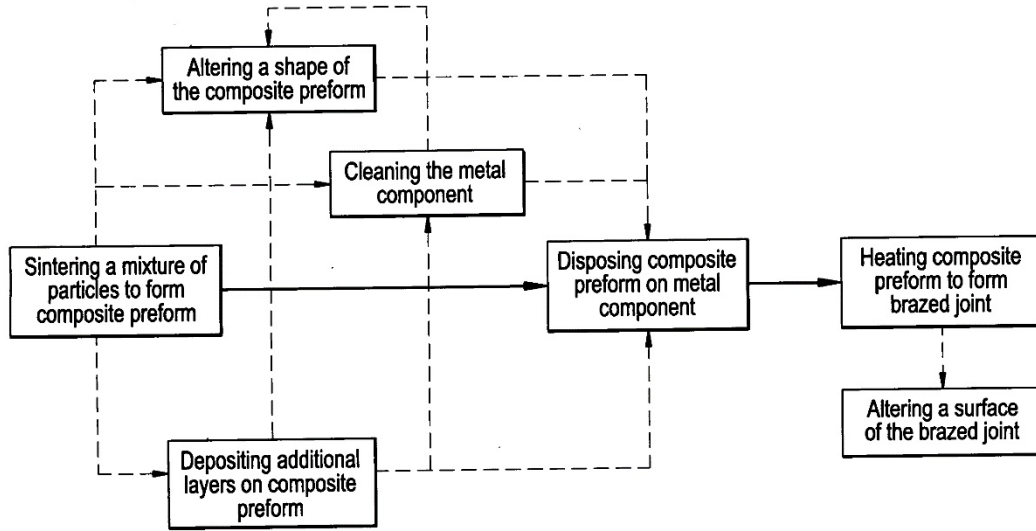


Figure 2.19. A process flow chart for repairing a damaged portion of a coated metal component [66].

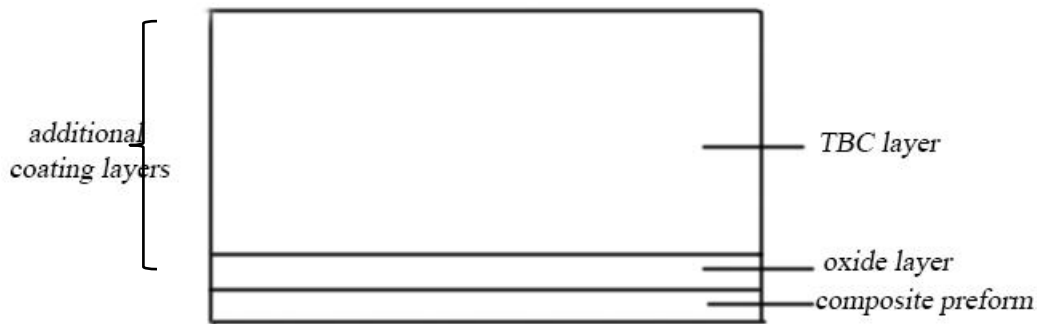


Figure 2.20. Schematic representation of a cross-section of a coated composite preform [66].

2.4 Assessment of Different Coating Removal and Repair Techniques

This report summarizes a review of the different methods used for repairing damaged thermal barrier coatings in the literature. The following two tables summarize and compare the different removal and repair methods for damaged coatings. Based on the literature survey data there is not a universal approach that can be used to all thermal barrier coating systems. The specific the removal and repair method should be chose for given damaged coatings, including its composition, process, type of damages, and available resources.

Table 2.1. Removal Methods for Thermal Barrier Coated Components.

Grit Blasting	Grit blasting	<u>Advantage</u> <ol style="list-style-type: none"> 1) Relatively inexpensive to operate and maintain 2) No harmful chemicals are needed 3) Creates a cleaner surface finish <u>Disadvantage</u> <ol style="list-style-type: none"> 4) Can result in uneven surfaces caused by uneven material removal. 5) It's usually a non-controlled process that leads to varying results. 6) Can potentially distort part geometry.
	Grit blasting with solid CO ₂	<u>Advantage</u> <ol style="list-style-type: none"> 7) Unlike other blast media, the CO₂ particles have a very low temperature of -109° F, giving a unique thermodynamically induced surface mechanism. 8) Preheating with IR lamps has two advantages. <ul style="list-style-type: none"> o The irradiation with IR allows performing the pre-heating during the solid CO₂ blasting. o The irradiation with IR can heat the substrate/coating system up to 1000° C. <u>Disadvantage</u> <ol style="list-style-type: none"> 1) State-of-the-art blasting machines for dry ice can use only a discontinuous (pulsed) solid CO₂ blasting flow. 2) The removal rate decreases if the pulsed flow is used.
	Pencil Blasting	<u>Advantage</u> <ol style="list-style-type: none"> 1) No chemicals involved 2) The pallets are recyclable <u>Disadvantage</u> <ol style="list-style-type: none"> 1) A columnar ceramic layer is very difficult to remove. 2) With repetitive use, grit blasting destroys the component.
	Grit	
Chemical Stripping	Autoclaving	<u>Advantages</u> <ol style="list-style-type: none"> 1) This invention enables the ceramic layer of an air-cooled component to be completely replaced without accumulating additional ceramic in the cooling holes. [3] 2) Because the present invention can completely remove ceramic from a cooling hole, the performance of an air-cooled component treated with this invention is promoted by the restored uniform film cooling of the component Surfaces. 3) This invention is less costly and time-consuming than if a waterjet were used to remove the ceramic layer from the substrate

Table 2.1 continued

		<u>Disadvantages</u> <ol style="list-style-type: none"> 1) Requires the use of an autoclave operating at high temperatures and pressures. 2) Equipment is expensive.
	The aqueous solution containing Acid Fluoride Slat	<u>Advantages</u> <ol style="list-style-type: none"> 1) Reduced labor, equipment, and processing cost. 2) Removes TBC from the cooling holes of air-cooled components. 3) Since all the TBC is removed from the holes, the performance of the component is increased.
		<u>Disadvantages</u> <ol style="list-style-type: none"> 1) It requires the use of corrosion inhibitors. 2) The process is toxic
	Acid Stripping	<u>Advantages</u> <ol style="list-style-type: none"> 1) Relatively inexpensive to operate and maintain. 2) Can be used to treat a variety of issues such as removing impurities including stains, rust, and contaminants.
		<u>Disadvantages</u> <ol style="list-style-type: none"> 1) Acid can result in cracking, corrosion, and other destructive effects on the material. 2) Environmental issues and regulations that limit usage. 3) Acid variability can lead to unexpected part damage. 4) Acid Stripping can contaminate the material interface. 5) Acid repair reduces part life and repair cycles.
Water Jet	Computer Numerically Controlled Abrasive Water Jet	<u>Advantages</u> <ol style="list-style-type: none"> 1) Environmentally friendly 2) Removes coatings without damaging components. 3) The surface produced is free of contamination. 4) NC proves which is controlled to promote consistency.
		<u>Disadvantages</u> <ol style="list-style-type: none"> 1) Could be slightly higher in cost due to required equipment and maintenance.
	Non-abrasive Water Jet	<u>Advantages</u> <ol style="list-style-type: none"> 1) Could remove the TBC layer without damaging the substrate. 2) The jet influences the surface roughness, which could promote the adhesion of new ceramic coating layers.
		<u>Disadvantages</u> <ol style="list-style-type: none"> 1) limited to use on thin or soft materials

Table 2.1 continued

	Localized Water Jet	<u>Advantages</u> <ol style="list-style-type: none"> 1) It can be used for components with complex geometries and is safe for the environment. 2) Since this process can be carried out locally, the service life of the component is increased.
		<u>Disadvantages</u> <ol style="list-style-type: none"> 1) The equipment cost is high. 2) Prone to leaks 3) It can inflict significant damage to the bond coat.
Laser Ablation		<u>Advantages</u> <ol style="list-style-type: none"> 1) The laser ablation process can be used as a cleaning system and for removing damaged TBC. 2) The level of accuracy is high. 3) The position of the laser work head can be adjusted. 4) It can be used as a laser-based analysis system. 5) It can clean the turbine in its housing.
		<u>Disadvantages</u> <ol style="list-style-type: none"> 4) Power requirement is high. 5) The skilled worker is required for operation. 6) It is expensive to set up.

Table 2.2. Repair Methods for Thermal Barrier Coated Components.

Plasma Spraying	<u>Advantages</u> <ol style="list-style-type: none"> 1) Coatings are dense and strongly bonded to the substrate. 2) They have higher integrity and perform better than coatings applied by other thermal-spray processes. 3) The repair method enables faster repairs as full coating removal is not necessary.
	<u>Disadvantages</u> <ol style="list-style-type: none"> 1) The inner gun electrodes or other components may have deformations during the plasma spray process. 2) The high temperatures associated with the plasma jet can result in carbide decomposition or excessive oxidation when spraying in the air, giving carbide coatings with lower hardness or metallic coatings with higher oxide levels compared with HVOF sprayed coatings.
Chemical Paste	<u>Advantages</u> <ol style="list-style-type: none"> 1) The gelation time can be manipulated by varying amounts of water added. 2) It takes comparatively less time. 3) A simple repair process
	<u>Disadvantages</u> <ol style="list-style-type: none"> 1) Sanding is needed to even out the surface. 2) It cannot be used for complex spot repairs. 3) The quality of repair is mediocre.

2.5 Summary and Remarks

In summary, the type of method used for repairing the damaged TBC depends on multiple factors. There is not a universal method applicable to all coating systems. The selection of the coating removal and repair process must be specific to damaged coating systems, based on their composition, type of damages, and available resources.

3. NUMERICAL SIMULATION OF IMPACT BEHAVIOR OF CERAMIC COATINGS USING SMOOTHED PARTICLE HYDRODYNAMICS METHOD

A version of this chapter has been published in the Journal of Engineering Materials and Technology (doi: 10.1115/1.4049021).

Abstract: In this work, the impact behavior of an alumina spherical particle on alumina coating is modeled using the smoothed particle hydrodynamics (SPH) method. The effects of impact angle (0° , 30° , and 60°) and velocity (100 m/s, 200 m/s, and 300 m/s) on the morphology changes of the impact pit and impacting particle, and their associated stress and energy are investigated. The results show that the combination of impact angle of 0° and velocity of 300 m/s produces the highest penetration depth and largest stress and deformation in the coating layer while the combination of 100 m/s & 60° causes the minimum damage to the coating layer. This is because the penetration depth is determined by the vertical velocity component difference between the impacting particle and the coating layer, but irrelevant to the horizontal component. The total energy of the coating layer increases with time, while the internal energy increases with the time after some peak values, which is due to energy transmission from the spherical particle to the coating layer and the stress shock waves. The energy transmission from impacting particle to coating layer increases with the increasing particle velocity and decreases with the increasing inclined angle. The simulated impact pit morphology is qualitatively similar to the experimental observation. This work demonstrates that the SPH method is useful to analyze the impact behavior of ceramic coatings.

3.1 Introduction

Thermal barrier coating (TBC) is a multi-layer material system that usually consists of a top ceramic coating, typically 8YSZ due to its low thermal conductivity and good thermomechanical durability; and a metallic bond coat, e.g., NiCrAlY [67, 68]. In practice, TBCs in gas turbines are susceptible to the damage caused by foreign particles. To protect TBC systems, an inlet particle separator is installed in most of the rotorcraft gas turbine engines to stop sand ingestion, but it is not completely efficient. Fine particles with a particle size of less than $75\text{ }\mu\text{m}$ cannot be filtrated [69]. Therefore, the top ceramic coat in TBCs has shown vulnerability to intake flows that contain

sand, dust, and/or fly ash, which adheres and reacts at high temperatures. It may cause premature failure in the components through both impingement and combined mechanical-thermal-chemical attack [70, 71].

There are several studies regarding TBC failure process due to foreign particle impact or the erosion process. The failure process of $\text{Al}_2\text{O}_3/\text{NiCrAlY}/\text{SUS304}$ atmospheric plasma spray coating was studied. It was found that the shear mode of microfracture occurred toward the center from the edges of the specimen [72]. In addition, turbine blade surface deterioration caused by erosion was investigated. The results indicated that both erosion and surface roughness increased with the impact angle and particle size [73]. Additionally, the optimization of blade section shape subject to particle erosion from an aerodynamic standpoint was investigated. It concluded that the erosive damage to the surface was represented by sand grains colliding with the blade leading edge [74]. In terms of modeling, simulation of ballistic impact on ceramic material was conducted with Johnson Holmquist ceramic model (JHC). Plate impact simulations on silicon carbide were performed and compared to experimental loading and unloading curves [75]. Also, the sand corrosion behavior for ceramic coating was studied using a computational fluid dynamics model. The numerical results for the eroded surface geometry and the performance deterioration showed the same tendency as the experimental data [76]. Also, non-ordinary state-based peridynamics were used to understand the fracture in brittle ice due to particle impact. However, the effects of velocity and impact angle on the fracture were not included in the study [77]. High-speed impacts and penetration processes usually cause large deformations. Traditional grid-based numerical methods such as the finite element method (FEM) are generally difficult to simulate large deformation due to severe mesh distortions. In comparison, the SPH method has shown to be very useful to model the high-speed particles to accommodate their extremely large deformation, which is important for the brittle fracture of ceramic materials [78]. As a mesh-free, Lagrangian particle method, the SPH method can be used to handle large distortions. It is particularly suitable to study some fast-transient dynamics problems and the severe deformation of the particle [14, 15]. The phenomena of impact onto ceramic/aluminum composites were modeled using the smoothed particle hydrodynamics (SPH) method. Results indicated that, with the increasing initial velocity and ceramic thickness, and decreasing support layer thickness, the penetration area was increased. However, the work used a projectile meshed with finite element [79].

In summary, despite the above-mentioned efforts, a detailed study of the impact behavior of particles on a ceramic coating is still lacking. In this study, the existing SPH methods implemented in LS-DYNA are used to simulate the impact behavior of an alumina particle on an alumina ceramic coating. The structure of the paper is as follows. Section 2 presents the model description. The general formulation of the SPH methods and the model details in the study are provided. The focus is to understand how the impacting particle's inclined angle and velocity affect the morphology changes of the impact pit and impacting particle, and their associated stress and energy. Section 3 gives the results and discussion. Section 4 presents the simulation results compared against experimental observation. Finally, Section 5 summarizes the conclusion.

The simulation results help deeply understand the impact process which is nearly impossible to complete in the lab. In addition, it can help to improve the manufacturing process of the thermal barrier coating. Also, the removal and repair process of damaged TBCs will be studied based on these simulation results.

3.2 Model Description

3.2.1 Smoothed Particle Hydrodynamics (SPH) Method

In SPH models, the value of a function f at a position r_i can be calculated by the following particle summation [80]:

$$f(r_i) = \sum_{j=1}^N \frac{m_j}{\rho_j} f(r_j) W(r_i - r_j, h) \quad (1)$$

$$W(r_i - r_j, h) = \frac{1}{h} \Theta \left[\frac{r_i - r_j}{h(r, y)} \right] \quad (2)$$

where m and ρ are the mass and density of a particle, respectively. W is a kernel function, which is the cubic B-spline function in LS-DYNA, where h is a smoothing length of the kernel to control the size of the summation domain. $W(r_i - r_j, h) \rightarrow \delta$ when $h \rightarrow 0$, where δ is the Dirac function [80]. The initial number of neighbors per particle in the model is set to 150. The number can be adjusted in the process.

In general, the compact support is defined by the smoothing length h and a scale factor κ that determines the spread of the specified smoothing function. So, the compact support means [80]:

$$W(r_i - r_j, h) = 0 \quad \text{when } |r_i - r_j| > 0 \quad (3)$$

An equation of state (EOS) is required for materials that undergo significant deformation such as large plastic deformation or compressible fluid. The EOS can build a relationship for the material's pressure and volume. Different types of EOS are selected according to the material compressibility [81]. A commonly used EOS is the Mie–Grüneisen equation of state as follows [82, 83]:

$$p = \frac{\rho_0 C^2 \mu [1 + (1 - \gamma/2)\mu - (\alpha/2)\mu^2]}{[1 - (S_1 - 1)\mu - S_2 \mu^2 / (\mu + 1) - S_3 \mu^3 / (1 + \mu)]^2} + (\gamma + \alpha\mu)E_0 \quad (4)$$

where p is pressure; S_1, S_2, S_3 are the coefficients of the slope of the $U_s - U_p$ curve, where U_s and U_p are shock wave velocity and particle velocity, respectively; γ is the Grüneisen factor; C is the Hugoniot intercept of the $U_s - U_p$ curve [83]; E_0 is internal energy; α is volume correction factor and $\mu = \rho/\rho_0 - 1$ is compression factor, where ρ/ρ_0 is the ratio of current density to initial density. The Johnson-Holmquist Plasticity Damage Model was first proposed to describe the response of brittle materials for large deformation in 1992 and proved to be useful for modeling ceramics, glass, and other brittle materials. The equivalent stress for a ceramic-type material is given in terms of the damage parameter D by [84]:

$$\sigma^* = \sigma_i^* - D (\sigma_i^* - \sigma_f^*) \quad (5)$$

where

$$\sigma_i^* = a (p^* + t^*) n (1 + c \ln \dot{\epsilon}^*) \quad (6)$$

represents the intact, undamaged behavior. The superscript, '*', indicates a normalized quantity. a is the intact normalized strength parameter, c is the strength parameter for strain rate dependence, $\dot{\epsilon}^*$ is the normalized plastic strain rate, and [84],

$$t^* = \frac{T}{P_{HEL}} \quad (7)$$

$$p^* = \frac{p}{P_{HEL}} \quad (8)$$

where T is the maximum tensile pressure strength, P_{HEL} is the pressure component at the Hugoniot elastic limit, and p is the pressure [84].

$$D = \sum \frac{\Delta \epsilon^p}{\epsilon_f^p} \quad (9)$$

represents the accumulated damage based upon the increase in plastic strain per computational cycle and the plastic strain to fracture [84]

$$\epsilon_f^p = d_1(p^* + t^*)^2 \quad (10)$$

and

$$\sigma_f^* = b(p^*)^m (1 + c \ln \dot{\epsilon}^*) \leq \text{SFMAX} \quad (11)$$

represents the damaging behavior. The parameter d_1 controls the rate at which damage accumulates. In undamaged material, the hydrostatic pressure is given by [84]

$$P = k_1\mu + k_2\mu^2 + k_3\mu^3 \quad (12)$$

in compression and [84]

$$P = k_1\mu \quad (13)$$

in tension where $\mu = \rho/\rho_0 - 1$.

3.2.2 Numerical Model Details

The SPH model setup is shown in Figure 3.1. A spherical alumina particle with a diameter of 60 μm is used as the impacting particle, which is meshed with the SPH particles. The layered alumina ceramic coating is modeled as a block with the dimension of $500 \times 500 \times 125 \mu\text{m}^3$. The top layer has meshed with SPH with a thickness of 25 μm , and the bottom layer is meshed by finite element with a thickness of 100 μm . Connect nodes are used to bond the top and bottom layers. The bottom of the bottom layer is fixed. The layered structure allows to efficiently capture the deformation process during impact and reduce the computational costs. Based on the mesh convergence analysis, the total number of particles for the SPH coating layer is 200,000. The total number of particles for the SPH sphere is 14,328. The total number of nodes for the FEM coating layer is 10,571. The used mesh density follows Ref. [85].

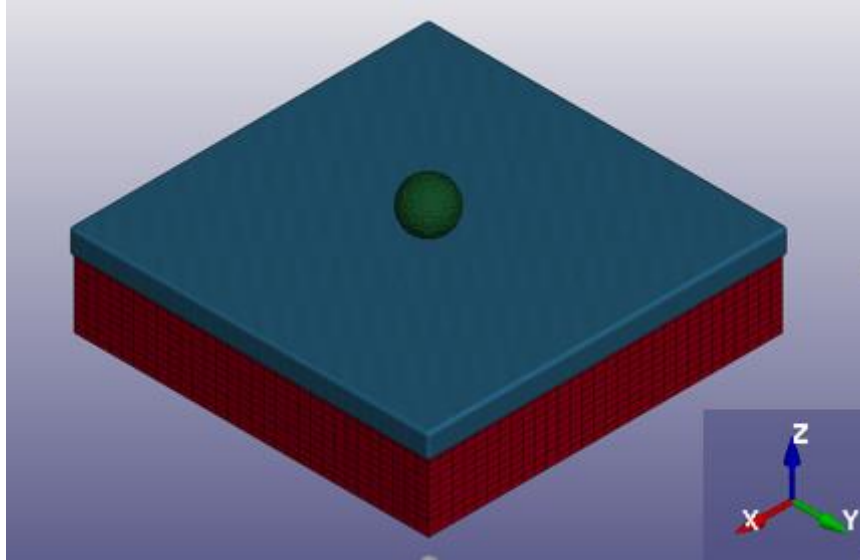


Figure 3.1. SPH model of a spherical alumina particle impacting on an alumina coating.

The spherical particle and the SPH coating layer are made of the same material. The density of the ceramic coating is 3420 kg/m^3 , the shear modulus is 108 GPa and the Poisson's ratio is 0.22 [82]. The parameters used in the SPH Mie–Grüneisen equation of state in Eq. 4 are shown in Table 3.1 [82], which assumes alumina. The parameters of *MAT_JOHNSON_HOLMQUIST_CERAMIC (JH-2) used in the FEM layer are shown in Table 3.2.

Table 3.1. Parameters used in the Mie–Grüneisen equation of state for the SPH ceramic layer. [82].

C(m/s)	S ₁	S ₂	S ₃	γ
9003	-3.06	2.350	-0.383	1

Table 3.2. JH-2 parameters of finite element ceramic layer [86].

Parameters	Value
A	0.93
B	0.31
C	0
M	0.6
N	0.6
HEL(GPa)	2.79
PHEL	1.46
D1	0.005
D2	1
K ₁ (GPa)	130.95
K ₂ (GPa)	0
K ₃ (GPa)	0

In order to couple the FEM bottom layer and SPH top layer, *AUTOMATIC_NODES_TO_SURFACE is selected to calculate the forces exchanging between FE elements and SPH particles near the coupling interface. Contact nodes to the surface are used between the top SPH layer and the bottom FEM layer. As a Lagrangian method, the interaction between SPH particles and FEM elements can be easily handled by a normal node to surface contact in LS-DYNA [87].

To evaluate the effect of impact angle and velocity on the impact behavior of the coatings, different impact angles and velocities are combined using a design matrix approach, as shown in Table 3.3. The impact velocity values are 100, 200, and 300 m/s, and the impact angles are 0°, 30°, and 60°. The impact angle is defined between the impacting velocity and the normal of the top coating surface. The corresponding velocity components, V_x and V_z, are also provided in Table 3.3. Design matrix of impact velocities V_x and V_z components (m/s) at three impact angles, 0°, 30°, and 60°.

Table 3.3. Design matrix of impact velocities V_x and V_z components (m/s) at three impact angles, 0° , 30° , and 60° .

0°		30°		60°	
V_x	V_z	V_x	V_z	V_x	V_z
0	100	50	86.6	86.6	50
0	200	100	173.2	173.2	100
0	300	150	259.8	259.8	150

Moreover, in order to understand the role of horizontal velocity component V_x on the penetration depth, the vertical velocity component V_z is fixed at 259.8 m/s. The V_x values are then varied as 0, 150, and 259.8 m/s, which corresponds to impact angles of 0° , 30° , and 60° .

To ensure stability and convergence of the energy absorbed by the coating decreases simulations, the Moving Least-Squares (MLS) approximation and an improved nodal integration scheme in LS-DYNA are used, which has shown to be much more stable in tension[88]. Additionally, option *CONTROL_BULK_VISCOSITY is enabled in the model since it slightly dampens out large oscillations at little numerical cost and with little energy cost [81].

3.3 Results and Discussion

3.3.1 Damage of the Ceramic Coating Layer

The side views of the impact process with different impact angles and velocities are summarized in Figure 3.2. Side view of the impact with different velocities and impact angles (a) 100 m/s & 0° , (b) 100 m/s & 30° , (c) 100 m/s & 60° , (d) 200 m/s & 0° , (e) 200 m/s & 30° , (f) 200 m/s & 60° , (g) 300 m/s & 0° , (h) 300 m/s & 30° , and (i) 300 m/s & 60° . It is clear that the penetration effect with the same angle increases with the increasing velocity. At the same time, the penetration effects decrease with the increasing impact angle at the same velocity. The case of velocity 300 m/s and impact angle 0° (Figure 3.2. Side view of the impact with different velocities and impact angles (a) 100 m/s & 0° , (b) 100 m/s & 30° , (c) 100 m/s & 60° , (d) 200 m/s & 0° , (e) 200 m/s & 30° , (f) 200 m/s & 60° , (g) 300 m/s & 0° , (h) 300 m/s & 30° , and (i) 300 m/s & 60°) has the maximum penetration effect, while the case of velocity 100 m/s and impact angle 60° (Figure 3.2 c) has the minimum penetration.

The extent of particle penetration and coating particle spattering increase with the vertical velocity component V_z , where the impact energy is proportional to $1/2mV_z^2$. Also shown in Figure 3.2, the spattered particles on the coating layer have a symmetric pattern along the impact surface when the impact angle is 0° . However, the spreading of particles increases with the increasing impact angle.

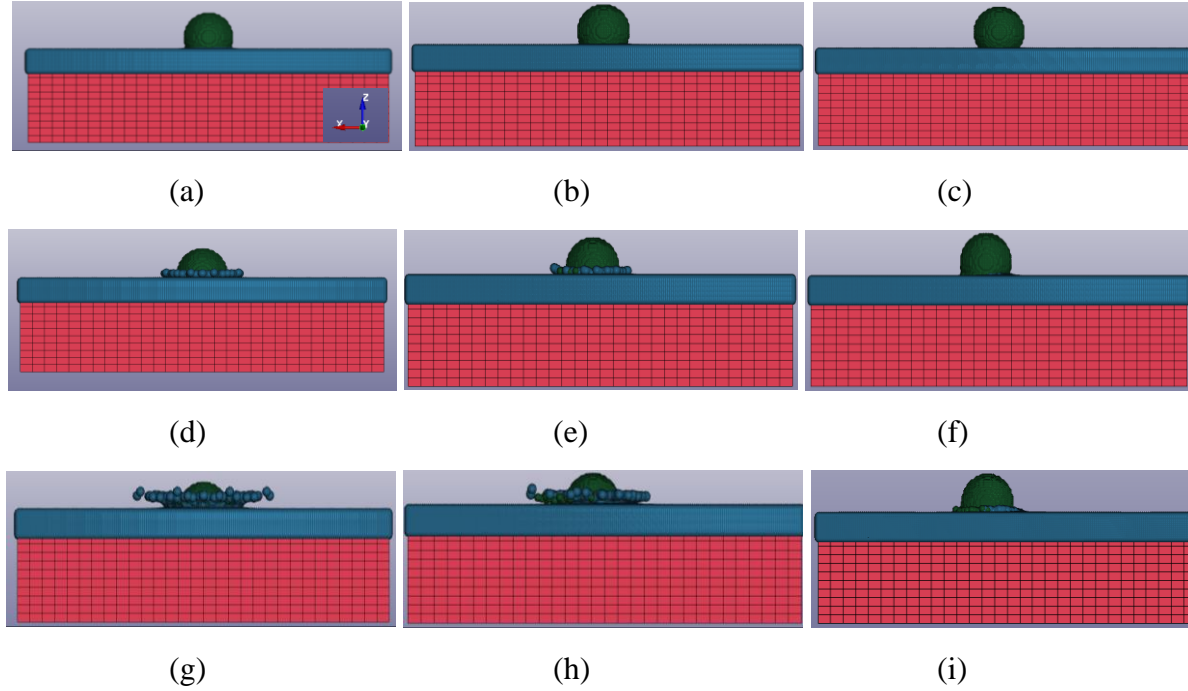


Figure 3.2. Side view of the impact with different velocities and impact angles (a) 100 m/s & 0° , (b) 100 m/s & 30° , (c) 100 m/s & 60° , (d) 200 m/s & 0° , (e) 200 m/s & 30° , (f) 200 m/s & 60° , (g) 300 m/s & 0° , (h) 300 m/s & 30° , and (i) 300 m/s & 60° .

Figure 3.3 shows the von Mises stress and impact penetration profiles of the coatings [89]. The von Mises stresses increase with the increasing velocity at the same impact angle. The distributions of the stress at the same angle have the same characteristics. The stress distribution is in a ring shape with an impact angle of 0° . The difference in stress distribution is caused by the horizontal velocity component V_x , which is most obvious in the case of the combination of 300 m/s & 60° .

On the other hand, it is clear that the penetration depth and area increase with the increasing velocity at the same angle. Also, the penetration depth and area decrease with the increasing impact angle at the same velocity. The case of velocity 300 m/s and impact angle 0° has the maximum

penetration depth. The case of velocity 100 m/s and impact angle 60° has the minimum penetration depth and area.

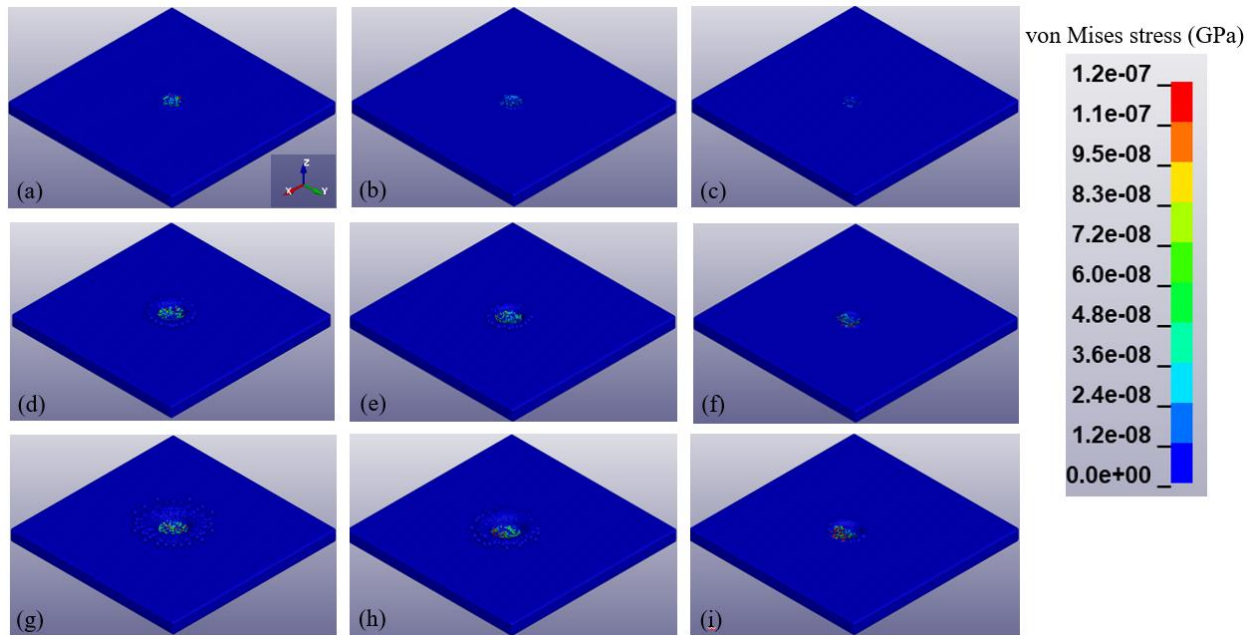
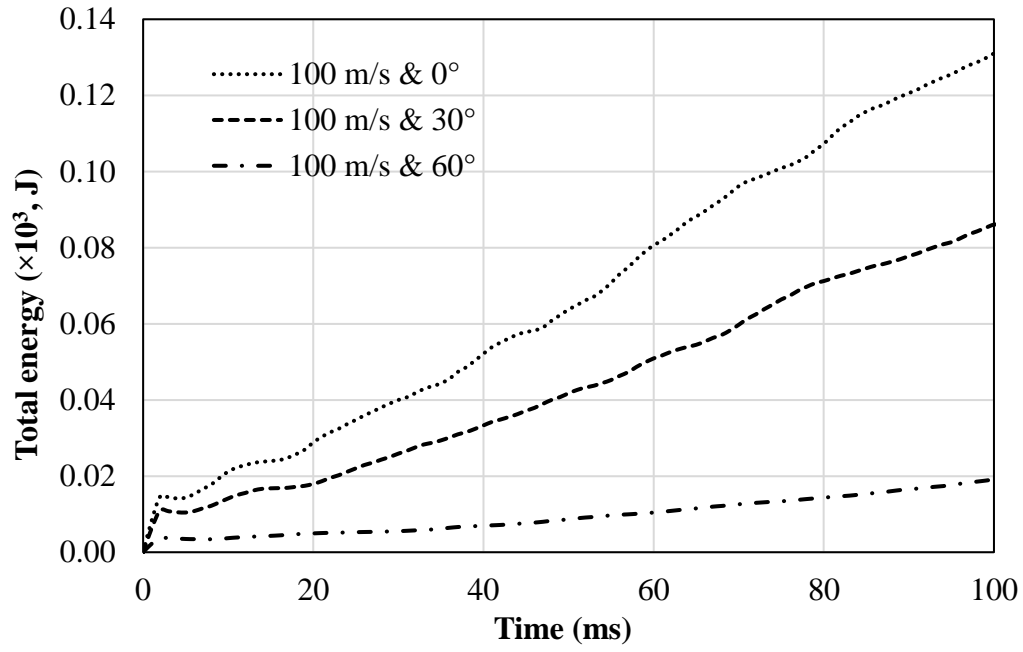
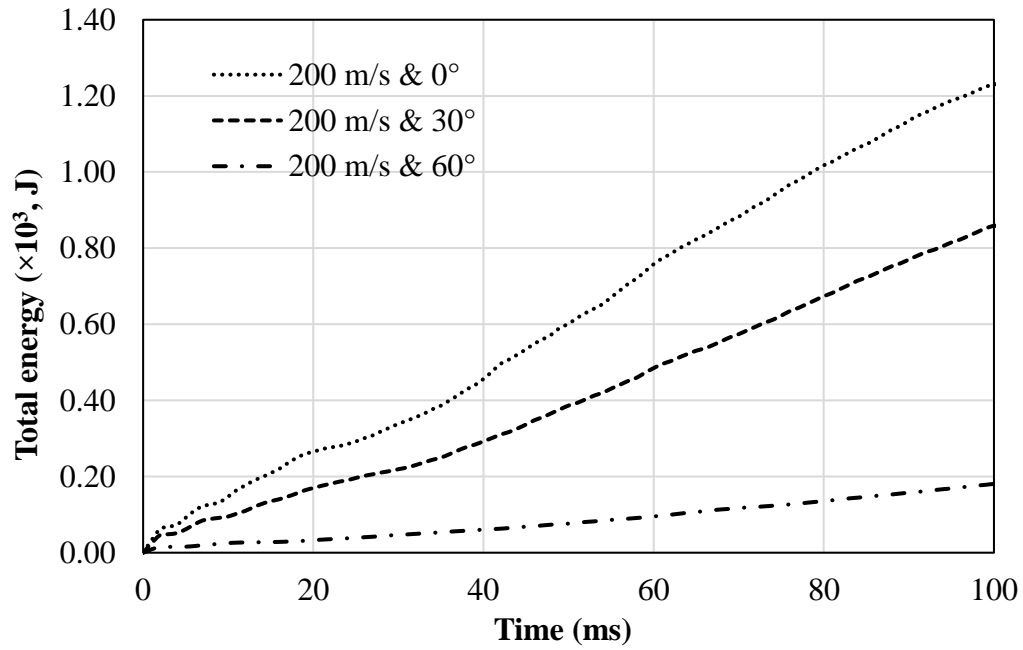


Figure 3.3. von Mises stress distributions in the coating layers at the end of impact: (a) 100 m/s & 0°, (b) 100 m/s & 30°, (c) 100 m/s & 60°, (d) 200 m/s & 0°, (e) 200 m/s & 30°, (f) 200 m/s & 60°, (g) 300 m/s & 0°, (h) 300 m/s & 30°, and (i) 300 m/s & 60°.

The coating's energy evolutions at different angles and velocities are shown from Figure 3.4 to Figure 3.7. Figure 3.4 shows the total energy and internal energy evolutions at different combinations of angles and velocities, respectively. In LS-DYNA, the total energy is the sum of internal energy, kinetic energy, contact (sliding) energy, hourglass energy, system damping energy and rigid wall energy [84, 90]. The results show that the total energy increases linearly with time.



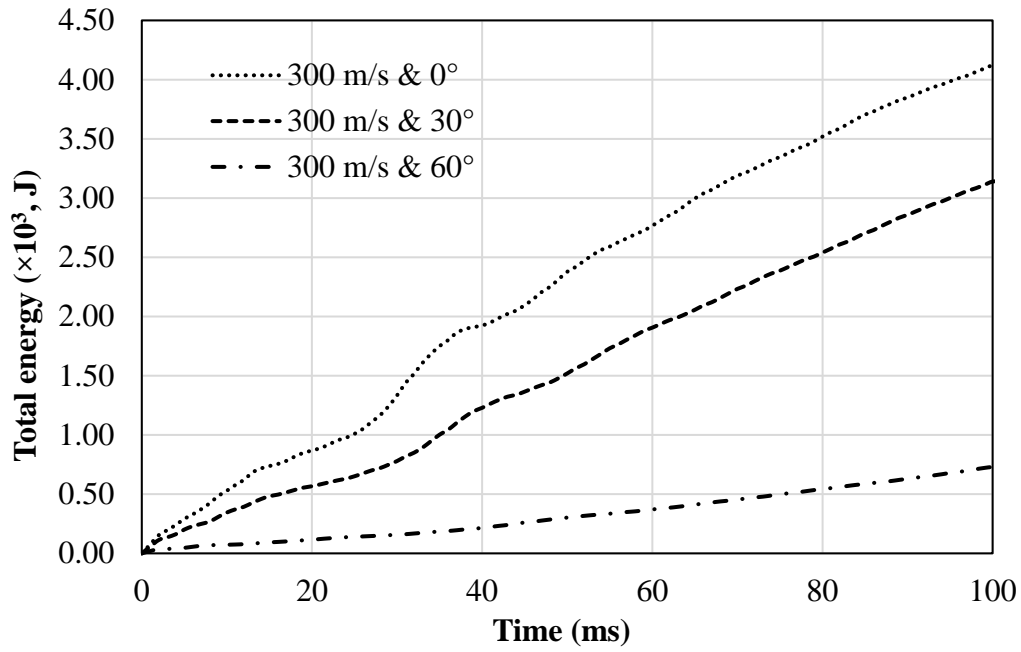
(a)



(b)

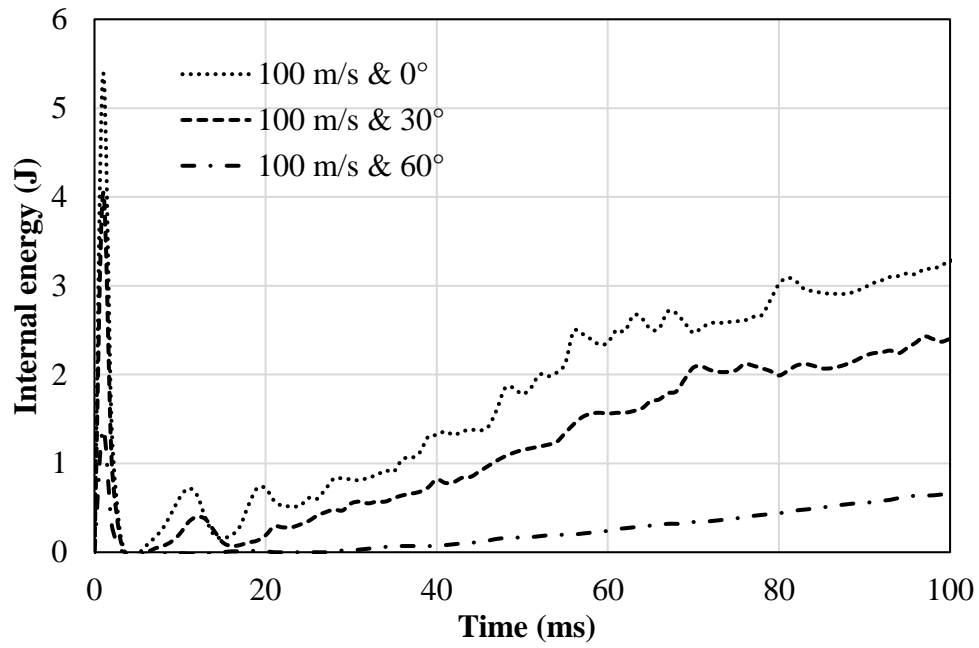
Figure 3.4. Total energy evolutions of the coating layer at different impact angles and velocities. (a) 100 m/s & 0°, 30°, 60°; (b) 200 m/s & 0°, 30°, 60°; (c) 300 m/s & 0°, 30°, 60°.

Figure 3.4 continued

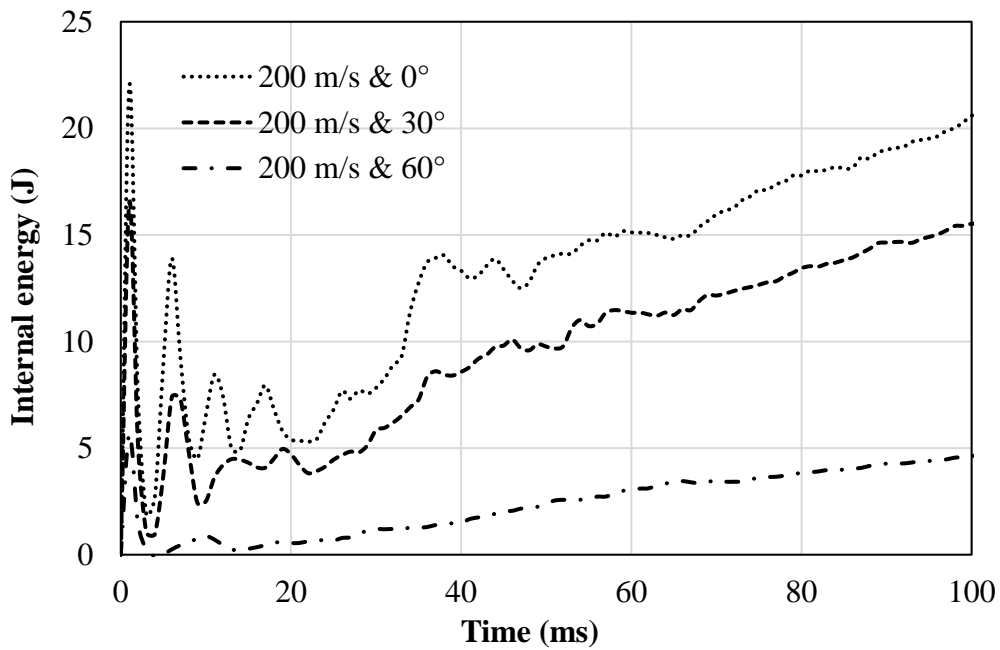


(c)

Figure 3.5 shows the internal energy evolutions at different combinations of angles and velocities. Internal energy is computed based on the six components of stress and strain (tensorial values). The calculation is done incrementally for each particle as follows: $(IE)_{new} = (IE)_{old} + \text{sum over all six directions of } (\text{stress} \times \text{incremental strain} \times \text{volume})$. The internal energies of all the elements are summed to give the total internal energy [84, 90]. The results show that the internal energy increases with time.



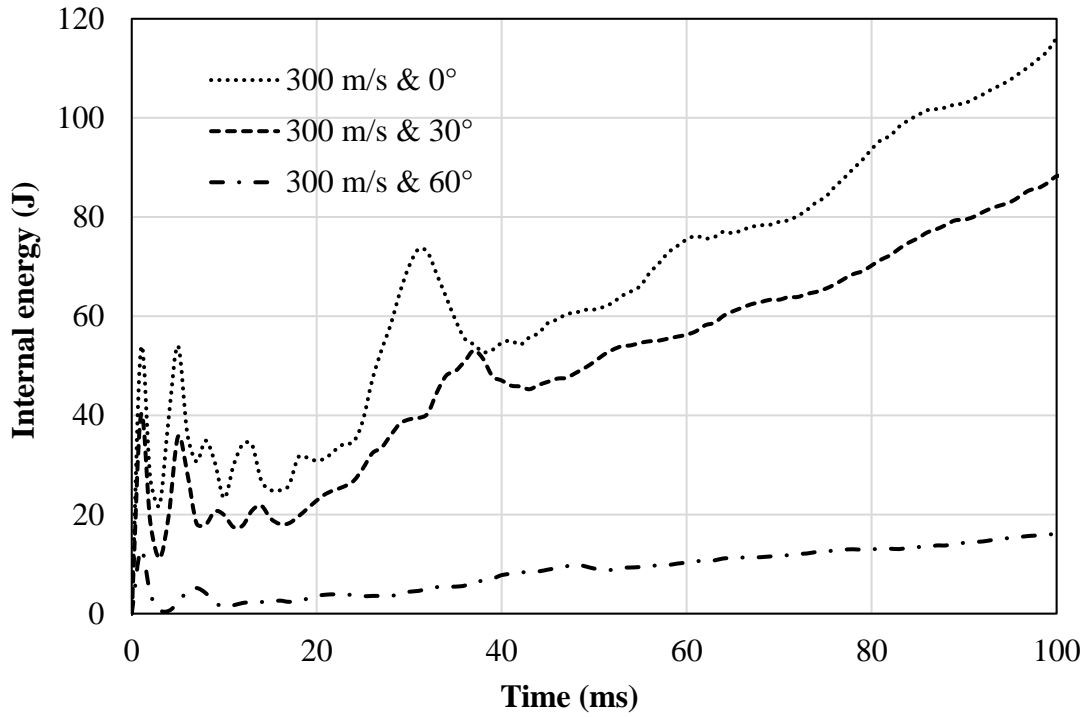
(a)



(b)

Figure 3.5. Internal energy evolution of the coating layer at different impact angles and velocities. (a) 100 m/s & 0°, 30°, 60°; (b) 200 m/s & 0°, 30°, 60°; (c) 300 m/s & 0°, 30°, 60°.

Figure 3.5 continued



(c)

Additionally, Figure 3.5 shows that the internal energy has a few peaks before it starts increasing gradually after a period of impact. This phenomenon is most evident with the combination of 100 m/s & 0°, 30°, and 60°. Taking 100 m/s & 0° for example, Figure 3.5 (a) shows that the internal energy has the maximum value at the time 1 ms and the minimum value nearly 0 J at 4 ms. It is due to the conversion of the kinetic energy of the spherical particle to internal energy immediately after the impact. As a result, the internal energy reaches the maximum value at the same time. The internal energy at the peak value is mainly stored at the impact point. As the impact process continues, the stress shock waves transmit through the coating. Then the internal energy decreases sharply. After 4 ms, the internal energy increases linearly as the impact area increases and the transition of stress wave becomes stable.

The total energy values of the coating at the end of the impact are shown in Figure 3.6. The total energy of the coating layer with the same velocity decreases with increasing impact angle. The highest velocity 300 m/s has the highest total energy and internal energy. The energy absorbed by the coating decreases with the increase of the angle. It is caused by the existence of the

horizontal velocity component V_x . The initial energy converted to the internal energy or doing work becomes less.

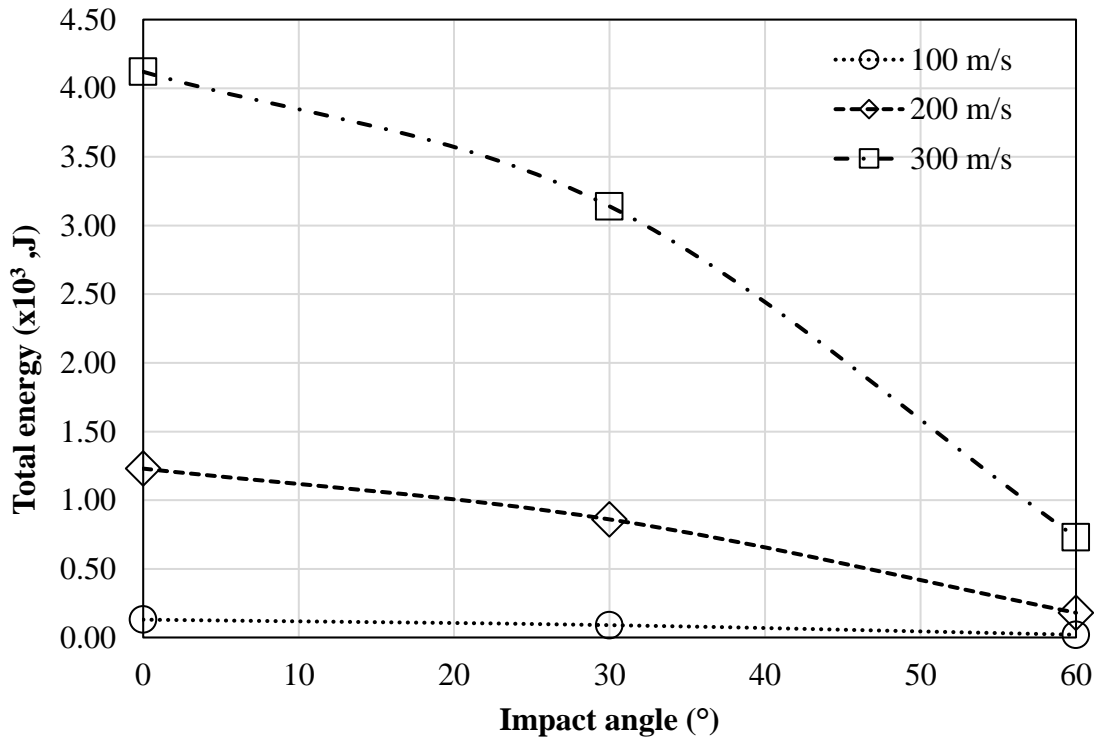


Figure 3.6. The final total energy values of SPH coating layer at different impact angles and velocities at the end of impact at 100 ms.

The internal energy values of the coating at different impact angles at the end of impact are shown in Figure 3.7. It shows the same regular pattern with the total energy, decreasing with the increasing angle. This is because more initial energy is absorbed by the impact parts to deformation when the impact effect is higher.

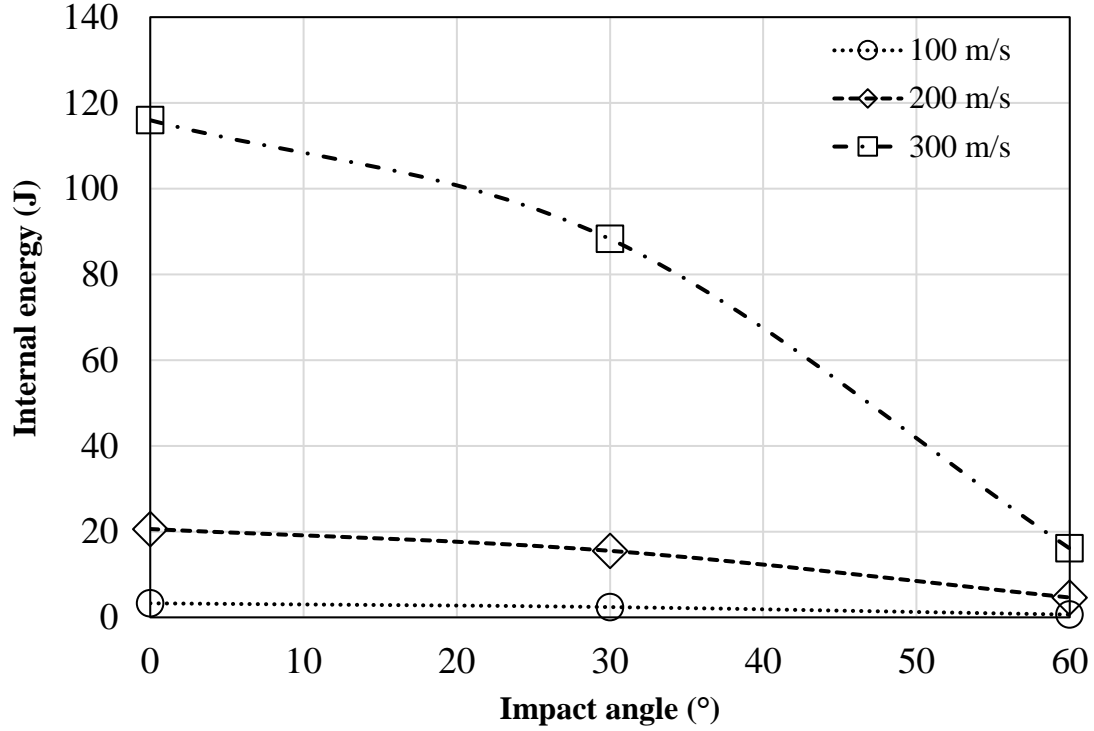


Figure 3.7. The final internal energy values of SPH coating layer at different impact angles and velocities at the end of impact at 100 ms.

To understand the effect of the vertical velocity component on the internal energy, the relation between the internal energy and the square of the vertical velocity is plotted in Figure 3.8. The figure shows that there is a linear correlation between the two quantities, suggesting the internal energy change of the coatings is controlled by the particle's kinetic energy.

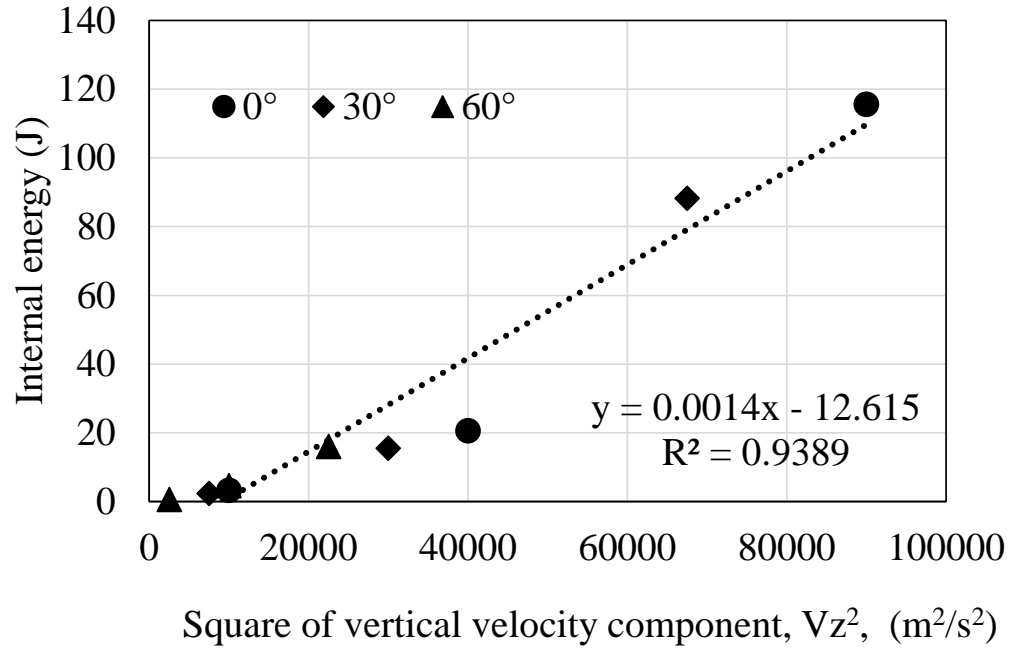


Figure 3.8. Internal energy of the coating as a function of the square of the vertical velocity component of the particle.

To understand the role of horizontal velocity component V_x on the impact behavior, V_x is varied to 0, 150, and 259.8 m/s, while keeping the same vertical velocity component V_z of 259.8 m/s. The combinations of the velocity components correspond to impact angles of 0°, 30° and 45°, respectively.

Figure 3.9 shows sectional views of the von Mises stress and impact penetration profiles of the coatings. The impact spherical particle comes from the right side of the figure. As the impact angle increases, high stresses concentrate on the left side of the impact pit, due to the increased horizontal velocity component.

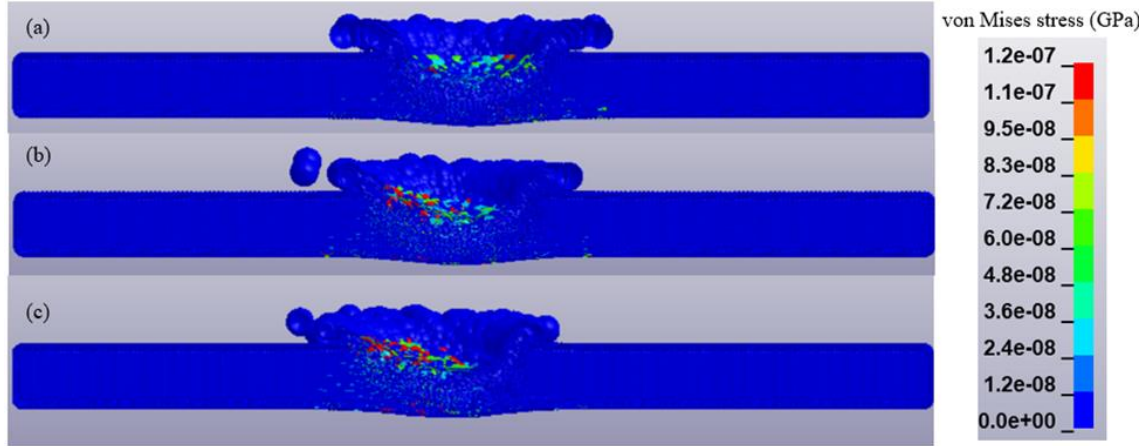


Figure 3.9. von Mises stress and penetration behavior of the coating layers after the impact: V_x and V_z are (a) $V_x=0$ m/s & 259.8 m/s, (b) 150 m/s & 259.8 m/s, and (c) 259.8 m/s & 259.8 m/s.

Figure 3.10 shows that the penetration depth is mainly controlled by the vertical velocity component, not the horizontal one, irrespective of the impact angles. A good linear relation ($R^2=0.9579$) is obtained between the vertical velocity component and the penetration depth.

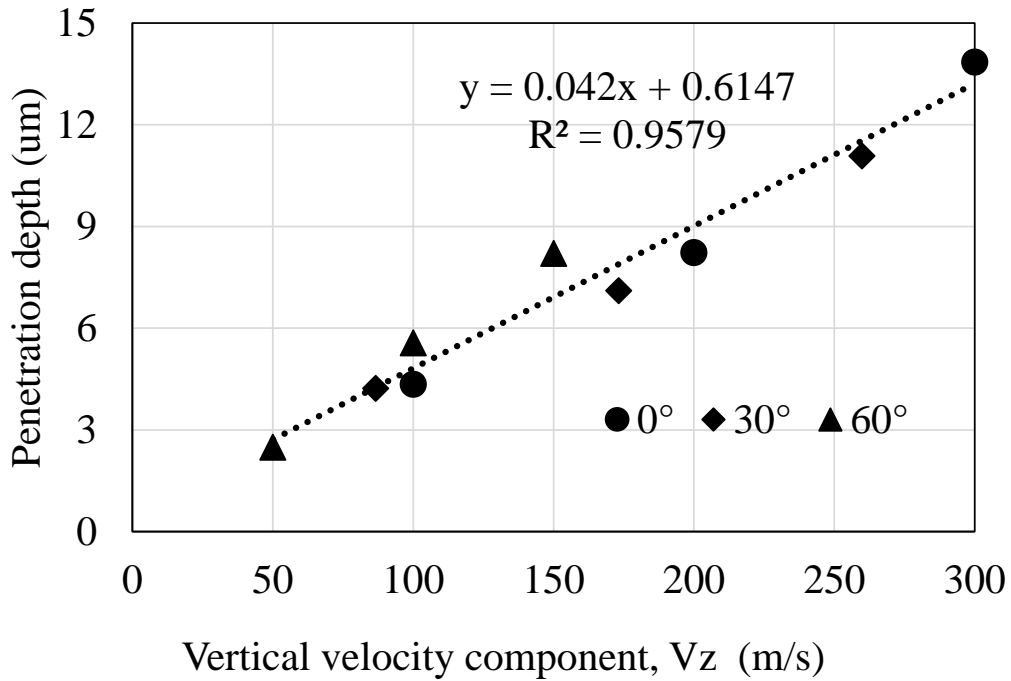


Figure 3.10. Coating penetration depth as a function of particle's vertical velocity component.

To better understand the interface between the SPH and FEM layer, the von Mises stresses and impact penetration profiles of the FEM layer are plotted in Figure 3.11, for the combination

300 m/s & 0° case. The distribution of stress is mainly concentrated on the impacted area. The maximum stress does not locate at the interface, but rather beneath it. It is consistent with the distribution of SPH layer. In addition, the domain of stress distribution is symmetrical in both vertical and horizontal directions because of no horizontal velocity existing. On the other hand, the magnitude of stress in the FEM layer is much higher than that in the SPH layer. It could be caused by the different formulations between the FEM and SPH layers.

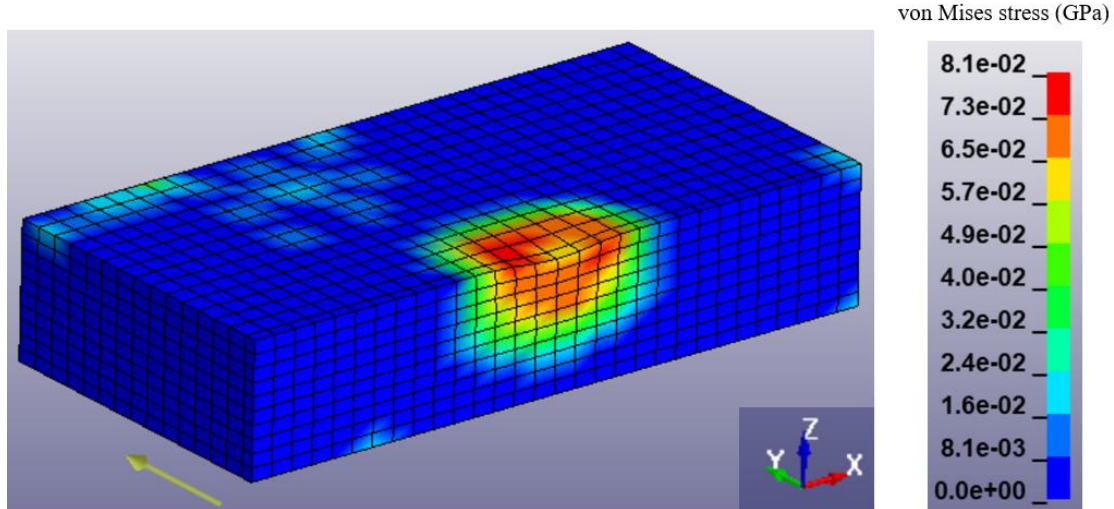


Figure 3.11. von Mises stress distribution in the FEM layer of the combination 300 m/s & 0°.

The von Mises stress evolution of the coating layer at different times of the combination 100 m/s & 0° is shown in Figure 3.12, which is consistent with the internal energy changes shown in Figure 3.5. At 1 ms, the von Mises stress is high and nearly no penetration occurs. At 4 ms, the stress decreases sharply, and the stress wave propagates around. A ring-shaped stress pattern is formed. As the impact process proceeds, the coating penetration occurs because the decreased energy is converted to coating deformation. As shown in Figure 3.12 (c), the particle protrusion at 50 ms is most evident.

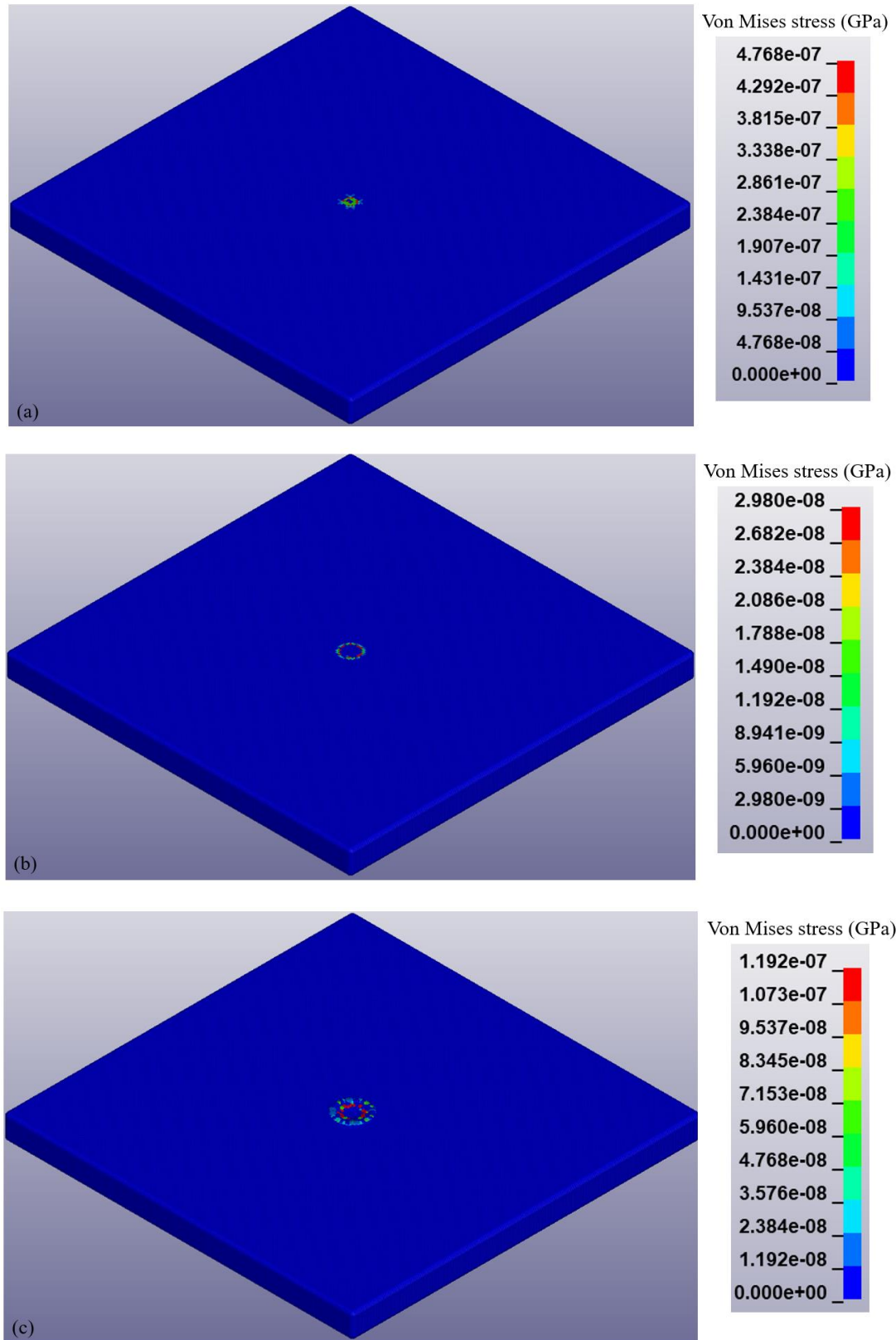


Figure 3.12. von Mises stress distribution evolutions of SPH coating layer at the combination 100 m/s & 0° at different times. (a) 1 ms; (b) 4 ms; and (c) 50 ms.

3.3.2 Deformation of Spherical Impacting Particle

Figure 3.13 and Figure 3.14 show the spherical particle deformation after the impact for different impact velocities and angles, respectively. It is clear that the deformation of the spherical particle increases with the increasing impact velocity and decreases with the increasing impact angle. The increasing deformation of the spherical particle with the same impact angle is consistent with the increasing depth of the impact pit shown in Figure 3.3 (a), (d) and (g). The damage of the spherical particle and the ceramic layer is increasing with the increasing impact velocity.

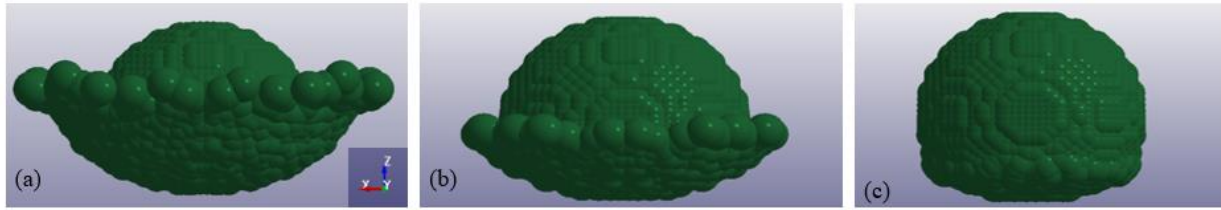


Figure 3.13. The spherical particle deformation after the impact: (a) 300 m/s & 0° , (b) 200 m/s & 0° , (c) 100 m/s & 0° .

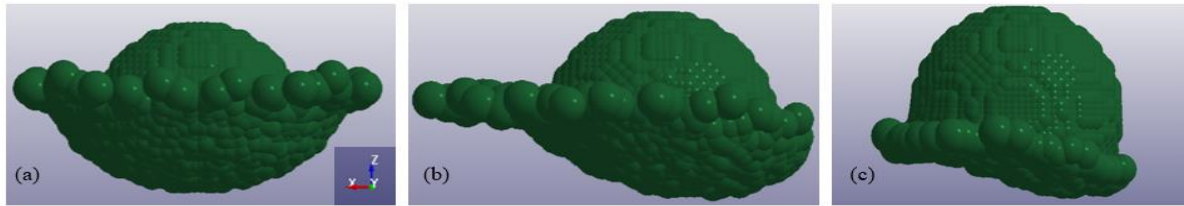


Figure 3.14. The spherical particle deformation after the impact: (a) 300 m/s & 0° , (b) 300 m/s & 30° , (c) 300 m/s & 60° .

During the impact, the kinetic energy of the spherical particle is transmitted to the coating layer, and it increases with the increasing velocity. This is confirmed by the increasing total and internal energies of the coating layer as shown in Figure 3.4 and Figure 3.5, and the decreased kinetic energy of the spherical particle as shown in Figure 3.15, Figure 3.16 and Figure 3.17. Figure 3.16 shows the spherical particle's maximum, minimum and range kinetic energy values at different impact velocities. The kinetic energy transmitted from the spherical particle to the coating layer is related to the vertical velocity difference between the particle and the coating layer. In addition, the energy transmitted from the spherical particle to the coating decreases with the

increasing of the impact angle as shown in Figure 3.16, suggesting the vertical velocity component is the dominant factor. It is also consistent with the particle deformation shown in Figure 3.14.

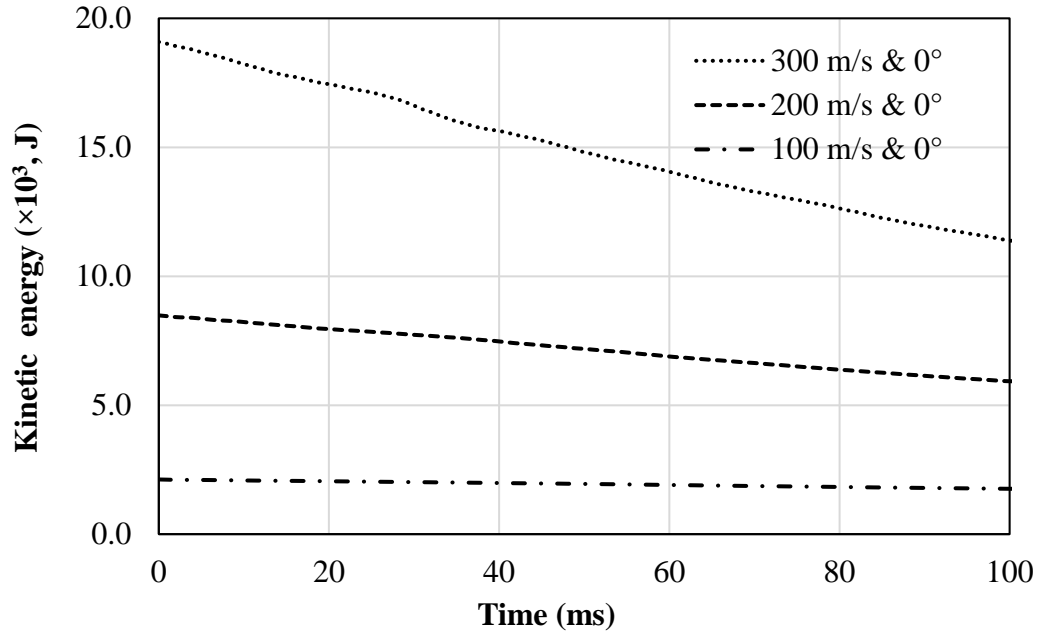


Figure 3.15. Kinetic energy evolutions of the spherical particle at different impact velocities.

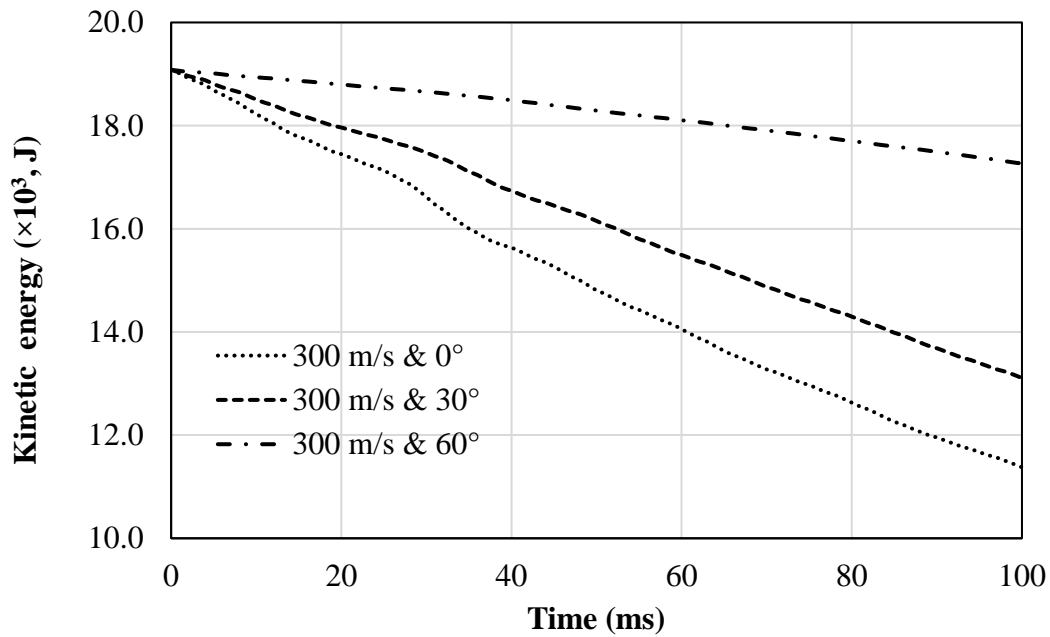


Figure 3.16. Kinetic energy evolution of the spherical particle at different impact angles.

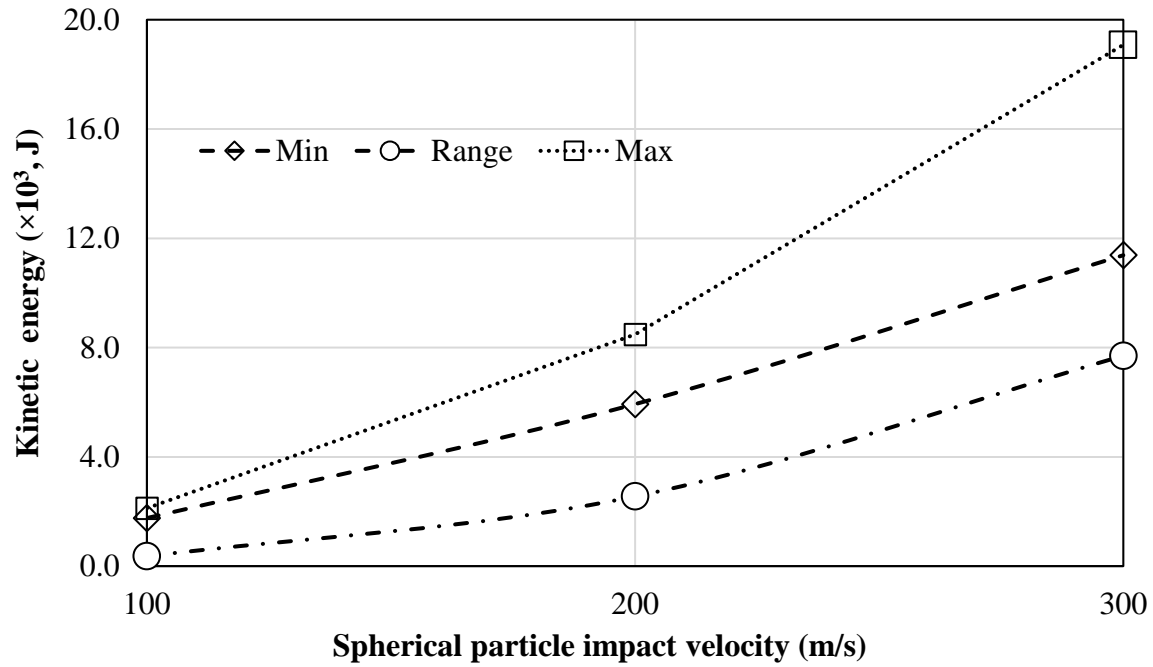


Figure 3.17. The spherical particle's maximum, minimum and range of kinetic energy values at different impact velocities: 300 m/s & 0°, 200 m/s & 0° and 100 m/s & 0°.

3.4 Experimental Comparison

To compare with the experimental data, a scanning electron microscope (SEM) image of the sphere compaction on an electron beam physical vapor deposition (EB-PVD) yttria-stabilized zirconia (YSZ) ceramic coating [91] is shown in Figure 3.18. It is evident that the impact pit observed in the experiment has a similar pattern as the simulated one shown in Figure 3.8 a. Thus, a qualitative agreement is achieved between the SPH model and the experiment. It is noted that more quantitative comparisons would be needed, which would be included in future work.

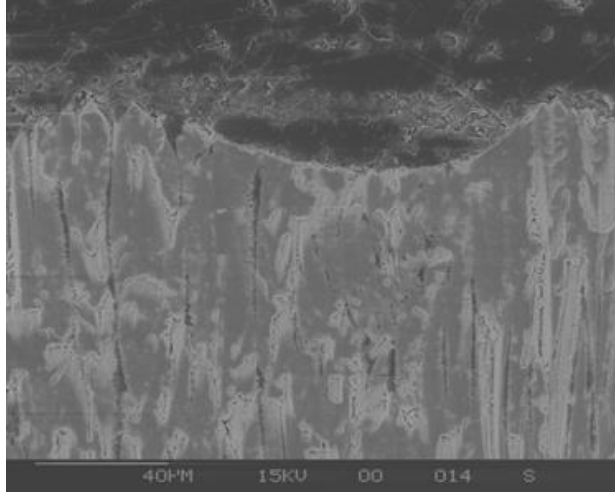


Figure 3.18: Cross sectional view of the experimental impact pit of YSZ ceramic coating [91].

3.5 Summary and Future Work

In this work, an SPH based model to simulate the impact of the spherical ceramic particle on ceramic coatings is developed. The detailed conclusions are summarized as follows.

1. Compared to previous studies, both the spherical particle and the coating are meshed with SPH, which allows us to study their large deformations during the impact.
2. Increasing impact velocity or reducing impact angle increases the penetration depth and area. The penetration depth is determined by the vertical velocity component difference between the particle and the coating layer. However, it is not related to the horizontal velocity component.
3. During the impact process, the coating's total energy increases gradually while the internal energy increases with the time after some peak values, which is due to the kinetic energy of the spherical particle converted to internal energy immediately after the impact, and the stress shock wave transmission in the coating layer.
4. At the end of impact, the coating's total energy increases with the increasing impact velocity but decreases with increasing impact angle. It is consistent with the deformations of the coating layer and spherical particles.
5. The penetration depth is mainly controlled by the vertical velocity component, in a linear relation.

6. The combination of 300 m/s & 0° has the maximum penetration to the coating layer and the combination of 100 m/s & 60° has the minimum penetration. It is due to the fact that penetration is dominated by the particle's vertical velocity component.
7. The simulated pit morphology is qualitatively similar to the experimental observation. This work demonstrates that the SPH method is useful for analyzing the impact effect in the ceramic coating.

In terms of future work, a more precise and quantitative validation experiment is recommended. This allows the model to be more accurately calibrated and can be used for industrial applications.

4. NUMERICAL SIMULATION OF REMOVING THERMAL BARRIER COATINGS USING ABRASIVE WATER JET WITH SMOOTHED PARTICLE HYDRODYNAMICS METHOD

A version of this chapter has been submitted to the journal for review.

Abstract: In this work, a newly smoothed particle hydrodynamics (SPH) based model is developed to simulate the removal process of thermal barrier coatings (TBCs) using the abrasive water jet (AWJ) technique. The effects of abrasive particle concentration, incident angle, and impacting time on the fracture behavior of the TBCs are investigated. The Johnson-Holmquist plasticity damage model (JH-2 model) is used for the TBC material, and abrasive particles are included in the water jet model. The results show that the simulated impact hole profiles are in good agreement with the experimental observation in the literature. Both the width and depth of the impact pit holes increase with impacting time. The deepest points in the pit hole shift gradually to the right when a 30° incident angle is used because the water jet comes from the right side, which is more effective in removing the coatings on the right side. A higher concentration of abrasive particles increases both the width and depth, which is consistent with the experimental data. The depths of the impact pit holes increase with incident angle, while the width of the impact holes decreases with the increase of the incident angle. The incident angle dependence can be attributed to the vertical velocity components. The erosion rate increases with the incidence angle, which shows a good agreement with the analytical model. As the incident angle increases, more vertical velocity component contributes to the kinetic energy which is responsible for the erosion process.

4.1 Introduction

Ceramic coatings are used in the high-temperature sections of gas turbine engines for improved efficiency due to their low thermal conductivity and mechanical properties [67]. A typical TBC topcoat is made of yttria-stabilized zirconia (YSZ) and a bond coat of MCrAlY. TBCs should resist chemical, mechanical, and thermal stresses resulting from the gas turbine operating conditions. However, due to coating degradation or foreign object damage, a routine maintenance

and repair process is needed, including removal of the damaged coatings [92, 93]. A recent review of ceramic coating removal and repair techniques is given in Ref. [93].

Among different techniques, abrasive waterjet (AWJ) has become a promising machining process to remove damaged coatings. AWJ is formed by mixing high-pressure waterjets with abrasive particles. The process has several advantages, such as relatively low cost compared to the laser-based process. Compared with traditional acid stripping and grit blasting methods, AWJ offers a clean and green solution for removing coatings from turbine components in a more cost-effective way. It also enables the penetration of thick cross-sections and has minimum stresses and small cutting forces on the parts [94-96]. Understanding the effects of the controlling factors (e.g., abrasive concentration, impact angle, impact time, and standoff distance) on the AWJ performance is essential to enhancing the machining performances of the process [97]. In Ref. [98], the effects of processing parameters, such as incident angle, impacting time, and abrasive particle concentration were investigated using a single-factor experiment. It is concluded that the AWJ process is an effective way to remove TBCs [98]. The effects of abrasive particle concentration on the impact performance of the AWJ were studied in Ref. [99], and the study showed that the mean impact force tends to increase linearly with the abrasive concentration [99]. In Ref. [96], as shown in the precision AWJ process is reported. Combined with a 5-axis computer numerically controlled (CNC), the AWJ removes the coating in iterative steps.

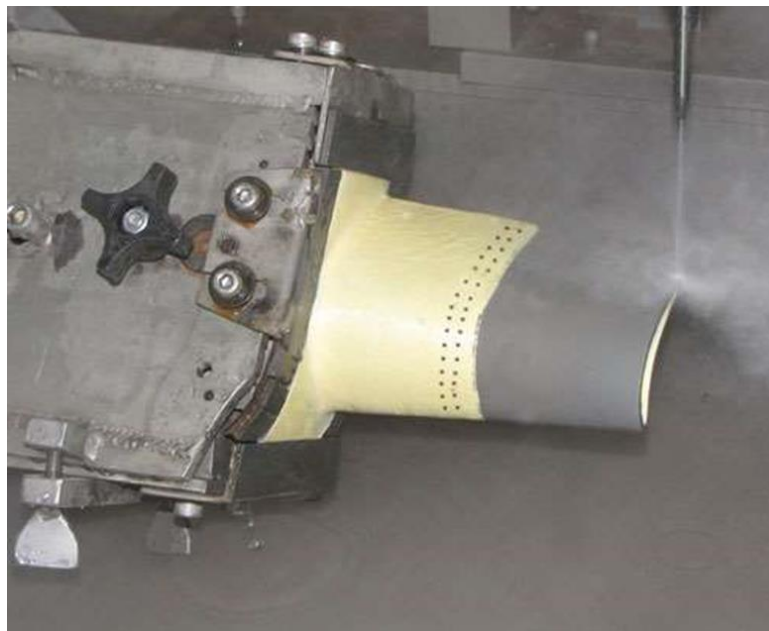


Figure 4.1. A precision abrasive waterjet process removing thermal barrier coating from a turbine blade component [96].

There are a few modeling studies on the optimization of the AWJ process. The Smoothed Particle Hydrodynamics (SPH) and Arbitrary Lagrangian-Eulerian (ALE) methods were employed to study the depth of water jet penetration and erosion mechanism in Ref. [100]. The SPH coupled finite element method (FEM) was adopted to simulate the abrasive water jet cutting progress in Ref. [78]. In addition, a statistical model was established to understand the effect of abrasive waterjet cutting parameters on the surface roughness [95]. The results show that improved surface roughness can be achieved by increasing the water pressure at low traverse speeds, or decreasing the pressure at high traverse speeds, or decreasing the standoff distance at low traverse speeds and low pressures in the investigating range [95]. In Ref. [101], an analytical model was developed to determine the heat flux at the contact surface during the AWJ machining process. The generated heat due to plastic deformation is diminished because the high-velocity waterjet serves as a coolant removing the heat through convection [101].

Despite the previous studies presented above, a systematic understanding of the fundamental mechanism of the AWJ process to remove TBCs is still missing, which hinders the full potential of the process. In this work, an SPH-based model to simulate the TBC removal process using the AWJ technique is proposed. The effects of abrasive particle concentration, incident angle, and impacting time on the TBC fracture are studied. The simulation results are compared against the experimental data and analytical model in the literature.

4.2 Model Description

4.2.1 The SPH Method

Compared with traditional grid-based methods, SPH method is a mesh-free method. It does not need a finite element mesh. As one of the earliest mesh-free methods, SPH method was initially applied to astrophysical problems since the particles in space move like liquid and gas flow. After that SPH method is extended to high-velocity impact and penetration problems for material dynamics response. While the SPH method was used for hydrodynamics problems initially, the governing equations were partial differential equations with strong formation. The solution of these partial differential equations contains two-step: kernel approximation and particle approximation. For kernel approximation, a smoothing function W was selected to represent the

partial differential equations f and their derivatives and the integration over the computational domain is as follows [102]. After the kernel approximation, the function f become the following:

$$\langle f(x) \rangle = \int_{\Omega} f(x') W(x - x', h) dx' \quad (1)$$

where x and x' are the position vectors at different points and W is the kernel function.

Then, Eq. (1) can be calculated through the summation with their closest neighbor particles in the support domain which is controlled by the smoothing length for a given particle j at a certain instant of time [102].

$$f(r) \approx \sum_{j=1}^N \frac{m_j}{\rho_j} f(r_j) W(r - r_j, h) \quad (2)$$

where m and ρ are the mass and density of a particle, respectively. W is a kernel function and h is a smoothing length to control the size of the summation domain[102].

4.2.2 SPH Model Details

4.2.2.1 Geometry of The Model

The SPH model of the TBC removal process is shown in Figure 4.2. The side view of the SPH model for the TBC layer removal using the AWJ process. The abrasive particles in the water jet are enlarged to show their existence. The inset shows the 3D view of the SPH model. The model includes abrasive particles, a water jet, and a TBC layer. The composition of the TBC layer is assumed to be zirconia (ZrO_2) since the SPH model parameters for yttria-stabilized zirconia are sparse. The abrasive particles are alumina (Al_2O_3) particles. The nozzle diameter is set to $200 \mu m$ which is the same as the experiment in Ref. [103]. The TBC layer's dimensions are $2000 \times 2000 \times 500 \mu m^3$. All the surfaces of the TBC layer are fixed except the top one. The incident angle is defined as the angle between the water jet and the horizontal plane of the TBC layer. Based on the mesh convergence analysis, the total number of particles for the SPH coating layer is 250, 000. The total number of particles for the abrasive water jet is 24, 960. The used mesh density follows Ref. [85]. In this model, default initial step size is used. In LS-DYNA, critical time step: $\Delta t = \frac{L}{c}$ where L is the length of the element and c is the sound speed.

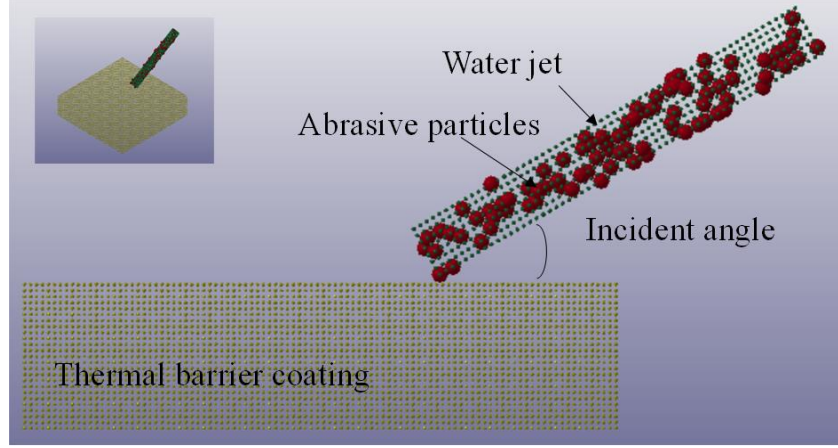


Figure 4.2. The side view of the SPH model for the TBC layer removal using the AWJ process. The abrasive particles in the water jet are enlarged to show their existence. The inset shows the 3D view of the SPH model.

4.2.2.2 Material Constitutive Model

For the ZrO_2 TBC layer, the Johnson-Holmquist plasticity damage model (JH-2 model) is used, which has been proven suitable for ceramics, glass, and other brittle materials [86]. In the JH-2 model, the equivalent stress for a ceramic-type material is given by [84]:

$$\sigma^* = \sigma_i^* - D (\sigma_i^* - \sigma_f^*) \quad (3)$$

where D is the damage parameter. The superscript asterisk (*) indicates a normalized quantity. σ_i^* is determined by [84]:

$$\sigma_i^* = a (p^* + t^*) n (1 + c \ln \dot{\epsilon}^*) \quad (4)$$

which represents the intact and undamaged behavior. a is the intact normalized strength parameter c is the strength parameter for strain rate dependence, and $\dot{\epsilon}^*$ is the normalized plastic strain rate.

Also [84]:

$$t^* = \frac{T}{P_{HEL}} \quad (5)$$

$$p^* = \frac{p}{P_{HEL}} \quad (6)$$

where T is the maximum tensile pressure strength, and P_{HEL} is the pressure component at the Hugoniot elastic limit and P is the pressure.

In an undamaged material in compression, the hydrostatic pressure is given by [104]:

$$P = k_1 \mu + k_2 \mu^2 + k_3 \mu^3 \quad (7)$$

And in tension, it becomes [84]:

$$P = k_1 \mu \quad (8)$$

where the compression factor $\mu = \rho/\rho_0 - 1$, and ρ/ρ_0 is the ratio of current density to initial density. Additionally, the damage parameter D is determined by [84]:

$$D = \sum \frac{\Delta \epsilon^p}{\epsilon_f^p} \quad (9)$$

which represents the accumulated damage based upon the increase in plastic strain per computational cycle. The plastic strain to fracture is [84] :

$$\epsilon_f^p = d_1 (p^* + t^*)^2 \quad (10)$$

where the parameter d_1 controls the rate at which damage accumulates [84] :

$$\sigma_f^* = b(p^*)^m (1 + c \ln \dot{\epsilon}^*) \quad (11)$$

For the water jet and abrasive particles, the pressure is calculated by the state equation Mie-Grueisen as follows [82, 83] :

$$p = \frac{\rho_0 C^2 \mu [1 + (1 - \gamma/2)\mu - (\alpha/2)\mu^2]}{[1 - (S_1 - 1)\mu - S_2 \mu^2 / (\mu + 1) - S_3 \mu^3 / (1 + \mu)]^2} + (\gamma + \alpha \mu) E_0 \quad (12)$$

where p is pressure; S_1 , S_2 , and S_3 are the coefficients of the slope of the $U_s - U_p$ curve, where U_s and U_p are the shock velocity and particle velocity, respectively; γ is the Grüneisen factor; C is the intercept of the $U_s - U_p$ curve; E_0 is the internal energy; α is the volume correction factor.

4.2.2.3 Material Properties

The ZrO_2 in the TBC layer has the following properties: density is 5850 kg/m³, the shear modulus is 95.31 GPa, tensile strength is 0.2 GPa, and the Poisson's ratio is 0.22. The coefficient values in the JH-2 model used for the TBC are listed in Table 4.1[106].

Table 4.1. JH-2 model parameters for the TBC layer [106].

Parameter	Value
A	0.93
B	0.31
C	0
M	0.6
N	0.6
HEL(GPa)	2.79
PHEL(GPa)	1.46
D1	0.005
D2	1
K ₁ (GPa)	130.95
K ₂ (GPa)	0
K ₃ (GPa)	0

The water in the AWJ has the following properties: the density is 1000 kg/m³, the cut-off pressure is 10⁻⁵ Pa, and the dynamic viscosity is 10⁻³ Pa.s [100]. The abrasive particles have the following properties: the density is 3420 kg/m³, the shear modulus is 108 GPa, and the Poisson's ratio is 0.22 [82]. The parameters in the Gruneisen equation used for the water jet and abrasive particles are summarized in Table 4.2 [82, 100].

Table 4.2. The parameters in the Gruneisen equation for the water jet and abrasive particles [82, 100].

Materials	C(m/s)	S ₁		S ₂	S ₃	γ
Water jet	1480	2.56		-1.986	0.2286	0.4934
Abrasive particles	9003	-3.06		2.350	-0.383	1

4.2.2.4 Boundary Conditions and Model Design Matrix

Three different AWJ processing parameters are considered, including incident angle abrasive particle concentration, and impacting time. The parameters are chosen using the same conditions as the previous experimental study, as close as possible [98]. Other parameters, such as velocity, particle size, nozzle diameter, and target distance are kept constant. The design matrix of specific processing parameters for all the simulation cases is summarized which is shown in Table 4.3.

Table 4.3. Design matrix of processing parameters used in the model.

Simulation case	Abrasive concentration (wt %)	Incident angle (°)	Impacting simulation time (ms)
A	1,3	30	20
B	1	30,45,60,90	20
C	1	30	7,14,21,28

4.2.2.5 Erosion Analytical Model

To quantify the coating removal efficiency, the erosion rate is investigated and compared with an analytical model. The removed mass from the TBC due to water jet impact needs to be quantified in order to evaluate the erosion rate. In the model, the eroded mass is characterized by the number of SPH particles whose particle density values are lower than the initial density. The mass for each SPH particle is a constant, and the density is defined as the mass per unit volume[107]. When the particles are scattered during impact, their densities are reduced.

An erosion model in brittle materials, based on the stress wave fracture mechanism was proposed by Zeng and Kim [108, 109] for the AWJ process. The total erosion volume (V_T) includes two components: one is caused by the plastic flow (V_p), and the other is due to the network cracking caused by impact induced stress waves (V_f) [108]:

$$V_T = V_p + V_f \quad (13)$$

The volume removal due to plastic flow, V_p , is calculated by [108] :

$$V_p = \frac{mv^2}{4\sigma_f} (\sin 2\alpha - 4\sin^2\alpha + 38.12v\sin^3\alpha \sqrt{\frac{\rho_p}{\sigma_f}}) \quad (14)$$

And the volume removal due to network cracking V_f is determined by [108] :

$$V_f = \frac{f_w \beta a \sigma_f m v^2 \sin^2 \alpha}{3 \gamma E} \quad (15)$$

where γ is the fracture energy per unit area; m is the mass of a single particle; v is the particle velocity at impact; σ_f is the flow stress of target material; f_w is the proportional factor (W_c/W), E is the modulus of elasticity; a is the grain size of ceramics, α is the impact angle, and $\beta = 14.33 - 6.25 \sin 2.8v$. Since the AWJ cutting is a multiple impact process, it is not reasonable to calculate the removal material directly from a summation of a series of single-particle impacts. The energy is lost in particles during the impact process which is represented in Eq. (15). It is super difficult to calculate the effects at each stage since the particle impacts each other and the same as the stress wave. Since there is no evidence of the dependence of these effects on material properties and AWJ parameters, a constant efficiency coefficient C , which is determined from experiments, is incorporated to predict the averaged material removal of individual particles. Therefore, the theoretical erosion rate, R , is calculated to be [109]:

$$R = \frac{C \rho V \dot{m}}{m} = C \left[\frac{f_w \beta a \sigma_f \rho \dot{m} v^2 \sin^2 \alpha}{3 \gamma E} + \frac{\rho \dot{m} v^2}{4 \sigma_f} (\sin 2\alpha - 4 \sin^2 \alpha + 38.12 v \sin^3 \alpha \sqrt{\frac{\rho_p}{\sigma_f}}) \right] \quad (16)$$

4.3 Results and Analysis

4.3.1 Effect of Incident Angle on The Morphology of The Impact Pit

Figure 4.3a shows the simulated impact pit hole, at the incident angle of 90° . It is close to a circular shape. The predicted shape is in reasonably good agreement with the experiment result [98], as shown in Figure 4.3b.

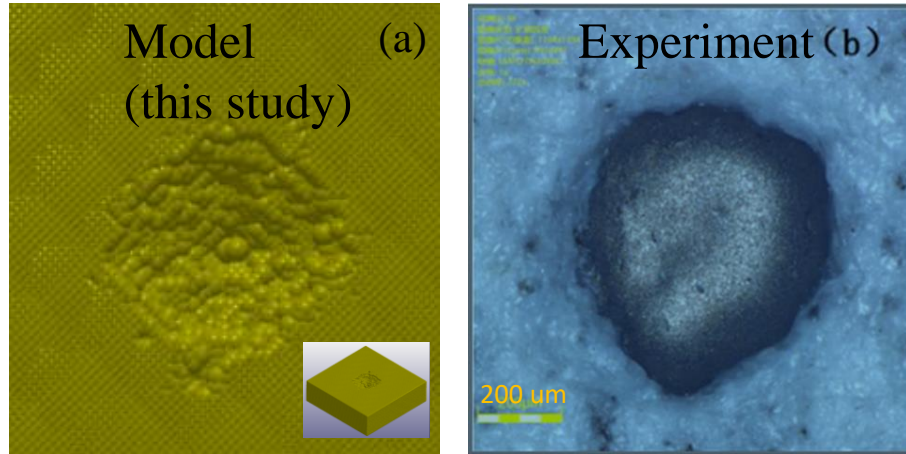
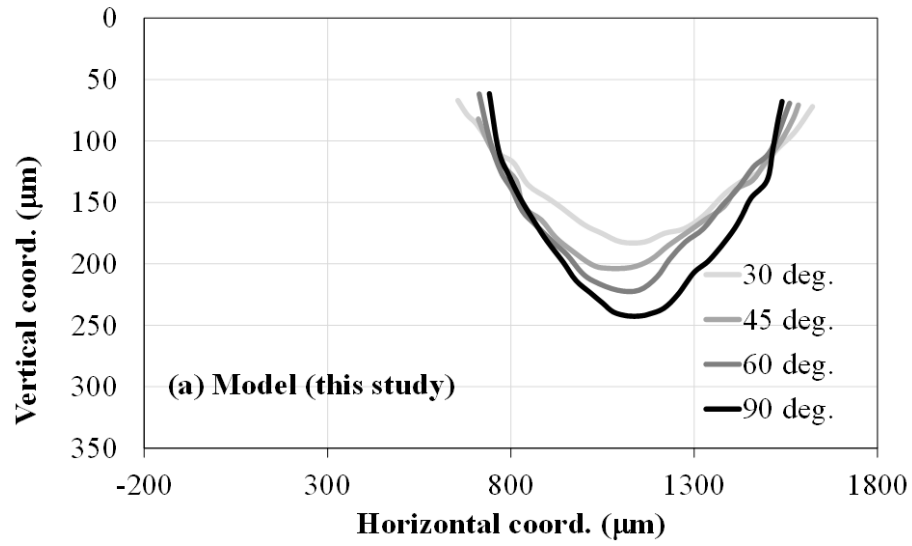


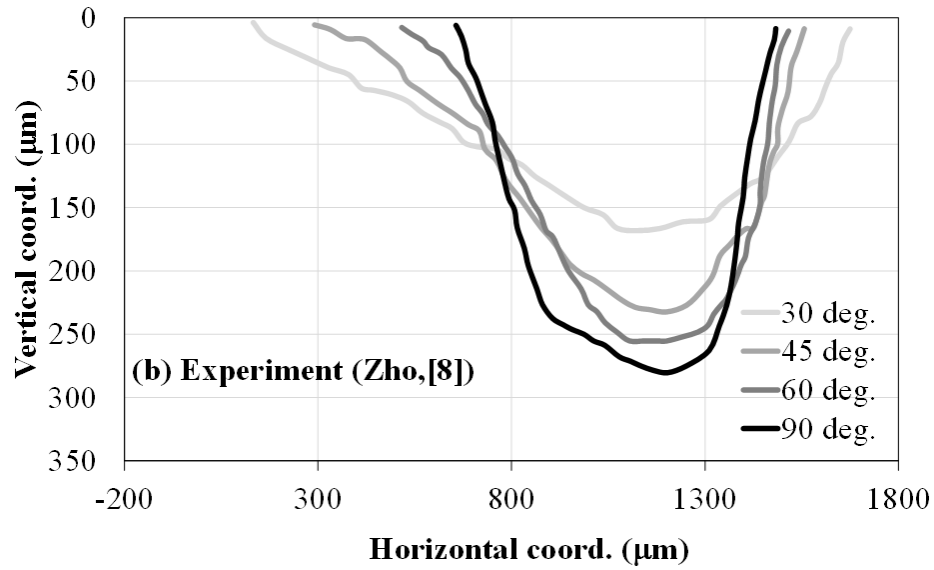
Figure 4.3. TBCs' typical features of the impact pit hole with incident angle 90° : (a) isometric view of simulation results, (b) top view of simulation results, (c) top view of experiment result [98].

Figure 4.4a shows the cross-sectional views of the simulated impact pit holes with the incident angles of 30° , 45° , 60° , and 90° . The impact velocity is kept at 300 m/s and abrasive particle concentration is 1%. Overall, the depth of the impact pit holes increases with the incident angle, while the width of the impact holes decreases with the increase of the incident angle. Among different incident angles, the width of the incident angle 30° is the largest and the depth of incident angle 90° is the largest. The simulated profiles, in terms of depth and width, are in the same trend as the experimental measurements, as shown in Figure 4.4b. The incident angle effect is more distinguishable in the experiment because of its longer impact time.

Additionally, it is noted that all the profile curves, for both model and experiment, coincide at coordinates around (700 mm, 120 mm), and (1600 mm, 120 mm), suggesting there is a transition incident angle of 45° . When the AWJ incident angle is greater than the transition angle, impact holes develop faster in-depth direction than the width direction.



(a)



(b)

Figure 4.4. The cross-sectional profiles of the impact pit holes with different incident angles: 30°, 45°, 60°, and 90°. (a) Simulated results from this study, (b) experiment result from Ref. [98]. (Water jet direction is towards the left).

The incident angle's dependence on the hole profile can be attributed to the vertical velocity components. The vertical velocity component (V_z) of the AWJ process increases with the incident angle, following a sine function relation.

Figure 4.5 shows the relations between the depth and vertical velocity components. It shows that the depth increases with the vertical velocity component. This is because both the depth and vertical velocities share the same direction, and the kinetic energy from the AWJ process, $\frac{1}{2}mv^2$, is responsible for the erosion. The fitted curve using the 2nd order polynomial is shown in Figure 4.5, which confirms the validity of kinetic energy.

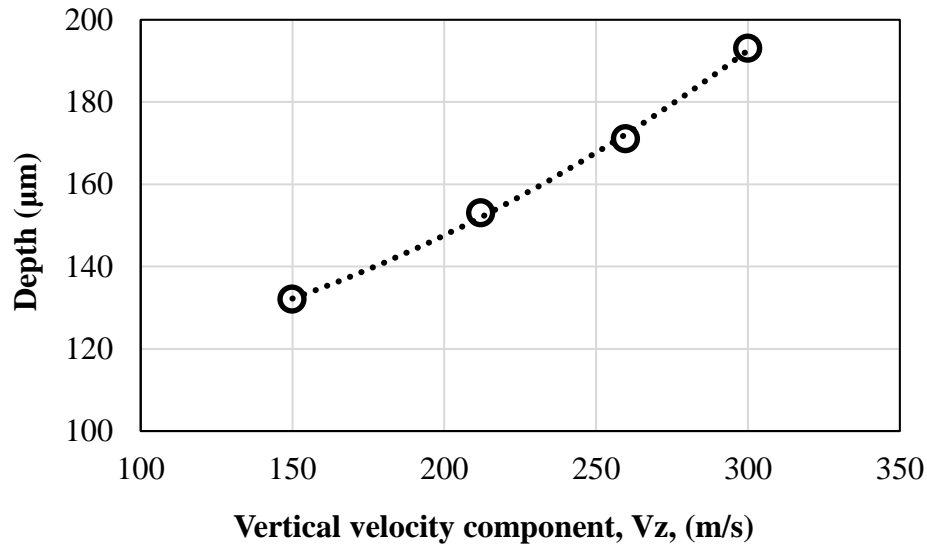


Figure 4.5. Pit hole depth's dependent on the vertical velocity component (V_z). The fitted curve using the 2nd order polynomial is also shown.

4.3.2 Effect of Abrasive Concentration on Morphology of The Impact Pit

Figure 4.6 shows the cross-sectional views of the impact pit hole profiles with abrasive particle concentrations of both 1% and 3%. The impact velocity is 300 m/s and the incident angle is 30°. It is clear that a higher concentration increases both the width and depth, which is consistent with the experimental data, as shown in Figure 4.6. However, our modeling results overpredict the 1% case and underpredict the 3% case. This may be due to the assumptions of perfect spherical shape and monosized particles used in our model.

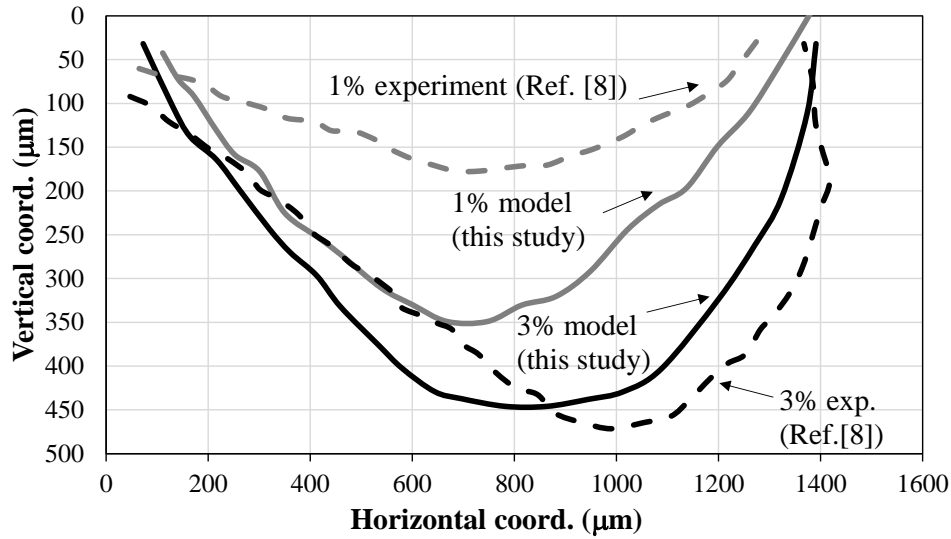


Figure 4.6. Cross-sectional views of impact pit hole profiles with abrasives (a) Simulated results (b) experiment results [98]. (Water jet direction is towards left).

4.3.3 Effects of Impacting Time on Impact Pit Hole Morphology

Figure 4.7 shows the cross-sectional views of the impact pit holes with the increasing impacting time, with the velocity of 300 m/s and incident angle of 30° . Both the width and depth of the impact pit hole increase with impacting time. In this work, the time scaling factor between the model and experiment is 4.4×10^3 , based on comparing the total simulation time and total experimental time. The scaling factor in the horizontal direction is determined to be 2.5.

It is noted that the deepest points in the pit hole shift gradually to the right, as labeled in Figure 4.7. This is because an incident angle of 30° is used. As the water jet is coming from the right side and towards the left side, the right side is eroded faster than the left side, causing the deepest points to move to the right side. By comparing the eroded thickness, the right side is eroded about 1.5 times the left side. The phenomena are observed in both modeling and experimental results, which further illustrates the effectiveness of the SPH model.

It is also noted that the left side of the top surface in the experiment is much longer than the right side. This is unusual as it is unlikely to remove a quite large thin layer at the beginning of the process, i.e., 0.5 min. It is possible that there was a peel off event of the top layer in the experiment which caused this abnormality.

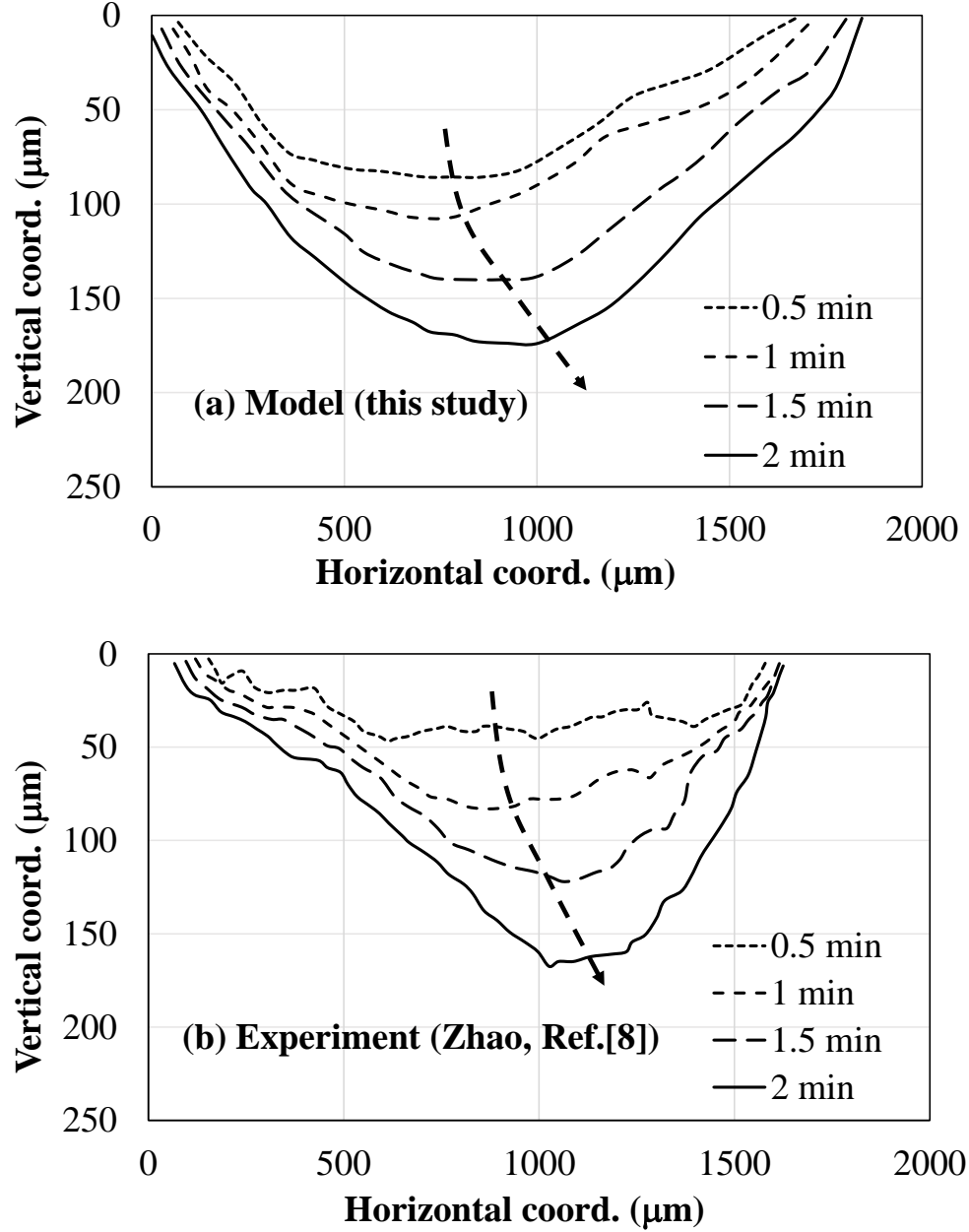


Figure 4.7. Cross-sectional views of the pit holes at different impacting times: (a) simulation results; (b) experiment results [98]. The curved arrows show the deepest points gradually shift to the right as the AWJ process proceeds, due to 30° of incident angle.

4.3.4 Analytical Erosion Model

Based on the analytical erosion model presented in Equation 16 [109], the erosion rates at different incidence angles are calculated, as shown in Figure 4.8. The following parameters are used in the analytical model: f_w is 6.65×10^{-4} , γ is 5.8 J/m^2 , σ_f is 23 GPa, a is 12 μm , and \dot{m} is the

particle flow rate, 12.9 g/s [108, 110, 111] . According to the SPH modeling results, the coefficient C is determined to be 0.0065.

As shown in Figure 4.8, the erosion rate increases with the incidence angle and the increase rate becomes slower as the incidence angle approaches 90°, which shows a good agreement with the analytical model. This is because the kinetic energy from the AWJ is responsible for the erosion process. As the incident angle increases, more vertical velocity component contributes to the kinetic energy.

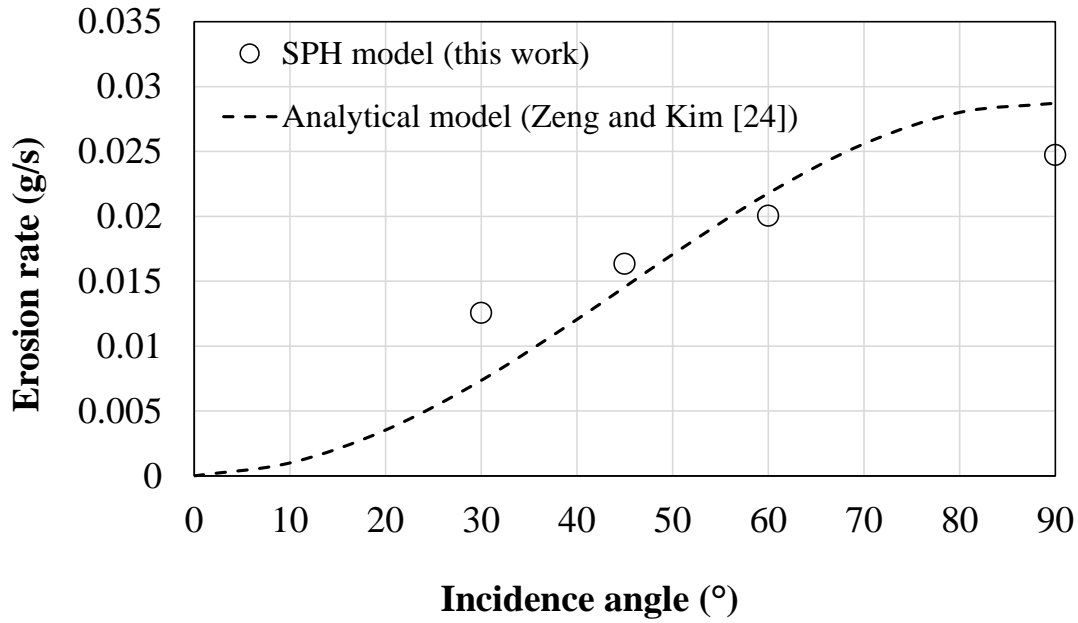


Figure 4.8. Simulated erosion rates at different incident angles. The analytical model [109] is also included for comparison.

4.4 Summary

In this work, a new SPH based model to simulate the thermal barrier coating removal process using the abrasive water jet technique is developed. The effects of the incident angle, abrasive concentration, impacting time are investigated. The main conclusions are summarized as follows.

1. Both the width and depth of the impact pit holes increase with impacting time. It is noted that the deepest points in the pit hole shift gradually to the right when a 30o incident angle is used. This is because the water jet comes from the right side, which is more effective in removing the coatings on the right side. The phenomena are observed in both modeling and experimental results, which further illustrates the effectiveness of the SPH model.

2. A higher concentration of abrasive particles increases both the width and depth, which is consistent with the experimental data.
3. The depths of the impact pit holes increase with incident angle, while the width of the impact holes decreases with the increase of the incident angle. The incident angle dependence can be attributed to the vertical velocity components.
4. The erosion rate increases with the incidence angle, which shows a good agreement with the analytical model. As the incident angle increases, more vertical velocity component contributes to the kinetic energy which is responsible for the erosion process.

5. MODELING OF MACHINING OF EB-PVD CERAMIC COATINGS USING SMOOTHED PARTICLE HYDRODYNAMICS METHOD

A version of this chapter has been submitted to the journal for review.

Abstract: In this work, an improved Smoothed Particle Hydrodynamics (SPH) based model for simulating the machining process of the thermal barrier coatings is presented. The columnar grain microstructure in the electron-beam physical vapor deposition (EB-PVD) coating is constructed. The Johnson-Holmquist 2 (JH-2) material model coupled with the Johnson-Holmquist plasticity damage model is used for the ceramic coating. The cutting processing parameters, such as cutting depth, cutting speed, cutting tool's edge radius, and rake angle, on the cutting force and temperature change, are studied. The results show that the fracture of the columnar grains during the cutting process is done through deflection and fracture of the grains, followed by pushing against neighboring grains. Both the cutting force and temperature of the coating increase with cutting depth due to increased cutting work transferred to heat. The cutting forces from the SPH model at the stable stage are in excellent agreement with the fracture mechanics analytical solution. The cutting force and temperature increase are higher for a larger edge radius, due to increased friction between the cutting tool and coating. The SPH model result follows the same trend as the main cutting force calculated by the analytical expression. The SPH cutting model developed in this work can be used as a design tool to optimize the coating machining process.

5.1 Introduction

Thermal barrier coating (TBC), such as fabricated using the electron-beam physical vapor deposition (EB-PVD) process (Figure 5.1), has been extensively used in the hot section of gas turbine components to provide thermal protection in harsh environments[112]. However, coating damage may occur over the service, which requires removing and repairing the damaged ceramic coating layer.

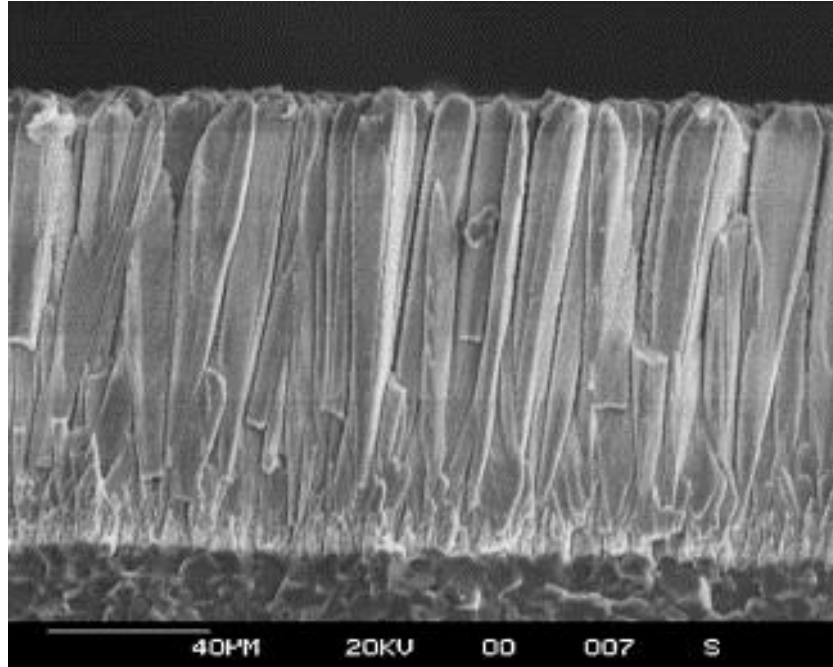


Figure 5.1. Cross-sectional view of an EB-PVD thermal barrier coating, which shows the columnar grains [113].

One of the coating removal processes is using tools, such as mechanical grinding [114-116]. The cutting tool is usually sharp and hard with special materials such as single crystal diamond [117]. In the cutting process, due to the interactions between the tool and coating, high stresses and high temperatures are expected [118]. In terms of cutting process parameters, the cutting tool geometry, cutting speed, lubrication conditions play important roles in both cutting quality and tool life [119]. In Ref. [120], the effect of cutting tool edge radius on the metal cutting process was studied. It is included that an optimal cutting tool edge can significantly increase the life of the cutting tool, reduce the cycle time of cutting operation, and obtain a better surface quality. In Ref. [121], the cutting tool wear and tool life for machining Inconel 718 were investigated based on optimizing the cutting speed.

The temperature in the cutting materials increases because of converting cutting work or friction into heat. In Ref. [122], the effect of cutting parameters, such as cutting speed, feed rate and cutting depth on temperature was studied. In Ref. [123], a varying coefficient of friction, as a function of plastic strain rate, was proposed. In Ref. [124], the cutting depth combined with cutting speed was focused on their effects on surface roughness [124].

In addition to experimental studies, several numerical and modeling approaches have been proposed to understand the cutting process. In Ref.[125], fracture mechanics analysis has been conducted, where the cracking is controlled by the normal-opening mode [125]. In Ref. [126] when the cutting tool is vertically applied to the cutting material, the cutting process can be analyzed in analogy as an indentation process. [126]. In Ref. [127], the beam theory was employed. The three stages were identified: (a) elastic deformation, (b) plastic bending, and (c) shear with bending, which are classified as a function of load and/or the rake angle of the cutting tool. Additionally, the finite element method (FEM) has been extensively used for simulating the metal cutting process[128]. One of the most widely used damage models in metal cutting simulations is the Johnson-Cook (J-C) shear failure model, which is typically used in conjunction with the J-C constitutive equation [128]. In Ref. [129], the discrete element method (DEM) was also used to simulate the mechanical behavior of alumina ceramics in the cutting process. Both crack's initiation and propagation were modeled. Moreover, the smoothed particle hydrodynamics (SPH) method has been used to investigate the cutting process of zirconia ceramics based on the Johnson-Holmquist II (JH-2) model[106]. The effects of tool and machining parameters on chip morphology and cutting force were studied [106]. Recently, the molecular dynamics (MD) method has been used to simulate the machining process and analyze the machining mechanism of brittle materials at the atomic level [130].

Although the above-mentioned experimental and numerical efforts, there are still limited studies on the cutting of thermal barrier coating materials. In this work, the SPH model will be employed to simulate the cutting process. The effects of cutting depth, cutting speed, tool geometry on cutting force, and temperature change will be investigated. The mesh-free technique SPH model is considered, since it may overcome some limitations in the FEM for brittle materials, such as severe FE mesh distortion [131]. There are several novelties in this work. The first one is the microstructure of the ceramic coating. Previous ones assume a uniform bulk sample. In this paper, discrete columnar grains will be used, which simulate EB-PVD (electron beam physical vapor deposition) thermal barrier coating microstructures. It will demonstrate the unique fracture behavior not available in the bulk material. The second one is focusing on the temperature effect since most previous studies were primarily focused on the mechanical behavior only. The temperature effect may have a profound effect on the tooling life and temperature-dependent material properties.

The structure of the paper is as follows. Section 1 is the introduction. Section 2 presents the SPH model validation and convergence studies. Section 3 shows the ceramic cutting process model where the columnar grain model, cutting tool model, and materials and damage models are discussed. Section 4 presents the results, with the focus on cutting depth, cutting speed, cutting tool edge radius, and cutting tool's rake angle. Section 5 provides the conclusions.

5.2 Model Validation and Convergence Studies

5.2.1 Mechanical Validation

In this section, we conduct the model validation and convergence studies using an impact model, in which a rectangular bar impacts on a rigid wall. The dimensions of the rectangular impact bars are 8 mm × 8 mm × 20 mm. As shown in Figure 5.2 (a-d), three SPH bars with different particle densities and one finite element bar are considered. The total numbers of particles for the three SPH bars, SPH01, SPH02, and SPH03 are 2,500, 20,000, and 160,000, respectively, which corresponds to normalized particle densities of 1, 2, 4, respectively. The density of the bars is 1000 kg/m³. The initial impact velocity of 50 m/s.

The total computational time for the three SPH models and FEA model is about 10 minutes using an 8-Symmetric Multi-Processing (SMP) thread solver in LS-Dyna SPH capacity. In this work, the three SPH models and FEA models were built in a single input file, and all the models are solved together.

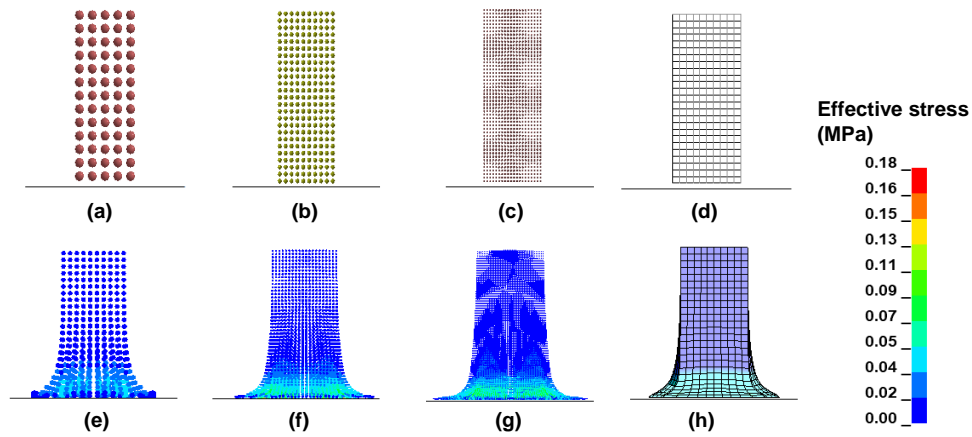


Figure 5.2. Side views of the impact bars of (a) undeformed SPH01, (b) undeformed SPH02, (c) undeformed SPH03, (d) undeformed FEM, (e) deformed SPH01, (f) deformed SPH02, (g) deformed SPH03, and (h) deformed FEM.

Figure 5.2 (e-h) shows the deformed bars and their effective stress distributions. It is clear that both the shape changes and the effective stress distributions are similar in all the cases. The maximum effective stress is concentrated at the bar bottom where the impact and deformation occurred. In addition, the deformation increases from the bar top to the bottom.

To get quantitative comparisons, the reductions of the bar lengths during the impact process for the SPH and FEM models are shown in Figure 5.3. For all the models, the reductions of the bar lengths follow the same pattern, which increases linearly with time.

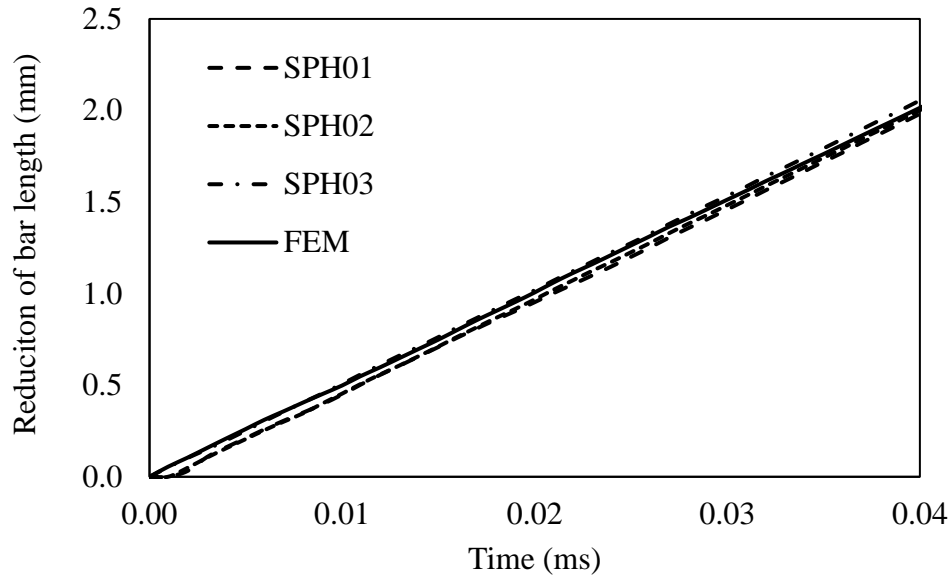


Figure 5.3. Reduction of the bar length vs. time for the SPH and FEM models.

Figure 5.4 shows the kinetic energy evolutions for the four models. The kinetic energy decreases with time after an initial drop. The drop occurs immediately when the bars first contact with the rigid walls. The kinetic energy recovers afterward due to the rebound of the bar. The discrepancy in the SPH03 model may be caused by the accumulative numerical error. That is excessive particles lead to more computations, leading to more numerical error. Also, note that the relative error is still small between the SPH3 and FEM models. As shown in Figure 5.4, the relative error is approximately $50/1500 = 3.3\%$.

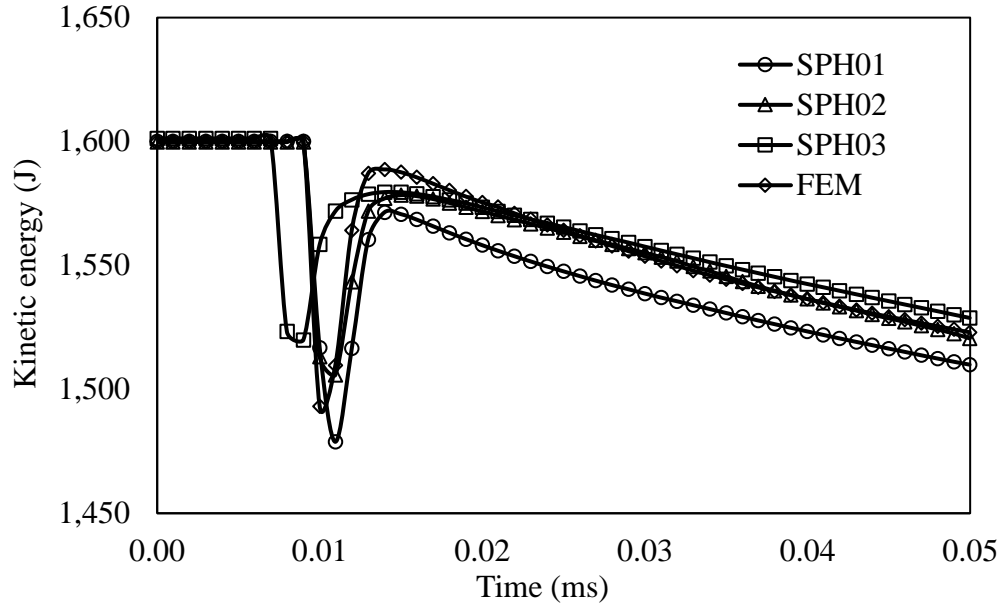


Figure 5.4. Evolution of kinetic energy for the SPH and FEM models.

Therefore, based on both the qualitative and quantitative comparisons, the SPH models have a reasonably good agreement with the FEM model, including deformation and stress distribution in Figure 5.2, reduction of the bar length in Figure 5.3, and the kinetic energy evolutions in Figure 5.4.

Additionally, convergence studies were conducted, as shown in Figure 5.5, which are the kinetic energy values of the three SPH bars at 0.012 ms, with different normalized particle densities. Remember that the mesh density of SPH01 is used for normalization, which is unity.

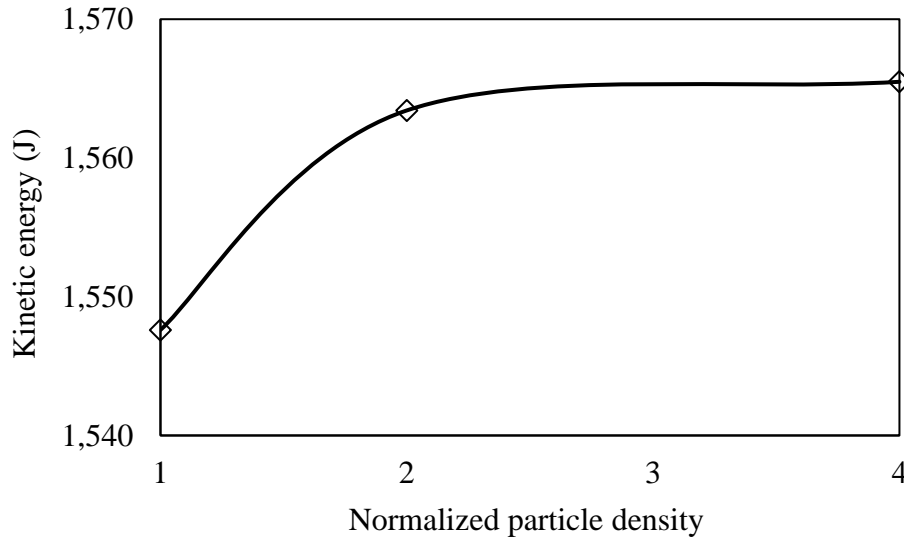


Figure 5.5. The kinetic energy of the SPH bars at different normalized particle densities.

As the particle density values increase from 1 to 4, the kinetic energy values gradually converge to a constant value of about 1,565 J. The results are consistent with the kinetic energy evolution shown in Figure 5.4. Therefore, the normalized particle density of 2, or the particle density of SPH02, meets the convergence requirements and will be used in the following studies.

5.2.2 Thermal Validation

To validate the thermal aspects in the SPH model, the Fourier equation in the 1-D x-axis direction, without internally generated heat is applied [132] :

$$\rho C_p \frac{\partial T}{\partial t} = k \frac{\partial^2 T}{\partial x^2} \quad (1)$$

where T is temperature; ρ is density, k is thermal conductivity, t is time, and C_p is heat capacity. The analytical solution to Eq. 1 is [132] :

$$T(x,t) = \frac{T_0}{\pi} x + \frac{2T_0}{\pi} \sum_{n=1}^{\infty} \frac{(-1)^n}{n} e^{-\frac{n^2 \pi^2}{L^2} A k t} \sin \frac{n \pi x}{L} \quad (2)$$

where L is total length and A is a constant, and the boundary conditions are $T(0, t) = T_0$ and $T(L, t) = 0$.

The initial temperature is set to be 20 °C, and the adiabatic thermal boundary condition is used in the model. The SPH thermal model and solved temperature field are shown in Figure 5.6. The temperature decreases from the top side to the bottom side. The analytical solutions of the

Fourier equation [132] compared with the SPH model results, as shown in Figure 5.7, which shows the temperature distributions along the model length at different times. The solutions from the SPH model and the analytical solutions show good agreement, which validates the SPH thermal solutions.

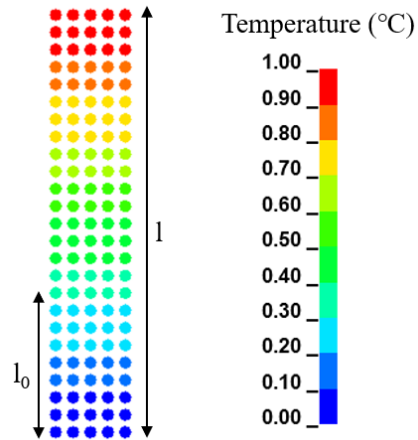


Figure 5.6. Temperature distribution in the SPH model.

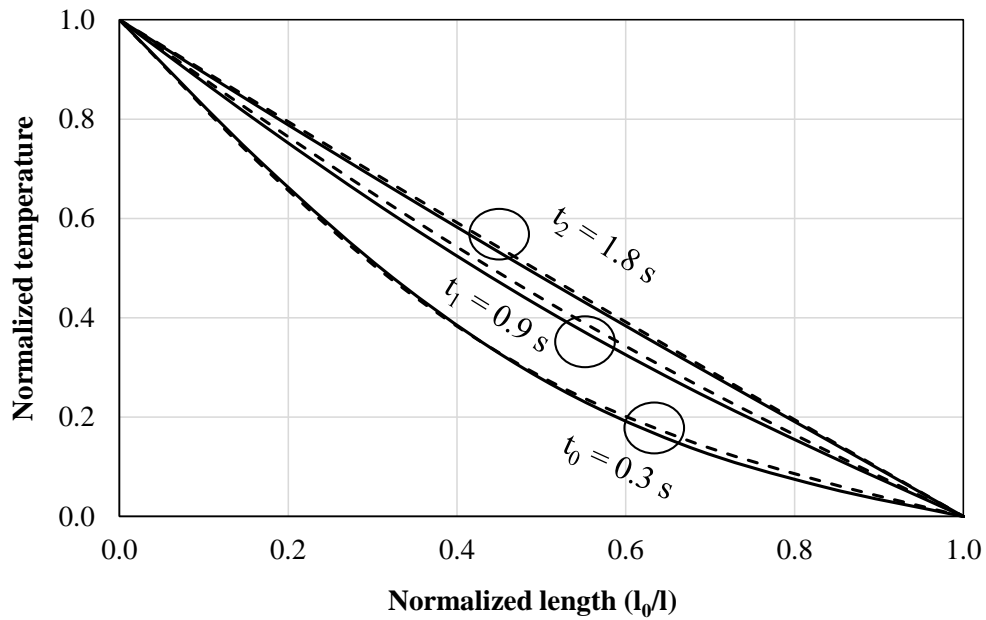


Figure 5.7. Temperature vs. length for the SPH model (solid lines) and the analytical solution (Eq. 2, dotted lines) at different moments.

5.3 Modeling of Ceramics Cutting Process

5.3.1 Columnar Grain Ceramic Cutting Model

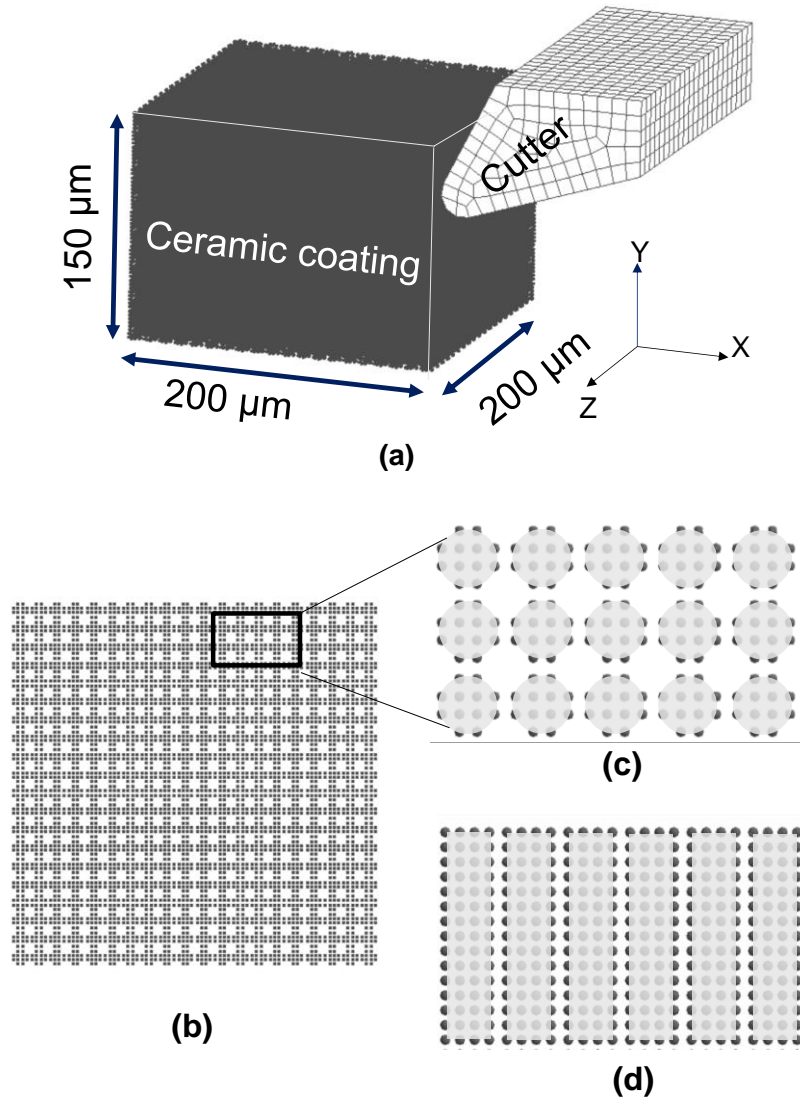


Figure 5.8. Ceramic coating cutting model set-up. (a) The whole model shows the ceramic coating and cutter, (b) Top view of the ceramic coating, (c) the magnified local view of the ceramic coating to illustrate the columnar grains, (d) the side view of the columnar grains corresponding to (c). The gray regions in (c) and (d) are artificial for better visualization of the columnar grains.

The ceramic cutting model is shown in Figure 5.8. A cutter is moving the top ceramic layer along the -X-axis direction. The ceramic coating is modeled using the SPH method, and its dimensions are $200 \times 200 \times 150 \mu\text{m}^3$.

A salient feature of the ceramic coating in this study is the columnar grain structure. To resemble the real EB-PVD coating structure, such as the one shown in Figure 5.1, the ceramic coating layer is modeled as 400 columnar grains, as shown in Figure 5.8b. As detailed in Figure 5.8b, each column is a cylinder with a diameter of $10\ \mu\text{m}$ and a height of $150\ \mu\text{m}$. The total number of SPH particles in the ceramic coating layer is 288,000.

5.3.2 Cutting Tool Model

The geometry of the cutting tools is shown in Figure 5.9. To study the effect of sharpness of the cutting tool, two cases with different radii of the cutting edge are considered, which are $10\ \mu\text{m}$ and $0\ \mu\text{m}$, respectively. Additionally, two rake angles, 26.6° and 11.6° are studied. The tool clearance angle keeps a constant of 18.4° [133].

The cutting tool is regarded as a rigid body, and it is modeled using the finite element mesh following Ref.[119]. The total number of the finite element of the cutting tool is 1,955.

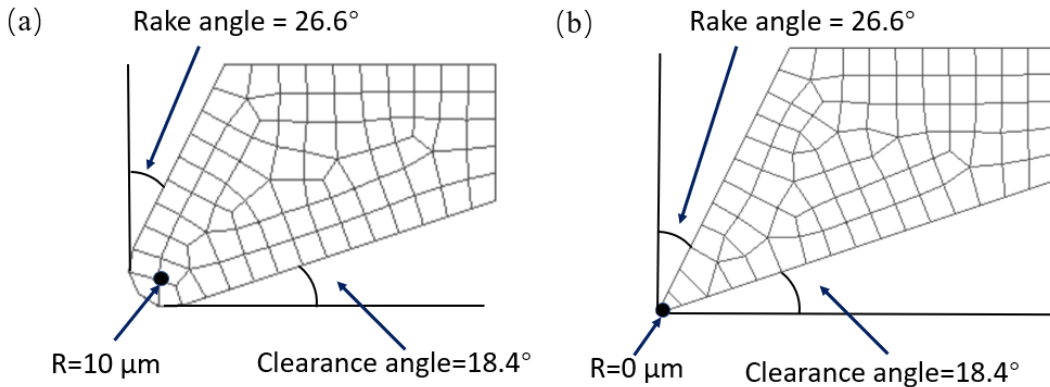


Figure 5.9. Side view of cutting tools and their finite element mesh, with different radii of cutting edge angle R:(a) $R=10\ \mu\text{m}$; (b) $R=0\ \mu\text{m}$. The rake angle and clearance angle are also labeled.

In terms of boundary conditions, the bottom of the SPH ceramic layer is fixed. The contact method between the cutting tool and the ceramic coating is `AUTOMATIC_NODES_TO_SURFACE` in LS-Dyna. The main contact surface is the tool surface, and the slave contact surface is the ceramic surface. The contact type is the penalty friction, and the coefficient of friction is taken as 0.2 [106]. The cutting speed is imposed using

BOUNDARY_PRESCRIBED_MOTION_RIGID in LS-Dyna [105]. The initial temperature is set to be 20 °C, and the adiabatic thermal boundary condition is used in the model.

5.3.3 Materials and Damage Models

The constitutive model of zirconia ceramic coating is the Johnson-Holmquist 2 (JH-2) material model, corresponding to the No.110 material MAT_JOHNSON_HOLMQUIST_CERAMICS in the LS-DYNA material library [86]. The cutting tool material is diamond. The constitutive model of the tool is the rigid model, corresponding to the No.020 material MAT_RIGID in the LS-DYNA material library. The Johnson-Holmquist plasticity damage model is also used, which has been proved to be effective for modeling large deformation and fracture in ceramics, glass, and other brittle materials [86]. The equivalent stress for a ceramic-type material is given by [84]:

$$\sigma^* = \sigma_i^* - D (\sigma_i^* - \sigma_f^*) \quad (3)$$

where

$$\sigma_i^* = a (p^* + t^*) n (1 + c \ln \dot{\epsilon}^*) \quad (4)$$

represents the intact, undamaged behavior. The superscript, '*', indicates a normalized quantity. a is the intact normalized strength parameter, c is the strength parameter for strain rate dependence, $\dot{\epsilon}^*$ is the normalized plastic strain rate, and [84],

$$t^* = \frac{T}{P_{HEL}} \quad (5)$$

$$p^* = \frac{p}{P_{HEL}} \quad (6)$$

where T is the maximum tensile pressure strength, P_{HEL} is the pressure component at the Hugoniot elastic limit, and p is the pressure [84],

$$D = \sum \frac{\Delta \epsilon^p}{\epsilon_f^p} \quad (7)$$

represents the accumulated damage based upon the increase in plastic strain per computational cycle and the plastic strain to fracture [84],

$$\epsilon_f^p = D_1 (p^* + t^*)^{D_2} \quad (8)$$

and

$$\sigma_f^* = b (p^*)^m (1 + c \ln \dot{\epsilon}^*) \leq SFMAX \quad (9)$$

represents the damage behavior. The parameter d_1 controls the rate at which damage accumulates. In an undamaged material in compression, the hydrostatic pressure is given by [84],

$$P = K_1\mu + K_2\mu^2 + K_3\mu^3 \quad (10)$$

and in tension

$$P = K_1\mu \quad (11)$$

where $\mu = \rho/\rho_0 - 1$.

The ceramic layer has the following properties of zirconia: density 5,850 kg/m³, shear modulus 95.31 GPa, tensile strength 0.2 GPa, Poisson's ratio 0.22, thermal conductivity 2.0 W/(m •°C) and heat capacity: 278 J/(Kg•°C). The coefficient values in the JH-2 model used for ceramic coating are shown in Table 5.1[106]. The diamond cutting tool is used with the following properties: density 3250 kg/m³, elastic modulus 1114 GPa, and Poisson's ratio 0.07 [106].

Table 5.1. JH-2 parameters of ceramic coating [106].

Parameters	Value
A	0.93
B	0.31
C	0
M	0.6
N	0.6
HEL(GPa)	2.79
PHEL(GPa)	1.46
D ₁	0.005
D ₂	1
K ₁ (GPa)	130.95
K ₂ (GPa)	0
K ₃ (GPa)	0

Heat generation in the ceramic layer is considered in the model by setting the keyword FWORK =1.0, which is the fraction of the mechanical work converted into heat. It follows W

$=\rho c V \Delta T$, where W is work, ρ is density, c is heat capacity, V is volume, ΔT is the temperature change. The initial temperature is set to be 20 °C, and the adiabatic thermal boundary condition is used in the model [132].

5.4 Results and Discussion

5.4.1 Effect of Cutting Depth on Cutting Force and Coating Temperature Increase

To understand the effect of cutting depth on cutting force and ceramic layer's temperature change, three tool cutting depths are selected: 20 μm , 30 μm , and 40 μm .

Figure 5.10 shows the main cutting force evolutions for the three cutting depths. The cutting force of the 40 μm case is the highest since it has the largest ceramic layer removal rate, among the three cases. Additionally, it shows the main cutting forces increase rapidly in the initial contacting the ceramic layer. Then there is a slower increase of the cutting force because of a gradually stable cutting phase, at around 0.20 ms. The cutting forces under the stable state increase with the cutting depth, with the 40 μm case as the highest. Finally, the cutting forces drop due to reaching the end of the ceramic layer.

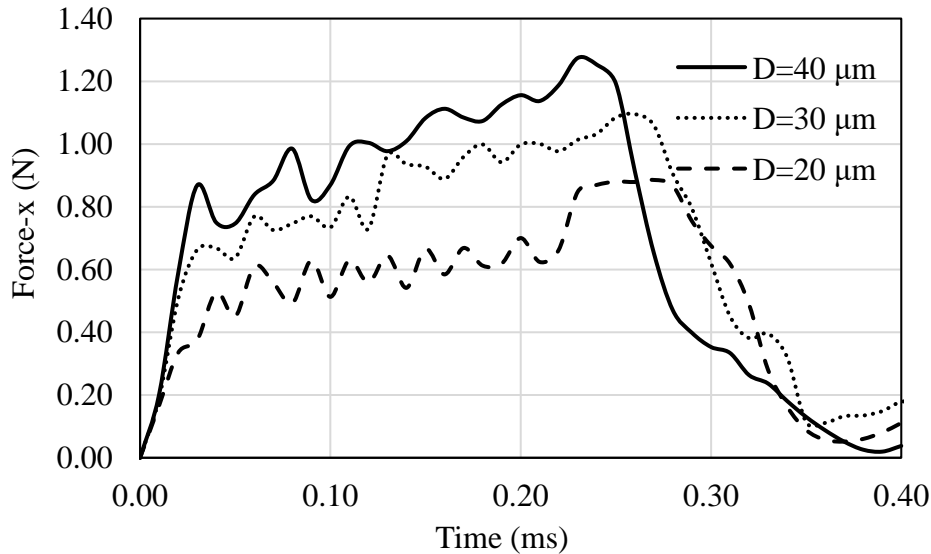


Figure 5.10. Main cutting force F_x evolution at different cutting depths.

Williams et al. proposed a fracture mechanics analytical solution for the normalized cutting force (F_x/b) at the stable stage as a function of the cutting depth h [133]:

$$\frac{F_x}{b} = G_c \left(1 + \frac{G_a}{\sqrt{1+\mu^2}} \frac{1}{\cos\alpha} \right) + \frac{G_a}{\sqrt{1+\mu^2}} + \left[\frac{1-\sin(\alpha-\beta)}{\cos(\alpha-\beta)} \right] \sigma_y h \quad (12)$$

where G_c is the energy release rate; α is the rake angle; μ is the friction coefficient $\tan\beta=\mu$; G_a is the adhesion toughness; σ_y is tensile yield stress; b is the specimen width; h is the cutting depth [133]. In this study, the following parameters of zirconia ceramics are used $G_a=0$, and $G_c=3.8 \text{ J/m}^2$ [110].

Our SPH model results are compared against previous work. Both the SPH model and the above analytical solution Eq. 12 [133] are plotted in Figure 5.11. Both models show that the main cutting forces increase linearly with the cutting depth. The SPH model shows excellent agreement with the analytical solution for the cutting process based on fracture mechanics.

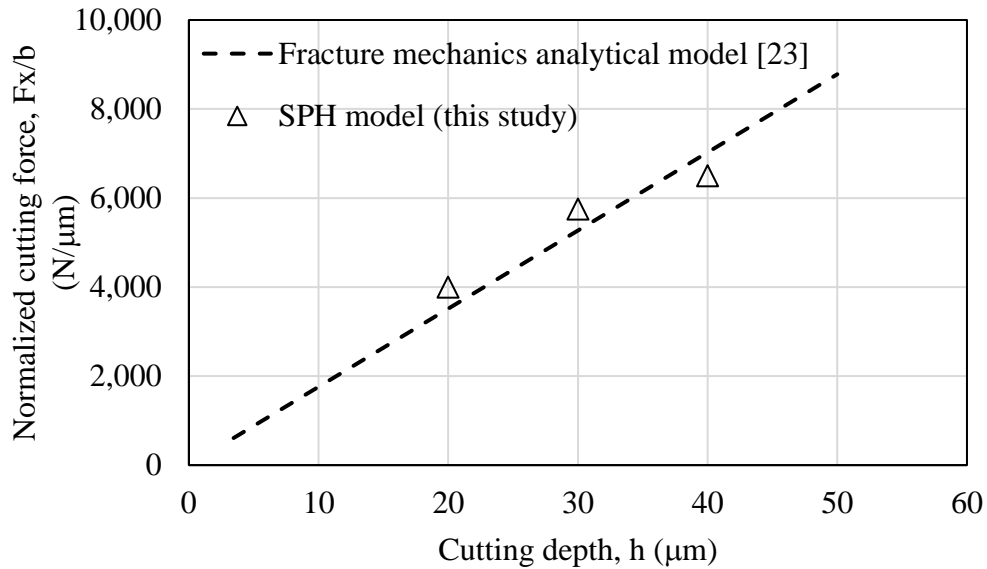


Figure 5.11. Main cutting force F_x at the stable stage at different cutting depths. SPH model vs. fracture mechanics analytical solution [133].

Figure 5.12 shows the maximum temperature in the ceramic layer at different cutting tool depths. The temperature increases with time, as more cutting work is converted to heat during the cutting process. Additionally, more temperature increases occur as the cutting depth is increased since more work is required for removing a thicker layer.

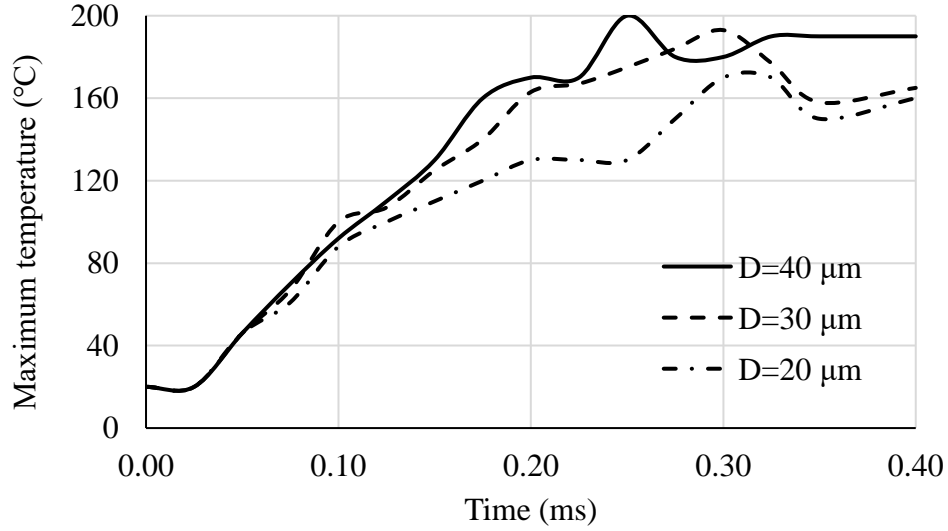


Figure 5.12. Maximum temperature evolution in the ceramic layer for different cutting depths

5.4.2 Effect of Cutting Speed on Cutting Force and Coating Temperature Increase

Figure 5.13 shows the main cutting force evolution at two different cutting speeds, 2.5 m/s, and 5 m/s, respectively. It is shown that the main cutting force with the speed of 2.5 m/s is smaller compared with the 5 m/s cases, at the same moment. However, the maximum main cutting force is almost the same, about 1.25 N, irrespective of the cutting speed, which is determined by the total amount of the removed chips.

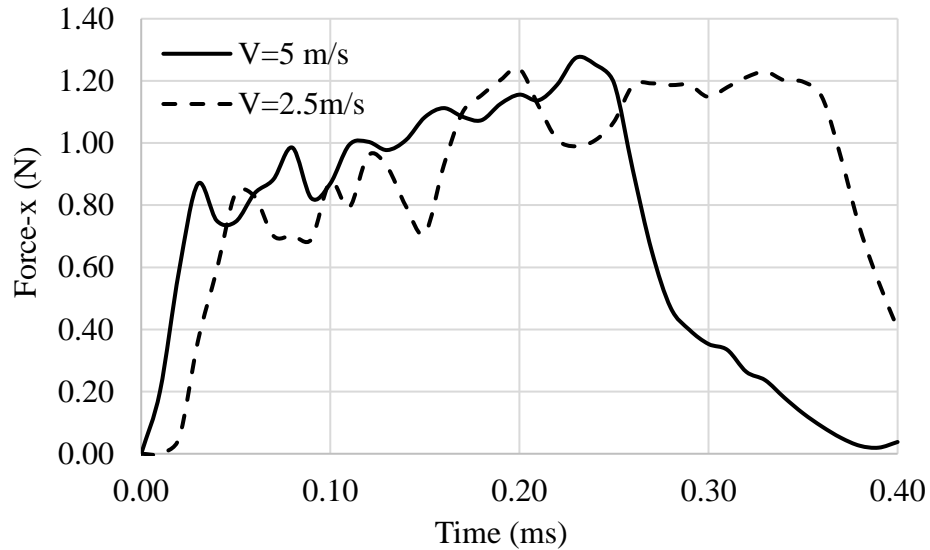


Figure 5.13. Main cutting force F_x evolution under different cutting speeds

Figure 5.14 shows the maximum temperature evolutions at the two different tool cutting speeds. It is evident that the temperature increase is less for the cutting speed of 2.5 m/s than the 5 m/s case. Lower cutting speed means less total work for the same duration, which is converted to heat $W = \rho c V \Delta T$. It's also consistent with the less cutting force shown in Figure 5.13.

The modeled phenomenon of temperature increasing with cutting speed is consistent with the previously reported experiment on milling of sintered zirconia [33]. The cutting temperature increased sharply from 140 °C at 100 m/min to 320 °C at 200 m/min cases [33].

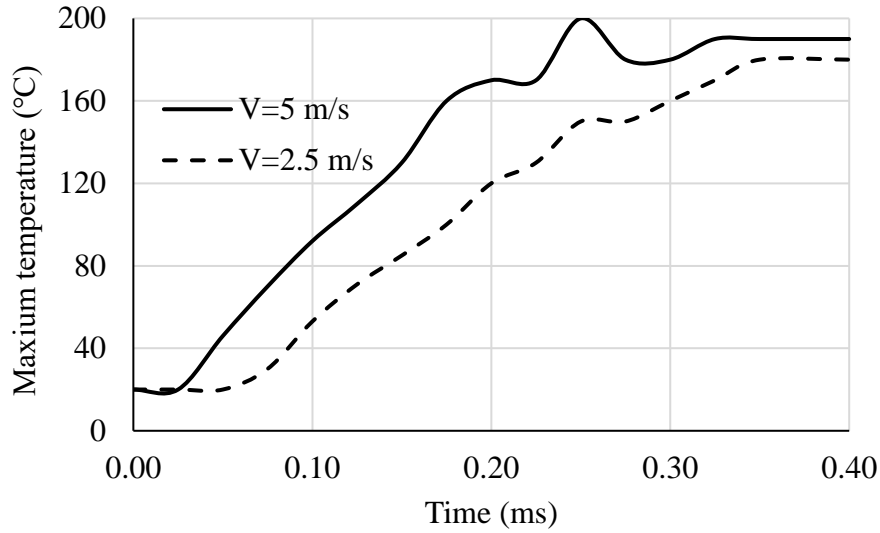


Figure 5.14. Maximum temperature evolution in the ceramic layer at different tool cutting speeds

5.4.3 Effect of Cutting Tool's Edge Radius on Cutting Force

The profile of the cutting tool plays a critical role in the cutting performance [119]. In this section, the sharpness of the cutting tool on the cutting force is investigated. Two different edge radii, $R=10 \mu\text{m}$ and $R=0 \mu\text{m}$, are considered.

The SPH model in this study is capable to examine the stress evolutions in the EB-PVD thermal barrier coatings with columnar grains, which is not available if a uniform bulk ceramic coating model is used. Figure 5.15 shows the effective stress distributions for $R=10 \mu\text{m}$ and $R=0 \mu\text{m}$. It is noted that the stresses in the columnar grains are illustrated with a brighter color, while the gaps between the grains are in a darker color. Additional analysis reveals that the fracture of the columnar grains during the cutting process is done through deflection and fracture of the grains, followed by pushing against neighboring grains. Comparing the two cases, the $R=10 \mu\text{m}$ case has

a broader high-stress region ahead of the cutting tool, suggesting a blunt cutter tip causes higher stresses. The machined ceramic chips show mostly a fine powder form, as illustrated in Figure 5.15, which is distinct from cutting metallic materials. The $R=10\text{ }\mu\text{m}$ case has a slightly coarser fragmentation than the $R=0\text{ }\mu\text{m}$ case.

In terms of the cutting tool, as observed in the experiment, the tool wear can cause higher cutting forces for the tool with a small edge radius[118]. In this model, the cutting tool is assumed as a rigid body, therefore, the tool wear is not considered in this model.

At the same time, the stress is distributed in front of the cutting tool. The magnitude of the stress decreases in the negative X-direction. It means that the area affected by the cutting tool decreases with the distance of the cutting tool. In addition, the affected area of $R=0\text{ }\mu\text{m}$ is smaller.

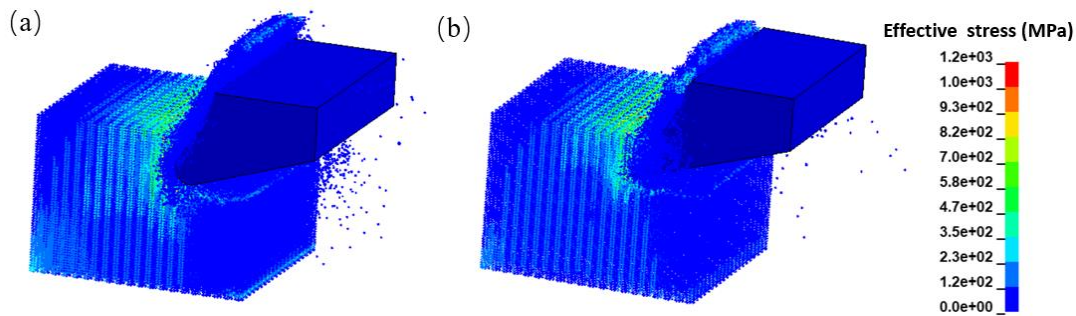


Figure 5.15. Stress distribution at different cutting tool edge radii: (a) $R=10\text{ }\mu\text{m}$; (b) $R=0\text{ }\mu\text{m}$. The tool rake angle is 26.6° .

Figure 5.16 shows the cutting force evolution under different cutting-edge radius. It also can be seen that the cutting force of $R=10\text{ }\mu\text{m}$ is higher than $R=0\text{ }\mu\text{m}$. The tool with a sharper edge radius generates lower cutting forces because this tool easier enters the material. In addition, the cutting forces become stable after some time when the cutting process comes to a stable state. The small increase of the cutting force is caused by the accumulation of the removed coating.

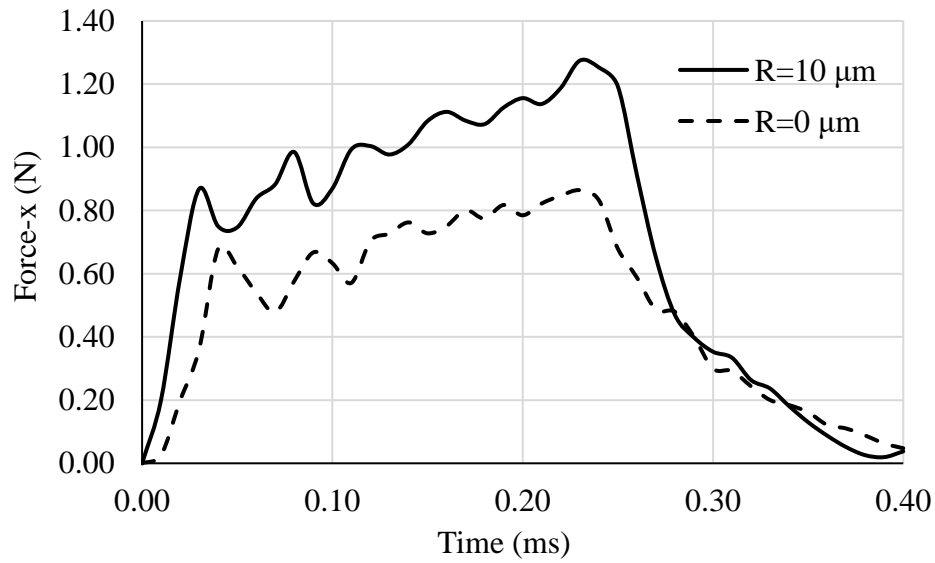


Figure 5.16. Cutting force evolution at different cutting tool edge radii.

Figure 5.17 shows the maximum temperature evolutions at different cutting tool edge radius. The maximum temperature increases initially until reaching a stable stage, where the equilibrium of heat transfer is reached in the ceramic coating layer.

The temperature increases with $R=10\ \mu\text{m}$ is higher since a higher cutting force is required, as shown in Figure 5.16. This is because a higher friction force is generated in a larger radius, and more work is done by the cutting tool. As a result, more heat is generated between the cutting tool and ceramic coating. The high temperature is one of the main factors which causes the cutting tool wear and affects the surface roughness [134]. To minimize the temperature, increase in the ceramic layer, a small cutting tool edge radius is preferred.

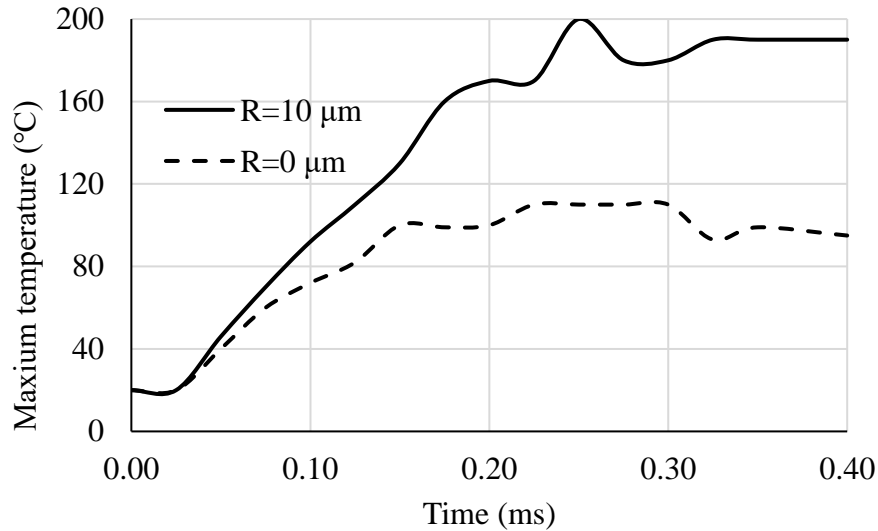


Figure 5.17. Maximum temperature evolution in the ceramic layer at different cutting tool edge radii.

5.4.4 Effect of Cutting Tool's Rake Angle on Coating Temperature Increase

The cutting tool rake angle has a profound effect on material removal, tool wear, surface generation, stresses, and crack formation [135]. It affects the contact area between the cutting tool and chips. Two different rake angles are selected to study the effect of different tool rake angles: 26.6° and 11.6° .

The decreasing rake angle can turn the cracking mode from the tensile mode to the sliding mode [125]. Figure 5.18 shows the stress distribution under the tool rake angle 11.6° . Compared with the stress distribution of rake angle 26.6° shown in Figure 5.15a, the maximum stress with the tool rake angle 11.6° is lower. However, the stress distribution area is much larger, suggesting the area affected by the cutting process is much bigger.

Figure 5.18 also shows the machined ceramic chips removed from the coating. Compared to the rake angle 26.6° case in Figure 5.15a, more continuous and thicker chips are generated with the tool angle 11.6° . This is because the primary shear zone becomes vertical with the decrease of the tool angle, and the friction along with the tool/chip interface increases.

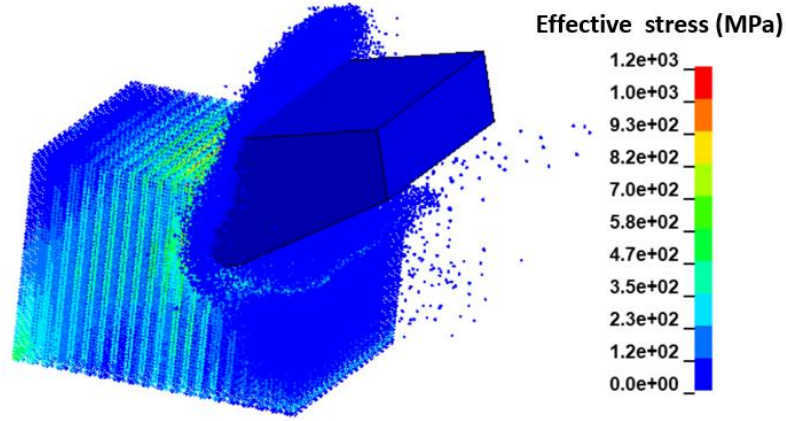


Figure 5.18. Stress distribution with the tool rake angle of 11.6° . The cutting tool edge radius is $10\text{ }\mu\text{m}$.

Figure 5.19 shows the cutting force evolution under different tool rake angles. It is clear that the cutting force increases with the decreasing of tool rake angle. It follows the same trend as the main cutting force F_x calculated by the analytical expression [136]:

$$F_x = A \cdot k_s \cdot k_v \cdot k_\gamma \cdot k_\alpha \cdot k_t \quad (13)$$

where A is the chip cross-section; k_s is the specific cutting force; k_v is the speed factor; k_γ is the tool rake angle factor; k_α is the tool wear factor and k_t is the material factor. $k_\gamma = \frac{C - 1.5\gamma}{100}$, where γ is the effective rake angle and C is the rake angle constant. The main cutting force decreases with the increase of the effective rake angle. For the orthogonal cutting process, the cutting angle is the effective rake angle [136].

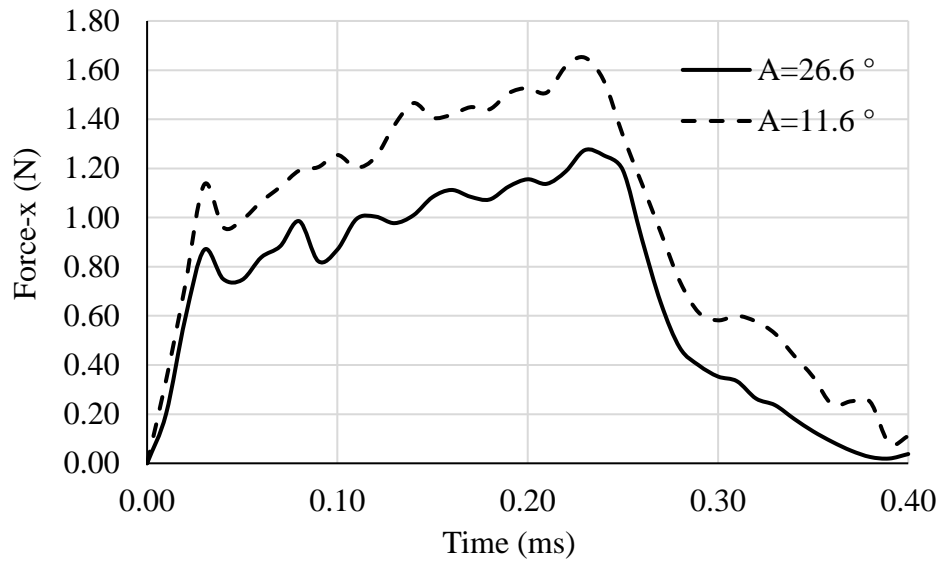


Figure 5.19. Cutting force evolution F_x under different tool rake angles.

Figure 5.20 shows the maximum temperature of ceramics under different tool rake angles. The temperature increases with cutting time till approximately 0.25 ms, before reaching a more stable state. It also shows that the temperature in the 22.6° case is only slightly higher than the 11.6° case, with a minimum difference. This is again due to the higher cutting force in the 22.6° case.

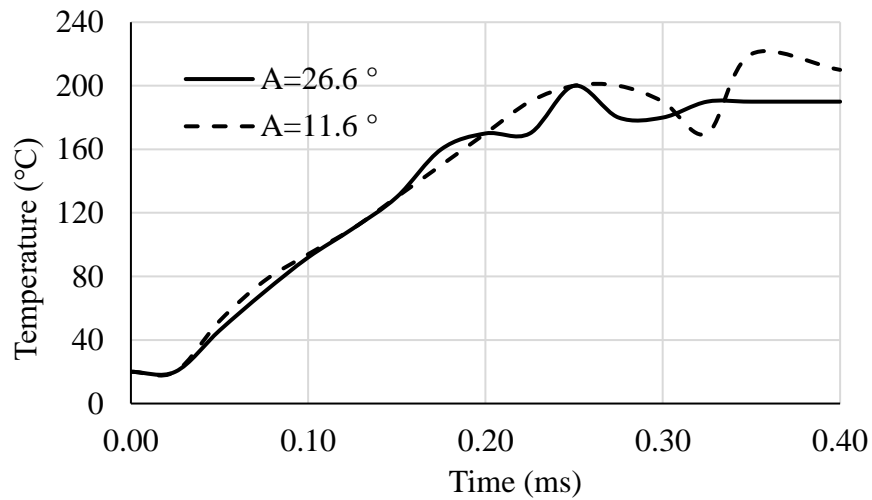


Figure 5.20. Maximum temperature evolution in the ceramic coating under different tool rake angles.

5.5 Summary and Future Work

A new SPH cutting model for thermal barrier coating has been successfully developed. The major conclusions are summarized as follows:

1. The SPH model in this study is capable to examine the stress evolutions in the EB-PVD thermal barrier coatings with columnar grains, which is not available if a uniform bulk ceramic coating model is used. Additional analysis reveals that the fracture of the columnar grains during the cutting process is done through deflection and fracture of the grains, followed by pushing against neighboring grains.
2. Model validation and convergence studies were conducted by comparing the SPH model with the FE model at different particle densities.
3. Both the cutting force and temperature of the coating increase with cutting depth due to increased cutting work transferred to heat. The cutting forces from the SPH model at the stable stage are in excellent agreement with the fracture mechanics analytical solution.
4. Both the cutting force and temperature of the coating increase with cutting speed due to increased coating removal rate.
5. In terms of the effect of the cutting tool's edge radius on cutting force, the cutting force and temperature increase of $R=10\text{ }\mu\text{m}$ are higher than $R=0\text{ }\mu\text{m}$, due to increased friction between the cutting tool and coating. The machined ceramic chips show mostly a fine powder form, which is distinct from cutting metallic materials. The $R=10\text{ }\mu\text{m}$ case has a slightly coarser fragmentation than the $R=0\text{ }\mu\text{m}$ case.
6. The cutting force decreases when the rake angle increases from 11.6° to 26.6° . The SPH model result follows the same trend as the main cutting force calculated by the analytical expression.

Although the detailed modeling studies are presented in this work, additional experiments should be conducted in the future for direct comparison with the modeling results.

6. MODELING OF MACHINING PROCESS OF EB-PVD CERAMIC COATINGS USING DISCRETE ELEMENT METHOD

A version of this chapter has been submitted to the journal for review.

Abstract: In this work, a new discrete element model (DEM) for simulating the machining process of thermal barrier coatings is presented. The effects of cutting processing parameters, including cutting depth and cutting speed, on the cutting force and chip morphology are studied. In the model, a columnar grain microstructure mimicking the electron-beam physical vapor deposition (EB-PVD) coating is used. The results show that, as the cutting depth increases, the cutting chip morphology changes from fine powder form (ductile mode) to large chunk pieces (brittle mode). The transition depth or the critical cutting depth is determined based on the Griffith fracture criterion. The transition is also illustrated using the numbers of broken bonds and cutting energy changes in the DEM model. In the ductile mode, the number of broken bonds is increased gradually. In contrast, at larger cutting depths, the brittle mode causes a step-wise increase. Moreover, the maximum cutting force is found correlated to the cutting depth, which agrees well with an analytical solution based on fracture mechanics principles. The period in the cutting force is consistent with the diameter of the column grain. Finally, the cutting speed has little effect on the cutting force and chip morphology due to no strain rate sensitivity.

6.1 Introduction

Thermal barrier coatings (TBCs) have been extensively used for protecting gas turbine hot sections, in order to achieve the demanding fuel efficiency and reduced emission goals [1]. The ceramic top layer is typically applied either by air plasma spray (APS) or by electron beam physical vapor deposition (EB-PVD). EB-PVD TBCs are preferred for aircraft engines due to their high strain tolerance imparted by the microstructure [19].

Since engines are subject to degradation such as erosion, foreign object damage, and oxidation, TBCs failure may occur during operations. Failure of TBCs can either induce critical damage or reduce the life of turbine components and must be removed and repaired [9]. Various methods have been proposed for the removal of TBCs for turbine components such as grit blasting, chemical stripping, water jet, grinding, and laser ablation [8]. Of these methods, grinding is an

efficient and effective technique. The major challenge for machining of TBCs is their high hardness, high brittleness, and low fracture toughness[21]. Brittle materials experience a transition from ductile mode cutting to brittle mode cutting when cutting from small to large machining depth [22].

Several experimental and modeling methods have been used to understand the grinding process. For example, in Ref. [137], experiments were conducted to study the grinding mechanisms of alumina (Al_2O_3). The results showed that a small feed rate and grinding depth and high grinding speed improve the surface quality [137]. In Ref. [26], an orthogonal cutting model was built to simulate the alumina machining process. The peak cutting force in the tangential direction was determined by combining the force of chip formation and the frictional force. The model showed a good agreement with experimental measurement [26]. In Ref. [138], a finite element model (FEM) with tension-shear coupled fracture criterion was established to study the difference between the brittle and ductile ceramic removal modes. The results showed that the model can capture the brittle-ductile transition in the ceramic grinding process [138]. Moreover, the smooth particle hydrodynamic (SPH) method was used to investigate the scratching process of SiC ceramics, which showed good agreement with the experiment [139, 140]. In Ref. [129], a discrete element model (DEM) was developed to simulate the cracks' initiation and propagation in the grinding of Al_2O_3 . Additionally, at the atomic level, the molecular dynamics (MD) method has also been used to simulate the machining process and analyze the machining mechanism of some brittle materials [130]. However, there is a limitation of simulation domain size in the MD model.

Compared with FEM, particle-based simulation methods, such as DEM and SPH, have the advantages of modeling fracture and fragmentation in brittle materials [141]. DEM has been used for predicting complex fracture patterns in ceramics [142]. However, there are very few publications on the machining of TBCs using DEM. In this paper, an orthogonal DEM cutting model is developed to study the EB-PVD coating machining process. The cutting processing parameters, such as cutting depth and cutting speed, are studied. There are several novelties in this work. The first one is the microstructure of the ceramic coating. Discrete columnar grains are used to simulate the EB-PVD TBC microstructures, which are distinct from the previous studies which used a uniform bulk coating. The columnar grains can demonstrate the unique fracture behavior not available in the bulk material. The second one is that the fracture and fragmentation of the

cutting chips due to the advantages of DEM for brittle materials. The structure of the paper is as follows. Section 1 is the introduction. Section 2 presents the DEM parameter calibration test and columnar grain structure model. Section 3 shows the results, with the focus on cutting depth and cutting speed. Section 4 presents the conclusions.

6.2 DEM Model Description

6.2.1 Governing Equations in DEM

DEM is a particle-scale numerical method for modeling the bulk behavior of granular materials proposed by Cundall and Strack [42]. In DEM, each particle is treated as a rigid 2D disc or 3D sphere. The particles are connected using contact bonds. Particle motions obey Newton's second law [43]:

$$m_i \frac{dv_i}{dt} = \sum_{j=1}^{k_i} (F_{c,ij} + F_{d,ij}) + m_i g \quad (1)$$

$$I_i \frac{d\omega_i}{dt} = \sum_{j=1}^{k_i} T_i \quad (2)$$

where v_i and ω_i are the vectors of the linear and angular velocities of an i th particle, respectively, m_i is the weight; I_i is inertia; $F_{c,ij}$ is the contact force of particle j to particle i , $F_{d,ij}$ is the damping force between particle j and i , and T_i is the resultant force moment.

In this paper, the parallel bond model is selected as the DEM contact model. The parallel bond model, proposed by Potyondy and Cundall [143], is a bonding model that enables the specification of tensile and shear strengths. The moment transfer/resistance is caused by the normal and tangential components of the contact force [143]. The parallel bond can be envisioned as a set of elastic springs with constant normal and shear stiffness, \bar{k}_n and \bar{k}_s , and it is always active if it is bonded or if the surface gap is less than or equal to zero [144]. By changing the particle size and the parameter of the parallel bond, the parallel bond model can be used to simulate the mechanical response in TBCs [145]. The contact force and moment are calculated as [143]:

$$F = (F_n + \bar{F}_n) \cdot \hat{n} + F_s + \bar{F}_s \quad (3)$$

$$M = \bar{M} \quad (4)$$

where the parallel bonds are delineated with bar accents and the subscripts n and s indicate the normal and shear direction, respectively. F_n and F_s encompass the contributions of the linear springs and viscous dashpots. When the force applied on the parallel bond is higher than its strength, the parallel bond will be broken, and the connection state will be changed to a non-bonded

connection, which indicates that the particles can only withstand compressive stress and sliding friction [146].

6.2.2 Model Parameter Calibration

To determine the parameters in the DEM parallel bond model, a model parameter calibration study is first conducted. In general, the mechanical properties of a TBC can be determined by its elastic modulus, unconfined compressive strength, Poisson's ratio, tensile strength, and fracture toughness. Using these macroscopic properties, the corresponding DEM particle and contact parallel bond model parameters can be derived [25, 147].

In this work, three mechanical tests are simulated to calibrate the DEM particle and contact model parameters, as shown in Figure 6.1, including (a) uniaxial compression test; (b) uniaxial tensile test, and (c) fracture toughness test, following Ref. [147]. The parameters in the parallel bond model are tuned, such that the simulated macroscopic mechanical properties match the experimental data, which are listed in Table 1 [148-150].

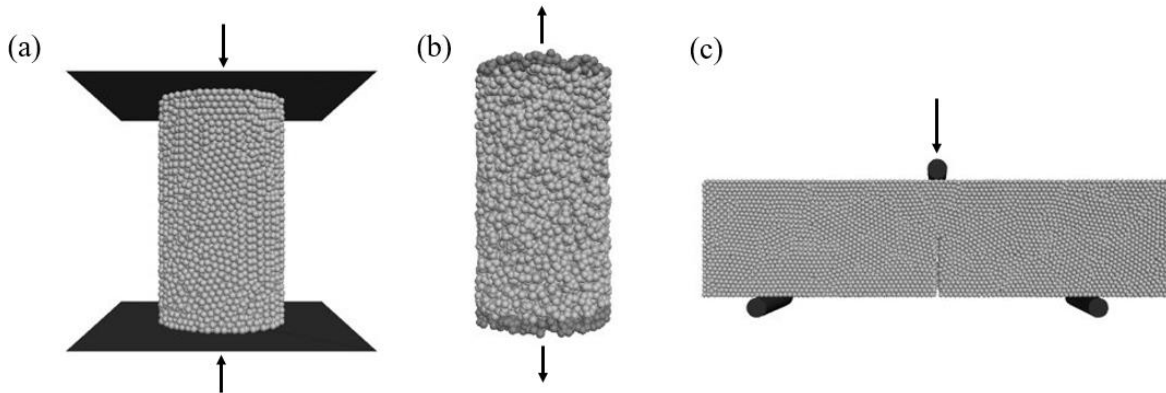


Figure 6.1. DEM model parameter calibration tests: (a) uniaxial compression test; (b) uniaxial tensile test, and (c) fracture toughness test.

As shown in Figure 6.1, the uniaxial compression test was carried out by moving two rigid walls to the specimen. The tensile test was done by moving two boundary layers at the end to the opposite direction. The height of specimens used for compression and tensile tests was two times their width. The fracture toughness test was carried out through a three-point bending test with the specimen notched at the bottom center. The depth of the notch is half of the height of the specimen. All the specimens used were assembled by the particles with a particle radius of $5\text{ }\mu\text{m}$ [145].

6.2.3 Columnar Grain Microstructure Model and Boundary Conditions

To mimic the EB-PVC columnar grain structure, such as the one shown in Figure 6.2[151] the DEM model's coating layer is comprised of 48 small square columns (Figure 6.3). The overall layer's dimension is $400\ \mu\text{m} \times 300\ \mu\text{m} \times 150\ \mu\text{m}$, and each columnar grain is $50\ \mu\text{m} \times 50\ \mu\text{m} \times 150\ \mu\text{m}$. The cutting tool is a rigid wedge. The total number of DEM particles is 24,781.

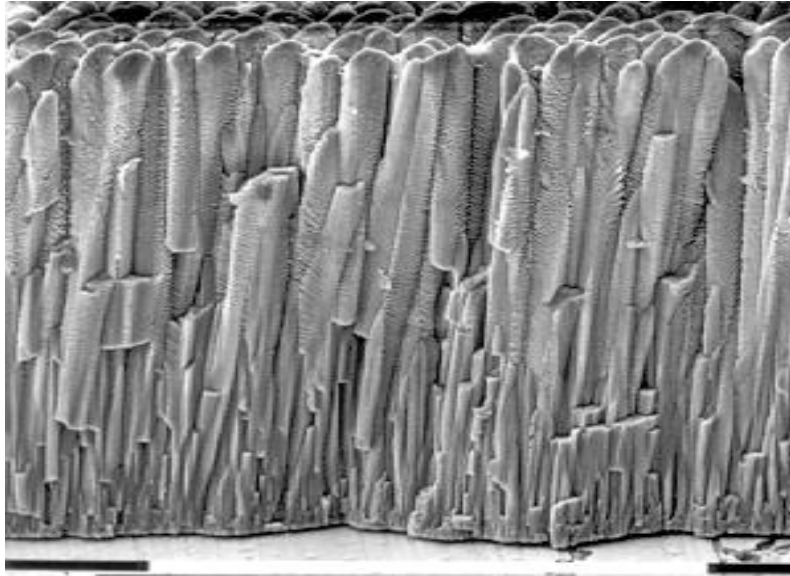


Figure 6.2. Cross-sectional view of an EB-PVD thermal barrier coating, which shows the columnar grain structure [151].

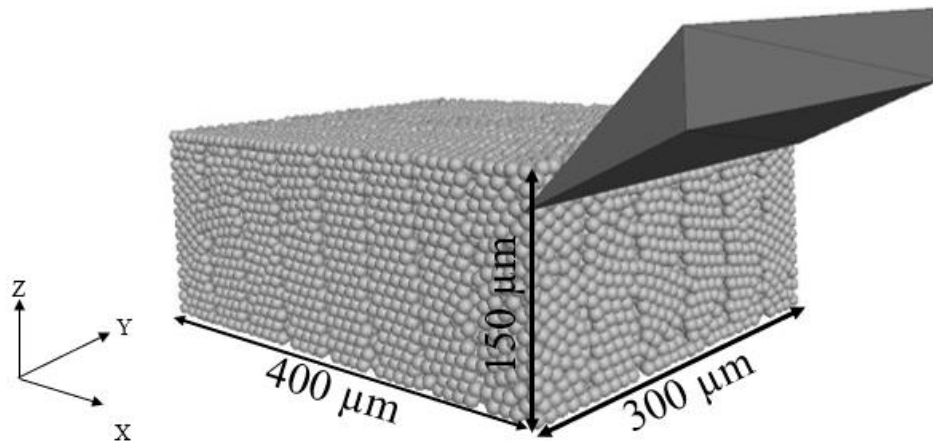


Figure 6.3. DEM cutting model of the TBC layer. The cutting tool is also shown.

In terms of the boundary conditions, the bottom of the coating layer is fixed with other surfaces free. A combination of cutting speed (2,4, and 8 m/s) and cutting depth (5, 25, and 75 μm) are used to investigate their effects. To reliably update the model state, an automatic timestep is selected. In the default setting, the stable timestep is calculated based on the current stiffness and masses of all objects in the system.

6.3 Results and Discussion

6.3.1 Model Calibration Parameter Results

Through the calibration process described in Section 6.2.2, the derived parameters for the DEM parallel bond are as follows: Young's modulus E_{bond} is 20 GPa, the ratio of shear to normal stiffness \bar{k}_s/\bar{k}_n is 3.0, tensile strength $\bar{\sigma}_c$ is 150 MPa, shear strength is $\bar{\tau}_c$ 75 MPa, and bond gap g is 2×10^{-7} m.

Using the above calibrated DEM parallel bond parameters, the simulated mechanical properties from this DEM model are summarized in Table 6.1. As shown in the table, the simulated DEM properties are in excellent agreement with the experimental data, indicating the correctness of the calibrated parameters.

Table 6.1. Simulated mechanical properties of the EB-PVD ceramic coating using the calibrated DEM parameters compared against the experimental data in the literature [148-150]

Mechanical properties (unit)	Simulated DEM results (this study)	Experimental results [148-150]
Poisson's ratio	0.2	0.2
Elastic modulus (GPa)	41	40
Compression strength (MPa)	513	510
Tensile strength (MPa)	22.4	22.3
Fracture toughness ($\text{MPa}\sqrt{m}$)	2.03	2.05

6.3.2 Effect of Cutting Speed on Cutting Force and Chip Morphology

The role of cutting speed in the cutting process is investigated by simulating different cutting speeds, as shown in Figure 6.4, at the same cutting depth of 25 μm . The chip formation and the

chip size has shown the similar deformation , suggesting the results are not sensitive to the cutting speed.

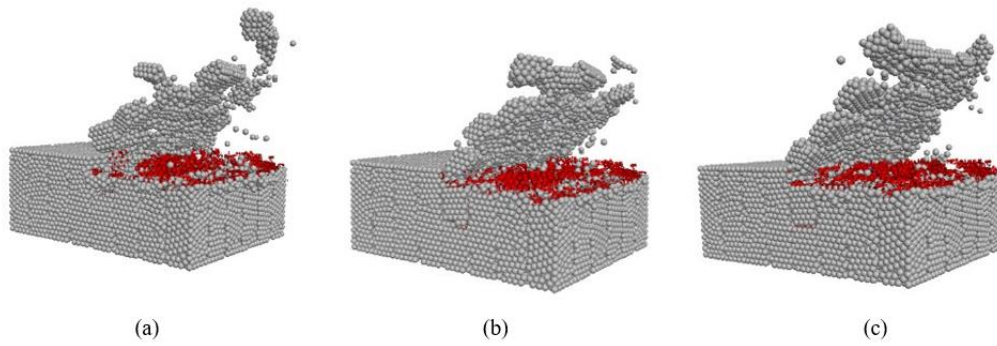


Figure 6.4. Chip formations at different speeds: (a) $v = 2$ m/s; (b) $v = 4$ m/s; (c) $v = 8$ m/s

To quantitatively evaluate the speed effect, the cutting force evaluations at different cutting speeds at the same cutting depth of $25\text{ }\mu\text{m}$ are plotted in Figure 6.5. The cutting force curves show the same pattern with little difference. This is because the ceramic material in our model is not strain rate sensitive.

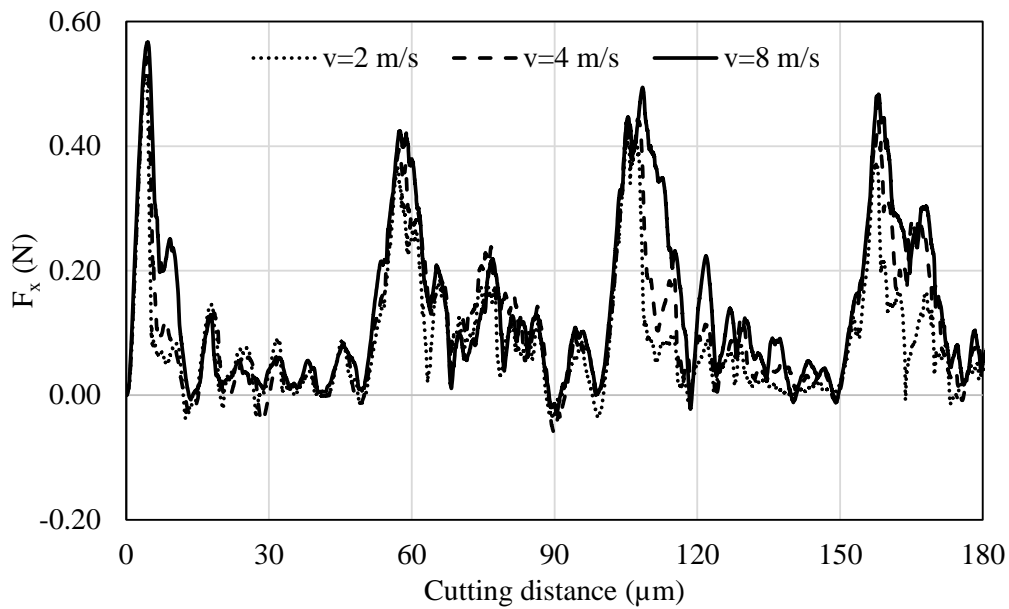


Figure 6.5. Horizontal cutting force at different cutting speeds.

Figure 6.6 shows the evolutions of the numbers of broken bonds at different cutting speeds. All the curves are very similar. Therefore, the cutting speed has little influence on the TBCs failure mode, which is consistent with the similar material in the previous study [152].

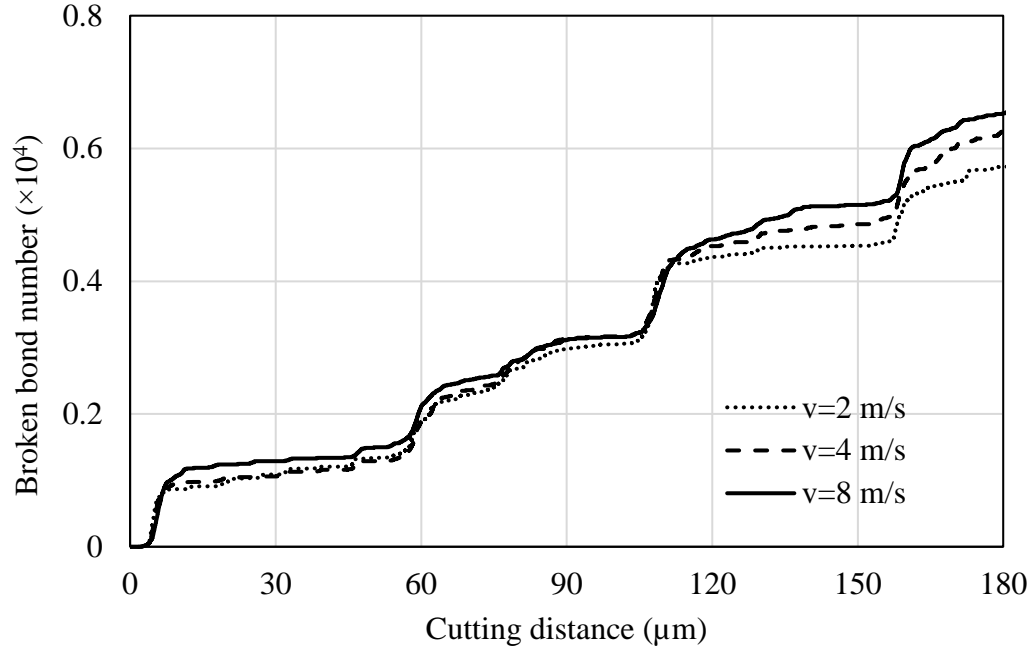


Figure 6.6. Evolutions of the number of broken bonds at different cutting speeds.

6.3.3 Effect of Cutting Depth on Cutting Force and Chip Morphology

Figure 6.7 shows the chip formation at different cutting depths (d) with a constant cutting speed of 2 m/s. When the cutting depth is small, i.e., 5 μm in Figure 6.7a, fine particles are formed, as discussed in Refs. [26, 153], it refers to a ductile failure mode. As the cutting depth is increased from 5 μm to 25 μm , as shown in Figure 6.7b, the chip morphology is changed from fine powder to small chunks combined with a fine powder, indicating a transition to a mixed ductile and brittle mode. For the large cutting depth of 75 μm , as shown in Figure 6.7c, the chunk-like chips are dominant, as mentioned in Refs. [26, 153] a brittle failure mode. Also in Figure 6.7c, it is noted that the ductile mode still exists at the crushing zone where the cutting tool and columnar grains are in contact.

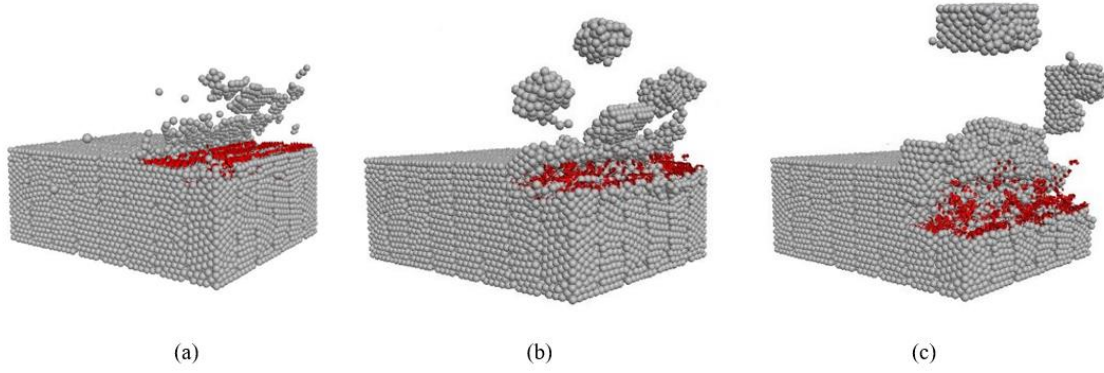


Figure 6.7. Chip formations at different cutting depths: (a) $d= 5 \mu\text{m}$, (b) $d= 25 \mu\text{m}$, and (c) $d= 75 \mu\text{m}$. The red color represents the broken bonds.

The DEM model results are consistent with the brittle-ductile transition failure mechanisms discussed in Refs. [25, 154]. The ceramic materials fail in the ductile mode when the cutting depth is small. As the cutting depth increases, the failure mode changes from the ductile to the brittle mode. A model based on the Griffith fracture criterion has been reported to predict the critical cutting depth d_c which predicts the ductile-to-brittle transition [22]:

$$d_c = \psi \frac{E}{H} \left(\frac{K_c}{H} \right)^2 \quad (5)$$

where E is Young's modulus, H is hardness, k_c is fracture toughness, and ψ is the material's brittle-ductile transition factor, which is varied for different brittle materials [22].

For typical ceramic materials including zerodur and silicon carbide, the material's brittle-ductile transition factor of 0.15 [155]. The ceramic hardness is assumed to be 3.3 GPa [156]. Using Equation 5, the calculated critical cutting depth d_c is $8.8 \mu\text{m}$. This calculated value is consistent with the DEM model results, that is, when the cutting depth is $5 \mu\text{m}$ in Figure 6.7a, which is less than the predicted critical cutting depth of $8.8 \mu\text{m}$, the dominant failure mode is the ductile mode.

Figure 6.8 shows the cutting force evolution at different cutting depths with a cutting speed of 2 m/s. The peak forces increase with the cutting depths. Take the first peak force values, for example, the peak force is increased from 0.31 N to 0.85 N when the cutting depth is increased from $5 \mu\text{m}$ to $75 \mu\text{m}$.

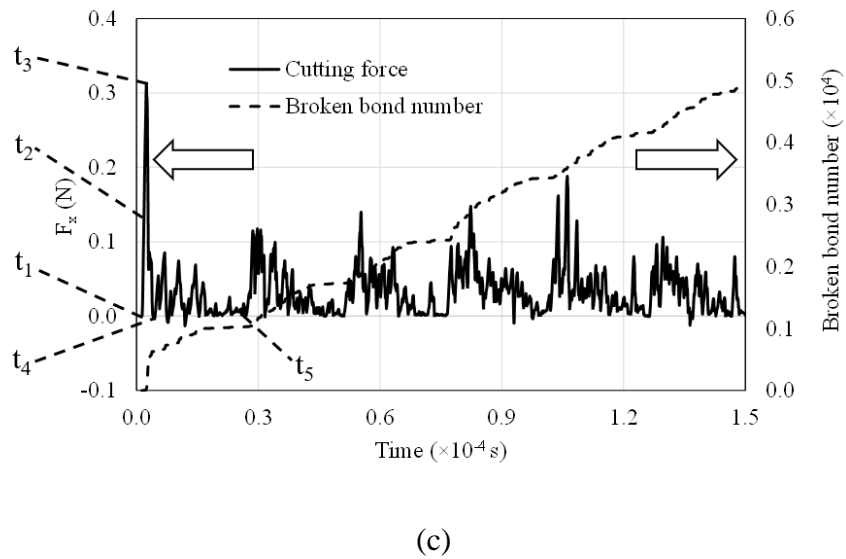
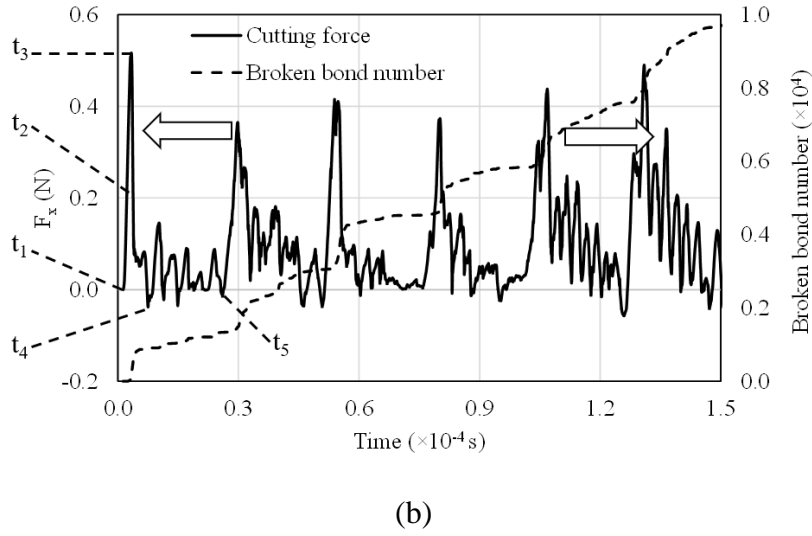
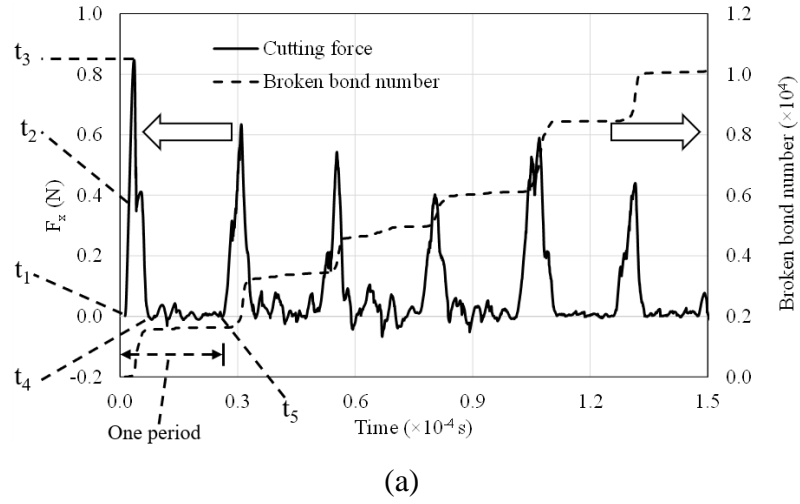


Figure 6.8. Horizontal cutting force (F_x) at different cutting depths: (a) $d = 5 \mu\text{m}$; (b) $d = 25 \mu\text{m}$; (c) $d = 75 \mu\text{m}$. $t_1 \sim t_5$ are the five key moments that will be discussed in Figure 9.

For all the cutting depths, the cutting forces oscillate during the orthogonal cutting process. The fluctuations consist of large periodic fluctuation and small periodic fluctuation. As mentioned in Refs. [26, 154, 157], the abruptly large fluctuation of cutting force is corresponding to the brittle failure mode, and the smaller fluctuation represents the ductile failure mode, which is observed in the ceramic cutting process in the experiments.

As shown in Figure 6.8a the period of large fluctuation is approximately 0.25×10^{-4} s, which corresponds to the time required to cut through a column grain. From Figure 6.8a through Figure 6.8a, with the increasing cutting depth, the large periodic fluctuations are more distinctive. As shown in Figure 6.8c, since the large periodic fluctuations are caused by the formation of chunk-like chips while the small periodic fluctuations are from the formation of fine powders, therefore, it demonstrates the transition from the ductile failure mode to brittle failure mode. Meanwhile, by comparing the cutting force at different cutting depths, the small periodic fluctuations follow the large periodic fluctuations, which correspond to the micro-cutting of a new surface after the chunk-like chip is broken off.

To better understand the cutting processes and failure mode, the cracks distribution and chips deformation at five key moments $t_1 \sim t_5$ labeled in Figure 6.8 are scrutinized. t_1 is the initial undeformed state; t_2 is the moment when the broken bonds firstly develop; t_3 is the moment corresponding to the first peak value; t_4 is the moment of the beginning of small force fluctuations, and t_5 is the moment corresponding to the end of the first period. It is concluded that only a few cracks come out for the first peak value and there is nearly no deformation in this stage. In the first period, most of the cracks occur between t_3 and t_4 , especially at large cutting depths. From the moments of t_4 and t_5 , the cutting chips keep falling with little new particles.

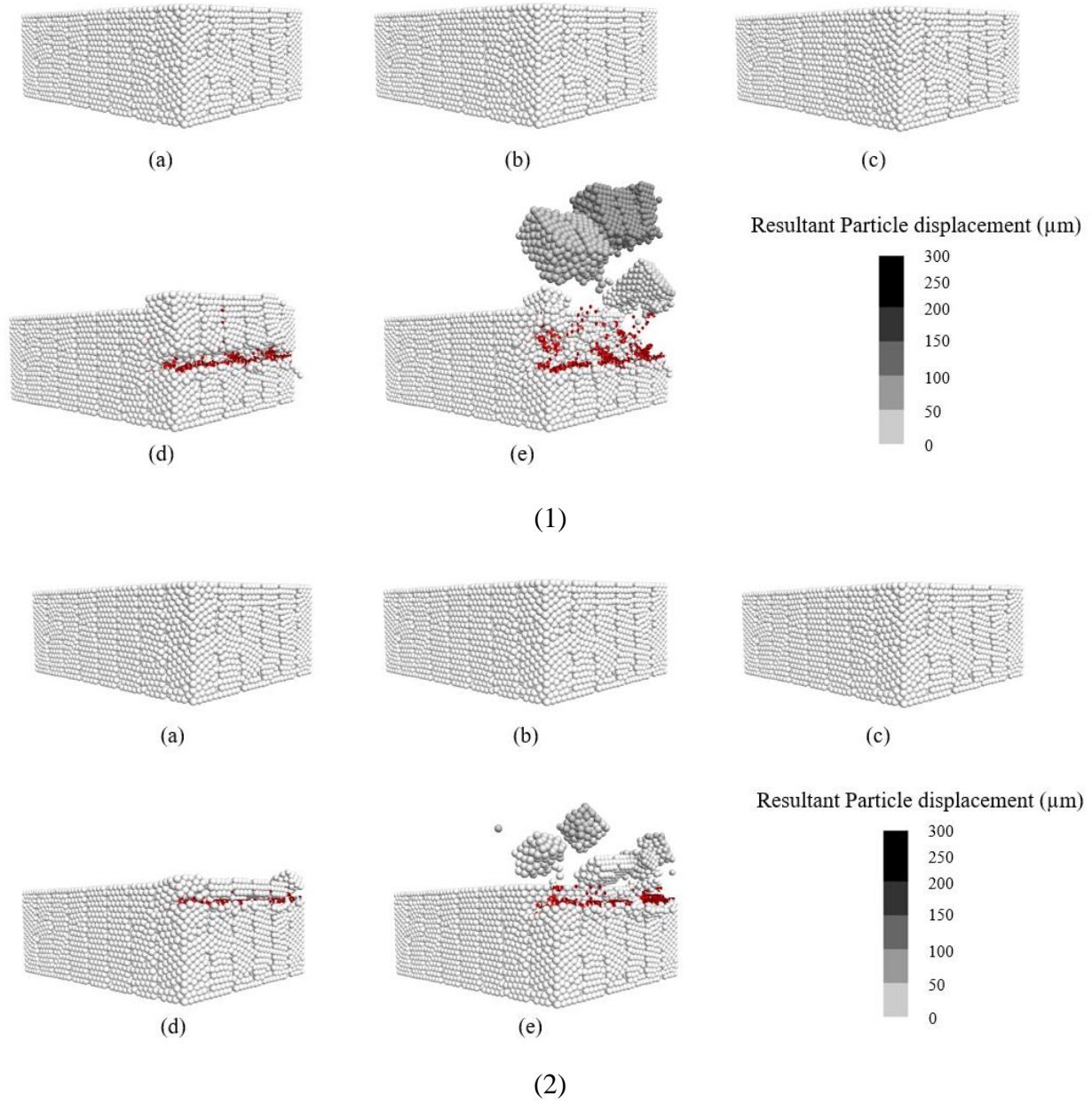
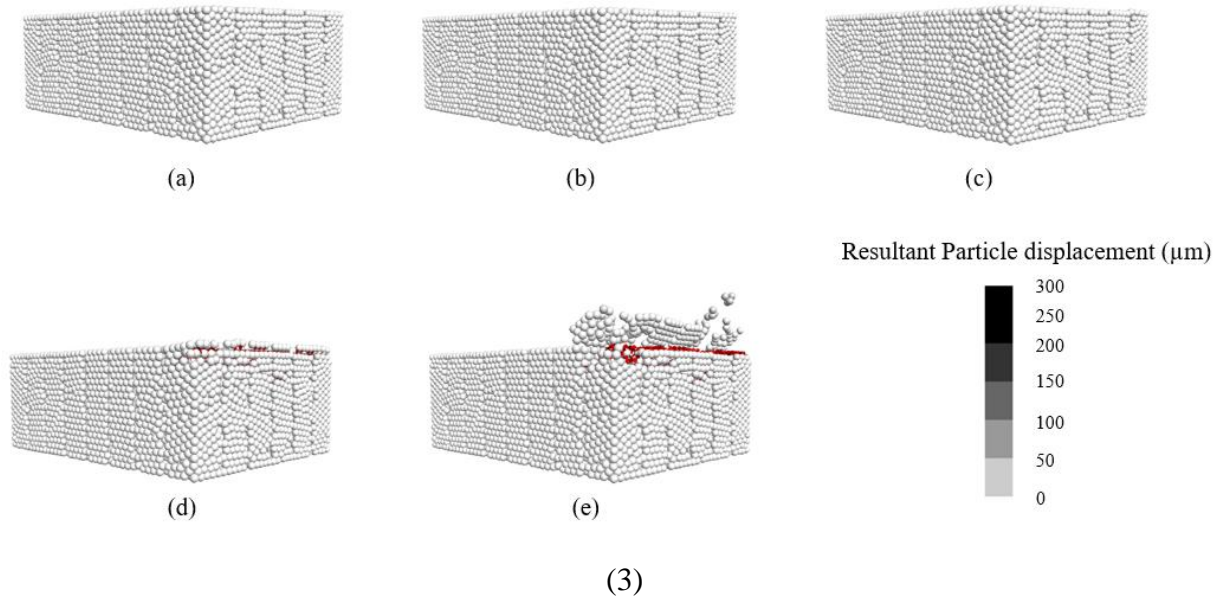


Figure 6.9. Cracks distribution and chips deformation at five key moments ((a) t_1 , (b) t_2 , (c) t_3 , (d) t_4 , and (e) t_5 .) for three cutting depths: (1) $d = 5 \mu\text{m}$; (2) $d = 25 \mu\text{m}$; and (3) $d = 75 \mu\text{m}$.

Figure 6.9 continued



The cutting process is further analyzed using the numbers of broken bonds. Figure 6.10 shows the evolutions of the numbers of broken bonds that increase with the cutting depths. By comparing the same time step as in Figure 6.8, it shows that the broken bond numbers jump at the peak forces, which corresponds to the formation of the chunk-like chips. For the large cutting depth of $75\ \mu\text{m}$, a step-wise curve is observed, and the bond number is unchanged afterward in the step. In comparison, a small cutting depth of $5\ \mu\text{m}$ shows a much smoother curve. The broken bond numbers agree well with the brittle and ductile failure modes, which further enforces the conclusion that there is a transition from the ductile to brittle mode with the increase of cutting depth.

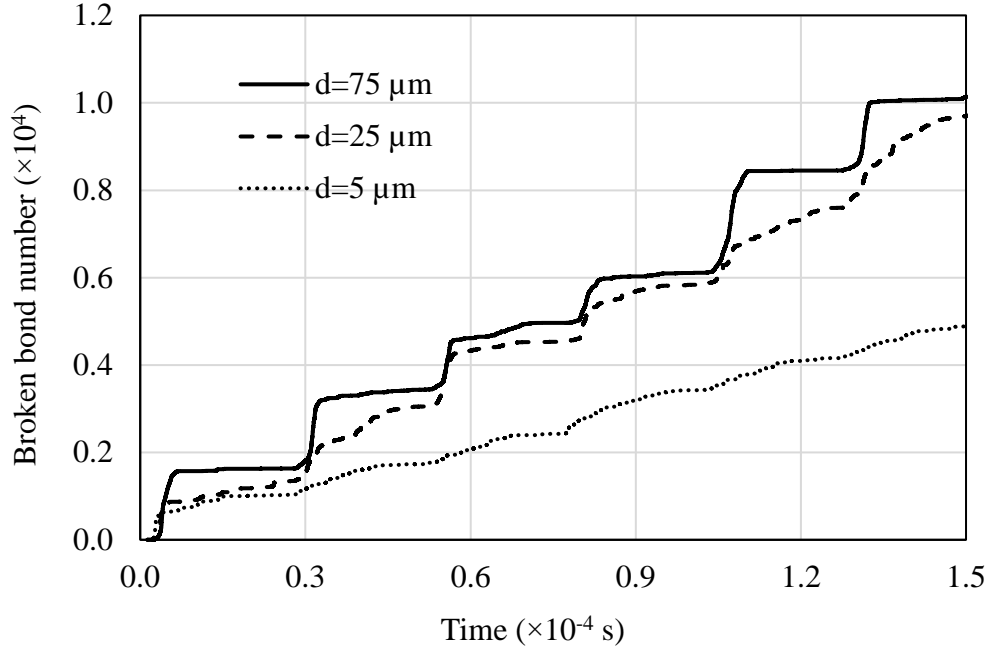


Figure 6.10. Evolution of the number of broken bonds under different cutting depths.

Figure 6.11 shows the cutting energy evolutions at different cutting depths. The cutting energy is calculated by integrating the cutting force over the cutting distance. The cutting energy evolution has a similar trend as the broken bond numbers in Figure 6.10. From the energy conservation principle, the consumed cutting energy or work is used to break the particles' bonds.

In addition, as shown in Figure 6.10, the broken bond number of the $75 \mu\text{m}$ case is about two times the broken bond number of $5 \mu\text{m}$. However, the cutting energy of $75 \mu\text{m}$ is about two-thirds of the cutting energy of $5 \mu\text{m}$, which means that the small cutting depth requires more cutting energy. It is because, at a small cutting depth, the bonds at both the cutting interface and within the ceramics need to be broken. While it is at a large cutting depth, due to brittleness of the ceramic coating, only the cutting interface between cutting tool and the ceramic needs to be broken [158].

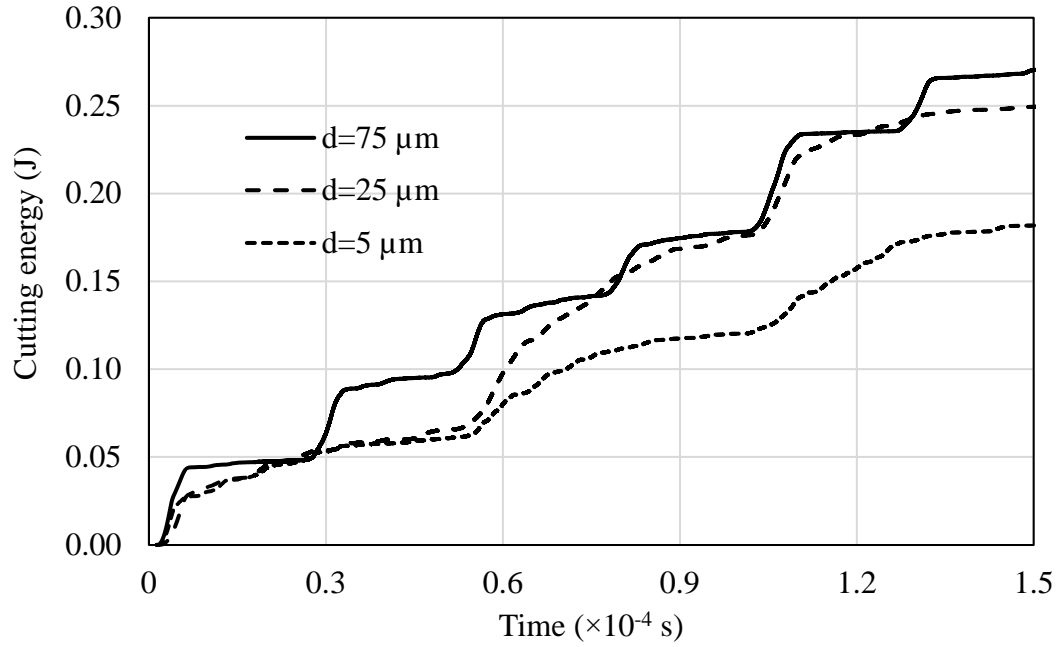


Figure 6.11. Evolution of cutting energy under different cutting depths.

Figure 6.12 shows the side views of the contact force distributions between the particles. From the side legend bars, the maximum contact force increases with the cutting depth. It is coincident with the cutting force increase applied by the cutting tool. At the same time, there are more contacts between the chips and column grains for the large cutting depth which affects the chip deformation mode.

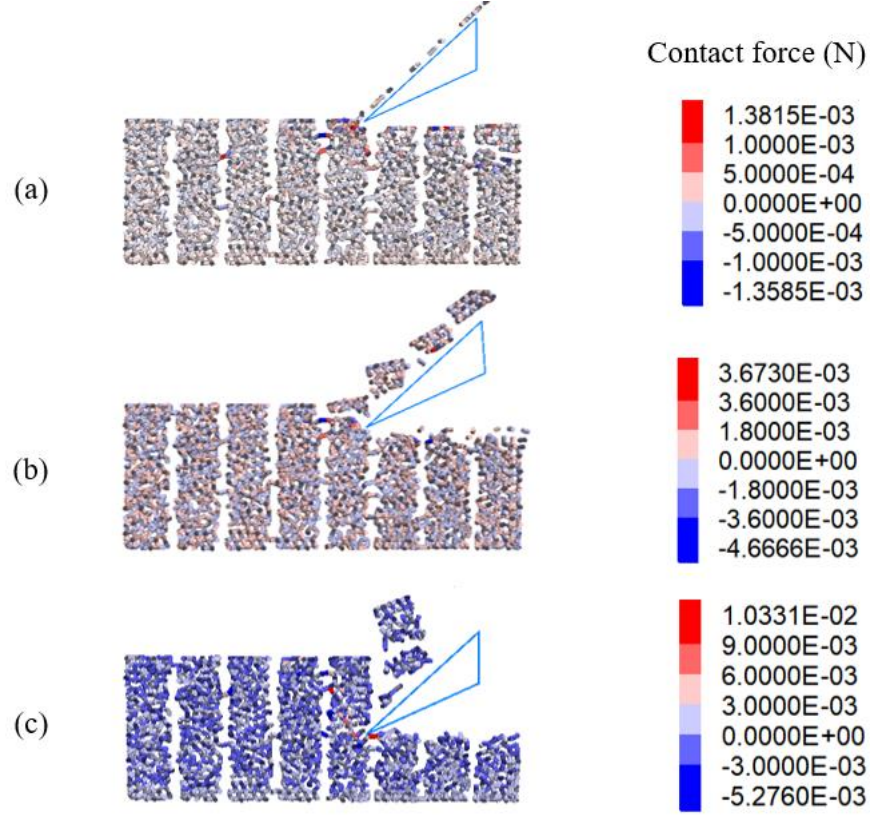


Figure 6.12. Side views of the cutting models where the contact forces between particles are shown.: (a) $d = 5 \mu\text{m}$; (b) $d = 25 \mu\text{m}$; (c) $d = 75 \mu\text{m}$.

6.3.4 Cutting Force and Cutting Speed Correlation

Liu et al. proposed an analytical solution based on brittle fracture mechanics [26]. In the model, the cutting force consists of two sources: the force of chip formation, F_c , and the friction force F_f between tool flank face and workpiece's machined surface [26]:

$$F_x = F_c + F_f = (k_{pi}\omega\sigma_p a_p \frac{d}{a_p}) + [y_0 + \frac{A}{\omega \times \sqrt{\pi/2}} e^{-2 \times (\frac{F_n - x_c}{\omega})^2}] \times [k_{pj}\omega\sigma_p a_p \frac{d}{a_p} \times \frac{1 - \cos 2\lambda}{\sin 2\lambda}] \quad (5)$$

where ω is the width of the workpiece; λ is the half-angle of the crush zone; a_p is the depth of the cut; k_{pj} is the force factor of F_p in the transverse directions; k_{pi} and k_{pj} are the force factors ranging $0 < k_{pi} \leq 1$, $0 < k_{pj} \leq 1$; F_x is the tangential cutting force; F_y is normal cutting force, F_f is the friction force between tool flank face and workpiece's machined surface; and d is the depth of the crush zone. In this study, the following parameters of zirconia ceramics are used: $y_0 = 0.57$, $A = 1.85 \times 10^5$, $k_{pi} = 1.1$, $k_{pj} = 0.62$, and $d = 0.055 \times a_p$ [26].

Both the DEM model and the above analytical solution are plotted in Figure 6.13. Both models show that the cutting forces increase linearly with the cutting depth. The DEM model shows an excellent agreement with the analytical solution, suggesting the cutting process primarily follows the fracture mechanics principles.

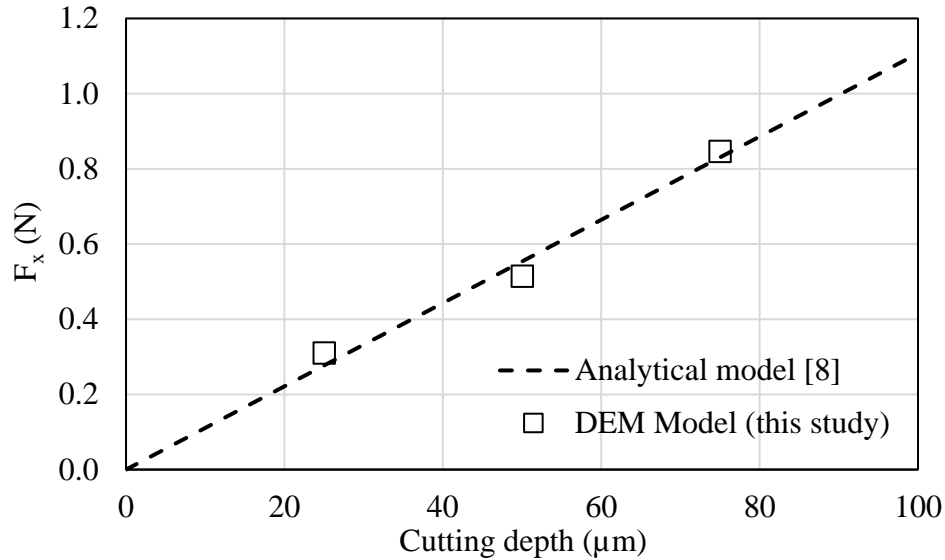


Figure 6.13. The DEM calculated cutting force at different cutting depths, compared with the analytical solution [26].

6.4 Summary

A new DEM for the thermal barrier coating cutting model has been successfully developed. The cutting processing parameters, cutting depth, and cutting speed, are studied. The major conclusions are summarized as follows:

1. During the coating removal process, a ductile-to-brittle transition depending on the cutting depth is identified. The transition occurs at the critical cutting depth based on the Griffith fracture criterion. At the small cutting depths, a ductile failure mode dominates the cutting process, leading to fine cut particles. As the cutting depth exceeds the critical cutting depth, a brittle failure mode is observed with chunk-like chips.
2. The evaluations of broken bonds and cutting energy show that a step-wise manner when the cutting depth is large, which is due to the brittle mode, while a smooth increase is observed in the small cutting depth because of the coating's ductile failure mode.

3. Due to the columnar grain structures of coating, the peak cutting forces show a periodic fluctuation, and the period is coincident with the width of the columnar grain.
4. The DEM model shows an excellent agreement with the analytical solution, in which the cutting force increases linearly with the cutting depth, suggesting the cutting process primarily follows the fracture mechanics principles.
5. The cutting speed has little effect on the cutting forces and chips morphology, which is due to the modeled ceramic material is not strain rate sensitive.

7. MODELING OF FAILURE MECHANISMS OF THERMAL BARRIER COATING WITH REALISTIC STRUCTURE USING DISCRETE ELEMENT METHOD

Abstract: In this work, a new DEM TBC model based on the real columnar structure was successfully developed. Based on the calibrated DEM model, an indentation test and three damage models were investigated. The deformations were consistent with the experiment results in previous literature. Within the DEM model, the TBCs' cracks' initiation and propagation processes under different damage modes were observed. The stress distributions under three different modes were calculated. The stress distribution area and the values increased from mode I to mode III, which are consistent with the impact momentum. For mode III, two different types: large particles at low velocities or smaller particles at higher velocities, were studied. The results show that the large particle with low velocities has a bigger impact zone and smaller particles at higher velocities caused higher stress. The DEM simulation results are consistent with the experiment result and could help deeply explain the failure mechanisms of TBC under the different impact momentum.

7.1 Introduction

Thermal barrier coating (TBC) was first applied to reduce the metal surface temperature more than fifty years ago. As a coating system, TBCs usually consists of the four layers a ceramic top coat, typically composed of yttria-stabilized zirconia (YSZ), a thin thermally grown oxide (TGO) layer, which acts as a protecting layer to retard oxygen diffusion and oxidation of the superalloy substrate, a metallic bond coat, typically composed of NiCoCrAlY and a Ni-base superalloy substrate [8]. Two main techniques are now widely used to manufacture the top layer coating: plasma spray deposition and EB-PVD (electron beam physical vapor deposition) [159]. For a high thermal loaded engine, EB-PVD coating with columnar grain structure is preferred. It has been proved that EB-PVD coating could result in significant improvement for coating durability [16]. However, TBCs meet a number of challenges during the period of operation process such as foreign object damage, erosion, oxidation, and sintering [160]. To evaluate the reliability and integrity of TBCs at high temperatures, it is critical to understand their plastic deformation behavior under loading. Indentation tests, which can be used to measure the hardness and plastic response of the TBC system, have been adopted to assess TBC performance[161]. Chen

et al developed a finite element model (FEM) indentation model with a columnar microstructure to explore the deformation behavior of TBC. The results indicate the indentation pressure is sensitive to friction coefficient between columns and their width but insensitive to the contact between the surface of TBC and indenter [162]. Makoto Tanaka and Yu-Fu Liu have done Rockwell indentation experimental and FEM test to identify the interface delamination in EB-PVD coating. The stress mapping in experiments and finite element analysis were compared, through which the size of the delaminated region, delamination crack front position, and delamination paths were presented [163]. Three erosion modes based on the dimension of the impact particles were reported by Chen et al where the impact processes were extracted as an indentation test. Three domains: domain I deeply penetrating plastic/densification zones, domain II shallow densified zones, and domain III an entirely elastic zone were determined according to the size of particle radius and column size [164]. The failure mechanism during EB-PVD TBCs' erosion process with non-uniform real morphology was presented by Yang et al. A series of indentation tests with uniform and non-uniform real structures were carried out to investigate the erosion behavior using FEM. Compared with the uniform structure, the non-uniform realstructure simulation results showed that it was more easier for the real morphology to be damaged [160].

In conclusion, the indentation test is an effective way to assess the mechanical properties of the TBC and the non-uniform real structure is preferable to the uniform columnar grain structure. However, most of the simulation models are based on uniform extracted structures and the conventional FEM method. In this paper, to overcome these limits, a non-uniform columnar grain structure from an SEM image is generated in DEM. With this non-uniform DEM model, the failure processes of TBCs with real morphology were simulated under three failure modes. The TBCs' cracks' initiation and propagation process will be observed and the stress distributions with different indentation depths will be also investigated. Meanwhile, three damage modes under three domains investigated in the previous reference [164] will be further studied based on the DEM model with real structure.

7.2 DEM Model

7.2.1 Geometrical Model

The DEM model used in this paper consisted of a top coat layer and a substrate layer. As shown in Figure 7.1, The EB-PVD coating layer was extracted from a scanning electron microscopy (SEM) image with non-uniform real morphology [140]. As shown in Figure 7.2, the thicknesses of the top layer and the substrate layer were 200 μm , and 800 μm , respectively and the width is 1028 μm [163]. The number of particle used in the model is 103374. The different sizes of impact particles are substituted with the rigid balls with radius 200 μm , and 50 μm individually.

To generate the real columnar grain structure, a grayscale-based image was generated from the SEM image through grayscale treatment using MATLAB code. By setting some pixel thresholds, a binary image could be obtained. Then import the binary image into the software Raster 2 Vector 5.x (R2V) and make the binary image vectorization. After that, save the file in dxf format which could be read by AutoCAD software. Revise morphology and improve the dimensions if it needs in the AutoCAD software before it is finally used to generate the DEM model. At last, the SEM image is transferred to a $[0, 1]$ digital image with values corresponding to each pixel and a matrix (F) with $m \times n$ dimensions can be generated in the following format [165]

$$F = \begin{bmatrix} f(0,0) & f(0,1) & \dots & f(0,n-1) \\ f(1,0) & f(1,1) & \dots & f(1,n-1) \\ \dots & \dots & \dots & \dots \\ f(m-1,0) & f(m-1,1) & \dots & f(m-1,n-1) \end{bmatrix} \quad (1)$$

The values of $f(i, j)$ in the matrix (F) for EB-PVD coating with real columnar grain structure were [165],

$$f(i,j) = \begin{cases} 0 & (\text{inter-columnar zone}) \\ 1 & (\text{columnar grain}) \end{cases} \quad (0 \leq i \leq m-1, 0 \leq j \leq n-1) \quad (2)$$

As shown in Figure 7.2, the non-uniform real structure geometric model is generated in a DEM model, which is the same as the real EB-PVD structure. The following simulations are based on this non-uniform real structure.

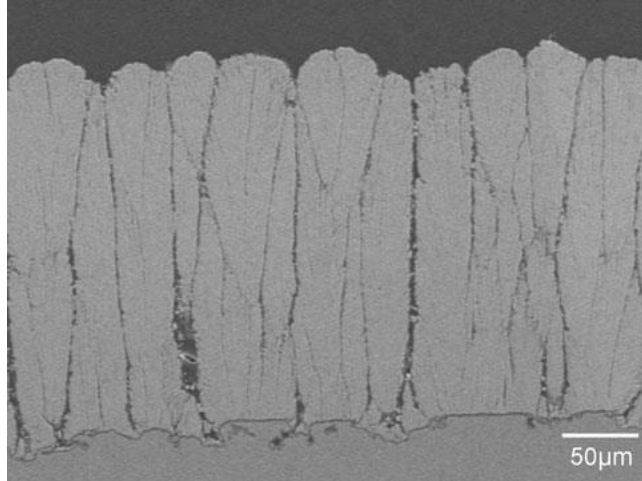


Figure 7.1. Cross-sectional microstructure of TBC system with columnar structure [166].

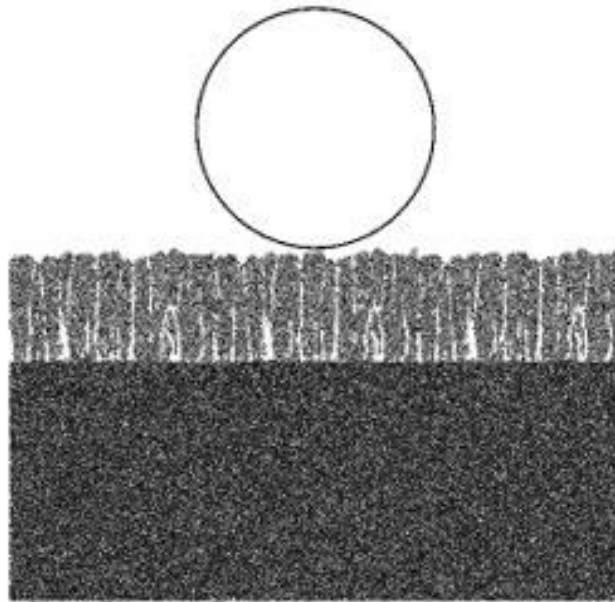


Figure 7.2. DEM model extracted from SEM image with realistic columnar grains and inter-columnar zone.

7.2.2 Governing Equations in DEM

DEM is a particle-scale numerical method for modeling the bulk behavior of granular materials proposed by Cundall and Strack [42]. In DEM, each particle is treated as a rigid 2D disc or 3D sphere. The particles are connected using contact bonds. For different material, selecting the proper bond is very critical for the simulation. Particle motions obey Newton's second law [43]:

$$m_i \frac{dv_i}{dt} = \sum_{j=1}^{k_i} (F_{c,ij} + F_{d,ij}) + m_i g \quad (3)$$

$$I_i \frac{d\omega_i}{dt} = \sum_{j=1}^{k_i} T_i \quad (4)$$

where v_i and ω_i are the vectors of the linear and angular velocities of an i th particle, respectively m_i is the weight; I_i is inertia; $F_{c,ij}$ is the contact force of particle j to particle i , $F_{d,ij}$ is the damping force between particle j and i , and T_i is the resultant force moment.

In this paper, the parallel bond model is selected as the DEM contact model. The parallel bond model, proposed by Potyondy and Cundall [143], is a bonding model that enables the specification of tensile and shear strengths. The moment transfer/resistance is caused by the normal and tangential components of the contact force [143]. The parallel bond can be envisioned as a set of elastic springs with constant normal and shear stiffness, \bar{k}_n and \bar{k}_s , and it is always active if it is bonded or if the surface gap is less than or equal to zero [144]. By changing the particle size and the parameter of the parallel bond, the parallel bond model can be used to simulate the mechanical response in TBCs [145]. The contact force and moment are calculated as [143]:

$$F = (F_n + \bar{F}_n) \cdot \hat{n} + F_s + \bar{F}_s \quad (5)$$

$$M = \bar{M} \quad (6)$$

where the parallel bonds are delineated with bar accents and the subscripts n and s indicate the normal and shear direction, respectively. F_n and F_s encompass the contributions of the linear springs and viscous dashpots. The parallel bond will be failed while the applied force is higher than its strength. While the bond failure happens, the bond state will be transferred to a non-bonded state, which means that the particles can bear only compression and friction [146].

7.2.3 Model Calibration

To determine the parameters in the DEM parallel bond model, a model parameter calibration study is first conducted. In general, the mechanical properties of a TBC can be determined by its elastic modulus, unconfined compressive strength, Poisson's ratio, tensile strength, and fracture toughness [25]. Using these macroscopic properties, the corresponding DEM particle and contact parallel bond model parameters can be derived [25, 147].

In this work, three mechanical tests are simulated to calibrate the DEM particle and contact model parameters, as shown in Figure 6.1, including (a) uniaxial compression test; (b) uniaxial tensile test, and (c) fracture toughness test, following Ref. [147]. The parameters in the parallel

bond model are tuned, such that the simulated macroscopic mechanical properties match the experimental data, which are listed in Table 7.1[148-150].

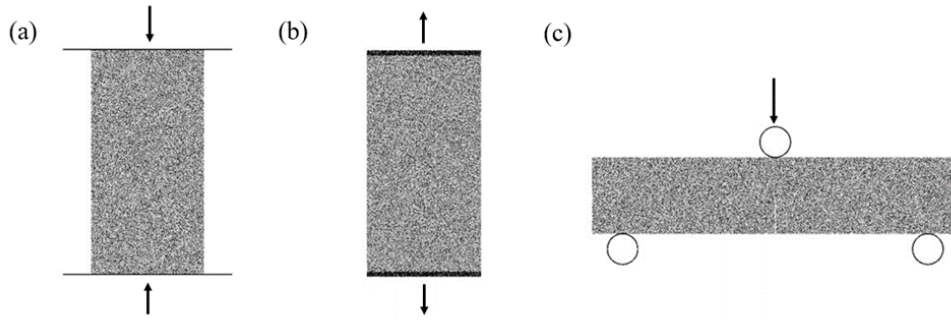


Figure 7.3. DEM model parameter calibration tests: (a) uniaxial compression test; (b) uniaxial tensile test, and (c) fracture toughness test.

As shown in Figure 7.3, the uniaxial compression test was carried out by moving two rigid walls to the specimen. The tensile test was done by moving two boundary layers at the end to the opposite direction. The height of specimens used for compression and tensile tests was two times of their width. The fracture toughness test was carried out through a three-point bending test with the specimen with a notched at the bottom center. The depth of the notch is half of the height of the specimen. All the specimens used were assembled by the particles with a particle radius of 5 μm [145].

Table 7.1. Calibrated mechanical properties of the EB-PVD ceramic coating from the experimental data in literature [148-150] and the simulated DEM results from this study

Mechanical properties (unit)	Experimental macroscopic data [148-150]	Simulated DEM modeling results (this study)
Elastic modulus (GPa)	40	41
Poisson's ratio	0.2	0.2
Compression strength (MPa)	510	513
Tensile strength (MPa)	22.3	22.4
Fracture toughness ($\text{MPa}\sqrt{m}$)	2.05	2.03

7.2.4 Fracture Criterion

Ceramics are generally brittle due to the difficulty of dislocation motion or slip. Even there is only a small plastic deformation, which separates the material into two, the brittle failure or the fracture comes out. The material failure happens while the maximum normal stress exceeds the strength of the material in any direction of the brittle material [167]. To obtain the principal stresses at critical points, the 1st principal distributions under different failure modes were calculated.

7.3 Results and Discussion

7.3.1 Indentation Test

An indentation test based on the experiment was set up in the DEM model (Figure 7.4). The Rockwell brale C indenter with a tip radius of 200 μm was used for the indentation test [6]. As shown in Figure 7.5a various damages, such as TBC columnar bulking, TBC cracks, and a densified zone, were observed in the DEM indentation test. On the other hand, the delamination occurred in the interface between the TBC layer and the substrate layer. These observations are similar to the experimental phenomenon as shown in Figure 7.5b. The test results further validated the DEM models.

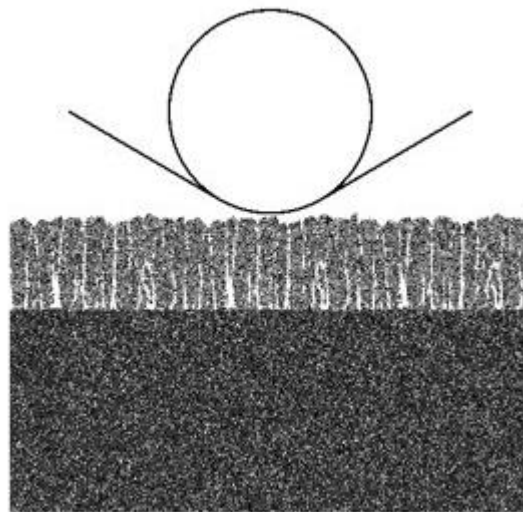
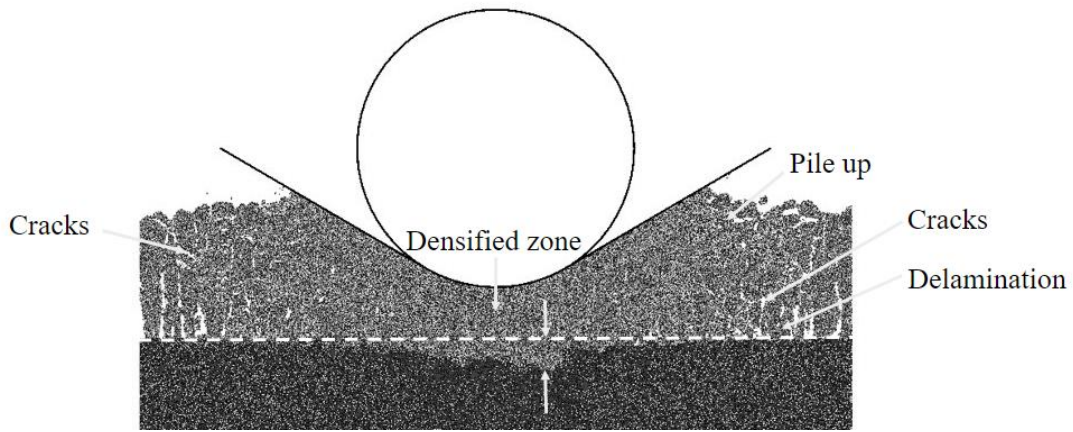
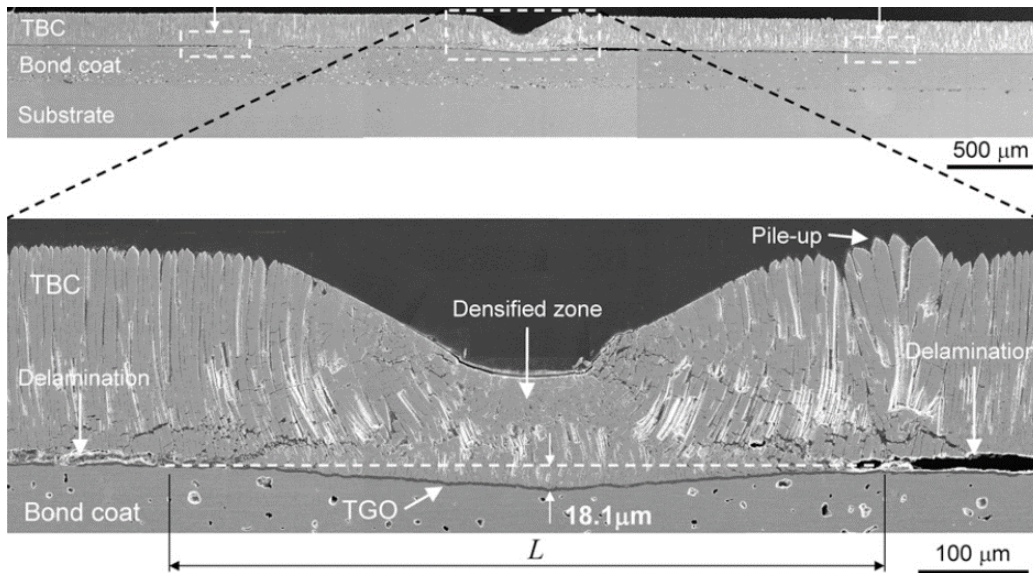


Figure 7.4. Indentation test DEM model [163].



(a)



(b)

Figure 7.5. Indentation test results: (a) DEM model; (b) experiment result [163].

7.3.2 Mode I - Erosion (Near Surface Cracking/Lateral Cracking)

As illustrated in Figure 7.6, mode I refers to the small particle impact and the surface region, the top 20 μm , of the individual columns, and a number of neighboring columns are cracked [164].

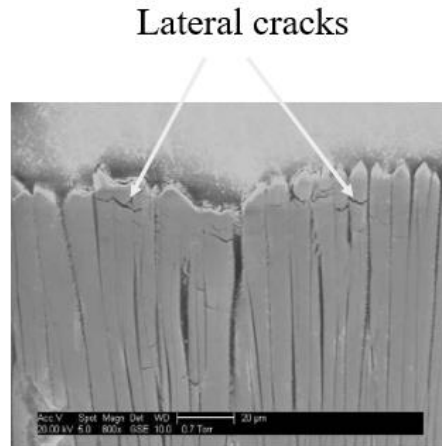


Figure 7.6. Cross-section of an eroded sample of TBCs showing mode I(near-surface cracking) mode [164].

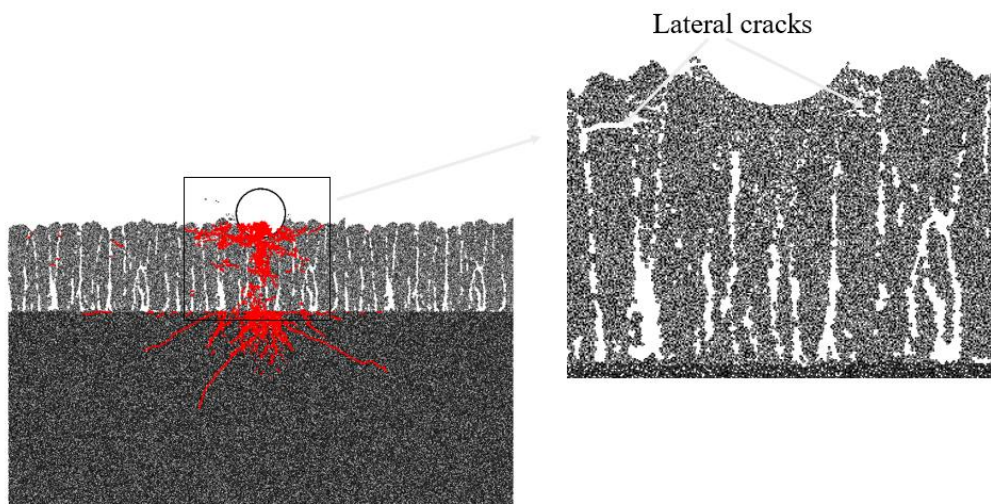


Figure 7.7. Crack distribution and TBC deformations of DEM model corresponding to mode I.

Crack distribution and TBC deformations of the DEM model corresponding to mode I (impact particle radius 50 μm) are shown in Figure 7.7. Similar to the experimental results, the micro-cracks initiated from the impact particle and columns' interface and the lateral joint crack occurred on both sides of the impact particle. The stresses distribution corresponding to this mode is shown in Figure 7.8. It can be seen that the area affected by the impact fore was small, which concentrated around the impact particle. In this mode, the damage of EB-PVD coating show only elastic and

parallel cracks close to the surface, which are caused by tensile stress generated by the forward and backward propagating elastic waves among each columnar grain around the impact site [168].

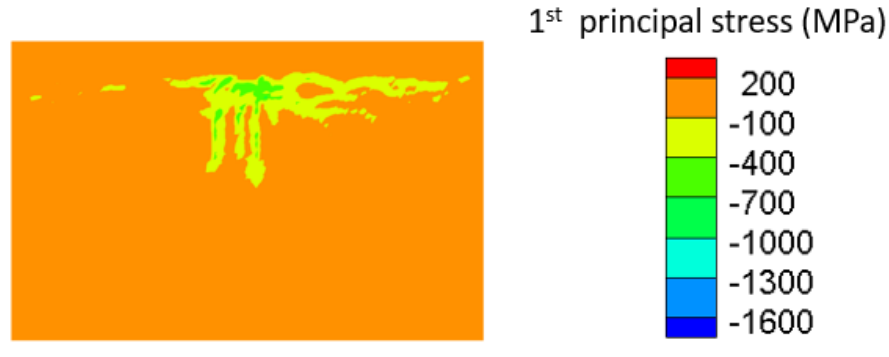


Figure 7.8. 1st principal stress distribution with mode I.

7.3.3 Mode II - Compaction Damage

As shown in Figure 7.9, mode II is a transition mode between mode I and mode III, where the compaction of the columns occurs. Due to the slightly high momentum of the impact particles, compared with the impact particle in mode I, densification is observed in the shallow top layer of TBC. Even though, no joint cracks occur. The deformation is dominated by plastic deformation. Crack distribution and TBC deformations of the DEM model corresponding to mode II (impact particle radius 200 μm) are shown in Figure 7.10. Similar to the experimental results, a compact zone, which is a densification layer, came out under the impact particle., cracks can nucleate and propagate at the interface between the densified layer and its underlying columns. The stresses distribution corresponding to this mode is shown in Figure 7.11, the affected domain by the impact particle is larger than the previous mode. A stress concentration induced by the impact particle came out, which is the reason for the formation of the densified layer.

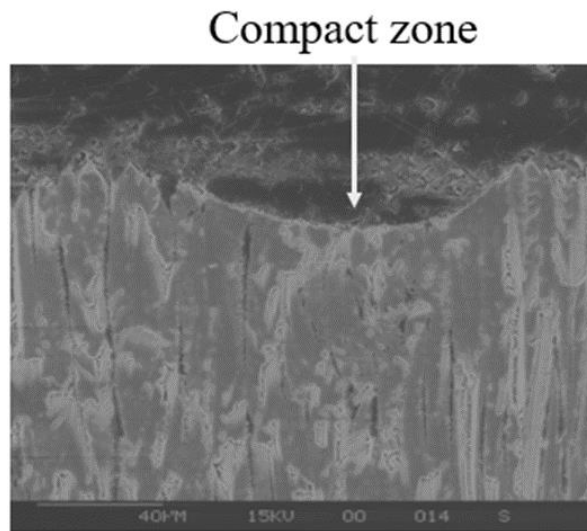


Figure 7.9. Cross-section of an eroded sample of TBCs showing mode II (compaction damage) mode [164].

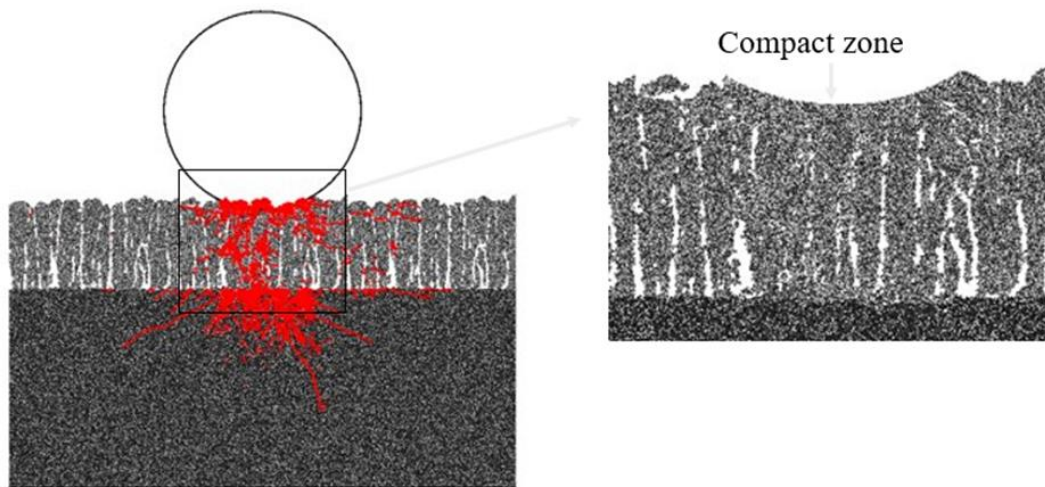


Figure 7.10. Crack distribution and TBC deformations of DEM model corresponding to mode II.

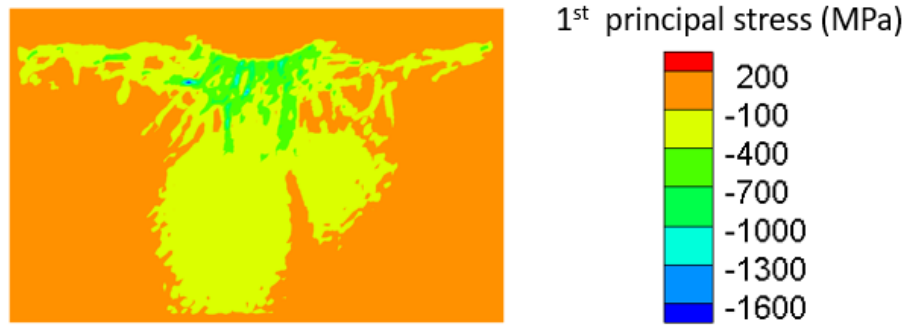


Figure 7.11. 1st principal stress distribution with mode II.

7.3.4 Mode III - Foreign Object Damage

As shown in Figure 7.12, mode III (foreign object damage) is caused by impact particles with high momentum, which are usually large particles traveling at low velocities or smaller particles at higher velocities. In this mode, the deformation came out in the form of the densified zone under the impact particle and crack band around the perimeter of the plastic zone. To mimic the large impact particle impact, the Rockwell brale C indenter with a tip radius of 200 μm was selected. Crack distribution and TBC deformations of the DEM model corresponding to mode III are shown in Figure 7.13 and Figure 7.5a. The simulation results show similar phenomena with the experimental results. Crack bands were formed around the perimeter of the plastic zone. A densified zone came out under the impact particle. The stresses distribution corresponding to this mode is shown in Figure 7.14, the affected domain by the impact particle is the largest. The deformations came out from both the TBC and the substrate. Similar to the experimental results, part of the TBC layer was pushed into the substrate. To mimic the small particle impact with high velocities, the same model but with a high velocity was selected (Figure 7.15). The stresses distribution corresponding to this mode is shown in Figure 7.16. Compared with the large particle with lower velocity, the small particle with high velocity caused high stress. In addition, more cracks occurred compared with the small particle with low velocity in mode II. A thicker densified zone came out and nearly all the columnar grain on the bottom were damaged.

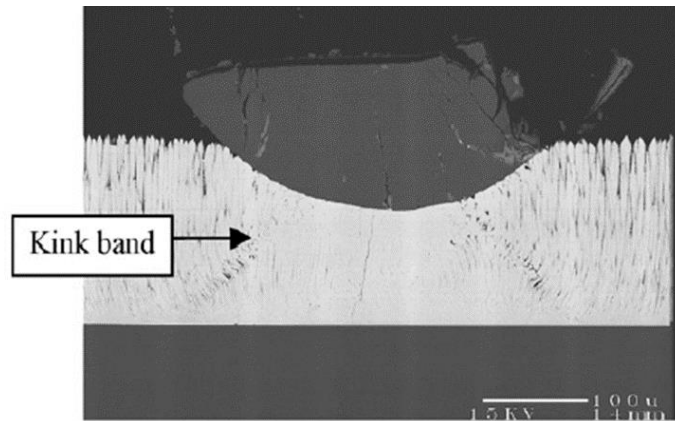


Figure 7.12. Cross-section of an eroded sample of TBCs showing mode III (foreign object damage) mode [164].

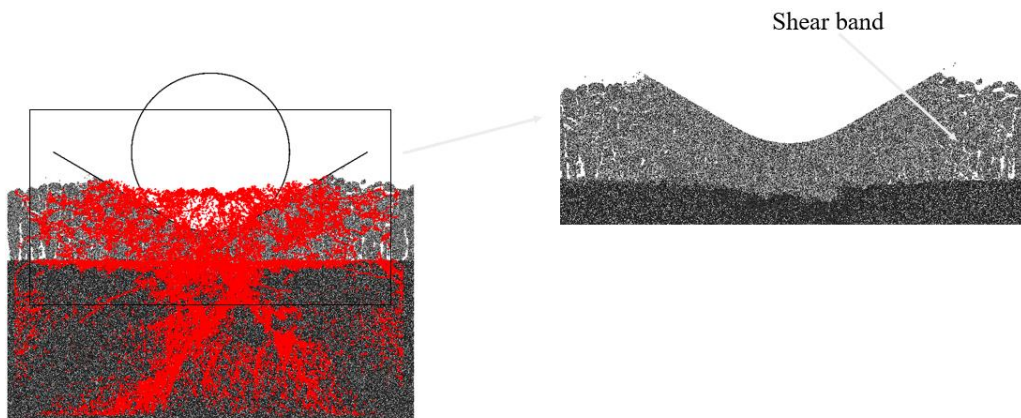


Figure 7.13. Crack distribution and TBC deformations of DEM model corresponding to mode III.

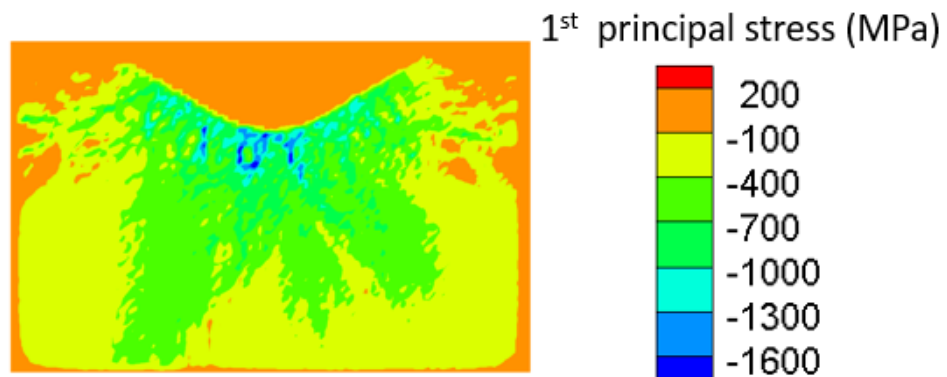


Figure 7.14. 1st principal stress distribution with mode III.

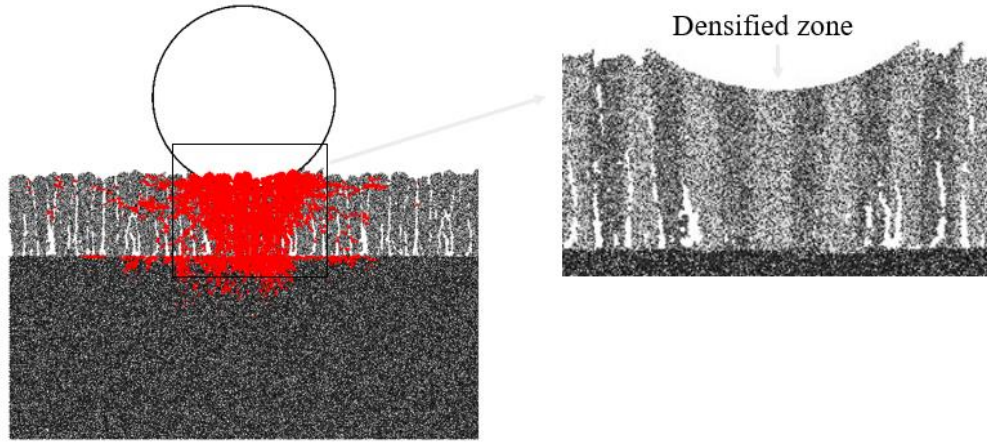


Figure 7.15. Crack distribution and TBC deformations of DEM model corresponding to mode III.

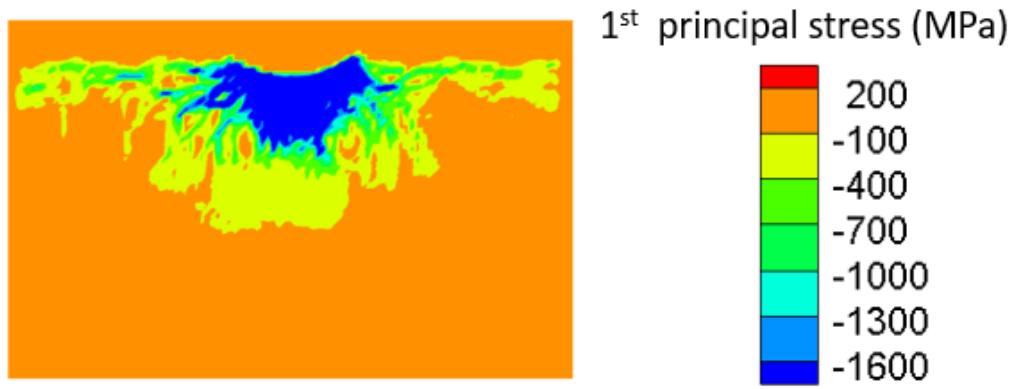


Figure 7.16. 1st principal stress distribution with mode III.

7.4 Summary

A new DEM TBC model based on the real columnar structure was successfully developed. Based on the calibrated DEM model, an indentation test and three damage models were investigated. The deformations were consistent with the experiment results in previous literature. The major conclusions are summarized as follows:

1. Within the DEM model, the TBCs' cracks' initiation and propagation processes under different damage modes and indentation tests were observed. The deformations in the simulations were consistent with the experiment results.

- Cracks came out from the top surface of each column in mode I, and the columns remain separate.
 - The compaction zone with micro-cracks came out in model II, which is usually close to individual columns.
 - The column deformation, kink bands, and cracks came out in mode III.
2. The 1st principal stress distributions under three different modes were calculated. The stress distribution area and value increased from mode I to mode III, which is consistent with the impact momentum.
 3. The DEM simulation results are consistent with the experiment result and could help deeply explain the failure mechanisms of TBC under the different impact momentum.

8. FRACTURE MECHANISM MAP FOR CERAMIC MACHINING

Based on the particle-based coating removal modeling framework results, this chapter proposes a new coating fracture mechanism map, which correlates the processing parameters and coating fracture modes.

For a fixed grinding wheel, a maximum cutting depth h_m (undeformed chip thickness) is derived, which primarily depends upon grinding parameters. The derived equation is expressed as [169]:

$$h_m = \left[\frac{3}{C \tan \theta} \left(\frac{V_w}{V_s} \right) \left(\frac{a}{d_s} \right)^{1/2} \right]^{1/2} \quad (1)$$

where h_m is the undeformed chip thickness; C is the number of cutting points per unit area; θ is the semi-included angle for the undeformed chip cross-section, d_s is the wheel diameter, V_w is the workpiece feed rate, V_s is the wheel speed and a is the wheel depth of cut.

As mentioned in Chapter 6 Eq. (5), a model based on the Griffith fracture criterion has been reported to predict the critical cutting depth d_c , which predicts the ductile-to-brittle transition. For brittle ceramics, the h_m should be smaller than the d_c in ductile grinding mode. The transition point is h_m is equals to d_c . The brittle mode happens while h_m should be higher than d_c . Based on these two criteria, a fracture mechanism map is proposed (Figure 8.1) for a fixed grinding wheel which correlates the processing parameters and coating fracture modes. V_c is defined as the wheel speed corresponding to the transition point where h_m is equals to d_c . For a fixed grinding wheel C equals 20; θ equals to 60° , d_s equals to 125 mm, V_w equals to 500 mm/min, and a equals to 100 μm [31, 170].

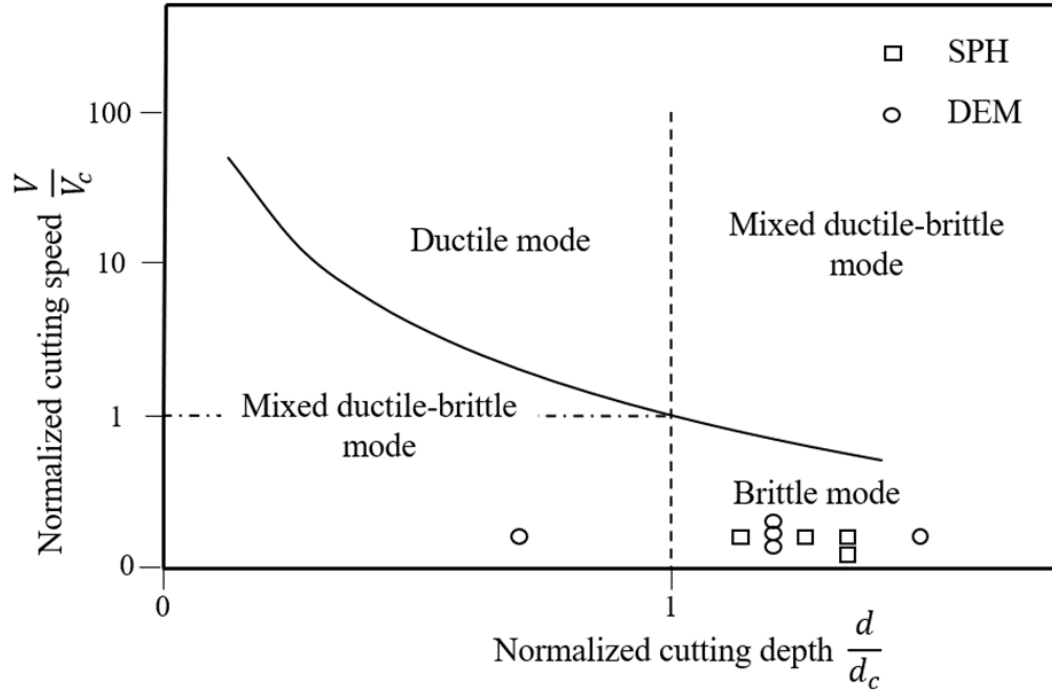


Figure 8.1 Fracture mechanism map for ceramic machining: processing parameters vs fracture mode.

A reduction in cutting depth and an increase in cutting speed can change the failure mode from brittle to ductile. To increase manufacturing efficiency, the proper machining parameters are critical. By decreasing the workpiece feed rate V_w and the wheel depth of cut a . However, it will reduce the productivity of the process. As a result, different parameter combinations should be chosen without compromising productivity.

As shown in Figure 8.1, the newly proposed coating fracture mechanism map provides a guideline for predicting three fracture modes, i.e., ductile, brittle, and mixed ductile-brittle, as a function of processing parameters, including cutting depth and cutting speed. The map can be used to determine the processing conditions based on required TBC removal operations: rough cut (brittle mode), semi-finish (mixed ductile-brittle mode), and finish (ductile mode). The brittle mode can be selected for a rough cut, the mixed ductile-brittle mode can be selected for semi-finish, and the ductile mode can be selected for a final finish.

9. CONCLUSIONS AND FUTURE WORK

9.1 Conclusions

The final conclusions of the TBC removal processes simulated using the SPH and DEM methods are summarized below.

1. The high-velocity particle impact TBC process is simulated using the SPH method. The effect of the impacting particle's inclined angle and velocity changes are studied. The morphology changes of the impact pit and impacting particles, and their associated stress and energy are presented.
 - Increasing impact velocity or reducing impact angle increases the penetration depth and area. The penetration depth is determined by the vertical velocity component difference between the particle and the coating layer, in a linear relation.
 - During the impact process, the coating's total energy increases gradually while the internal energy increases with the time after some peak values. At the end of impact, the coating's total energy increases with the increasing impact velocity but decreases with increasing impact angle. It is consistent with the deformations of the coating layer and spherical particles.
2. The AWJ TBC removal process is simulated using the SPH method. The simulation results are compared with the experiment results. The effects of abrasive particle concentration, incident angle, and drilling time are studied.
 - The increase of the abrasive particle concentration from 1% to 3% causes more damaged particles and increases the removal ratio of TBCs.
 - The depth of the impact pit hole increases with the increase of the incident angle from 30° to 90° while the width of the impact hole decreases. The depth of the impact pit hole increases linearly with the increase of the magnitude of the vertical velocity component.
 - Both the width and depth of the impact pit hole increase with the increase of the drilling time. The damaged particles increase linearly with the increasing drilling time and the increase of the kinetic energy.

3. The TBC surface grinding process is simulated using the orthogonal cutting model by the SPH method. The cutting model is built on the real microstructure of EB-PVD coating. The effect of factors: cutting tool geometry, cutting rake angle, cutting depth, and cutting speed, is investigated.
 - The cutting tool with edge radius $R=10\text{ }\mu\text{m}$ causes higher effective stress, reaction force, and temperature. The surface roughness with the cutting tool edge radius $R=0\text{ }\mu\text{m}$ is much better. The main reaction force F_x decreases when the rake angle increases from 11.6° to 26.6° .
 - The main cutting force F_x and temperature increases with the increase of the cutting depth. The simulation results are consistent with the main cutting force F_x calculated with the equation based on fracture mechanics. The cutting speed of 5 m/s has a higher main cutting force F_x and temperature. More chips are cumulated along with the tool/chip interface under the cutting speed of 2.5 m/s.
4. The TBC surface grinding process is simulated using the orthogonal cutting model by the DEM method. The cutting model is built on the real microstructure of EB-PVD coating. The effect of factors: cutting depth, and cutting speed, is investigated.
 - As the cutting depth increases, the ceramic failure mode shifts from ductile failure mode to brittle failure mode. The powdery chips (ductile mode) came out when the cutting depth is shallow and chunk-like chips (brittle mode) come when the depth is deep.
 - The calculated value of the critical cutting depth $8.8\text{ }\mu\text{m}$ based on the Griffith fracture criterion is consistent with the DEM simulation results. The cutting force increases with the increasing cutting depth, and it is validated by the analytical solution from previous literature. Compared with cutting depth, the cutting speed has nearly no effects on the cutting forces and chips formation.
 - The broken bond number and energy evolution reflected and proved the failure mode shift. The broken bond number and energy had an abrupt increase when the brittle failure came out. For ductile mode, both of them increased linearly.
 - Due to the special columnar structure of EB-PVD TBCs, the peak force fluctuations were periodic, and it was coincident with the length of one small cubic column.

5. A new DEM TBC model based on a real columnar structure was successfully developed. Based on the calibrated DEM model, three damage models were investigated.
 - Within the DEM model, the TBCs' cracks' initiation and propagation processes under different damage modes and indentation tests were observed. The deformations in the simulations were consistent with the experiment results.
 - The top surface of the individual columns is cracked due to the impact in mode I and the columns remain separate.
 - The compaction zone with micro-cracks came out in model II, which is most in the form of the densification of the near surface individual columns.
 - The deformation of the columns, shear bands and extensive cracking of the TBC ceramic came out in mode III.
 - The 1st principal stress distributions under three different modes were calculated. The stress distribution area and value increased from mode I to mode III, which is consistent with the impact momentum.
 - The DEM simulation results are consistent with the experiment result and could help deeply explain the failure mechanisms of TBC under the different impact momentum.
6. A new coating fracture mechanism map is proposed based on the particle-based coating removal modeling framework results, which correlates the processing parameters and coating fracture modes.
 - The newly proposed coating fracture mechanism map provides a guideline for predicting three fracture modes, i.e., ductile, brittle, and mixed ductile-brittle, as a function of processing parameters, including cutting depth and cutting speed. The map can be used to determine the processing conditions based on required TBC removal operations: rough cut (brittle mode), semi-finish (mixed ductile-brittle mode), and finish (ductile mode).

9.2 Contributions of the Thesis Work

The major contributions of the thesis work are summarized as follows:

1. A new fracture mechanism map is proposed, which correlates the processing parameters and coating fracture modes. It can be used to as a guideline to determine the processing conditions based on required TBC removal operations.

2. The SPH high-velocity particle impact model and the SPH AWJ model provide a design tool to optimize the coating removal process.
3. The uniform columnar grain structures, in both the SPH and DEM cutting models, are capable to examine the unique effects of the processing parameters, which are not available in the bulk coating model.
4. The non-uniform realistic columnar grain structure in the DEM model allows understanding the failure mechanisms under different impact momenta.

9.3 Future Work

The particle-based models developed in this work have technological importance. There are still several areas that can be improved in the future.

1. The study in this thesis is mainly focused on the grinding and AWJ removal processes and most of the models in this thesis neglect the temperature effects and non-uniform characteristics of columnar grain structures. The coupled mechanical and thermal approaches can be considered.
2. Non-uniform columnar grain structures reconstructed with 3D images can be explored.
3. Emerging methods such as the machine learning-based approach to optimize the removal process can be studied.
4. In-depth theoretical analyses and direct experimental validations are suggested.

REFERENCES

- [1] C. U. Hardwicke and Y.-C. Lau, "Advances in thermal spray coatings for gas turbines and energy generation: a review," *Journal of Thermal Spray Technology*, vol. 22, no. 5, pp. 564-576, 2013.
- [2] D. Zhu and R. A. Miller, "Development of advanced low conductivity thermal barrier coatings," *International Journal of Applied Ceramic Technology*, vol. 1, no. 1, pp. 86-94, 2004.
- [3] S. Kumar, S. Kant, N. Suri, and R. Verma, "Effects of thermal barrier coatings on diesel and gas turbine engines: a review," *International Research Journal of Engineering and Technology*, vol. 3, no. 6, pp. 134-139, 2016.
- [4] G. Thomas and K. Rangaswamy, "Strengthening of cement blended soft clay with nano-silica particles," *Geomechanics and Engineering*, vol. 20, no. 6, pp. 505-516, 2020.
- [5] Thermal barrier coatings market research report
(<https://www.researchandmarkets.com/reports/4829823/thermal-barrier-coatings-market-research-report>; accessed 11/06/2020).
- [6] S. Shahsavani, A. H. Vakili, and M. Mokhberi, "The effect of wetting and drying cycles on the swelling-shrinkage behavior of the expansive soils improved by nanosilica and industrial waste," *Bulletin of Engineering Geology and the Environment*, vol. 79, pp. 4765-4781, 2020.
- [7] Global thermal barrier coatings market by 2025
(https://www.coatingsworld.com/contents/view_market-research/2018-09-07/global-thermal-barrier-coatings-market-to-surpass-2279-million-by-2025/; accessed 9/10/2019).
- [8] X. Yang et al., "Removal and repair techniques for thermal barrier coatings: A review," *Transactions of the IMF*, vol. 98, no. 3, pp. 121-128, 2020.
- [9] K. P. Jonnalagadda, "Thermal barrier coatings: failure mechanisms and life prediction," Linköping University Electronic Press, 2019.
- [10] R. Darolia, "Thermal barrier coatings technology: critical review, progress update, remaining challenges and prospects," *International materials reviews*, vol. 58, no. 6, pp. 315-348, 2013.

- [11] C. G. Levi, J. W. Hutchinson, M.-H. Vidal-Sétif, and C. A. Johnson, "Environmental degradation of thermal-barrier coatings by molten deposits," *MRS bulletin*, vol. 37, no. 10, pp. 932-941, 2012.
- [12] M. Murugan, A. Ghoshal, M. J. Walock, B. D. Barnett, M. S. Pepi, and K. A. Kerner, "Sand particle-Induced deterioration of thermal barrier coatings on gas turbine blades," *Advances in Aircraft and Spacecraft Science*, vol. 4, no. 1, p. 037, 2017.
- [13] S. Ghosh, "Thermal barrier ceramic coatings—A review," *Adv. Ceram. Process*, pp. 111-138, 2015.
- [14] N. P. Padture, M. Gell, and E. H. Jordan, "Thermal barrier coatings for gas-turbine engine applications," *Science*, vol. 296, no. 5566, pp. 280-284, 2002.
- [15] T. Strangman, D. Raybould, A. Jameel, and W. Baker, "Damage mechanisms, life prediction, and development of EB-PVD thermal barrier coatings for turbine airfoils," *Surface and Coatings Technology*, vol. 202, no. 4-7, pp. 658-664, 2007.
- [16] J. R. Nicholls, Y. Jaslier, and D. Rickerby, "Erosion and foreign object damage of thermal barrier coatings," in *Materials science forum*, 1997, vol. 251: Trans Tech Publ, pp. 935-948.
- [17] R. Wellman, J. Nicholls, and K. Murphy, "Effect of microstructure and temperature on the erosion rates and mechanisms of modified EB PVD TBCs," *Wear*, vol. 267, no. 11, pp. 1927-1934, 2009.
- [18] I. Alfred et al., "Advanced high pressure turbine blade repair technologies," *Procedia CIRP*, vol. 74, pp. 214-217, 2018.
- [19] A. Feuerstein, J. Knapp, T. Taylor, A. Ashary, A. Bolcavage, and N. Hitchman, "Technical and economical aspects of current thermal barrier coating systems for gas turbine engines by thermal spray and EBPVD: a review," *Journal of Thermal Spray Technology*, vol. 17, no. 2, pp. 199-213, 2008.
- [20] GE announces plans to invest up to \$60M to create new global repair engineering and development center in Singapore for its industry-leading HA gas turbines (<https://www.ge.com/news/press-releases/ge-announces-plans-invest-60m-create-new-global-repair-engineering-and-development>; accessed 11/10/2020).
- [21] B. Zhang, X. Zheng, H. Tokura, and M. Yoshikawa, "Grinding induced damage in ceramics," *Journal of materials processing technology*, vol. 132, no. 1-3, pp. 353-364, 2003.

- [22] E. K. Antwi, K. Liu, and H. Wang, "A review on ductile mode cutting of brittle materials," *Frontiers of Mechanical Engineering*, vol. 13, no. 2, pp. 251-263, 2018.
- [23] Y. Liu, J. Deng, H. Yue, R. Duan, X. Li, and K. Ehmann, "Material removal behavior in processing green Al₂O₃ ceramics based on scratch and edge-indentation tests," *Ceramics International*, vol. 45, no. 9, pp. 12495-12508, 2019.
- [24] Q. Wang et al., "Rock-cutting mechanics model and its application based on slip-line theory," *International Journal of Geomechanics*, vol. 18, no. 5, p. 04018025, 2018.
- [25] H. Huang, B. Lecampion, and E. Detournay, "Discrete element modeling of tool-rock interaction I: rock cutting," *International Journal for Numerical and Analytical Methods in Geomechanics*, vol. 37, no. 13, pp. 1913-1929, 2013.
- [26] Y. Liu and J. Deng, "Machining process modeling of green alumina ceramics in orthogonal cutting and fragmentation process," *The International Journal of Advanced Manufacturing Technology*, vol. 113, no. 3, pp. 1009-1027, 2021.
- [27] K. Kitajima, G. Cai, N. Kurnagai, Y. Tanaka, and H. Zheng, "Study on mechanism of ceramics grinding," *CIRP annals*, vol. 41, no. 1, pp. 367-371, 1992.
- [28] S. Malkin and T. Hwang, "Grinding mechanisms for ceramics," *CIRP annals*, vol. 45, no. 2, pp. 569-580, 1996.
- [29] I. Inasaki, "Grinding of hard and brittle materials," *CIRP annals*, vol. 36, no. 2, pp. 463-471, 1987.
- [30] M. Yang et al., "Effect of friction coefficient on chip thickness models in ductile-regime grinding of zirconia ceramics," *The International Journal of Advanced Manufacturing Technology*, vol. 102, no. 5, pp. 2617-2632, 2019.
- [31] A. Choudhary and S. Paul, "Surface generation in high-speed grinding of brittle and tough ceramics," *Ceramics International*, vol. 47, no. 21, pp. 30546-30562, 2021.
- [32] H. Huang, "High speed grinding of advanced ceramics: a review," in *Key Engineering Materials*, 2009, vol. 404: Trans Tech Publ, pp. 11-22.
- [33] Y. Ito, N. Sugita, T. Fujii, T. Kizaki, and M. Mitsuishi, "Precision Machining of Sintered Zirconia Ceramics by High-Speed Milling," (in English), *International Journal of Automation Technology*, vol. 11, no. 6, pp. 862-868, Nov 2017

- [34] F. Toriz, A. Thakker, and S. Gupta, "Flight service evaluation of thermal barrier coatings by physical vapor deposition at 5200 H," *Surface and coatings technology*, vol. 39, pp. 161-172, 1989.
- [35] J. Nicholls, M. Deakin, and D. Rickerby, "A comparison between the erosion behaviour of thermal spray and electron beam physical vapour deposition thermal barrier coatings," *Wear*, vol. 233, pp. 352-361, 1999.
- [36] S. Mahade, A. Venkat, N. Curry, M. Leitner, and S. Joshi, "Erosion performance of atmospheric plasma sprayed thermal barrier coatings with diverse porosity levels," *Coatings*, vol. 11, no. 1, p. 86, 2021.
- [37] T. Bergs, J. Borrmann, M. Schüler, T. Herrig, and J.-E. Döring, "Pure waterjet controlled depth machining for stripping ceramic thermal barrier coatings on turbine blades," *Procedia CIRP*, vol. 85, pp. 261-265, 2019.
- [38] R. H. Hayes, M. Miller, and W. Thompson, "Abrasive waterjet coating removal: efficient and cost-effective," *Advanced Materials & Processes*, vol. 166, no. 11, pp. 76-79, 2008.
- [39] R. H. Hayes, M. O. Miller, and W. R. Thompson, "Removing turbine component coatings without damage," *Power Engineering*, vol. 113, no. 2, pp. 56-59, 2009.
- [40] M. Liu and G. Liu, "Smoothed particle hydrodynamics (SPH): an overview and recent developments," *Archives of computational methods in engineering*, vol. 17, no. 1, pp. 25-76, 2010.
- [41] G.-R. Liu and M. B. Liu, *Smoothed particle hydrodynamics: a meshfree particle method*. World scientific, 2003.
- [42] S. Liakas, C. O'Sullivan, and C. Saroglou, "Influence of heterogeneity on rock strength and stiffness using discrete element method and parallel bond model," *Journal of Rock Mechanics and Geotechnical Engineering*, vol. 9, no. 4, pp. 575-584, 2017.
- [43] J. Ghaboussi and R. Barbosa, "Three-dimensional discrete element method for granular materials," *International Journal for Numerical and Analytical Methods in Geomechanics*, vol. 14, no. 7, pp. 451-472, 1990.
- [44] F. Ma'arif, Z. Gao, and F. Li, "A Review of the Discrete Element Method Application on Concrete Materials," in *Journal of Physics: Conference Series*, 2020, vol. 1625, no. 1: IOP Publishing, p. 012009.

- [45] J. Horabik and M. Molenda, "Parameters and contact models for DEM simulations of agricultural granular materials: A review," *Biosystems engineering*, vol. 147, pp. 206-225, 2016.
- [46] W. D. Grossklaus Jr and P. A. Charles, "Repair of high pressure turbine shrouds," ed: Google Patents, 2001.
- [47] X. J. S. Chen and C. Technology, "Calcium–magnesium–alumina–silicate (CMAS) delamination mechanisms in EB-PVD thermal barrier coatings," vol. 200, no. 11, pp. 3418-3427, 2006.
- [48] A. Scrivani, C. Giolli, and B. A. Allegrini, "Method and equipment for removal of ceramic coatings by co2 coatings," ed: Google Patents, 2013.
- [49] B. A. Nagaraj, S. Mannava, and B. K. Gupta, "Method for repairing a thermal barrier coating," ed: Google Patents, 1998.
- [50] R. W. Bruce, "Method of removing a thermal barrier coating," ed: Google Patents, 2001.
- [51] R. G. Zimmerman Jr, W. C. Brooks, R. D. Wustman, and J. D. Evans Sr, "Method of removing ceramic coatings," ed: Google Patents, 2002.
- [52] D. A. Snow and P. F. Tye, "Education and training," in *Plant Engineer's Reference Book*: Elsevier, 2002, pp. 46-1-46-5.
- [53] R. H. Hayes, M. O. Miller, and W. R. J. P. E. Thompson, "Removing turbine component coatings without damage," vol. 113, no. 2, pp. 56-59, 2009.
- [54] W. C. Brooks, "Method of selectively stripping an engine-run ceramic coating," ed: Google Patents, 2011.
- [55] J. L. Segrest, D. V. Bucci, M. R. Brown, and J. A. DeBarro, "Process of selectively removing layers of a thermal barrier coating system," ed: Google Patents, 2005.
- [56] K. Potter, J. Wang, M. Bailey, and D. Bucci, "Local repair process of thermal barrier coatings in turbine engine components," ed: Google Patents, 2007.
- [57] C. Kilburn, "Method and apparatus for removing a thermal barrier coating from a power generation component," ed: Google Patents, 2005.
- [58] D. Sangeeta, C. A. Johnson, and W. A. Nelson, "Method for smoothing the surface of a protective coating," ed: Google Patents, 2001.
- [59] M. T. Ucasz, "Thermal barrier coating repair," ed: Google Patents, 2016.

- [60] R. Barbini et al., "Laser induced breakdown spectroscopy for semi-quantitative elemental analysis in soils and marine sediments," in Proceedings of EARSeL-SIG-Workshop LIDAR, 2000, vol. 1, pp. 122-129.
- [61] M. Lentjes, K. Dickmann, and J. Meijer, "Controlled laser cleaning of artworks via low resolution LIBS and linear correlation analysis," in 24th International Congress on Applications of Lasers & Electro-Optics, ICALEO 2005, 2005: LIA, pp. M286-M292.
- [62] D. J. A. S. Anglos, "Laser-induced breakdown spectroscopy in art and archaeology," vol. 55, no. 6, pp. 186A-205A, 2001.
- [63] G. R. Leverant, S. T. Schwab, P. P. Paul, and N. S. Cheruvu, "Method of repairing a thermal barrier coating," ed: Google Patents, 2001.
- [64] J. A. Ruud and K. H. Janora, "In-situ method and composition for repairing a thermal barrier coating," ed: Google Patents, 2009.
- [65] D. A. Snow, Plant engineer's reference book. Elsevier, 2001.
- [66] D. V. Bucci, W. M. Miglietti, and M. D. Arnett, "Repair process for coated articles," ed: Google Patents, 2010.
- [67] J. Zhang and Y.-G. Jung, Advanced ceramic and metallic coating and thin film materials for energy and environmental applications. Springer, 2018.
- [68] J. Zhang, X. Guo, Y.-G. Jung, L. Li, and J. Knapp, "Lanthanum zirconate based thermal barrier coatings: A review," Surface and Coatings Technology, vol. 323, pp. 18-29, 2017.
- [69] N. Chawla and K. Chawla, "Microstructure-based modeling of the deformation behavior of particle reinforced metal matrix composites," Journal of Materials Science, vol. 41, no. 3, pp. 913-925, 2006.
- [70] M. Murugan, A. Ghoshal, M. J. Walock, B. B. Barnett, M. S. Pepi, and K. A. Kerner, "Sand particle-Induced deterioration of thermal barrier coatings on gas turbine blades," Advances in aircraft and spacecraft science, vol. 4, no. 1, pp. 37-52, 2017.
- [71] X. Liu, P. Tang, Q. Geng, and X. Wang, "Effect of Abrasive Concentration on Impact Performance of Abrasive Water Jet Crushing Concrete," Shock and Vibration, vol. 2019, 2019.
- [72] S. Nishinoiri, M. Enoki, and K. Tomita, "Evaluation of microfracture mode in ceramic coating during thermal cycle test using laser AE technique," Materials Transactions, vol. 45, no. 1, pp. 92-101, 2004.

- [73] A. A. Hamed, W. Tabakoff, R. B. Rivir, K. Das, and P. Arora, "Turbine blade surface deterioration by erosion," *Journal of turbomachinery*, vol. 127, no. 3, pp. 445-452, 2005.
- [74] G. Fiore and M. S. Selig, "Optimization of wind turbine airfoils subject to particle erosion," in *33rd AIAA Applied Aerodynamics Conference*, 2015, p. 3393.
- [75] A. Lamberts, M. Geers, J. van Dommelen, H. de Lange, A. Huizinga, and P. A. BV, "Numerical simulation of ballistic impacts on ceramic material," *Eindhoven University of Technology*, 2007.
- [76] M. Suzuki and M. Yamamoto, "Numerical simulation of sand erosion phenomena in a single-stage axial compressor," *Journal of Fluid Science and Technology*, vol. 6, no. 1, pp. 98-113, 2011.
- [77] Y. Song, J. Yan, S. Li, and Z. Kang, "Peridynamic Modeling and Simulation of Ice Craters By Impact," *CMES-COMPUTER MODELING IN ENGINEERING & SCIENCES*, vol. 121, no. 2, pp. 465-492, 2019.
- [78] L. Guo, S. Deng, and X. Yang, "Numerical simulation of abrasive water jet cutting chemical pipeline based on SPH coupled FEM," *Chemical Engineering Transactions*, vol. 51, pp. 73-78, 2016.
- [79] E. Hedayati and M. Vahedi, "Numerical investigation of penetration in ceramic/aluminum targets using smoothed particle hydrodynamics method and presenting a modified analytical model," *Computer Modeling in Engineering & Sciences*, vol. 113, no. 3, pp. 295-323, 2017.
- [80] M. Ray, X. Yang, and S.-C. Kong, "Simulation of Drop Impact on a Hot Wall using SPH Method with Peng-Robinson Equation of State," *arXiv preprint arXiv:1707.03850*, 2017.
- [81] LS-DYNA® Analysis for Structural Mechanics
(<https://www.predictiveengineering.com/sites/default/files/ls-dyna-analysis-for-structural-mechanics-2014.pdf>, accessed 5/4/2020).
- [82] K. Vahedi and N. Khazraiyani, "Numerical modeling of ballistic penetration of long rods into ceramic/metal armors," in *8th International LS-DYNA Users Conference*, 2004, vol. 14, pp. 39-50.
- [83] J. Johnson, "General features of Hugoniot," *Report LANL LA*, vol. 13137, 1996.

- [84] J. O. Hallquist, "LS-DYNA® keyword user's manual: volumes I, II, and III LSDYNA R7.1," Livermore Software Technology Corporation, Livermore (LSTC), Livermore, California, vol. 1265, 2014.
- [85] M. Barsotti, "Comparison of FEM and SPH for modeling a crushable foam aircraft arrestor bed," in 11th International LS-DYNA Users Conference (accessed 10/23/2020, <https://www.dynalook.com/conferences/international-conf-2010/Aerospace-2-3.pdf>), 2010, vol. Aerospace (2), pp. 16-37.
- [86] D. S. Cronin, K. Bui, C. Kaufmann, G. McIntosh, T. Berstad, and D. Cronin, "Implementation and validation of the Johnson-Holmquist ceramic material model in LS-Dyna," in Proc. 4th Eur. LS-DYNA Users Conf, 2003, vol. 1, pp. 47-60.
- [87] J. Xu and J. Wang, "Node to node contacts for SPH applied to multiple fluids with large density ratio," presented at the Proceedings of the 9th European LS-DYNA users conference, Manchester, U.K., 2013.
- [88] E. Yreux, "MLS-based SPH in LS-DYNA ® for Increased Accuracy and Tensile Stability," presented at the 15th International LS-DYNA Users Conference, 2018.
- [89] Ho and Philip, "LS-PRE/POST v1.0," ed: Livermore Software Technology Corporation, Livermore 2002.
- [90] J. O. Hallquist, "LS-DYNA theory manual," Livermore software Technology corporation, vol. 3, pp. 25-31, 2006.
- [91] R. G. Wellman and J. R. Nicholls, "A review of the erosion of thermal barrier coatings," Journal of Physics D: Applied Physics, vol. 40, no. 16, pp. R293-R305, 2007.
- [92] M. Murugan et al., "Microstructure Based Material-Sand Particulate Interactions and Assessment of Coatings for High Temperature Turbine Blades," in ASME Turbo Expo 2017: Turbomachinery Technical Conference and Exposition, 2017: American Society of Mechanical Engineers Digital Collection.
- [93] X. Yang et al., "Removal and repair techniques for thermal barrier coatings: a review," Transactions of the IMF, vol. 98, no. 3, pp. 121-128, 2020.
- [94] T. Bergs, J. P. Borrmann, M. Schöler, T. Herrig, and J. E. Döring, "Pure waterjet controlled depth machining for stripping ceramic thermal barrier coatings on turbine blades," Procedia CIRP, vol. 85, pp. 261-265, 2019.

- [95] T. M. Ahmed, A. S. El Mesalamy, A. Youssef, and T. T. El Midany, "Improving surface roughness of abrasive waterjet cutting process by using statistical modeling," *CIRP Journal of Manufacturing Science and Technology*, vol. 22, pp. 30-36, 2018, doi: 10.1016/j.cirpj.2018.03.004.
- [96] W. Thompson. (2011) Coating Removal for Turbine Components Modern Machine Shop (<https://www.mmsonline.com/articles/coating-removal-for-turbine-components>, accessed 6/18/2021).
- [97] K. Kalpana, O. Mythreyi, and M. Kanthababu, "Review on condition monitoring of Abrasive Water Jet Machining system," in 2015 International Conference on Robotics, Automation, Control and Embedded Systems (RACE), 2015: IEEE, pp. 1-7.
- [98] K. Zhao, C. Gao, Z. Liu, and C. Guo, "Investigation of removing thermal barrier coatings from Nickel based super-alloy using abrasive water jet," in *IOP Conference Series: Materials Science and Engineering*, 2018, vol. 452, no. 2: IOP Publishing, p. 022112.
- [99] X. Liu, P. Tang, Q. Geng, and X. Wang, "Effect of Abrasive Concentration on Impact Performance of Abrasive Water Jet Crushing Concrete," *Shock and Vibration*, vol. 2019, pp. 1-18, 2019.
- [100] H. Shahverdi, M. Zohoor, and S. M. Mousavi, "Numerical simulation of abrasive water jet cutting process using the SPH and ALE methods," 2011.
- [101] D. S. S. Ngangkham Peter Singh, *N. Ramesh Babu, "Thermal Analysis of Abrasive Waterjet Machining Process," presented at the Proceedings of 10th International Conference on Precision, Meso and Nano Engineering, India, 2017.
- [102] G.-R. Liu and Y.-T. Gu, *An introduction to meshfree methods and their programming*. Springer Science & Business Media, 2005.
- [103] A. Guha, R. M. Barron, and R. Balachandar, "An experimental and numerical study of water jet cleaning process," *Journal of Materials Processing Technology*, vol. 211, no. 4, pp. 610-618, 2011.
- [104] Z. Zhao, D. Feng, Q. Fang, J. Song, and N. Song, "Dynamics simulation of photonic crystal fiber end face polishing," *Advances in Mechanical Engineering*, vol. 9, p. 168781401771181, 2017.
- [105] J. O. Hallquist, "LS-DYNA keyword user's manual," Livermore Software Technology Corporation, vol. 970, pp. 299-800, 2007.

- [106] B. Denga, M. Yanga, L. Zhoua, H. Wanga, R. Yana, and F. Penga, "Smoothed particle hydrodynamics (SPH) simulation and experimental investigation on the diamond fly-cutting milling of zirconia ceramics," *Procedia CIRP*, vol. 82, pp. 202-207, 2019.
- [107] Density definition (<http://www.lstc.com/lspc/content/pages/7/sphgen/sphgen.shtml>, accessed 5/3/2020).
- [108] J. Zeng and T. J. Kim, "An erosion model for abrasive waterjet milling of polycrystalline ceramics," *Wear*, vol. 199, no. 2, pp. 275-282, 1996.
- [109] J. Zeng and T. J. Kim, "An erosion model of polycrystalline ceramics in abrasive waterjet cutting," *Wear*, vol. 193, no. 2, pp. 207-217, 1996.
- [110] A. N. Kumar and B. F. Sørensen, "Fracture energy and crack growth in surface treated Yttria stabilized Zirconia for SOFC applications," *Materials Science and Engineering: A*, vol. 333, no. 1-2, pp. 380-389, 2002.
- [111] F. Tang and J. M. Schoenung, "Evolution of Young's modulus of air plasma sprayed yttria-stabilized zirconia in thermally cycled thermal barrier coatings," *Scripta Materialia*, vol. 54, no. 9, pp. 1587-1592, 2006.
- [112] J. Zhang and Y.-G. Jung, *Advanced Ceramic and Metallic Coating and Thin Film Materials for Energy and Environmental Applications*. Springer International Publishing, 2017.
- [113] R. G. Wellman, M. J. Deakin, and J. R. Nicholls, "The effect of TBC morphology on the erosion rate of EB PVD TBCs," *Wear*, vol. 258, no. 1, pp. 349-356, 2005.
- [114] J. W. Janssen and J. Malek, "Method and apparatus for milling thermal barrier coated metals (US Patent US20080298920A1)," 2007.
- [115] S. Kar, P. P. Bandyopadhyay, and S. Paul, "Precision superabrasive grinding of plasma sprayed ceramic coatings," *Ceramics International*, vol. 42, no. 16, pp. 19302-19319, 2016.
- [116] S. Kar, P. P. Bandyopadhyay, and S. Paul, "High speed and precision grinding of plasma sprayed oxide ceramic coatings," *Ceramics International*, vol. 43, no. 17, pp. 15316-15331, 2017.
- [117] J. Williams and Y. Patel, "Fundamentals of cutting," *Interface focus*, vol. 6, no. 3, p. 20150108, 2016.
- [118] J. Fulemova and Z. Janda, "Influence of the cutting edge radius and the cutting edge preparation on tool life and cutting forces at inserts with wiper geometry," *Procedia Engineering*, vol. 69, pp. 565-573, 2014.

- [119] T. Zhao, J. Zhou, V. Bushlya, and J. Ståhl, "Effect of cutting edge radius on surface roughness and tool wear in hard turning of AISI 52100 steel," *The International Journal of Advanced Manufacturing Technology*, vol. 91, no. 9-12, pp. 3611-3618, 2017.
- [120] V. Ramesh, "Cutting edge preparation," in *Proceedings of the 9th IFR International Conference*, Indianapolis, IN, USA, 2014, pp. 24-28.
- [121] L. Li, N. He, M. Wang, and Z. Wang, "High speed cutting of Inconel 718 with coated carbide and ceramic inserts," *Journal of Materials Processing Technology*, vol. 129, no. 1-3, pp. 127-130, 2002.
- [122] M. B. da Silva and J. Wallbank, "Cutting temperature: prediction and measurement methods—a review," *Journal of materials processing technology*, vol. 88, no. 1-3, pp. 195-202, 1999.
- [123] T. Childs, "Friction modelling in metal cutting," *Wear*, vol. 260, no. 3, pp. 310-318, 2006.
- [124] C. Rao, D. N. Rao, and P. Srihari, "Influence of cutting parameters on cutting force and surface finish in turning operation," *Procedia Engineering*, vol. 64, pp. 1405-1415, 2013.
- [125] D. Roylance, "Introduction to fracture mechanics," 2001.
- [126] W. Liu, "The Grinding Mechanism of Nanostructured Ceramic Coatings," *Applied Mechanics and Materials*, vol. 341-342, pp. 183-186, 2013.
- [127] J. G. Williams, Y. Patel, and B. Blackman, "A fracture mechanics analysis of cutting and machining," *Engineering Fracture Mechanics*, vol. 77, pp. 293-308, 2010.
- [128] M. N. Nasr and M. M. Ammar, "An evaluation of different damage models when simulating the cutting process using FEM," *Procedia CIRP*, vol. 58, pp. 134-139, 2017.
- [129] Y. Tan, C. Zhang, S. Jiang, and Y. Feng, "Simulation of ceramic grinding mechanism based on discrete element method," *International Journal of Computational Methods*, vol. 16, no. 04, p. 1843008, 2019.
- [130] H. Dai, G. Chen, S. Li, Q. Fang, and B. Hu, "Influence of laser nanostructured diamond tools on the cutting behavior of silicon by molecular dynamics simulation," *RSC advances*, vol. 7, no. 25, pp. 15596-15612, 2017.
- [131] J. Limido, C. Espinosa, M. Salaün, and J.-L. Lacome, "A new approach of high speed cutting modelling: SPH method," *Journal de Physique IV (Proceedings)*, vol. 134, 08/01 2006.

- [132] W. Schirén, "Finite element method for 1D transient convective heat transfer problems," ed, 2018.
- [133] G. Williams, Y. Patel, and B. Blackman, "An analysis of cutting and machining using fracture mechanics concepts," in Proc. 17th European Conf. on Fracture, Brno, Czech Republic, 2–5 September 2013, 2013.
- [134] O. Özbek and H. Saruhan, "The effect of vibration and cutting zone temperature on surface roughness and tool wear in eco-friendly MQL turning of AISI D2," *Journal of Materials Research and Technology*, 2020.
- [135] A. Mir, X. Luo, K. Cheng, and A. Cox, "Investigation of influence of tool rake angle in single point diamond turning of silicon," *Int J Adv Manuf Technol*, vol. 94, no. 5-8, pp. 2343-2355, 2018.
- [136] M. Günay, E. Aslan, I. Korkut, and U. Şeker, "Investigation of the effect of rake angle on main cutting force," *International Journal of Machine Tools and Manufacture*, vol. 44, no. 9, pp. 953-959, 2004.
- [137] J.-x. ZHENG and J.-w. XU, "Experimental research on the ground surface quality of creep feed ultrasonic grinding ceramics (Al_2O_3)," *Chinese Journal of Aeronautics*, vol. 19, no. 4, pp. 359-365, 2006.
- [138] J. Dai et al., "Finite element implementation of the tension-shear coupled fracture criterion for numerical simulations of brittle-ductile transition in silicon carbide ceramic grinding," *International Journal of Mechanical Sciences*, vol. 146, pp. 211-220, 2018.
- [139] J. Cao, Y. Wu, J. Li, and Q. Zhang, "Study on the material removal process in ultrasonic-assisted grinding of SiC ceramics using smooth particle hydrodynamic (SPH) method," *The International Journal of Advanced Manufacturing Technology*, vol. 83, no. 5-8, pp. 985-994, 2016.
- [140] J. Limido, C. Espinosa, M. Salaün, and J.-L. Lacome, "SPH method applied to high speed cutting modelling," *International journal of mechanical sciences*, vol. 49, no. 7, pp. 898-908, 2007.
- [141] P. W. Cleary and M. Prakash, "Discrete–element modelling and smoothed particle hydrodynamics: potential in the environmental sciences," *Philosophical Transactions of the Royal Society of London. Series A: Mathematical, Physical and Engineering Sciences*, vol. 362, no. 1822, pp. 2003-2030, 2004.

- [142] A. A. Munjiza, E. E. Knight, and E. Rougier, Computational mechanics of discontinua. John Wiley & Sons, 2011.
- [143] D. O. Potyondy and P. Cundall, "A bonded-particle model for rock," International journal of rock mechanics and mining sciences, vol. 41, no. 8, pp. 1329-1364, 2004.
- [144] H. Li, C. Yang, X. Ding, N. William, H. Yin, and S. Zhang, "Weibull linear parallel bond model (WLPBM) for simulating micro-mechanical characteristics of heterogeneous rocks," Engineering Analysis with Boundary Elements, vol. 108, pp. 82-94, 2019.
- [145] Y. Tan, D. Yang, and Y. Sheng, "Discrete element method (DEM) modeling of fracture and damage in the machining process of polycrystalline SiC," Journal of the European ceramic society, vol. 29, no. 6, pp. 1029-1037, 2009.
- [146] S. Jiang et al., "Mechanical behavior of SiC ceramics with single flaw under three-point bending," Ceramics International, vol. 47, no. 13, pp. 18625-18634, 2021.
- [147] S. Jiang, X. Li, Y. Tan, H. Liu, Z. Xu, and R. Chen, "Discrete element simulation of SiC ceramic with pre-existing random flaws under uniaxial compression," Ceramics International, vol. 43, no. 16, pp. 13717-13728, 2017.
- [148] A. Jadhav, N. P. Padture, F. Wu, E. H. Jordan, and M. Gell, "Thick ceramic thermal barrier coatings with high durability deposited using solution-precursor plasma spray," Materials Science and Engineering: A, vol. 405, no. 1-2, pp. 313-320, 2005.
- [149] X. Cao, R. Vaßen, and D. Stöver, "Ceramic materials for thermal barrier coatings," Journal of the European Ceramic Society, vol. 24, no. 1, pp. 1-10, 2004.
- [150] Y. Wang, M. Li, and H. Suo, "Mechanical properties of YSZ thermal barrier coatings with segmented structure," Surface engineering, vol. 28, no. 5, pp. 329-332, 2012.
- [151] W. Kaysser, K. Fritscher, B. Saruhan-Brings, and U. Schulz, "Processing of Advanced EB-PVD Thermal Barrier Coating Systems," in International Symposium on Advanced Thermal Barrier Coatings and Titanium Aluminides for Gas Turbines, 2002: DLR, Institut für Werkstoff-Forschung, pp. 32-34.
- [152] G. Boothroyd, Fundamentals of metal machining and machine tools. Crc Press, 1988.
- [153] X. He and C. Xu, "Discrete element modelling of rock cutting: from ductile to brittle transition," International Journal for Numerical and Analytical Methods in Geomechanics, vol. 39, no. 12, pp. 1331-1351, 2015.

- [154] A. Beaucamp, P. Simon, P. Charlton, C. King, A. Matsubara, and K. Wegener, "Brittle-ductile transition in shape adaptive grinding (SAG) of SiC aspheric optics," *International Journal of Machine Tools and Manufacture*, vol. 115, pp. 29-37, 2017.
- [155] S. Arefin, X. Li, M. Cai, M. Rahman, K. Liu, and A. Tay, "The effect of the cutting edge radius on a machined surface in the nanoscale ductile mode cutting of silicon wafer," *Proceedings of the Institution of Mechanical Engineers, Part B: Journal of Engineering Manufacture*, vol. 221, no. 2, pp. 213-220, 2007.
- [156] L. Łatka, D. Chicot, A. Cattini, L. Pawłowski, and A. Ambroziak, "Modeling of elastic modulus and hardness determination by indentation of porous yttria stabilized zirconia coatings," *Surface and Coatings Technology*, vol. 220, pp. 131-139, 2013.
- [157] M. C. Jaime, Y. Zhou, J.-S. Lin, and I. K. Gamwo, "Finite element modeling of rock cutting and its fragmentation process," *International Journal of Rock Mechanics and Mining Sciences*, vol. 80, pp. 137-146, 2015.
- [158] P. Huang and J. Zhang, "Strain rate effect on the ductile brittle transition in grinding hot pressed SiC ceramics," *Micromachines*, vol. 11, no. 6, p. 545, 2020.
- [159] X. Guo, Z. Lu, Y.-G. Jung, and J. Zhang, "Overview of Lanthanum Zirconate-Based Thermal Barrier Coatings," in *Novel Lanthanum Zirconate-based Thermal Barrier Coatings for Energy Applications*: Springer, 2021, pp. 1-11.
- [160] L. Yang, H. Li, Y. Zhou, W. Zhu, Y. Wei, and J. Zhang, "Erosion failure mechanism of EB-PVD thermal barrier coatings with real morphology," *Wear*, vol. 392, pp. 99-108, 2017.
- [161] A. Vasinonta and J. L. Beuth, "Measurement of interfacial toughness in thermal barrier coating systems by indentation," *Engineering Fracture Mechanics*, vol. 68, no. 7, pp. 843-860, 2001.
- [162] X. Chen, J. W. Hutchinson, and A. G. Evans, "Simulation of the high temperature impression of thermal barrier coatings with columnar microstructure," *Acta Materialia*, vol. 52, no. 3, pp. 565-571, 2004.
- [163] M. Tanaka, Y.-F. Liu, and Y. Kagawa, "Identification of delamination through TGO stresses due to indentation testing of an EB-PVD TBC," *Journal of Materials Research*, vol. 24, no. 12, pp. 3533-3542, 2009.

- [164] X. Chen, M. He, I. Spitsberg, N. Fleck, J. Hutchinson, and A. Evans, "Mechanisms governing the high temperature erosion of thermal barrier coatings," *Wear*, vol. 256, no. 7-8, pp. 735-746, 2004.
- [165] L. Wang, Y. Wang, X. Sun, Z. Pan, J. He, and C. Li, "Influence of pores on the surface microcompression mechanical response of thermal barrier coatings fabricated by atmospheric plasma spray—Finite element simulation," *Applied Surface Science*, vol. 257, no. 6, pp. 2238-2249, 2011.
- [166] K. Von Niessen and M. Gindrat, "Plasma spray-PVD: a new thermal spray process to deposit out of the vapor phase," *Journal of thermal spray technology*, vol. 20, no. 4, pp. 736-743, 2011.
- [167] M. A. Meyers and K. K. Chawla, *Mechanical behavior of materials*. Cambridge university press, 2008.
- [168] F. Cernuschi et al., "Solid particle erosion of thermal spray and physical vapour deposition thermal barrier coatings," *Wear*, vol. 271, no. 11-12, pp. 2909-2918, 2011.
- [169] S. Malkin and C. Guo, *Grinding technology: theory and application of machining with abrasives*. Industrial Press Inc., 2008.
- [170] H. Huang and L. Yin, "High speed grinding performance and material removal mechanism of silicon nitride," in *Initiatives of Precision Engineering at the Beginning of a Millennium*: Springer, 2002, pp. 416-420.

VITA

Jian Zhang was born in Anqiu, Shandong, Peoples Republic of China in 1985. He graduated from Lanzhou Jiaotong University (China) with a B.S. degree in Civil Engineering in 2008. Then he obtained an M.S. degree in Civil Engineering from Shanghai Jiaotong University in 2017. He is currently a Ph.D. candidate in the School of Mechanical Engineering at Purdue University. His research under the direction of Professor Jing Zhang and Professor Carl Wassgren focuses on the TBCs removal processes.

LIST OF PUBLICATIONS

Journal papers

- **Jian Zhang**, Sugrim Sagar, Dan Daehyun Koo, Hyunhee Choi, Yeon-Gil Jung, Heesung Park, Jing Zhang. Modeling of removing thermal barrier coatings by abrasive water jet using smoothed particle hydrodynamics method. Under review.
- **Jian Zhang**, Sugrim Sagar, Dan Daehyun Koo, Hyunhee Choi, Yeon-Gil Jung, Heesung Park, Jing Zhang. Modeling of ceramic coatings grinding behavior using smoothed particle hydrodynamics method. Under review.
- **Jian Zhang**, Sugrim Sagar, Tejesh Dube, Xuehui Yang, and Jing Zhang, Modeling of thermal barrier coating grinding Process using discrete element method. Under review.
- **Jian Zhang**, Zhe Lu, Sugrim Sagar, Hyunhee Choi, Heesung Park, Dan Daehyun Koo, Yeon-Gil Jung, and Jing Zhang. Numerical simulation of impact behavior of ceramic coatings using smoothed particle hydrodynamics method. Journal of Engineering Materials and Technology, 2021, 143(2), p. 1-8. [DOI: 10.1115/1.4049021](https://doi.org/10.1115/1.4049021)
- Xuehui Yang, **Jian Zhang**, Zhe Lu, Hye-Yeong Park, Yeon-Gil Jung, Heesung Park, Dan Daehyun Koo, Ray Sinatra, and Jing Zhang. Removal and repair techniques for thermal barrier coatings: a review. Transactions of the IMF, 2020, 98(3), p. 121-128. [DOI: 10.1080/00202967.2020.1750204](https://doi.org/10.1080/00202967.2020.1750204)
- Yang, Xuehui, **Jian Zhang**, Hye-Yeong Park, Yeon-Gil Jung, Alan Jones, and Jing Zhang. "Water surface reinforcement effect in 3D printed polymer derived SiOC ceramics." Applied Physics A 127, no. 2 (2021): 1-7. [DOI:10.1007/s00339-021-04305-2](https://doi.org/10.1007/s00339-021-04305-2)
- Li, Yafeng, Anvesh Dhulipalla, **Jian Zhang**, Hye-Yeong Park, Yeon-Gil Jung, Dan Daehyun Koo, and Jing Zhang. "Finite element modeling of coating thickness using heat transfer method." CIRP Journal of Manufacturing Science and Technology 32 (2021): 249-256. [DOI: 10.1016/j.cirpj.2021.01.005](https://doi.org/10.1016/j.cirpj.2021.01.005)
- Dhulipalla, Anvesh, Budireddy Uday Kumar, Varupula Akhil, **Jian Zhang**, Zhe Lu, Hye-Yeong Park, Yeon-Gil Jung, and Jing Zhang. Synthesis and machining characteristics of novel TiC ceramic and MoS₂ soft particulate reinforced aluminum alloy 7075 matrix composites. Manufacturing Letters, 2020, 24, p. 82-86. [DOI: 10.1016/j.mfglet.2020.04.001](https://doi.org/10.1016/j.mfglet.2020.04.001)

Conference papers

- **Jian Zhang**, Sugrim Sagar, Tejesh Dube, Xuehui Yang, and Jing Zhang, Modeling of thermal barrier coating cutting Process using discrete element method. POWDERMET2021 & AMPM2021 conferences, Orlando, FL, June 20-23 in Orlando, 2021.
- **Jian Zhang**, Harshal G. Dhamade, Sugrim Sagar, Dan Daehyun Koo, Hyunhee Choi, Yeon-Gil Jung, Heesung Park, and Jing Zhang. Design and extrusion process of water atomized 17-4 PH stainless steel powder. POWDERMET2019 & AMPM2019 conferences, Phoenix, AZ, June 23-26, 2019.